

# DISSERTATION / DOCTORAL THESIS

Titel der Dissertation / Title of the Doctoral Thesis

„Predictive Value and Limitations of Preclinical Methods  
in PET- Tracer Development“

verfasst von / submitted by

Mag.pharm. Theresa Balber

angestrebter akademischer Grad / in partial fulfilment of the requirements for the degree of

Doktorin der Naturwissenschaften (Dr.rer.nat.)

Wien, 2019 / Vienna 2019

Studienkennzahl lt. Studienblatt /  
degree programme code as it appears on the student  
record sheet:

A 796 610 449

Dissertationsgebiet lt. Studienblatt /  
field of study as it appears on the student record sheet:

Pharmazie

Betreut von / Supervisor:

O. Univ.-Prof. Mag. Dr. Helmut Viernstein

Prof. Mag. Dr. Markus Mitterhauser

# ACKNOWLEDGEMENTS

---

I would like to express my deep gratitude to O. Univ.-Prof. Mag. Dr. Helmut Viernstein, my research supervisor, for his valuable advices in the development of this thesis. My deepest appreciation goes to Prof. Mag. Dr. Markus Mitterhauser, who patiently guided me in the right direction, for his enthusiastic encouragement and constructive discussions during my research. I would like to thank Prof. Mag. Dr. Wolfgang Wadsak for mentoring my thesis all times and his useful critiques. I received generous support from Univ.-Prof. Dr. Marcus Hacker, who provided the necessary resources, which made my work possible. I would also like to express my gratitude to Prof. Dr. Erika Jensen-Jarolim, who provided access to her research facilities.

I would like to thank the post-doctoral fellows Dr. Christina Rami-Mark, MSc and Dr. Josef Singer, PhD for their support in the beginning of my studies and their willingness to give their time so generously. I wish to thank Dipl. Chem. Neydher Berroterán-Infante, Dr. Chrysoula Vraka, MSc and Mag. Dr. Cécile Philippe for their helpfulness and valuable contribution to this research. I am grateful for the experimental assistance given by Judit Fazekas-Singer, PhD, MSc. I thank Mag. Dr. Verena Pichler and Dipl.-Ing. Ivo Rausch, PhD for their cooperation and permission to include graphic material. My grateful thanks are extended to Ing. Andreas Krcal, Ing. Thomas Zenz, Friedrich Girschele and Mag. Mirosława Matz for their technical support.

Finally, I want to thank my family and Mag.pharm. Felix Bachmair for their support and encouragement throughout my studies.



# ABSTRACT

---

In an era, where personalized medicine is envisioned, molecular imaging is significant to the realization of an individually tailored therapy according to the patient's needs. Positron emission tomography (PET) uses the favorable physical properties of positron decay to trace the distribution of a radio-labeled pharmaceutical (PET-tracer) *in vivo*. PET enables a non-invasive, quantitative and highly sensitive visualization of any molecular event or biological process – depending on the employed PET-tracer. In this manner, PET serves as a molecular diagnostic tool that provides an accurate and sensitive detection of diseases in an early stage.

The ideal PET imaging strategy combines the favorable characteristics of the target, a suitable physicochemical and pharmacokinetic profile of the PET-tracer and a specific target-ligand-interaction. One key challenge in PET-tracer development is the precise evaluation of these characteristics, as the translational and predictive value of preclinical methods regarding the suitability of newly developed PET-tracers for human application is controversially discussed.

PET imaging strategies within the scope of this thesis included the A<sub>3</sub> adenosine receptor (A<sub>3</sub>AR), the 18 kDa translocator protein (TSPO) and the melanin-concentrating hormone receptor 1 (MCHR1). [<sup>18</sup>F]FE@SUPPY, the first A<sub>3</sub>AR PET-tracer, evinced as a highly lipophilic compound and showed unspecific binding, unfavorable pharmacokinetics and low *in vivo* stability in a mouse model. Thus, in its given form, [<sup>18</sup>F]FE@SUPPY is inadequate to serve as a PET-tracer for A<sub>3</sub>AR imaging. The well-established TSPO PET-tracer [<sup>18</sup>F]FEPPA, which is currently in clinical use for microglia activation, was evaluated *in vitro* in colorectal cancer for the first time. Preliminary testing showed promising results regarding the specificity of [<sup>18</sup>F]FEPPA binding to colon cancer tissue and cells. However, clinical TSPO PET imaging using [<sup>18</sup>F]FEPPA is limited due to the polymorphism rs6971. Therefore, this imaging strategy provides only a temporary solution until a PET-tracer is developed, which binds with equal affinity to TSPO in all patients. In a detailed *in vitro* and *in vivo* evaluation, the MCHR1 PET-tracers, [<sup>11</sup>C]SNAP-7941 and [<sup>18</sup>F]FE@SNAP, were compared regarding affinity, selectivity, metabolic stability and quality of PET imaging data. [<sup>11</sup>C]SNAP-7941 emerged as the superior tracer compared to [<sup>18</sup>F]FE@SNAP for future human use. In a further study, special emphasis was placed on the evaluation of [<sup>11</sup>C]SNAP-7941 for brown adipose tissue imaging, as preliminary data indicated MCHR1 expression. Thus, besides a clinical application of [<sup>11</sup>C]SNAP-7941 in mental and neurologic disorders, an application in metabolic related diseases is becoming more and more realistic.





# ZUSAMMENFASSUNG

---

Molekulare Bildgebung ist essentiell für die Realisierung einer individuell auf die Bedürfnisse des Patienten zugeschnittenen Therapie (personalisierte Medizin). Die Positronen-Emissions-Tomographie (PET) nutzt die physikalischen Eigenschaften des Positronen-Zerfalls, um die Verteilung eines radioaktiv markierten Arzneimittels (PET-Tracer) *in vivo* zu verfolgen. PET ermöglicht die nicht-invasive, quantitative und hochsensitive Darstellung molekularer Ereignisse und biologischer Prozesse in Abhängigkeit des eingesetzten PET-Tracers. Auf diese Weise dient PET als molekular-diagnostisches Bildgebungsverfahren, um Krankheiten frühzeitig und präzise zu erkennen.

Die ideale PET-Bildgebungsstrategie kombiniert die günstigen Eigenschaften der Zielstruktur mit einem geeigneten physikochemischen und pharmakokinetischen Profil des PET-Tracers sowie einer spezifischen Zielstruktur-Liganden-Wechselwirkung. Eine Herausforderung in der Entwicklung von neuen PET-Tracern ist die genaue Bewertung dieser Eigenschaften, da der translatorische und prädiktive Wert präklinischer Methoden hinsichtlich der Eignung von neu entwickelten PET-Tracern zur Anwendung am Menschen kontrovers diskutiert wird.

Die Bildgebungsstrategien im Rahmen dieser Arbeit umfassten den A<sub>3</sub>-Adenosinrezeptor (A<sub>3</sub>AR), das 18 kDa Translokator-Protein (TSPO) und den Melanin-konzentrierenden-Hormonrezeptor 1 (MCHR1). [<sup>18</sup>F]FE@SUPPY, der erste PET-Tracer für den A<sub>3</sub>AR, erwies sich als lipophile Verbindung und zeigte in einem Mausmodell eine hohe unspezifische Bindung, ungünstige pharmakokinetische Eigenschaften und eine geringe Stabilität. Daher ist [<sup>18</sup>F]FE@SUPPY in seiner gegebenen Form als PET-Tracer ungeeignet für die A<sub>3</sub>AR-Bildgebung. Der TSPO PET-Tracer [<sup>18</sup>F]FEPPA, welcher zur Darstellung der Mikroglia-Aktivierung klinisch angewendet wird, wurde erstmals *in vitro* bei Darmkrebs untersucht. Vorläufige Tests zeigten vielversprechende Ergebnisse hinsichtlich der Spezifität der Bindung von [<sup>18</sup>F]FEPPA zu Darmkrebsgewebe und -zellen. Jedoch ist [<sup>18</sup>F]FEPPA aufgrund des Polymorphismus im TSPO-Gen für die klinische Anwendung nur bedingt geeignet. In einer detaillierten *in vitro* und *in vivo* Untersuchung wurden die beiden MCHR1 PET-Tracer [<sup>11</sup>C]SNAP-7941 und [<sup>18</sup>F]FE@SNAP hinsichtlich Affinität, Selektivität, metabolischer Stabilität und Qualität der PET-Bildgebungsdaten verglichen. [<sup>11</sup>C]SNAP-7941 erwies sich als der überlegene PET-Tracer gegenüber [<sup>18</sup>F]FE@SNAP für eine zukünftige Anwendung am Menschen. Der Fokus einer weiteren Studie lag auf der Evaluierung von [<sup>11</sup>C]SNAP-7941 für die Bildgebung von braunem Fettgewebe. Neben einer klinischen Anwendung von [<sup>11</sup>C]SNAP-7941 bei psychischen und neurologischen Störungen wird eine Anwendung bei Stoffwechselerkrankungen immer realistischer.



# TABLE OF CONTENT

---

Acknowledgements .....	II
Abstract.....	IV
Zusammenfassung .....	VI
Table of Content .....	VIII
<b>GENERAL PART .....</b>	<b>1</b>
1. INTRODUCTION .....	3
1.1 Molecular Imaging .....	3
1.1.1 Key Strengths of Positron Emission Tomography .....	3
1.1.2 General Aspects of Radiopharmaceuticals for PET .....	7
1.2 Preclinical PET-tracer development.....	11
1.2.1 The Rationale for the Development of Novel PET-tracers.....	11
1.2.2 The Pursuit of a Successful Imaging Strategy.....	12
1.2.3 Characterization of the Target.....	13
1.2.4 Characterization of the Radioligand .....	14
1.2.5 Characterization of the Target-Ligand Interaction.....	18
1.3 Targets of Interest and Imaging Strategies .....	23
1.3.1 A <sub>3</sub> Adenosine Receptor .....	23
1.3.2 18 kDa Translocator Protein .....	25
1.3.3 Melanin-Concentrating Hormone Receptor 1 .....	27
2. AIM.....	29
<b>SPECIFIC PART .....</b>	<b>31</b>
3. SCIENTIFIC PAPERS.....	33
3.1 Manuscript #1 .....	35
3.2 Manuscript #2.....	49
3.3 Manuscript #3.....	63
3.4 Manuscript #4.....	83
3.5 Manuscript #5.....	97
4. UNPUBLISHED RESULTS .....	119
4.1. <i>Ex vivo</i> tumor autoradiography .....	119
4.2. [ <sup>18</sup> F]FE@SUPPY uptake in mouse brain .....	119
4.3 <i>Ex vivo</i> metabolic stability.....	120
4.4 Cell binding and internalization studies .....	121
4.5 Characterization of A <sub>3</sub> AR expression in multicellular spheroids .....	123
5. DISCUSSION .....	125
5.1 Characterization of the Target.....	125
5.2 Characterization of the Radioligand .....	127
5.3 Characterization of the Target-Ligand-Interaction .....	128
6. CONCLUSION AND FUTURE CONSIDERATIONS .....	133
Bibliography.....	137
List of Figures.....	151





# GENERAL PART

---





# 1. INTRODUCTION

---

## 1.1 Molecular Imaging

### 1.1.1 Key Strengths of Positron Emission Tomography

The basic principle behind molecular imaging involves the visualization, characterization and measurement of biological processes in a living organism on a molecular and cellular level. (1) The rapidly growing field of molecular imaging employs optical, magnetic resonance and nuclear imaging techniques among others. (2) In positron emission tomography (PET), the favorable properties of positron decay ( $\beta^+$  decay) are used to trace the distribution of a radiolabeled pharmaceutical *in vivo* (Figure 1): When a proton is converted into a neutron inside a neutron-deficient nucleus, a positron ( $\beta^+$ ) and an electron neutrino ( $\nu_e$ ) are subsequently emitted. Depending on the emission energy, the positron travels a certain distance in the surrounding tissue (positron range) until it collides with its respective antiparticle - an electron. This annihilation process results in the emission of two high-energy gamma rays (511 keV)  $180^\circ$  apart, which can be detected outside the body in coincidence. The registration of coincident photons is assigned to a line of response (LOR), providing positional information of the positron decay. Mathematical image reconstruction and the application of correction factors for attenuation and scatter enable the computation of cross-sectional images depicting the concentration of the radiopharmaceutical in a respective tissue. (3)

The uniqueness of PET lies in the application of a positron-emitting radiopharmaceutical, which is fundamental to the key strengths of this imaging technique: The most abundant elements in bioorganic molecules - carbon, nitrogen and oxygen - have positron-emitting isotopes. This fact facilitates direct substitution resulting in a radiolabeled molecule, which displays biologically identical properties as the native compound. (4) In this manner, PET realizes the concept of molecular imaging most accurately as theoretically any biological process can be imaged. Moreover, high molar activity of the radiopharmaceutical combined with the sensitivity of radioactivity detection allows for a very low injected mass of radiopharmaceutical. Consequently, the administered pico- to nanomolar drug amount does not exert pharmacological effects and does not interfere with the biological process to be imaged. The regional tissue concentration (*in vivo* distribution) of these trace amounts of radiopharmaceutical (PET-tracer) can be measured as a function of time. Thus, PET permits dynamic and quantitative imaging while being among the most sensitive imaging techniques. (5)

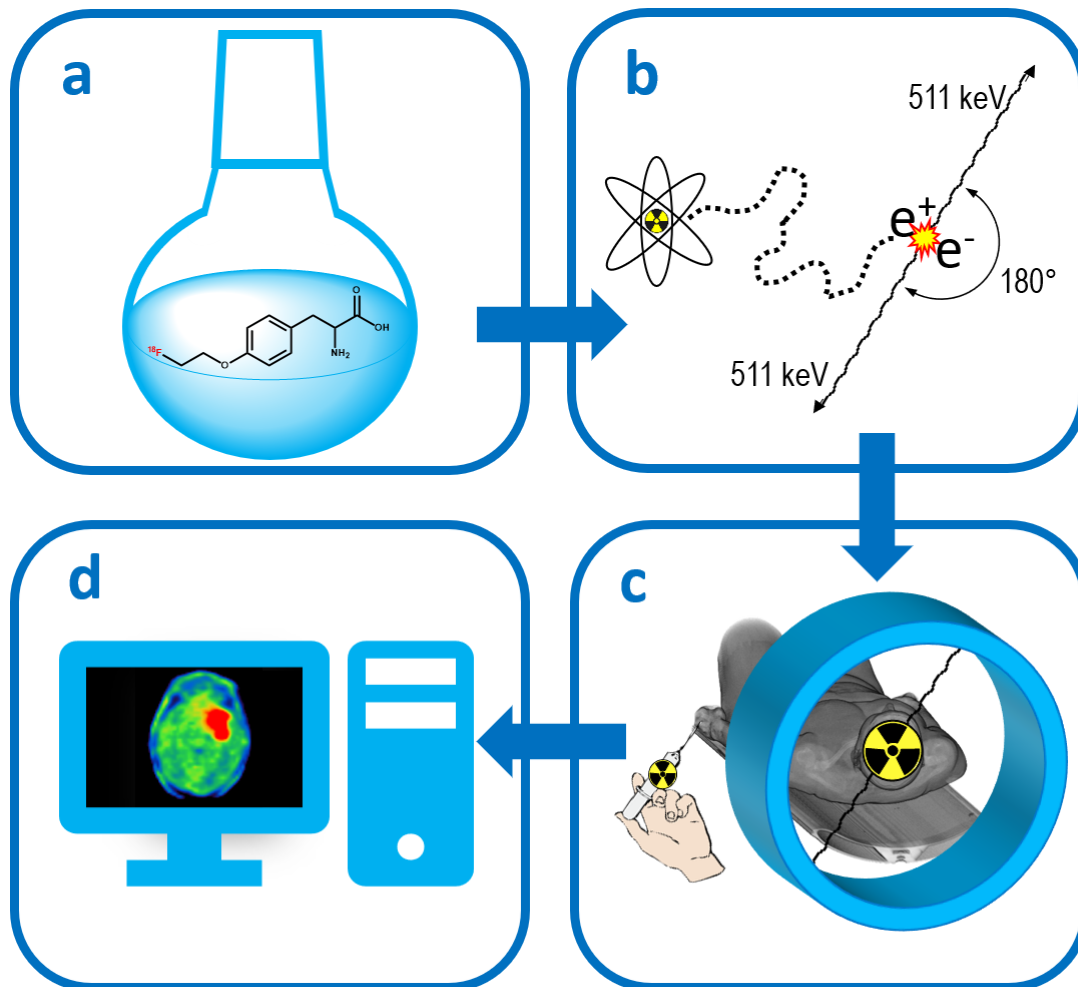


**Figure 1:** Principles of Positron Emission Tomography (PET) exemplified by *O*-(2-[<sup>18</sup>F]fluoroethyl)-L-tyrosine ([<sup>18</sup>F]FET): (a) pharmaceutical preparation of a biomolecule labeled with a positron-emitting nuclide (PET-tracer), i.e. radio-fluorinated amino acid derivative, (b) physical principle of positron decay (positron ejection from nucleus, annihilation with electron and emission of two gamma rays), (c) intravenous PET-tracer administration with subsequent biodistribution and registration of two annihilation photons in coincidence by a PET detector ring, (d) processing of measured PET raw data and image reconstruction: [<sup>18</sup>F]FET accumulation indicates brain regions with enhanced amino acid metabolism. (Figure reworked with permission of Dipl.-Ing. Ivo Rausch, PhD, Center for Medical Physics and Biomedical Engineering, Medical University of Vienna, Austria.)

The clinical significance of PET bases on the fact that many diseases have their origin in preceding metabolic changes. Morphological manifestation and the onset of symptoms occur later, often when the disease has already progressed to severity. In this way, PET serves as a molecular diagnostic tool that enables an accurate and sensitive detection of diseases in an early stage. Noteworthy, deficits in cerebral glucose metabolism were detected with PET in asymptomatic patients suffering from Huntington's or familial Alzheimer's disease 5 to 7 years before clinical symptoms were expressed. (6)

One of the main advantages of PET is its capability to characterize molecular alterations in diseased tissues without invasive biopsy or surgical procedure. This is particularly beneficial for diagnosing diseases affecting the central nervous system as biopsies of the brain are hardly feasible. Neuroimaging became one of the broadest fields in nuclear medicine including imaging of brain tumors, mood disorders and neurodegenerative diseases: The applications for PET range from serotonin-1A-receptor imaging in depression to tau imaging in neurodegenerative disorders. (7-9) The molecular detection of beta-amyloid plaques using e.g. [ $^{11}\text{C}$ ]Pittsburgh compound B or [ $^{18}\text{F}$ ]Florbetapir provides an *in vivo* measure of one of the key pathologic hallmarks of Alzheimer's disease. (10, 11) Imaging of the presynaptic dopaminergic system using [ $^{18}\text{F}$ ]FDOPA is fundamental in Parkinson's disease and other motion disorders as well as schizophrenia. (12)

Evidently, PET plays a crucial role in the diagnosis of cancer, where the early detection of tumors contributes significantly to a reduction in mortality for certain tumor-related pathologies. (13) Moreover, PET does not only allow for tumor localization but also for imaging of biological processes involved, such as angiogenesis and hypoxia which are relevant to tumor behavior and microenvironment. (14) It is well recognized that changes in tumor volume, which are measured by anatomical imaging methods, occur with a time delay and often do not reflect efficacy of therapy. Conversely, the characterization of the tumor's metabolic profile is significant in the assessment of the tumor stage and aggressiveness. (2) In this context, it is important to recognize that PET provides functional imaging data, which substantially differentiates this technique from others providing anatomical or morphological information such as computer tomography (CT), X-ray or magnetic resonance imaging (MRI). Multimodality imaging (e.g. PET/CT, PET/MRI) combining the functional information from PET with anatomical structures provides a more advanced technology and opens new perspectives in clinical and preclinical imaging (Figure 2). (15)

The capability of PET to visualize a targeted molecular event non-invasively, repeatedly and continuously in a living organism made a distinct impact in biomedical research. (16) The combination of an imaging biomarker with a therapeutic agent allows for the prediction of treatment efficacy and monitoring of subsequent therapy response. Confirmation of target expression using diagnostic imaging followed by targeted radionuclide therapy proved to be remarkable effective in thyroid cancer (iodine symporter), neuroendocrine tumors (somatostatin receptors) and prostate cancer (prostate specific membrane antigen, Theragnostic Concept). (17) In this context, molecular imaging is decisive in the realization of an individually tailored therapy depending on the specific patient's metabolic profile. Thus, molecular imaging modalities including PET are recognized as indispensable for the implementation of "Precision Medicine". (18)

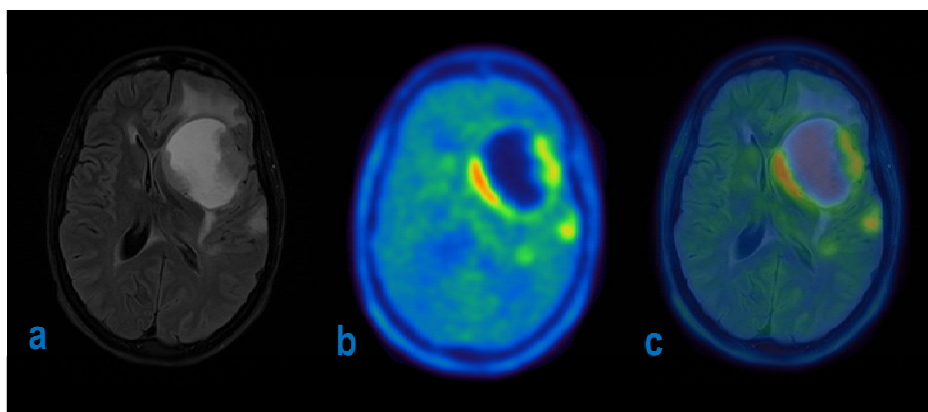


Figure 2: [ $^{18}\text{F}$ ]FET PET/MRI of a patient with recurrent glioma: Data acquisition was performed for 10 min time starting at 30 min post injection of  $\sim 200$  MBq [ $^{18}\text{F}$ ]FET on a Siemens Biograph mMR at the Division of Nuclear Medicine, Vienna General Hospital. (a) T2-weighted MRI image (dark-fluid, TIRM sequence), (b) PET image, (c) fused PET/MRI image combining complementary information of both imaging modalities (Figure provided by Dipl.-Ing. Ivo Rausch, PhD, Center for Medical Physics and Biomedical Engineering, Medical University of Vienna, Austria).

Moreover, there is an upcoming interest in using PET in early drug development. The possibility of radiolabeling a candidate drug and the subsequent performance of molecular imaging enable to address questions central to drug development. Biodistribution studies reveal a successful delivery of the drug to its site of action, which is crucial for central nervous system (CNS) and oncologic drugs. Additionally, parameters relevant for the pharmacological activity of a drug e.g. free drug (radioligand) concentration, blood clearance and receptor occupancy can be derived from PET imaging data. These data may have a major impact on dose finding and dosing frequency in later human studies. Ultimately, PET improves decision-making upon the selection or rejection of a compound in an early stage of drug development reducing drug attrition in later (clinical) phases. (19, 20)

PET is not only a powerful clinical tool, but also a scientific instrument for probing biochemical processes and exploring new targets *in vivo*. Main advances in neuroscience have been made due to imaging modalities such as PET: The understanding of the brain's function and structure evolved as the identification of specific parts of the brain responsible for different aspects of thinking and emotion became possible. (21) Meanwhile, PET is widely appreciated in the broad field of basic research among various disciplines. In endocrinology, the valuable contribution of PET was ultimately recognized, when the serendipitous discovery of functional brown adipose tissue in human adults was reported. (22-24)

## 1.1.2 General Aspects of Radiopharmaceuticals for PET

As mentioned above, PET requires the administration of a radiolabeled tracer, which usually occurs intravenously prior to PET acquisition. These radiopharmaceuticals (PET-tracers) are considered *“the heart of molecular imaging, pumping life into PET/CT”*. (25)

Radionuclides employed in PET imaging are characterized by a relative short physical half-life which is beneficial to a reduced radiation burden but is challenging to radiochemistry aspects. Prerequisite for the preclinical evaluation of a PET-tracer and a potential clinical application is the successful radiolabeling in high (radio)chemical purity and yield. Ideally, radiosynthesis occurs fully-automatized to reduce radiation burden for the operator. (25-27)

The preparation of a radiopharmaceutical involves (Figure 3):

- the production of the radionuclide and its chemical activation,
- the radiolabeling procedure (radiosynthesis),
- the purification of the crude reaction mixture, and
- the physiological formulation of the product.

Generally, PET nuclides are produced in a cyclotron by bombardment of appropriate target material with accelerated, high-energy protons or deuterons. For example, carbon-11 is produced through proton bombardment of nitrogen-14 gas containing trace amounts of either hydrogen or oxygen to yield  $[^{11}\text{C}]\text{CH}_4$  or  $[^{11}\text{C}]\text{CO}_2$ , respectively. For the production of fluorine-18, oxygen-18 enriched water ( $[^{18}\text{O}]\text{H}_2\text{O}$ ) serves as liquid target yielding  $[^{18}\text{F}]\text{fluoride}$ . (28, 29) One exception applies for gallium-68, which is a generator-produced positron emitter making this radiometal readily available. However, radiometals require the use of chelators and are inadequate to label small molecules covalently. (30) Radiolabeling procedures using radiometals are thus not further discussed here.

The production and processing of carbon-11 require an on-site cyclotron and a dedicated radiochemistry facility close by due to its short half-life of 20.3 min. Fluorine-18 is a common alternative owing to its favorable physical properties regarding its half-life of 109.7 min and its low positron energy, thus providing the best image quality in terms of spatial resolution. Additionally, the relatively long half-life allows for a commercial distribution according to the “satellite” principle, which makes both, fluorine-18 labeled radiopharmaceuticals and  $[^{18}\text{F}]\text{fluoride}$ , for further radiochemical synthesis available to hospitals or research centers not equipped with a cyclotron. (26)

The cyclotron-produced radionuclides are usually obtained in chemically unreactive species e.g. aqueous [ $^{18}\text{F}$ ]fluoride solution. Methods to enhance fluoride reactivity include the addition of a large counter-ion (e.g. tetrabutylammonium salts), azeotropic drying and phase transfer catalysis (e.g. using acetonitrile and Kryptofix K<sub>222</sub>). Similar applies for the relatively unreactive building blocks [ $^{11}\text{C}$ ]CO<sub>2</sub> and [ $^{11}\text{C}$ ]CH<sub>4</sub>, which require subsequent transformation to alkylating reagents (e.g. [ $^{11}\text{C}$ ]methyl iodide or [ $^{11}\text{C}$ ]methyl triflate). To obtain a PET-tracer in reasonable yields, the synthesis time including purification steps and quality control should be conducted within 2-3 times the physical half-life of the respective radionuclide. The introduction of the radiolabel should be straightforward and as late as possible during radiosynthesis. Alkylation with [ $^{11}\text{C}$ ]methyl iodide is straightforward and thus the most widely used method for introducing carbon-11 into an organic molecule. In aliphatic nucleophilic fluorinations, trifluoromethanesulfonate esters (triflates), toluenesulfonyl esters (tosylates) and halogens are useful leaving groups. In some cases, reactive centers in the precursor molecule must be protected which requires subsequent removal of the protective groups. (16, 31) To achieve an increased reaction rate, unlabeled precursor molecules are usually introduced in a 10<sup>3</sup> to 10<sup>4</sup>-fold excess compared to the radioactive agent. For many radiolabeled compounds, microwave technology led to reduced reaction times and increased yields. (4) The (radio)chemical purification of the crude reaction mixture can be achieved by high performance liquid chromatography (HPLC) and solid phase extraction (SPE). Finally, the product is physiologically formulated and sterile filtrated under aseptic conditions for parental use (Figure 3). (25, 32)

Stability of the PET-tracer in this formulation has to be guaranteed for several hours (with respect to the half-life of the nuclide) to allow for a clinical application as well as for preclinical testing. At least partial water solubility is fundamental for the physiological formulation of a PET-tracer. Ethanolic solutions have to be diluted with buffer to obtain an isotonic injectable. (33) Attention should be paid to pharmaceutical excipients and solubilizers, as cell membranes are prone to solvent-mediated disruption. Certain chemicals and detergents are membrane-destabilizing, thus causing disruption of the blood brain barrier (BBB), herewith allowing entrance for substances, which would normally not cross the BBB. Ethanol or dimethyl sulfoxide at doses of 1-4 g/kg body weight may cause solvent-mediated disruption. In the case of polysorbate-80, doses of 3-30 mg/kg and for sodium dodecyl sulfate even doses of 1 µg/kg are enough to damage BBB integrity. This is significant to small animal models as such doses are frequently used to dissolve compounds administered to rodents. (34)

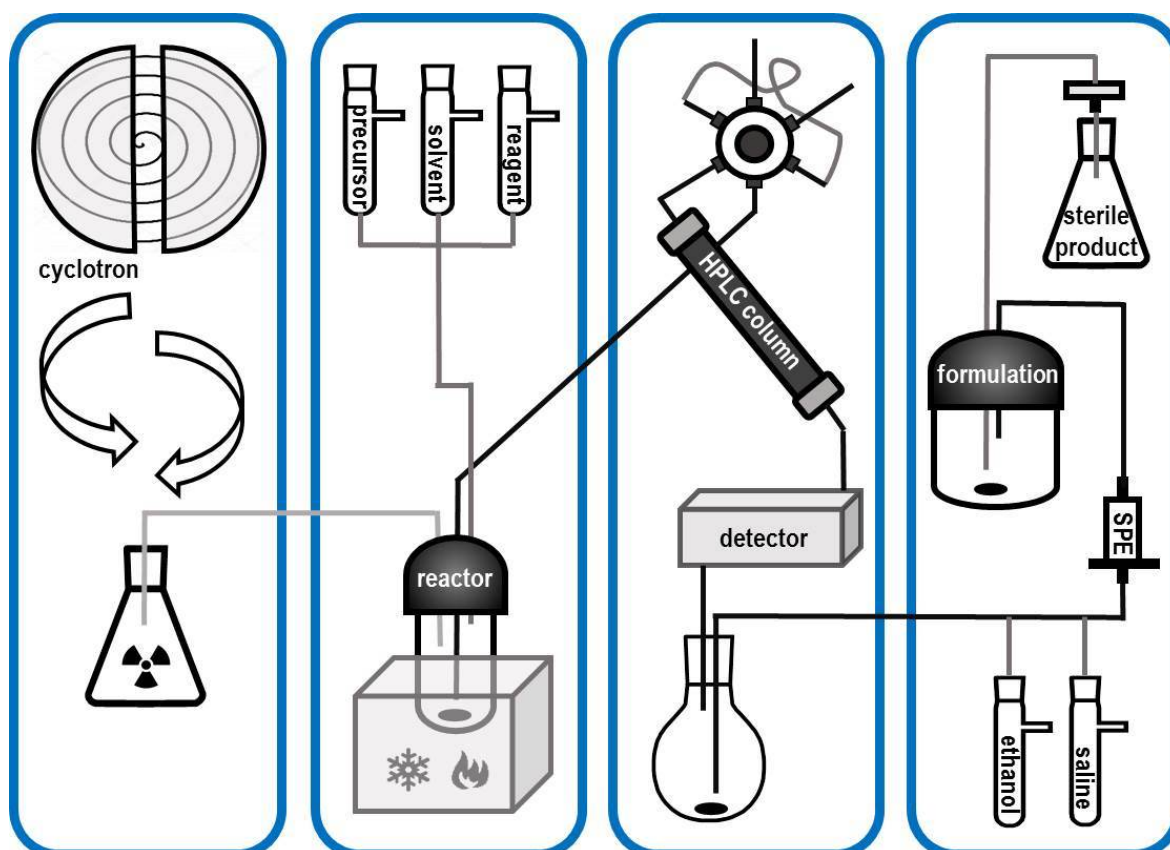


Figure 3: Schematic overview of the major steps involved in the preparation of a radiopharmaceutical: (a) radionuclide production using a cyclotron and subsequent chemical transformation to yield reactive species, (b) radiolabeling of a respective precursor molecule, (c) radiochemical purification using high performance liquid chromatography (HPLC), (d) chemical purification using solid phase extraction (SPE), elution of the product, physiological formulation and sterile filtration (Figure reworked with permission of Mag. Dr. Verena Pichler, Department of Biomedical Imaging and Image-guided Therapy, Medical University of Vienna, Austria.)

The maximum allowed masses of unknown substances in frequently used medications (e.g. aspirin) are greater than the mass of a PET-tracer dose applied a few times in a lifetime – if at all. (35) Due to this low injected mass and the concomitant low receptor occupancy, the probability of pharmacological side effects is negligible. Thus, radiopharmaceuticals are generally considered as pharmacologically safe. However, a diagnostic radiopharmaceutical of poor quality may yield false information about the patient's condition leading to wrong diagnosis and moreover, an inappropriate choice of therapy. On the other hand, repeated examinations due to low quality of the diagnostic agent lead to an unnecessary radiation dose for the patient, which must be avoided in any case. (36) Therefore, it becomes understandable that radiopharmaceuticals (including PET-tracers), though not pharmacologically active themselves, are considered as drugs already since 1960. (37) This fact bears the fulfilment of strict regulatory requirements that ensure that a drug meets the requirements for safety and has the appropriate identity, quality and purity. Quality control and quality assurance are equally important to all kind of drugs, however, there are several specific issues for PET-tracers. Especially,

the short physical half-lives of positron emitting nuclides create logistical challenges to perform quality control before the product's release for human use. In Austria, the quality of radiopharmaceuticals is covered by the Austrian Drug Law and must comply with the quality requirements of the European Pharmacopoeia. (36, 38)

The quality control parameters for parenteral radiopharmaceuticals include (27):

- physical parameters
- radionuclidic purity
- radiochemical purity
- chemical purity
- molar activity
- solvent residues
- sterility of the product

The physical parameters include pH, osmolality and the visual appearance of the formulated product. Radionuclidic purity is determined via the radionuclide's characteristic  $\gamma$ -spectrum (511 keV) and its matchless half-life. The acceptance of radioactive by-products is limited, as the radioactive signal cannot be allocated accurately. Radiochemical purity greater than 95% is therefore a main criterion regarding the release of a radiopharmaceutical product. Chemical purity is equally important as the interaction of the radiotracer with the target site and thus the radioactive signal can be affected severely by unlabeled by-products or remaining precursor molecules which are present in high excess compared to the molar mass of the radio-tracer. This is particular important when saturable systems (receptor occupancy) are investigated rather than metabolism or non-saturable systems (e.g. [ $^{18}\text{F}$ ]fluoride in bone). In this terms, molar activity, which is defined as the measured radioactivity per mole of compound (e.g. GBq/ $\mu\text{mol}$ ) is a main quality criterion for a radiopharmaceutical product. (39) As molar activity depends on radioactive decay, it decreases over time and thus, short-lived radionuclides such as carbon-11 are more prone to low molar activities than longer-lived PET-nuclides. (40) Finally, testing for residual solvents and for microbial contamination (pyrogens, endotoxins, sterility testing) is required. (27)



## 1.2 Preclinical PET-tracer development

### 1.2.1 The Rationale for the Development of Novel PET-tracers

Nowadays, 2-[ $^{18}\text{F}$ ]fluoro-2-deoxy-D-glucose ([ $^{18}\text{F}$ ]FDG) is the most commonly used PET-tracer worldwide and represents the gold standard in oncologic imaging by reflecting the enhanced energy utilization of cancer cells. In the meantime, there are growing applications of [ $^{18}\text{F}$ ]FDG PET/CT in non-oncologic conditions including endocrinology, neurology, cardiology, rheumatology and other disciplines. (41) *"[ $^{18}\text{F}$ ]FDG is the best clinically known and the most successful commercial PET radiopharmaceutical. All experts in the field agree that there would be no clinical PET imaging without [ $^{18}\text{F}$ ]FDG."* (4)

The broad availability and applicability of [ $^{18}\text{F}$ ]FDG often leads to the assumption that there is no demand for newly developed tracers, which is certainly untrue. Due to increased glycolytic activity of inflammatory cells, [ $^{18}\text{F}$ ]FDG is also accumulating at sites of infection and inflammation. (41) Consequently, there are limitations in the detection of certain primary tumors using [ $^{18}\text{F}$ ]FDG: False positive findings can occur with [ $^{18}\text{F}$ ]FDG PET acquisition, due to comparably high uptake in inflammatory diseases. Moreover, small, slowly growing and well differentiated tumors may have uptake levels similar to those of healthy, non-neoplastic tissues. (42, 43)

Tumorigenesis is a multistep process involving genetic alterations that drive the transformation of healthy cells into highly malignant cells. Most cancer types acquire capabilities during their development to evade apoptosis, become insensitive to growth-inhibiting signals and sustain angiogenesis, among others. It is well recognized that cancer is a multi-factorial disease involving dynamic changes in the genome that manifest in malignant cell growth. (44) Due to this complex pathogenesis, there is a demand for novel biomarkers, visualizing more specific features of the underlying tumor biology apart from basic biochemical processes such as increased glycolysis. (13, 45) *"In an era where molecular profiling is identifying specific and mechanistically important alterations in diseased cells, a logical progression of PET- tracer development is to go beyond probing of basic biochemical processes [...]."* (46)

## 1.2.2 The Pursuit of a Successful Imaging Strategy

Generally, radiopharmaceuticals consist of a molecule (ligand) and a radioactive label. The ligand targets a specific biomarker and determines the pharmacodynamic and pharmacokinetic properties of the PET-tracer. The signaling moiety (radionuclide) provides a detectable signal due to its physical decay (cf.1.1.1). (25) As PET-tracers are molecular imaging agents, the target and the ligand are equally important for successful imaging. For the realization of a successful imaging strategy, the following prerequisites must be met, which are evaluated during preclinical evaluation (Figure 4):

- High abundance, targetability and specificity of the target
- Suitable physicochemical and pharmacokinetic profile of the radioligand
- Favorable target-ligand interaction (pharmacodynamics)

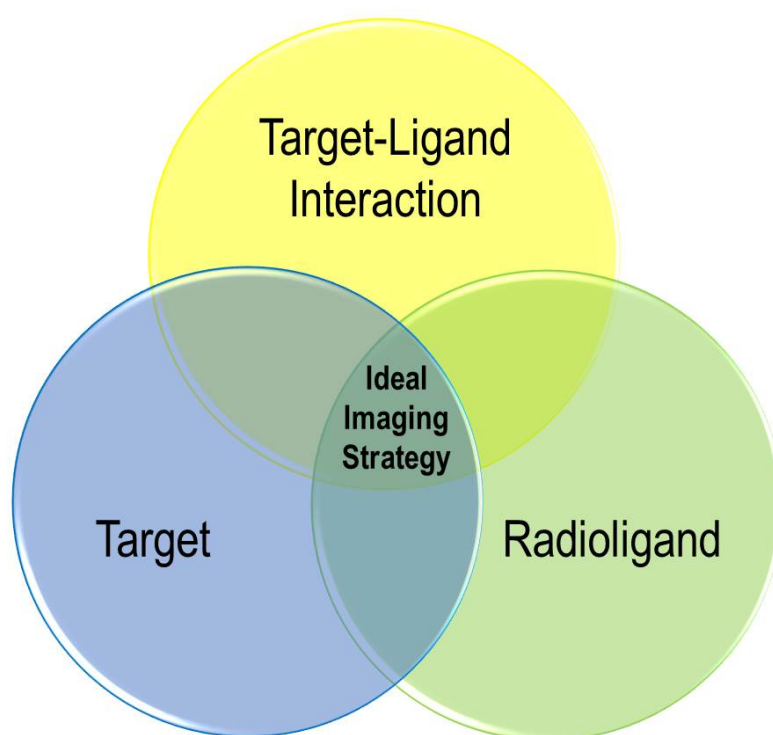


Figure 4: The ideal imaging strategy combines the favorable characteristics of the target, the radioligand and their specific interaction. Many drugs including PET-tracers are not successful, which is illustrated by the minimal overlap of the three areas. To develop ligands within this small intersection is one of the key challenges in tracer development.

### 1.2.3 Characterization of the Target

The onset for the development of novel PET-tracers usually lies in the recognition of a clinical need due to existing limitations of the available tracers or shortfalls in other imaging modalities and diagnostic tools. The key prerequisite for developing a new PET-tracer is the identification of the target to be imaged which is based on the understanding of disease causation. (46) The target displays a biomarker such as a receptor, enzyme, transporter or any biological process, which is up- or down-regulated in a specific pathologic setting. Such biological processes include substrate utilization, specific metabolic alterations and differences in tissue oxygenation – theoretically any process which is significantly altered during disease compared to the physiological state or normal cell functionality (specificity). (47) Especially in oncology, where therapies become increasingly target-specific, molecular biomarkers gain in relevance. Expression of protein biomarkers can be used to refine the prognosis of certain cancers and are used to predict therapy response. (48) There are other cases, where no obvious clinical need is given, but there is a demand for a radiolabeled tracer to elucidate the (patho)physiologic expression of a poorly characterized target (academical biomedical research). In this case, newly developed PET-tracers can also contribute to basic understanding on a molecular level.

High target abundance in a specific pathology *versus* low expression under physiologic conditions is favorable for a high signal to noise ratio (specific to non-specific signal) and successful disease imaging. Target availability, which means that the respective target protein is accessible for the PET-tracer, is mandatory. Difficulties may arise for intracellular targets, as cell penetration of the PET-tracer has to be given. G-protein coupled receptors are conformationally complex; different affinity states (G-protein coupled or uncoupled state) and even inactive forms are described. Moreover, receptor desensitization including arrestin-mediated internalization into endosomes and lysosomal degradation may occur. (49) Significant differences in mRNA expression levels between different biological conditions are assumed to be related to differences in cell function and to be reflected on protein levels. Generally, cellular concentrations of proteins correlate with the abundance of their respective mRNAs, but this correlation might be poor. Protein abundances reflect a dynamic balance between transcription, translation and protein degradation and can only be partially predicted by mRNA abundances. (50, 51) Thus, attention has to be paid when relying on mRNA data or genomics for the identification of an imaging target. The characterization of the target expression on a protein level lays the foundation for the establishment of appropriate preclinical models for testing potential ligands.

## 1.2.4 Characterization of the Radioligand

For a successful imaging strategy, the PET-tracer must be able to reach its target *in vivo* within the lifetime of the radionuclide. Low solubility, extensive metabolism or unfavorable pharmacokinetics may prevent the successful delivery of the radioligand to its respective site of action (e.g. receptor, transporter, enzyme). The intrinsic physicochemical parameters of the radioligand affect its pharmacokinetics and direct drug delivery to the target tissue. Physicochemical parameters include molecular attributes related to size and shape, stability, ionization and solvation properties (such as solubility and lipophilicity). Generally, pharmacokinetics is defined by the fate of a drug upon its administration to the body including its uptake (absorption), metabolic transformation, the distribution of the drug and its metabolites through the blood stream, and their excretion. (52)

Upon the intravenous administration of the PET-tracer, it is immediately exposed to metabolizing enzymes in blood and tissues diminishing the fraction of unchanged radiotracer rapidly. As already discussed above (cf. 1.1.1), the radionuclide allows for the physical allocation of the annihilation events caused by radioactive decay. PET detectors do not take the integrity of a radiolabeled molecule into account: metabolism of radiopharmaceuticals may result in radioactive metabolites, which cannot be differentiated from the parent compound by the means of radioactivity. (53) Thus, the position of the radiolabel should be chosen with respect to the expected metabolic fate of the ligand in order to avoid troublesome and interfering radio-metabolites. (26) A major issue regarding the metabolism of PET-tracers radiolabeled with fluorine-18 is defluorination. The resultant [ $^{18}\text{F}$ ]fluoride accumulates avidly in bone including the skull, which is especially problematic in brain imaging as due to the limited spatial resolution of PET, bone uptake could be falsely interpreted as brain uptake (spill-over effect). (53) Moreover, the half-life of the radionuclide has to meet the pharmacokinetics of the ligand to be labeled: To study biochemical processes with slow pharmacokinetics, positron-emitting radionuclides with longer half-lives than carbon-11 or fluorine-18 are useful (e.g. copper-64 (12.7 h) and bromine-76 (16.2 h)). (4)

In most cases, an “authentic” labeling approach is preferred, which is feasible by isotopic substitution using carbon-11 (half-life 20.38min), nitrogen-13 (half-life 9.97min) or oxygen-15 (half-life 2.04min). As the isotopic effect is negligible, this approach yields biochemically identical PET-tracers indistinguishable from the non-radiolabeled counterparts. The choice of the adequate radionuclide is a balancing act between the radionuclide’s availability, half-life and the authenticity of the resulting radiopharmaceutical. Fluorine-18 is broadly available, however, fluorine is hardly contained in biomolecules. The bioisosteric replacement of a hydrogen atom or a hydroxyl group by a fluorine atom is one

of the most commonly applied substitutions due to their similar van der Waal's radii. However, the introduction of a fluorine-18 atom into a molecule, not bearing a fluorine atom originally, generates analogous tracers, which are similar, but not identical to the natural occurring molecule. As most enzymes in the body work very substrate-specific, such analogous radiotracers may undergo altered metabolism. Additionally, unpredictable changes in pharmacokinetics may occur. This fact has to be considered in tracer development and ultimately when interpreting PET imaging data, otherwise this leads to a dramatic simplification of the actual *in vivo* situation. (4, 25)

Therefore, metabolic stability and the potential formation of radiometabolites should be investigated in early PET-tracer development. For this purpose, the PET-tracer is incubated with pooled plasma, whole blood, tissue homogenates (e.g. liver) or specific enzymes (e.g. carboxylesterases, cytochrome P450). After precipitation with acetonitrile or methanol and subsequent centrifugation, the obtained supernatant is analyzed using e.g. HPLC coupled to a radioactivity detector: The amount of unchanged radiotracer (parent compound) is determined over a certain time interval (e.g. 30 to 120 min depending on the half-life of the radionuclide, PET acquisition time and time-to-equilibrium). (54-56) The extent of metabolism can vary between species and is usually less pronounced or slower in higher species. Thus, the assessment of metabolic stability should not only be conducted in humans, but also in laboratory animal species such as rodents. Knowledge about tracer stability and metabolism may contribute to the right choice of an adequate animal model in advanced stages of PET-tracer development.

Moreover, upon intravenous administration, the PET-tracer may bind to plasma proteins (e.g. albumin, alpha-glycoprotein), whereby the fraction of free (unbound) radiotracer, that is theoretically available for the target site, is reduced. Low plasma protein binding (PPB) and rapid blood clearance of nonspecifically bound tracer is thus desirable in terms of a high target to background ratio. (4) On the other hand, targeted drug delivery can be achieved by using albumin as a carrier due to the enhanced permeability and retention effect (EPR effect), which is observed for solid tumors. (57, 58) The impact of PPB on blood brain barrier penetration is currently disputed. (59) PPB is widely assessed by incubation of the radioligand in plasma and subsequent centrifugation and/or filtration, whereby the free tracer fraction is contained in the filtrate. Another option is to use a high throughput method based on high performance bioaffinity chromatography using a stationary phase containing immobilized human serum albumin in a silica matrix. (60)

Another challenge in radiotracer quantification *in vivo* is non-specific binding. This phenomenon is defined as non-saturable binding to any biological component – in the worst case adjacent to the target – in a tissue or to artificial material used in the process of radiosynthesis. In terms of PET, *in*

*in vivo* non-specific binding is unfavorable as it entails a high background signal which in turn leads to low image contrast. Generally, lipophilic molecules have a higher probability to interact nonspecifically with fatty acid residues in plasma membrane bilayers and are thus usually associated with a higher non-specific binding. (26) On the other hand, a certain degree of lipophilicity is favorable as interactions with plasma membrane bilayers and partitioning in-between govern cell membrane penetration to some extent. A common measure for lipophilicity is the partition-coefficient between two immiscible phases such as 1-octanol and water ( $\log P_{OW}$ ). Traditionally, the  $\log P$  of a radiotracer is determined by means of shake-flask or shake-tube allowing the radiotracer to distribute between the phases and subsequent radioactivity detection. However, the reproducibility of this measure is rather low. (61) Advanced methodologies to measure  $\log P$  include HPLC methods e.g. using short octadecyl-poly(vinyl alcohol) HPLC columns and a rapid methanol-water gradient. (62)

Biodistribution and successful delivery of the PET-tracer to its respective target site strongly depends on the tracer's ability to penetrate cell membranes (permeability). Permeability measurements include cell-based assays and methods using artificial membranes (parallel artificial membrane permeability assay (PAMPA), immobilized artificial membrane (IAM) chromatography). (63, 64)

PET-tracers for the human brain must meet many criteria, among which an ability to enter the brain is the most crucial. The development of PET-tracers for neuroimaging purposes is very challenging, as only ~2% of small molecules are able to cross the blood-brain barrier (BBB) and thus enter the brain, while large molecules such as antibodies and recombinant proteins are substantially excluded from the brain. Brain entry is facilitated either by passive diffusion (lipid-mediated transport) or by active transport systems (e.g. for sugars and amino acids). Broadly speaking, passive brain entry is promoted by a small molecular weight (<400Da), a small cross-sectional area (<80Å), low hydrogen-bonding (high lipid solubility) and lack of formal charge. (65) However, there are no generally applicable thresholds as they base on a dramatic simplification of the complex interactions at the BBB. Meanwhile, it is well recognized that a single parameter is insufficient to reliably predict BBB penetration and that the translational importance of  $\log P$  is rather low. The permeability, measured using IAM chromatography, (i.e. permeability  $P_M$ , membrane partition coefficient  $K_M$ ) is considered a better predictor of brain uptake than  $\log P$ . (59, 66, 67)

Taken together, *in vitro* measures only provide estimations about a radioligand's *in vivo* behavior. Ultimately, biodistribution studies in animals are indispensable to appropriately assess pharmacokinetics. Therefore, animals (mostly rodents) are injected with the PET-tracer (injected dose) and sacrificed after certain time points. Organs of interest are removed, weighted and gamma-counted. After decay correction, percentage of injected dose per gram organ (%ID/g) can be calculated. Such ex-

perimental set-up does not necessitate anesthesia, which causes fewer stress to the animals. However, biodistribution may differ substantially between conscious and anesthetized animals due to enhanced muscle activity and/ or altered blood flow. (32, 68)

Conventional biodistribution studies and  $\mu$ PET imaging ultimately demonstrate the successful delivery of a PET-tracer to its target tissue (e.g. tumor, brain). One major hindrance to sufficient brain uptake is the susceptibility of a tracer to brain efflux, i.e. the rejection of substances from the brain by transporters or pumps. The most prominent efflux transporter expressed on the BBB is the permeability protein (P-gp, genetic name: MDR1) among other ATP-binding cassette (ABC) transporters. (53) Such efflux transporters are also expressed on tumor cells (e.g. breast cancer resistance protein, BCRP) impeding drug delivery and thus, efficient chemotherapy. (69) Exclusively, *in vivo* biodistribution or imaging experiments either with co-injection of a specific efflux transporter inhibitor or the use of MDR1 knockout mice allow for the assessment if a PET-tracer is a substrate for an efflux transporter. (4, 53)

## 1.2.5 Characterization of the Target-Ligand Interaction

After successful drug delivery, the PET-tracer interacts with its target. Pharmacodynamics comprises the reactions with and binding to cell constituents and the biological and physiological effects of these actions. (52) The latter is of minor importance for radiopharmaceuticals, as only insignificant receptor occupancy is achieved owing to the low injected mass (tracer principle). In molecular imaging, the focus is therefore the target-ligand interaction.

Depending on the nature of the target, target-ligand interactions are manifold: reversible receptor binding, substrate-enzyme interaction, transportation and metabolic trapping, receptor internalization upon ligand binding and subsequent specific retention – to name a few.

The reversible binding of a ligand to a receptor under the formation of a ligand-receptor-complex is characterized by the law of mass action. The equilibrium dissociation constant ( $K_d$ ) of a ligand-receptor-complex is the ligand concentration that binds to half of the receptor population (50% receptor occupancy). The  $K_d$  value is a common pharmacodynamic measure to rank the strength of ligand-receptor binding: The smaller the  $K_d$  value, the higher the affinity of a ligand for its biological target.  $K_d$  values are generally determined in receptor saturation experiments. In case of competitive antagonists, the affinity can be indirectly determined by competition binding assays, providing that a radioligand with known  $K_d$  is available. While the  $IC_{50}$  (inhibitory concentration of antagonist that blocks half the specific binding of the radioligand) strongly depends on the chosen experimental conditions, the inhibition constant ( $K_i$ ) is a function of the  $IC_{50}$  of the competitor, of the  $K_d$  of the radioligand and of the used radioligand concentration. (70) The  $K_i$  value is thus a more reliable and comparable measure than  $IC_{50}$ .

As a side note, the choice for an agonistic or antagonistic tracer should be made carefully. G-protein coupled receptors exist in a high-affinity and a low-affinity, uncoupled state. Agonists preferentially bind to receptors which are coupled to G-proteins, whereas antagonists do not discriminate between receptor states and equally bind to receptors whether they are coupled or uncoupled to G-protein. (71)

Ideally, a PET-tracer exhibits high affinity towards its respective target receptor (i.e.  $K_d$  value in the (sub)nanomolar range) and low affinity towards other targets (selectivity). It is therefore useful to assess binding affinities not only towards the target of interest, but also to familiar receptors or receptor subtypes (off-target binding). High binding affinities are indispensable when investigating re-



ceptor system with limited number of available binding sites (low receptor densities). However, it should be emphasized that extremely high binding affinities, may be unsuitable as equilibrium is not reached in a feasible time frame (considering the half-life of the PET-nuclide).

Receptor binding techniques are frequently conducted using cell membrane preparations expressing the respective target or using whole cells. The general experimental setting involves radioligand incubation to allow for binding equilibrium, separation of bound (ligand-receptor-complex) and free (unbound) radioligand through centrifugation or filtration (e.g. Brandel® Cell Harvester) and subsequent detection of radioactivity. (72) For determination of  $K_d$  values, the respective biological material is incubated with rising radioligand concentrations to achieve receptor saturation. The binding plateau can be extrapolated to the maximal available binding sites ( $B_{max}$ ), which provides information about receptor densities. Competitive binding experiments measure equilibrium-binding of a single radioligand concentration in the presence of rising concentrations of unlabeled competitor. That approach is more appropriate in early stages of PET-tracer development, since the test compounds do not yet have to be radiolabeled.

Recently, a novel *in vitro* real-time kinetic approach to assess binding parameters was presented. The experimental set-up bases on confluent grown cells, a rotating cell dish support and a radioactivity detector (LigandTracer® technology, Ridgeview Instruments AB, Uppsala, Sweden). It allows for investigating radioligand-receptor binding kinetics including time-to-equilibrium, association and dissociation rate constants (i.e.  $k_{on}$  and  $k_{off}$ ) in real-time. (73)

Radioligand incubation with whole cells at 37°C accounts for active processes such as receptor internalization. Subsequent acid washes (e.g. using acidic glycine solution) and cell lysis allows for separation of membrane-bound fractions and internalized fractions of radioligand. (74) Active transportation and internalization are downregulated at lower temperatures and usually not observed at 4°C. Receptor internalization leads to specific retention, which is favorable for the visualization of tumors (high tumor to background ratio) or potential theragnostic approaches.

In summary, binding studies using cell membranes investigate single receptor sites, while using whole cells, cell-uptake related processes such as active transportation, passive diffusion and internalization can be assessed additionally. However, *in vivo* situations are far more complex than interactions mimicked in two-dimensional cell monolayers: Cells grown in cell culture flasks underlie two-dimensional cell growth, which implies optimal supply of nutrients and oxygen. Moreover, cell monolayers essentially lack cell-cell-interactions, cell-matrix-interactions and cellular communication. (75)

To overcome this translational gap, three-dimensional cell culture models are a valuable tool with intermediate complexity between tumors and standard cell culture models. The formation of cell aggregates is governed by cell adhesion molecules, which allow for the attachment of cells to adjacent cells or to extracellular matrix proteins. (76) Three-dimensional grown tumor cell aggregates (tumor spheroids) mimic physiological tumor growth, which is microenvironment- dependent and is often associated with an increasing deprivation of nutrients and/or oxygen. After an initial phase of exponential tumor growth, retardation occurs as a result of nutrient deprivation. Similarly, as multicellular tumor spheroids increase in size, the formation of a penetration barrier for soluble nutrients and reduced oxygen supply lead to hypoxia, necrosis and/or apoptosis. Cellular heterogeneity, which is an inherent characteristic of most solid tumors, is reflected in multicellular tumor spheroids: The surface layer consists of proliferating (viable) cells, whereas in the inner layers mainly non-proliferating, hypoxic cells are found. The spheroid's inner core consists of necrotic and apoptotic cells (Figure 5). (75, 77, 78) Thus, multicellular spheroids enable the simulation of tumor physiology *in vitro*, which has been exploited to study drug efficacy and radiation resistance. (79-81) Although not widely used yet, multicellular tumor spheroids serve as useful models to investigate PET-tracer uptake. (82-84)

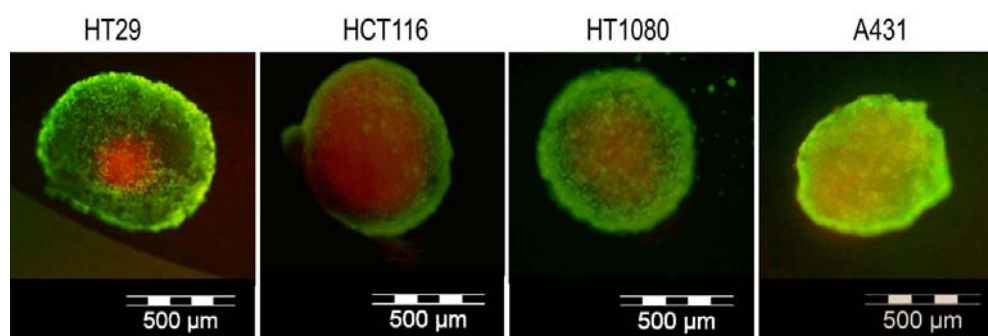


Figure 5: Live/dead staining of tumor spheroids derived from different human cancer cell lines: colorectal carcinoma (HT-29, HCT116), fibrosarcoma (HT-1080) and epidermoid carcinoma (A-431). Viable cells appear in green (calcein acetoxymethyl ester) and dead cells in red (propidium iodide), respectively. (Figure provided by Mag. Dr. Verena Pichler, Department of Biomedical Imaging and Image-guided Therapy, Medical University of Vienna, Austria.)

Furthermore, radioligand binding to tissues is investigated frequently. Amongst these, autoradiography is one of the most sensitive imaging techniques and can be conducted *in vitro* (incubation of tissue slices with radioligand) or *ex vivo* (*in vivo* biodistribution followed by organ removal and tissue slicing). The latter involves physiological PET-tracer distribution and *in vivo* binding, whereby the radioactivity detection is carried out *post mortem* using dedicated phosphor storage plates. Blocking or displacement experiments are used to determine specific binding: Co-injection (*ex vivo*) or co-incubation (*in vitro*) of an unlabeled competitor or inhibitor targeting the receptor of interest reduces the specific signal of the PET-tracer. (85)

The verification of a target-ligand interaction is ultimately conducted *in vivo*. Small animal imaging using PET ( $\mu$ PET) enables longitudinal studies and offers the possibility that every animal serves as its own control subject (pre- and post-treatment). The use of healthy subjects allows for studying tracer distribution under physiological conditions. Blocking or displacement studies lead to the identification of organs with specific PET-tracer accumulation and thus high target expression. Disease models enable to study tracer distribution under pathologic conditions and to investigate the potential of a PET-tracer to image a certain disease. *Vice versa*, animal disease models have become the pillars for understanding the pathogenesis of certain diseases and for the development of new drugs including PET-tracers. In this context, murine models depict a resource of immense potential, as genome editing made knock-in or knock-out models of any conceivable gene possible. (71)

Extrapolating findings obtained from animal studies to expectations of tracer performance in humans have to be treated with caution. There are several examples in literature, where biodistribution results obtained in preclinical settings were of limited predictive value for subsequent clinical utility of PET-tracers. (46) PET imaging in small animals requires subject immobilization to avoid motion artefacts, which can be accomplished by physical restraint or anesthesia. Physical restraint during image acquisition causes stress and can lead to unusual physiological responses which may distort experimental results. Therefore,  $\mu$ PET imaging is mostly carried out in anesthetized animals, however, full consideration must be given to type and dosage of the anesthetic drug, as alterations in blood flow, receptor binding and neuronal activities have been described. (86, 87)



## 1.3 Targets of Interest and Imaging Strategies

### 1.3.1 A<sub>3</sub> Adenosine Receptor

Adenosine is an ubiquitous purine nucleoside in the mammalian cell type as it serves as the essential building block for ribonucleic acids (RNA), nucleotides used in energy transfer (ATP, ADP, AMP) or cell signaling (88) and coenzymes (FAD, NAD, coenzyme A). (89) Adenosine unfolds its various effects by the activation of up to four different G-protein coupled receptors (GPCRs), denoted as Adenosine-1, Adenosine-2A, Adenosine-2B and Adenosine-3 adenosine receptors (A<sub>1</sub>AR, A<sub>2A</sub>AR, A<sub>2B</sub>AR and A<sub>3</sub>AR, respectively). The adenosine receptors are named after their main endogenous ligand, despite they can further be activated by its metabolite inosine, although to a lesser extent. (90)

Adenosine is extracellularly formed by dephosphorylation of adenine nucleotides through ectoenzymes (CD37, CD39) and intracellularly also by hydrolysis of S-adenosyl-L-homocysteine. (89, 91, 92) Large amounts of adenosine are generated during phases of high energy consumption or increased metabolic rates. In response to stress (e.g. ischemia, tissue injury), extracellular adenosine levels can instantly raise to micromolar concentrations leading to a generalized receptor activation, whereas under basal conditions adenosine levels are about 20 nM (brain) to 100 nM (heart). On the other hand, adenosine is rapidly degraded by deamination (*via* adenosine deaminase to inosine) or by cellular reuptake (*via* nucleoside transporters), where it is phosphorylated to AMP (*via* adenosine kinase). (90, 93) Thus, adenosine has a brief physiological lifetime and its effects are limited to the local environment of its synthesis site. (94)

Raised adenosine levels have been demonstrated in areas of increased metabolism and in numerous pathologic states such as epilepsy, ischaemia, pain and inflammation. In such conditions, adenosine exerts cytoprotective effects. Adenosine mediates tissue protection by preconditioning, stimulating angiogenesis, restoring the oxygen supply/demand ratio and/or suppressing inflammation. (95) Hypoxic conditions often stem from inflammation and *vice versa*. During inflammation, hypoxia inducible factor (HIF)-driven adenosine signaling and metabolism is crucial to ensure tissue protection. (96) Moreover, an essential characteristic of most solid tumors is hypoxia, which inevitably leads to accumulation of adenosine within the tumor microenvironment as a result of ATP breakdown. Therefore, adenosine exerts a leading role in immunity, inflammation and cancer. (97, 98) The immunosuppressive effects of adenosine impede anti-tumor immunity and promote cancer progression. (99-

102) It was reported that adenosine exerts a profound inhibitory effect on the induction of mouse cytotoxic T-cells through the A<sub>3</sub>AR thereby suppressing lymphocyte-mediated tumor cell destruction. (103)

Due to the high expression of A<sub>3</sub>ARs in tumor cells, this receptor subtype was proposed as a potential target to combat cancer. (94) A<sub>3</sub>AR expression was detected in various human tumor cell lines including leukemia (Jurkat T, HL60), melanoma (A375), glioblastoma (ADF), as well as prostate (PC-3) and colon carcinoma (Caco-2, HT-29, HCT-116, DLD-1). (104-110) Moreover, the A<sub>3</sub>AR was found to be highly expressed in breast, colon and hepatocellular carcinoma tissue compared to adjacent, healthy tissue of the same individual. (111) Importantly, even higher A<sub>3</sub>AR expression levels were reported for lymph node metastasis than for the corresponding primary tumor, pointing at a direct correlation between A<sub>3</sub>AR expression level and disease progression. (112) Both, A<sub>3</sub>AR agonists and antagonists have been tested as new therapeutic agents for cancer. (94, 113)

The A<sub>3</sub>AR is also upregulated in inflammatory diseases including rheumatoid arthritis, psoriasis, Crohn's disease and chronic obstructive pulmonary disease (COPD). (114, 115)

As the A<sub>3</sub>AR serves as an exceptional target in the clinical setting of neurological, cardiovascular and tumor-related pathologies (116), PET imaging of A<sub>3</sub>AR expression is of high scientific and clinical interest. The A<sub>3</sub>AR is the latest identified receptor of the adenosine receptor family and was originally isolated from rat testis. Remarkably, the A<sub>3</sub>AR shares little sequence homology between human and rat (72%), but 85% homology between human and sheep. (117) The structural species differences are reflected in different pharmacological profiles and receptor expression patterns.

Amongst a set of pyridine-based A<sub>3</sub>R antagonists FE@SUPPY displayed the highest affinity and was thus selected for radiolabeling by our group. (118, 119) Apart from [<sup>18</sup>F]FE@SUPPY (5-(2-[<sup>18</sup>F]fluoroethyl)2,4-diethyl-3-(ethylsulfanylcarbonyl)-6-phenylpyridine-5-carboxylate) and the slightly modified PET-tracer [<sup>18</sup>F]FE@SUPPY:2, a second group at the National Institutes of Health (Bethesda, USA) developed PET-tracers for the A<sub>3</sub>AR so far. (120) However, [<sup>76</sup>Br]MRS3581 and [<sup>76</sup>Br]MRS5147 showed high accumulation in metabolizing organs and specific uptake could not be demonstrated *in vivo*. (121) Radiosynthesis of carbon-11 labeled 1,2,4-triazolo[4,3-a]quinoxalin-1-one derivatives was presented, but these PET-ligands were not further evaluated *in vivo* so far. (122) Thus, no proven specific PET-tracer for A<sub>3</sub>AR imaging is available up to now.

### 1.3.2 18 kDa Translocator Protein

The 18 kDa translocator protein (TSPO) is mainly located in the outer mitochondrial membrane, where it regulates cholesterol transport – a crucial step in the biosynthesis of steroid hormones and bile salts. TSPO also binds and transports porphyrin thus contributing to heme biosynthesis. Moreover, TSPO has a function in protein import, which is involved in membrane biogenesis. (123) Accordingly, highest levels of TSPO expression are found in Leydig cells, ovarian granulosa and luteal cells – cells known to synthesis steroids de novo. (124)

Importantly, TSPO is expressed on microglia cells, which become activated as a response to brain injury (e.g. ischemic stroke). As TSPO upregulation in glia cells occurs prior to (behavioral) disease manifestation, TSPO PET imaging is of high interest in pathological settings of neurodegeneration and neuroinflammation. A low basal expression of TSPO in the healthy brain contributes to the sustained interest in this target. Clinical applications of TSPO PET include Parkinson's disease, Alzheimer's disease and Huntington's disease. (125, 126)

Moreover, TSPO expression has been reported in human peripheral organs including respiratory, digestive and endocrine tissues. (127) A role for TSPO in the regulation of tumor cell proliferation has been proposed, as elevated levels of TSPO expression have been reported in gliomas, breast cancer, colon adenocarcinoma, hepatocellular carcinoma, esophageal carcinoma, prostate cancer and ovarian carcinomas compared to the corresponding normal tissues. It was shown that TSPO expression and TSPO-mediated cholesterol transport correlate with human breast cancer cell aggressiveness. Moreover, TSPO expression is associated with tumor progression and malignancy in prostate cancer and astrocytomas. Additionally, TSPO was found to be a relevant prognostic factor in stage III colorectal cancer. (128-132)

Besides its endogenous ligands, TSPO has a binding site for benzodiazepines and -derivatives, which have given this receptor its former name; peripheral benzodiazepine receptor (PBR). (123) [<sup>11</sup>C](*R*)-PK11195 ((*R*)-1-(2-chlorophenyl)-*N*-[<sup>11</sup>C]methyl-*N*-(1-methylpropyl)-isoquinoline) – the first and most used PET-tracer for TSPO imaging to date – suffers from high lipophilicity and a concomitant low signal-to-noise ratio. Moreover, high non-specific binding, high plasma protein binding and low brain penetration have been observed with [<sup>11</sup>C](*R*)-PK11195. The development of improved radiopharmaceuticals for quantitative TSPO PET imaging led to the introduction of several new classes of compounds, referred to as the 2<sup>nd</sup> generation of TSPO PET-tracers. Among these are phenoxyarylacetamides (e.g. [<sup>11</sup>C]DAA1106, [<sup>11</sup>C]PBR28), quinoline carboxamides, imidazopyridazines

and pyrazolopyrimidines among others. (88) The radiofluorinated phenoxyanilide [ $^{18}\text{F}$ ]FEPPA has shown high affinity towards TSPO, a favorable metabolic profile and high brain penetration. (133, 134)

However, TSPO PET imaging using the 2<sup>nd</sup> generation of PET-tracers has been dramatically hampered by a polymorphism, which results in high inter-individual variability in binding affinity of the PET-tracer. A mutation within the TSPO gene causes an amino acid substitution from alanine to threonine at position 147 (Ala147Thr) within the fifth transmembrane domain of the TSPO protein, which results in a high and a low binding site (polymorphism rs6971). Thus, three different binding patterns have been identified leading to a patient classification into high affinity binders (HABs), low affinity binders (LABs) and a mixed form, expressing approximately equal amounts of high and low affinity receptor sites (mixed affinity binders, MABs). (135, 136)



### 1.3.3 Melanin-Concentrating Hormone Receptor 1

The melanin-concentrating hormone is a cyclic 19 amino acid polypeptide with a cysteine-cysteine bond that exhibits structural identity among different mammalian species. (137) MCH is the endogenous ligand for two distinct G-protein coupled receptors in humans among other species, denoted as melanin-concentrating hormone receptor 1 (MCHR1) and 2 (MCHR2), whereby sharing only 38% identity at the amino acid level. (138, 139) Several mammalian species including rat, mouse, hamster, guinea pig and rabbit do not express functional MCHR2 or encode a MCHR2 pseudogene complicating the exploration of this receptor in animal models. (140)

MCH is generated by posttranslational cleavage from its respective hormone precursor (pre-proMCH) and is mainly expressed in the lateral hypothalamus and zona incerta of the mammalian brain. (137, 141, 142) MCH has a key role in the hypothalamic regulation of feeding behavior and body weight. (143) MCH - as an orexigenic peptide - induces obesity in mice, while MCH-deficient mice are lean due to hypophagia and increased metabolism. (144-146) Besides, MCHR1 is expressed in the third ventricle, where MCH regulates ciliary beat frequency and contributes to cerebrospinal fluid circulation. (147, 148) MCH neurons are furthermore described in dorsal and median raphe nuclei, areas responsible for sleep control. There is experimental evidence that MCH promotes rapid-eye-movement (REM) sleep and is additionally involved in the pathophysiology of depression. (149)

As a neuropeptide, MCH projects through the central nervous system (CNS), but MCH expression is also found in peripheral endocrine organs and in human and rat plasma. (150, 151) Both, MCH and MCHR1, are expressed in mouse and human islets of the pancreas, where MCH enhances insulin secretion in a dose dependent manner. An autocrine role for MCH in the regulation of the hypothalamic-pancreatic axis is thus proposed. (152) MCH stimulates leptin secretion and MCH receptor is expressed in adipocytes suggesting that fat cells may be targets of MCH under physiological condition. (150) Moreover, colonic epithelial cells express functional MCH receptor and MCH has a role in mediating intestinal inflammation. (153)

The involvement of the MCH system in energy homeostasis led to the development of several MCHR1 antagonists to identify new anti-obesity drugs. (154, 155) First attempts for targeting the MCHR1 were to develop peptide analogs of human MCH. (156, 157) These ligands were not able to cross the blood brain barrier, however, central activity of MCHR1 antagonists is required to be effective in food intake inhibition and body weight reduction. (158) Thus, several small molecule MCHR1 antagonists were developed to target central receptors. (159-162) Among those was the high-affinity

(K<sub>d</sub>=0.18nM) and highly selective (>1000-fold) antagonist SNAP-7941, which was efficient in decreasing body weight in a rat obesity model, but also exerted antidepressant and anxiolytic effects. (163)

PET imaging of the MCHR1 expression pattern would provide a deeper understanding of the involvement of the MCH system in neurotransmission and several related pathologic settings including obesity, diabetes, colitis, hydrocephalus and depression. Our radiolabeling strategy was based on SNAP-7941, which contains a methyl ester moiety enabling the introduction of a [<sup>11</sup>C]methyl group or a 2-[<sup>18</sup>F]fluoromethyl moiety. (164) Consequently, [<sup>11</sup>C]SNAP-7941 and [<sup>18</sup>F]FE@SNAP were developed as the first MCHR1 PET-tracers. (165, 166)

First preclinical evaluation provided evidence that both tracers may serve as suitable imaging agents for the MCHR1. Specificity was demonstrated for both tracers in MCHR1 positive tissues including the lateral hypothalamus and the ventricular system. (167-169) Metabolic stability of [<sup>11</sup>C]SNAP-7941 was high in human plasma and against human and rat liver microsomes. In rat plasma, the formation of a hydrophilic metabolite was observed. Plasma free fraction and lipophilicity (logD) were favorable for an imaging strategy. (170) Similarly, [<sup>18</sup>F]FE@SNAP is highly stable in human plasma and against liver microsomes. However, it is rapidly metabolized in rat plasma and shows a lower plasma free fraction than [<sup>11</sup>C]SNAP-7941, while displaying slightly higher lipophilicity. (171) Surprisingly, rat brain uptake of [<sup>11</sup>C]SNAP-7941 increased dramatically after administration of the P-gp inhibitor tariquidar. This data suggests that [<sup>11</sup>C]SNAP-7941 is a substrate of this efflux transporter diminishing availability for central MCHR1. (170) This finding is somewhat contradictory to the assumption that blood brain barrier penetration is significant to the anti-obesity effects of MCHR1 antagonists. (158) Certainly, this recognition contributes to MCHR1 drug development.

Recently, a novel carbon-11 labeled compound was proposed for MCHR1 PET imaging (Compound II, Takeda Pharmaceutical Co., Ltd., Fujisawa, Japan). (172)

## 2. AIM

---

There is a controversial discussion of the translational and predictive value of preclinical methods on the performance of newly developed PET-tracers in humans. Within the scope of this thesis, a plethora of *in vitro* and *in vivo* methods were applied to address specific research questions in different stages of PET-tracer development. The presented PhD-thesis deals with the preclinical evaluation of newly developed and revisited PET-tracers for A<sub>3</sub> adenosine receptor (A<sub>3</sub>AR) imaging, translocator protein (TSPO) imaging and melanin-concentrating hormone receptor 1 (MCHR1) imaging to cover a broader variety of targets in the fields of oncology, neurology and endocrinology. The specific research questions revealed a tour from bench to the preclinical bed and back to the bench.

The following specific research questions were assessed:

- the usefulness of a human xenograft mouse model for tumor imaging for an A<sub>3</sub> adenosine receptor targeting PET-tracer ([<sup>18</sup>F]FE@SUPPLY)
- the predictive value of a new *in vitro* method measuring interactions with the efflux transporter P-gp for *in vivo* blood brain barrier penetration
- the power and limitation of immunohistochemistry and autoradiography for target identification in colorectal cancer for TSPO PET
- the predictive value of binding characteristics considering the polymorphism within the TSPO-gene
- a critical review of the applied *in vitro* methods for the identification of the appropriate MCHR1 PET-tracer ([<sup>11</sup>C]SNAP-7941 *versus* [<sup>18</sup>F]FE@SNAP) for future application in humans
- the elucidation of a potential involvement of MCHR1 in brown adipose tissue using a reverse approach (from *in vivo* back to *in vitro*)

The employed preclinical methods were critically assessed regarding their potential and limitations for subsequent clinical use.



# SPECIFIC PART

---



### 3. SCIENTIFIC PAPERS

---

I hereby declare to have significantly contributed to the realization of each scientific paper included in the presented thesis. If not stated otherwise, the scientific studies were carried out at the Department for Biomedical Imaging and Image-guided Therapy, Division of Nuclear Medicine, Medical University of Vienna. Small animal PET imaging was performed at the Preclinical Imaging Laboratory with support of the Medical Imaging Cluster of the Medical University of Vienna.

Regarding the first manuscript, entitled “Preclinical *In Vitro* and *In Vivo* Evaluation of [<sup>18</sup>F]FE@SUPPY for Cancer PET Imaging: Limitations of a Xenograft Model for Colorectal Cancer”, I designed the study together with Dr. Josef Singer, PhD and I wrote the ethics. I performed the radiosyntheses of [<sup>18</sup>F]FE@SUPPY and all the *in vitro* experiments, which were partly conducted at the Department for Pathophysiology and Allergy Research, Medical University of Vienna. I further participated in the performance of the animal experiments (*in vivo* and *ex vivo*). I analyzed and interpreted the data and finally, I drafted the manuscript.

Concerning the second paper, titled “A new method measuring the interaction of radiotracers with the human P-glycoprotein (P-gp) transporter”, I performed the radiosyntheses of [<sup>18</sup>F]FE@SUPPY and the preliminary cell line characterization. Additionally, I participated in the conventional and in the kinetic cell experiments. I co-drafted and revised the manuscript.

In the third study (“[<sup>18</sup>F]FEPPA: Improved Automated Radiosynthesis, Binding Affinity, and Preliminary *In Vitro* Evaluation in Colorectal Cancer”), I contributed to the experimental design and I established the working protocols for autoradiography, immunohistochemistry, Western Blot and kinetic cell binding experiments. I performed these experiments and I interpreted the *in vitro* data.

Regarding the fourth manuscript, entitled “SNAPShots of the MCHR1: a Comparison Between the PET-Tracers [<sup>18</sup>F]FE@SNAP and [<sup>11</sup>C]SNAP-7941”, I participated in the *ex vivo* metabolic stability measurements and performed the biodistribution studies. Moreover, I was significantly involved in the conception of the manuscript.

I designed the fifth study, titled “First Radiopharmaceutical Evidence for MCHR1 Expression in Brown Adipose Tissue”, and implemented the experimental procedures. I carried out the analysis and interpretation of the data, as well as the drafting of the manuscript.





## 3.1 Manuscript #1

Title: Preclinical *In Vitro* and *In Vivo* Evaluation of [<sup>18</sup>F]FE@SUPPY for Cancer PET Imaging: Limitations of a Xenograft Model for Colorectal Cancer

Authors: Theresa Balber, Josef Singer, Neydher Berroterán-Infante, Monika Dumanic, Lukas Fetty, Judit Fazekas-Singer, Chrysoula Vraka, Lukas Nics, Michael Bergmann, Katharina Pallitsch, Helmut Spreitzer, Wolfgang Wadsak, Marcus Hacker, Erika Jensen-Jarolim, Helmut Viernstein and Markus Mitterhauser

Associated Content: Supplementary Material DOI: 10.1155/2018/1269830

**Rationale and Aim:** Several lines of evidence indicate high A<sub>3</sub>AR expression in cancerous tissues (primary tumors and metastases) *versus* low expression in normal (healthy) tissues suggesting this receptor as a tumor marker. (94, 110, 112, 173) PET imaging and quantification of A<sub>3</sub>AR expression levels would help to characterize the microenvironment and biological status of certain cancers. [<sup>18</sup>F]FE@SUPPY was developed as the first PET-tracer for A<sub>3</sub>AR imaging and initially evaluated for brain imaging in recent years. (55, 119, 174, 175)

In the course of previous conducted animal experiments, several challenges regarding the *in vivo* evaluation of [<sup>18</sup>F]FE@SUPPY emerged. The low amino acid sequence homology of 74% between the human A<sub>3</sub>AR and the rat A<sub>3</sub>AR protein results in a pronounced species difference regarding affinity: FE@SUPPY displays high affinity for the human A<sub>3</sub> adenosine receptor ( $K_i$  hA<sub>3</sub>AR =  $4.22 \pm 0.66$  nM), but only low affinity for the rat transcript ( $K_i$  rA<sub>3</sub>AR =  $600 \pm 166$  nM). (116, 118) This circumstance led to moderate to low uptake of [<sup>18</sup>F]FE@SUPPY in rat target tissues and difficulties in proving specific binding in the respective rodent model using blocking agents. In these terms, [<sup>18</sup>F]FE@SUPPY could not be reasonably evaluated for potential human application using a rodent model.

However, the transplantation of human cancer cells into immunocompromised mice offers the opportunity to study human receptors in small animals. A pilot study using CHO-K1 cells, stably transfected with the human A<sub>3</sub>AR, provided promising results: Tissue mass derived from CHO-K1-A<sub>3</sub>AR cell inoculation evinced significantly higher uptake of [<sup>18</sup>F]FE@SUPPY compared to the parent CHO-K1 cell mass. Whereas the gold standard in oncologic PET imaging, [<sup>18</sup>F]FDG, was not able to distinguish between cell masses. (176) Thus, we conclude that by transplanting human tumor cell lines

into immune-deficient animals, the species differences can be overcome. Accordingly, we pursued the evaluation of [ $^{18}\text{F}$ ]FE@SUPPY for human cancer imaging using a xenograft model.

To this, an appropriate human cancer cell line, expressing the human A<sub>3</sub>AR in high abundance had to be identified, which was subsequently chosen for tumor inoculation. *In vivo* imaging ( $\mu\text{PET}$ ) was applied to explore the potential of [ $^{18}\text{F}$ ]FE@SUPPY to serve as a tumor tracer. Target and tracer specificity was investigated by the means of autoradiography and immunohistochemistry using human colorectal cancer tissue samples and healthy colon tissue. Metabolic tracer stability in the mouse organism was analyzed *in vitro* and *ex vivo*. Moreover, missing data on FE@SUPPY affinity towards the other human adenosine receptor subtypes had to be obtained in order to clarify binding selectivity

## Research Article

# Preclinical *In Vitro* and *In Vivo* Evaluation of [ $^{18}\text{F}$ ]FE@SUPPY for Cancer PET Imaging: Limitations of a Xenograft Model for Colorectal Cancer

**T. Balber,<sup>1,2</sup> J. Singer,<sup>1,3,4</sup> N. Berroterán-Infante,<sup>1</sup> M. Dumanic,<sup>1</sup>  
L. Fetty,<sup>1,5</sup> J. Fazekas-Singer,<sup>3,6</sup> C. Vranka,<sup>1</sup> L. Nics,<sup>1,7</sup> M. Bergmann,<sup>8</sup> K. Pallitsch,<sup>9</sup>  
H. Spreitzer,<sup>10</sup> W. Wadsak,<sup>1,11</sup> M. Hacker,<sup>1</sup> E. Jensen-Jarolim,<sup>3,6</sup>  
H. Viernstein,<sup>2</sup> and M. Mitterhauser<sup>1,12</sup>**

<sup>1</sup> Biomedical Imaging and Image-Guided Therapy, Division of Nuclear Medicine, Medical University of Vienna, Vienna, Austria

<sup>2</sup> Department of Pharmaceutical Technology and Biopharmaceutics, Faculty of Life Sciences, University of Vienna, Vienna, Austria

<sup>3</sup> Institute of Pathophysiology and Allergy Research, Center of Pathophysiology, Infectiology and Immunology, Medical University of Vienna, Vienna, Austria

<sup>4</sup> Department of Internal Medicine II, University Hospital Krems, Karl Landsteiner University of Health Sciences, Krems an der Donau, Austria

<sup>5</sup> Department of Radiation Oncology, Division of Medical Physics, Medical University of Vienna, Vienna, Austria

<sup>6</sup> Comparative Medicine, The Interuniversity Messerli Research Institute, The University of Veterinary Medicine Vienna, Medical University of Vienna, and University of Vienna, Vienna, Austria

<sup>7</sup> Department of Nutritional Sciences, Faculty of Life Sciences, University of Vienna, Vienna, Austria

<sup>8</sup> Department of Surgery, Surgical Research Laboratories, Medical University of Vienna, Vienna, Austria

<sup>9</sup> Institute of Organic Chemistry, University of Vienna, Vienna, Austria

<sup>10</sup> Department of Pharmaceutical Chemistry, Faculty of Life Sciences, University of Vienna, Vienna, Austria

<sup>11</sup> CBmed GmbH, Graz, Austria

<sup>12</sup> Ludwig Boltzmann Institute Applied Diagnostics, Vienna, Austria

Correspondence should be addressed to M. Mitterhauser; [markus.mitterhauser@meduniwien.ac.at](mailto:markus.mitterhauser@meduniwien.ac.at)

Received 23 November 2017; Accepted 27 December 2017; Published 13 February 2018

Academic Editor: Giorgio Biasiotto

Copyright © 2018 T. Balber et al. This is an open access article distributed under the Creative Commons Attribution License, which permits unrestricted use, distribution, and reproduction in any medium, provided the original work is properly cited.

Molecular imaging probes such as PET-tracers have the potential to improve the accuracy of tumor characterization by directly visualizing the biochemical situation. Thus, molecular changes can be detected early before morphological manifestation. The A<sub>3</sub> adenosine receptor (A<sub>3</sub>AR) is described to be highly expressed in colon cancer cell lines and human colorectal cancer (CRC), suggesting this receptor as a tumor marker. The aim of this preclinical study was the evaluation of [ $^{18}\text{F}$ ]FE@SUPPY as a PET-tracer for CRC using *in vitro* imaging and *in vivo* PET imaging. First, affinity and selectivity of FE@SUPPY and its metabolites were determined, proving the favorable binding profile of FE@SUPPY. The human adenocarcinoma cell line HT-29 was characterized regarding its hA<sub>3</sub>AR expression and was subsequently chosen as tumor graft. Promising results regarding the potential of [ $^{18}\text{F}$ ]FE@SUPPY as a PET-tracer for CRC imaging were obtained by autoradiography as  $\geq 2.3$ -fold higher accumulation of [ $^{18}\text{F}$ ]FE@SUPPY was found in CRC tissue compared to adjacent healthy colon tissue from the same patient. Nevertheless, first *in vivo* studies using HT-29 xenografts showed insufficient tumor uptake due to (1) poor conservation of target expression in xenografts and (2) unfavorable pharmacokinetics of [ $^{18}\text{F}$ ]FE@SUPPY in mice. We therefore conclude that HT-29 xenografts are not adequate to visualize hA<sub>3</sub>ARs using [ $^{18}\text{F}$ ]FE@SUPPY.

## 1. Introduction

Colorectal cancer (CRC) is the fourth leading cause of cancer-related deaths in men and women worldwide [1]. The primary diagnosis is usually made by colonoscopy and biopsy, which often does not reflect the full extent of the disease due to tumor heterogeneity and disregard of potential metastases. Positron Emission Tomography (PET) provides a noninvasive imaging technique, which is valuable for tumor staging and clinical decision making and to estimate the patient's prognosis [2]. Besides the routinely used PET-tracer [ $^{18}\text{F}$ ]FDG, the availability of specific tumor tracers would enhance the characterization of colorectal tumors and help in CRC staging and with the choice of treatment.

An essential characteristic of most solid tumors is hypoxia, which inevitably leads to accumulation of adenosine within the tumor microenvironment as a result of the breakdown of adenine nucleotides, which has been recognized in the 1990s [3, 4]. Since then, many efforts have been made to clarify the role of adenosine and its receptors in cancer [5–7]. The expression of the  $\text{A}_3$  adenosine receptor ( $\text{A}_3\text{AR}$ ), which is one of four subtypes of the adenosine receptor family, has been reported in several human tumor cell lines including leukemia (Jurkat T, HL-60), melanoma (A375), and astrocytoma (ADF) [8–12]. In particular, there is a rising interest in the involvement of  $\text{A}_3\text{AR}$ s in CRC as  $\text{A}_3\text{AR}$  protein expression has been reported for various colon cancer cell lines, including Caco-2, HCT-116, CCL-228, DLD-1, and HT-29 [13–15]. Merighi et al. have shown that caffeine leads to hypoxia-inducible factor-1 (HIF-1) protein accumulation and increased vascular endothelial growth factor (VEGF) expression through  $\text{A}_3\text{AR}$  stimulation in HT-29 cells under hypoxic conditions [16]. According to Sakowicz-Burkiewicz et al., treatment with the  $\text{A}_3\text{AR}$  agonist IB-MECA (1  $\mu\text{M}$ ) results in an  $\text{A}_3\text{AR}$ -dependent growth promoting effect in HT-29 cells. In contrast, IB-MECA causes cell apoptosis in HCT-116 cells, similarly in an  $\text{A}_3\text{AR}$  dependent manner [13].

High expression of  $\text{A}_3\text{AR}$  mRNA and protein has been reported in colon and breast carcinoma compared to adjacent nonneoplastic tissue by Madi et al. Remarkably, even higher levels of  $\text{A}_3\text{AR}$  mRNA have been found in lymph node metastases than in primary tumor tissue, suggesting  $\text{A}_3\text{AR}$ -overexpression as a marker for tumor progression [17]. Additionally, Gessi et al. studied  $\text{A}_3\text{AR}$  expression in colorectal cancer tissue samples of 73 patients and provided evidence that the  $\text{A}_3\text{AR}$  has the potential to be used as a diagnostic marker for colon cancer. The authors have shown  $\geq 2$ -fold increased  $\text{A}_3\text{AR}$  protein expression in primary colon carcinomas compared to normal mucosa and describe a tendency towards higher  $\text{A}_3\text{AR}$  expression in large adenomas compared to small adenomas. Therefore, the authors proposed a major role of the  $\text{A}_3\text{AR}$  in cancer aggressiveness [18]. Moreover, radioligand binding experiments using the  $\text{A}_3\text{AR}$  antagonist [ $^3\text{H}$ ]MRE 3008F20 and western blot analysis indicated that the  $\text{A}_3\text{AR}$  is the most abundant of all four adenosine receptor subtypes in colorectal cancer tissues as well as in colon cancer cell lines (Caco-2, DLD-1 and HT-29). On the contrary, RT-PCR experiments showed relatively

low levels of  $\text{A}_3\text{AR}$  mRNA in the mentioned colon cancer cell lines compared to mRNA levels of the other adenosine receptor subtypes [15]. As mRNA levels do not necessarily correlate with protein levels [19] and protein transcription is a prerequisite for targeted receptor imaging approaches such as PET imaging, protein expression data is the most relevant for this study.

The  $\text{A}_3\text{AR}$  antagonist [ $^{18}\text{F}$ ]FE@SUPPLY has been presented as the first PET-tracer for  $\text{hA}_3\text{AR}$  imaging in 2008 by Wadsak et al. [20, 21]. First preclinical PET imaging using CHO-K1- $\text{hA}_3\text{AR}$  xenografts has shown promising results leading to further evaluation of this PET-tracer in oncology [22]. Besides [ $^{18}\text{F}$ ]FE@SUPPLY and [ $^{18}\text{F}$ ]FE@SUPPLY:2, only a few other PET-ligands have been proposed for  $\text{A}_3\text{AR}$  imaging, including carbon-11 labeled 1,2,4-triazolo[4,3-a]quinoxalin-1-one derivatives and bromine-76 labeled nucleoside ligands ([ $^{76}\text{Br}$ ]MRS3581 and [ $^{76}\text{Br}$ ]MRS5147) [23–25]. To our knowledge, no preclinical *in vivo* PET imaging has been reported for these  $\text{A}_3\text{AR}$  PET-ligands so far. In our preclinical study, we aimed to evaluate [ $^{18}\text{F}$ ]FE@SUPPLY as a PET-tracer for human cancer using *in vitro* imaging and *in vivo* PET imaging in a CRC tumor model.

## 2. Methods

### 2.1. General

**2.1.1. Cell Culture.** HT-29 cells and CHO-K1 cells were purchased from ATCC. HT-29 cells were cultured in RPMI 1640 medium supplemented with 10% fetal calf serum, 2 mM L-glutamine, and 10  $\mu\text{g}/\text{mL}$  gentamicin sulfate. Human  $\text{A}_3$  adenosine receptor-expressing CHO-K1 cells (CHO-K1- $\text{hA}_3\text{AR}$ ) were purchased from PerkinElmer (ValiScreen® GPCR cell line) and were grown using Ham's F12 supplemented with 10% FCS, 2 mM L-glutamine, penicillin (100 U/M), streptomycin (100  $\mu\text{g}/\text{mL}$ ), and 0.4 mg/mL G418. Parental CHO-K1 cells were cultured likewise, but without selection antibiotics. Cells were maintained under standard conditions in a humidified incubator (37°C, 5%  $\text{CO}_2$ ).

**2.1.2. Animals.** Six-week-old male BALB/c mice (BALB/cAnNRj, Division of Laboratory Animal Science and Genetics, Himberg, Austria) were kept under conventional housing conditions, with food and water supply ad libitum and a 12 h day/night cycle. Male, immunodeficient CB17-SCID mice (CB-17/Icr-*Prkdc*<sup>scid</sup>/Rj, Janvier Labs, France) of the same age were kept under specific pathogen-free conditions in individually ventilated cages. All animals were treated according to the European Union rules on animal care. The corresponding animal experiments were approved by the Austrian Ministry of Sciences (BMWWF-66.009/0031-WF/V/3b/2015, BMWWF-66.009/0029-WF/V/3b/2015).

**2.1.3. Tumor Grafting.** After 10 to 14 days upon arrival, CB17-SCID mice were injected subcutaneously with  $2 \times 10^6$  HT-29 cells into one flank and  $2 \times 10^6$  CHO-K1 cells in the opposite flank ( $n = 9$ ). Body weight and tumor development

were monitored every second day by caliper measurement. The respective tumor volume was calculated according to the following equation: tumor volume ( $\text{mm}^3$ ) =  $d^2 \times D/2$  (where  $d$  is the shortest diameter and  $D$  the longest diameter). Animals were subjected to  $\mu\text{PET}$  imaging 10 days after inoculation, when tumors reached a volume of at least  $300 \text{ mm}^3$ . Tumor volume never exceeded  $1 \text{ cm}^3$ .

**2.1.4. Human Tissues.** Colorectal carcinoma tissue and adjacent healthy colon tissue were obtained directly after tumorectomy from two patients after full informed consent and quick-frozen in 2-methylbutane ( $-40^\circ\text{C}$ ). Tissue was sliced into  $16 \mu\text{m}$  slices using a microcryotome (Thermo Scientific Microm HM 560) and stored at  $-80^\circ\text{C}$  until usage. Depending on the sample size, 3 to 4 different regions were defined and analyzed by means of autoradiography and immunohistochemistry.

## 2.2. Characterization of Binding and Target Expression

**2.2.1. Competitive Binding Assay.** Competitive binding assays were performed using  $\text{hA}_1\text{AR}$ ,  $\text{hA}_{2\text{A}}\text{AR}$ , or  $\text{hA}_3\text{AR}$  expressing cell membranes ( $18.5 \text{ ng}/\mu\text{L}$ ,  $16.7 \text{ ng}/\mu\text{L}$ , or  $1.7 \text{ ng}/\mu\text{L}$  final protein concentration, resp.) and  $1.7 \text{ nM}$  [ $^3\text{H}$ ]DPCPX ( $K_D = 1.7 \text{ nM}$ ),  $50 \text{ nM}$  [ $^3\text{H}$ ]CGS21680 ( $K_D = 23 \text{ nM}$ ), or  $0.4 \text{ nM}$  [ $^{125}\text{I}$ ]AB-MECA ( $K_D = 0.78 \text{ nM}$ ) as the respective radioligands (all purchased from PerkinElmer, Inc. Waltham, USA). The assay was performed according to the manufacturer's instructions in a final volume of  $500 \mu\text{L}$ . Increasing concentrations of test compounds were added, whereby the concentration of dimethyl sulfoxide (DMSO) in final assay volume remained  $\leq 10\%$  ( $\text{hA}_1\text{AR}$  and  $\text{hA}_{2\text{A}}\text{AR}$  assay) and  $\leq 1\%$  in the  $\text{hA}_3\text{AR}$  assay. Nonspecific binding was determined using  $1 \mu\text{M}$  DPCPX ( $\text{hA}_1\text{AR}$  assay),  $1 \mu\text{M}$  SCH-442,416 ( $\text{hA}_{2\text{A}}\text{AR}$  assay), or  $10 \mu\text{M}$  I-AB-MECA ( $\text{hA}_3\text{AR}$  assay). Filtration through GF/B filters (Whatman®, presoaked in 0.1% PEI or 0.5% BSA) was performed using a cell harvester (Brandel®), and receptor-bound radioactivity was determined via gamma counting (2480 Wizard<sup>2</sup>, PerkinElmer) or liquid scintillation counting (Hidex 300 SL).  $\text{IC}_{50}$  fitted binding curves were generated using the GraphPad Software 5.0, and  $K_i$  values were calculated using the Cheng-Prusoff equation.

**2.2.2. Flow Cytometry.** For the flow cytometric evaluation of  $\text{hA}_3\text{AR}$  expression, single-cell suspensions of HT-29 cells ( $2 \times 10^5$  per tube) were fixed and permeabilized using Cytotfix/Cytoperm™ kit (BD Biosciences). Cells were incubated with mouse monoclonal anti-human  $\text{A}_3\text{AR}$  ( $100 \mu\text{L}$  of  $4 \mu\text{g}/\text{mL}$  in PBS + 2% FCS, Abnova H00000140-M01) or mouse IgG2b kappa isotype control ( $100 \mu\text{L}$  of  $4 \mu\text{g}/\text{mL}$  in PBS + 2% FCS, eBioscience™ 14-4732-85) for 1 h at  $4^\circ\text{C}$ . Following a washing step, bound primary antibodies were detected with rabbit anti-mouse IgG FITC ( $100 \mu\text{L}$  of  $40 \mu\text{g}/\text{mL}$  in PBS + 2% FCS, Dako F0261) for 30 min at  $4^\circ\text{C}$  in the dark. Samples were analyzed on a FACSCalibur™ flow cytometer (BD Bioscience), whereby 10,000 single cells were recorded.

**2.2.3. Western Blot.** Cell lysates were prepared from  $75 \text{ cm}^2$  cell culture flasks when cells reached 80% confluency using radioimmunoprecipitation assay (RIPA) buffer and protease inhibitor cocktail according to the manufacturer's instructions. Tissue lysates from HT-29 xenografts were prepared according to a standard protocol using RIPA buffer (according to sample size approx. 4 times of lysis buffer), protease inhibitor, and Ultra-Turrax® for homogenization. The protein concentration of cell lysates was determined using Pierce™ BCA Protein Assay Kit (Thermo Scientific), and  $20 \mu\text{g}$  protein per well was loaded onto TGX™ precast gels (Bio-Rad). After gel electrophoresis (200 V, 30 min), proteins were transferred to nitrocellulose membranes (Amersham™ Protran™ Premium  $0.2 \mu\text{m}$  NC, GE Healthcare Life Sciences) via semidry blotting (80 mA per gel). Membranes were incubated with rabbit polyclonal anti- $\text{A}_3\text{AR}$  (Santa Cruz Biotechnology, Inc. sc-13938) (1:750, 2 h, RT) and further incubated with goat anti-rabbit IgG HRP conjugate (1:5000, 1 h, RT). Detection was performed using the dedicated kit (SuperSignal West Pico Chemiluminescent Substrate detection kit, Thermo Scientific), and chemiluminescence imaging was conducted (Bio-Rad VersaDoc™ Imaging System).

## 2.3. In Vitro Imaging

**2.3.1. Immunofluorescence Microscopy.** HT-29 cells were seeded on chamber slides ( $3 \times 10^5/\text{mL}$ ,  $200 \mu\text{L}$  per well, 8 well slides) and incubated at  $37^\circ\text{C}$  until 50% confluency was reached. Cells were then fixed (4% paraformaldehyde in PBS, 15 min,  $4^\circ\text{C}$ ), permeabilized (0.2% Triton X in PBS, 2 min, room temperature (RT)), and blocked (2% FCS in PBS, 30 min, RT). Mouse monoclonal anti-human  $\text{A}_3\text{AR}$  (Abnova H00000140-M01) and mouse IgG2b kappa isotype control (eBioscience 14-4732-85) were used 1:50 in PBS + 2% FCS and incubated for 1 h at RT. Cells were washed three times with PBS and incubated with the secondary antibody (rabbit anti-mouse IgG FITC, Dako F0261) for 1 h at RT. After washing, cells were incubated with DAPI (1:5000) for 10 min at RT, and subsequently, slides were embedded with an aqueous mounting medium (Fluoromount™, Sigma F4680). Slides were recorded on an Axioplan II fluorescence microscope (Carl Zeiss Microscopy).

**2.3.2. Autoradiography.** Tissue slices were thawed and reconstituted in assay buffer (50 mM Tris-HCl pH 7.4, 100 mM NaCl, 1 mM EDTA, 1% BSA, 1 unit adenosine deaminase/100 mL) for 30 min at RT. Radiosynthesis of [ $^{18}\text{F}$ ]FE@SUPPY was performed as previously described and the product was physiologically formulated (EtOH/0.9% saline 10/90) [20]. Tissue slices were incubated with 50 kBq [ $^{18}\text{F}$ ]FE@SUPPY (40–200 GBq/ $\mu\text{mol}$ ) in  $100 \mu\text{L}$  assay buffer for 1 h at RT. Slices were thoroughly washed with ice-cold wash buffer (50 mM Tris-HCl pH 7.4), dried, and exposed to a phosphor screen overnight. The readout of the phosphor storage screen was performed on a Cyclone Phosphor Imager (Perkin Elmer), and data analysis was performed using OptiQuant® Software as previously described [26]. Statistical testing was performed using GraphPad Prism 5.0 Software. Differences among groups (colorectal cancer



versus healthy colon) were analyzed using a two-tailed, unpaired Student's *t*-test with Welch's correction.

**2.3.3. Immunohistochemistry.** Vicinal cryosections of colorectal carcinoma and healthy colon tissue were stained to identify regions with hA<sub>3</sub>AR expression following a standard protocol. In brief, cryosections were fixed (96% ethanol, 10 min), permeabilized (0.2% Triton X-100 in PBS, 5 min), and blocked using Bloxall™ Blocking Solution and a dedicated avidin/biotin blocking kit (Invitrogen, Thermo Fisher Scientific). Additionally, sections were incubated with goat serum (1:10 in PBS) to reduce nonspecific binding. Rabbit polyclonal anti-A<sub>3</sub>AR (1:100, ab203298; Abcam) was used 1:100 in PBS + 0.1% BSA for 1 h in a humid, dark chamber. Purified rabbit IgG (Life technologies) was used as an isotype control likewise. Cryosections were washed 3 times for 5 min (PBS + 0.1% Tween-20) and incubated with biotinylated anti-rabbit IgG (1:200, PBS + 5% goat serum) for 30 min. After washing, further detection was performed with the Vectastain® ABC kit (Vector Laboratories) according to the manufacturer's instructions. DAB substrate kit (Abcam) was used as a chromogen to detect peroxidase, and haematoxylin was used for counterstaining of cell nuclei. Immunohistochemically stained slides were acquired on an automated TissueFAXS microscope system (TissueGnostics, Vienna, Austria) at a 5-fold and 20-fold magnification.

#### 2.4. Tracer Stability in Mice

**2.4.1. In Vitro Stability Tests.** Stability of [<sup>18</sup>F]FE@SUPPY was tested against mouse liver microsomes, mouse S9 fraction, and mouse plasma (BD Sciences). Amount of intact tracer (%) was determined after 5, 10, 20, 40, 60, and 120 min using an Agilent series 1100/1200 HPLC system connected to a radioactivity detector (Raytest, Ramona Star) (*n* = 2 in triplicate). The assay was conducted as previously described for respective rat and human enzymes [27].

**2.4.2. Ex Vivo Blood Stability.** Radiosynthesis was performed as described elsewhere [20] and the product was processed as follows: ethanol was totally evaporated and the dry product was again physiologically formulated in 1.5–2 mL Tween-20/EtOH/0.9% saline 1/9/90 to obtain activity concentrations of approximately 1 GBq/mL. Healthy BALB/c mice were injected with 18 ± 2 MBq (molar activity = 70–200 GBq/μmol) retroorbitally and sacrificed after 5, 10, 20, 40, and 70 min (*n* = 3 for each time point). Blood samples were collected and immediately precipitated using acetonitrile/methanol (10:1) and centrifuged (12,000 rpm, 5 min, 4°C). The obtained supernatants were subjected to radio-HPLC as previously described [22].

**2.5. Biodistribution.** Ex vivo biodistribution of [<sup>18</sup>F]FE@SUPPY was assessed 70 min after tracer application in BALB/c mice. Radioactivity was determined using a gamma counter (2480 Wizard<sup>2</sup>, PerkinElmer), organs were wet-weighted, and percentage of injected dose per gram of organ was calculated (%ID/g).

**2.6. In Vivo Imaging.** Xenograft-bearing CB17-SCID mice were anesthetized using isoflurane (2.5%) mixed with oxygen (1.5 L/min) to avoid movement during the imaging. Blocking agents (2 mg/kg BW FE@SUPPY or MRS1523) or the respective vehicle control (Tween-20/EtOH/0.9% physiological saline 1/9/90) was administered retroorbitally 2 min prior to the radiotracer administration (*n* = 3 per group). Subsequently, the animals received another retroorbital injection of 17.42 ± 4.5 MBq [<sup>18</sup>F]FE@SUPPY into the venous plexus of the opposite eye. With a minor delay after the application of the radiotracer (2–3 min), mice were placed into the field of view of the scanner (μPET/CT Inveon, Siemens Medical Solution, Knoxville, USA), and dynamic imaging was performed for 60 min to follow tracer distribution. Vital parameters (respiration, body temperature) were continuously monitored using a dedicated monitoring unit (bioVet; m2m imaging, Cleveland, OH, USA) to ensure the depth of anesthesia and wellbeing of the animals. Retroorbital application volumes did not exceed 100 μL per application.

### 3. Results and Discussion

**3.1. Characterization of Binding and Target Expression.** Affinity and selectivity of FE@SUPPY and its potential metabolites upon cleavage by carboxylesterases, DFE@SUPPY, and FE@SUPPY:11 [28] were determined in competitive binding assays. FE@SUPPY has been first described by Li et al., who reported a *K<sub>i</sub>* value of 4.22 ± 0.7 nM for human A<sub>3</sub>AR. However, this study only provided the selectivity ratio towards rat A<sub>1</sub>AR (rA<sub>1</sub>AR/hA<sub>3</sub>AR = 7400) [29]. Here, we confirmed the affinity of FE@SUPPY towards the human A<sub>3</sub>AR (*K<sub>i</sub>* = 6.02 ± 0.4 nM, *n* = 3) and demonstrated its selective hA<sub>3</sub>AR binding compared to the other human adenosine receptors. Moreover, the respective theoretical metabolites show little affinity for the hA<sub>3</sub>AR, supporting the potential of FE@SUPPY as a ligand for human *in vivo* application (Table 1).

The human colorectal adenocarcinoma cell line (HT-29) was characterized regarding its hA<sub>3</sub>AR protein expression using flow cytometry and western blot. Flow cytometric analysis resulted in mean fluorescence intensity (ΔMFI) of 53.6 ± 22 in three independent experiments (Figure 1). Additionally, A<sub>3</sub>AR protein expression in HT-29 cells was determined by western blot (Figure 8) (western blot results are discussed separately below). This is in line with previous studies, which reported A<sub>3</sub>AR expression for this cell line as well [13, 15]. Thus, HT-29 cells were subsequently chosen for tumor graft experiments.

**3.2. In Vitro Imaging.** Fluorescence microscopy of HT-29 cells showed cell membrane-specific staining, pointing at the expression of hA<sub>3</sub>AR on the cell surface, which is typical for GPCRs (Figure 2).

In all investigated regions of the two CRC patients, [<sup>18</sup>F]FE@SUPPY accumulation was higher in colorectal carcinoma tissue slices than in healthy colon tissue slices of the same individual (for detailed analysis see supplementary (available here)). In 5 of 7 regions, a ≥2.3-fold higher binding

TABLE 1: Affinity and selectivity data of FE@SUPPY and metabolites towards adenosine receptor subtypes ( $n = 3-5$  in triplicate; amount of DMSO never exceeded 1% of total assay volume in hA<sub>3</sub>AR assay; DMSO was added up to 10% in hA<sub>1</sub>AR and hA<sub>2A</sub>AR assay; \* $n = 2$  in triplicate; exact  $K_i$  value could not be determined due to limited solubility).

Compound	hA <sub>1</sub> AR	hA <sub>2A</sub> AR	hA <sub>3</sub> AR	hA <sub>1</sub> /hA <sub>3</sub> AR	hA <sub>2A</sub> /hA <sub>3</sub> AR
FE@SUPPY	$4.03 \pm 1.0 \mu\text{M}$	$1.72 \pm 0.4 \mu\text{M}$	$6.02 \pm 0.4 \text{ nM}$	669	285
DFE@SUPPY	$5.46 \pm 0.4 \mu\text{M}$	$37.13 \pm 16 \mu\text{M}$	$2.58 \pm 1.2 \mu\text{M}$	324	112
FE@SUPPY:11	$\geq 57 \mu\text{M}^*$	$5.86 \pm 0.8 \mu\text{M}$	$2.80 \pm 1.4 \mu\text{M}$	$\geq 20$	2

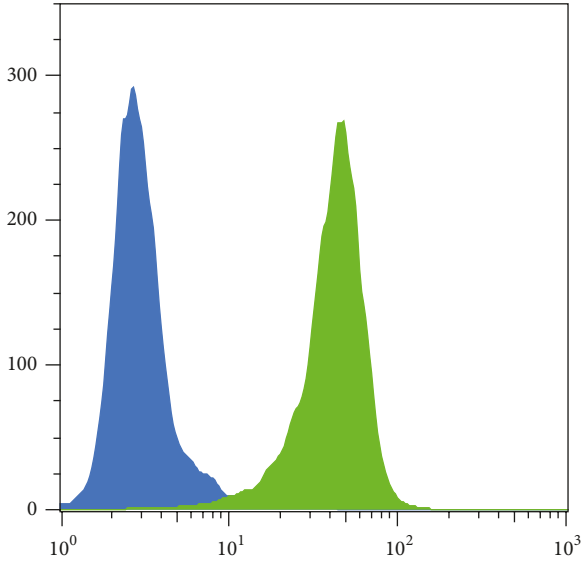


FIGURE 1: Flow cytometric analysis of HT-29 cells revealed expression of hA<sub>3</sub>AR protein (green). The isotype control did not show fluorescence signal (blue).

of [<sup>18</sup>F]FE@SUPPY was found ( $P < 0.05$ ). This finding is in accordance with Gessi et al., who reported similar ratios by means of [<sup>3</sup>H]MRE 3008F20 binding [18]. Regions with high accumulation of [<sup>18</sup>F]FE@SUPPY corresponded to regions with high hA<sub>3</sub>AR expression identified by immunohistochemistry (Figure 3).

**3.3. Tracer Stability in Mice.** [<sup>18</sup>F]FE@SUPPY exhibited high stability in mouse plasma, as  $92.6 \pm 0.7\%$  of intact tracer could still be detected after 120 min of incubation at 37°C. *In vitro* stability tests against mouse liver homogenates (S9 fraction) and purified mouse liver microsomes showed  $66.9 \pm 6.7\%$  and  $31.4 \pm 7.8\%$  intact tracer after 120 min, respectively. Ex vivo blood stability analysis demonstrated more rapid degradation of [<sup>18</sup>F]FE@SUPPY *in vivo* than that observed in *in vitro* testing as only  $2.2 \pm 0.4\%$  intact [<sup>18</sup>F]FE@SUPPY could be determined after 70 min (Figure 4). This data indicates higher metabolism in mice compared to rats described in previously conducted studies, where  $25.8 \pm 5.3\%$  intact tracer was found in plasma after 60 min [22]. However, these data could also be mimicked by the fact that intact [<sup>18</sup>F]FE@SUPPY is rapidly cleared from blood hepatobiliary (into the bile fluid, compare

Figures 5 and 7), and the equilibrium in blood is therefore shifted to the metabolites.

**3.4. Biodistribution.** Biodistribution was assessed 70 min after tracer application in healthy BALB/c mice and revealed a high accumulation of radioactivity in fat-rich regions (brown adipose tissue, BAT) likely due to the tracer's lipophilicity [30]. Regarding the emunctory organs, liver showed the highest accumulation ( $14.57 \pm 0.20\%$  ID/g), followed by the kidneys ( $2.67 \pm 0.24\%$  ID/g). The additional analysis of body liquids pointed at a mainly hepatobiliary excretion of [<sup>18</sup>F]FE@SUPPY, as the highest amount was found in bile fluid ( $162.78 \pm 37.51\%$  ID/g). The amount of radioactivity in the kidneys and urine ( $43.33 \pm 9.23\%$  ID/g) suggests the excretion of the hydrophilic radioactive metabolite, 2-[<sup>18</sup>F]fluoroethanol [31], which was already proposed by Haeusler et al. [28]. The circulating radioactivity in blood was low after 70 min ( $1.6 \pm 0.1\%$  ID/g). This finding is in accordance with the results obtained by the *ex vivo* blood analysis. Moreover, pronounced accumulation of [<sup>18</sup>F]FE@SUPPY was found in A<sub>3</sub>AR rich tissues such as the heart ( $1.13 \pm 0.04\%$  ID/g) and lung ( $1.50 \pm 0.23\%$  ID/g). A similar biodistribution pattern was observed for rats in a previously conducted study [20]. [<sup>18</sup>F]FE@SUPPY accumulation in the brain was low after 70 min ( $0.23 \pm 0.03\%$  ID/g) (Figure 5).

**3.5. In Vivo Imaging.**  $\mu$ PET imaging of the mouse xenograft model revealed high uptake of [<sup>18</sup>F]FE@SUPPY in the emunctory organs, which was again most pronounced in the liver ( $\text{SUV} = 6.68 \pm 0.80$ ). Low standardized uptake values were observed in tumor masses of both HT-29 and CHO-K1 xenograft tumors ( $\text{SUV} = 0.23 \pm 0.06$  and  $0.25 \pm 0.33$ ), respectively. There was no difference between CHO-K1 xenografts, which served as a negative control (human A<sub>3</sub>AR negative), and HT-29 xenografts. Moreover, significant blocking could not be achieved (Figure 6). The affinity of FE@SUPPY for the mouse A<sub>3</sub>AR is uncertain but is expected to be lower than that for the human A<sub>3</sub>AR due to the known species differences. The lack of adequate rodent models, mainly due to the low affinity of most hA<sub>3</sub>AR ligands to the rodent A<sub>3</sub>AR, was already recognized by Yamano et al. who proposed a humanized mouse model [32]. Specific uptake was therefore not expected in mouse tissues. Interestingly, a significant influence of the blocking was observed in BAT (decrease in uptake) and lung (increase in uptake). However, the data is based on a set of three individuals in each group, and displacement was not performed in the same individuals.

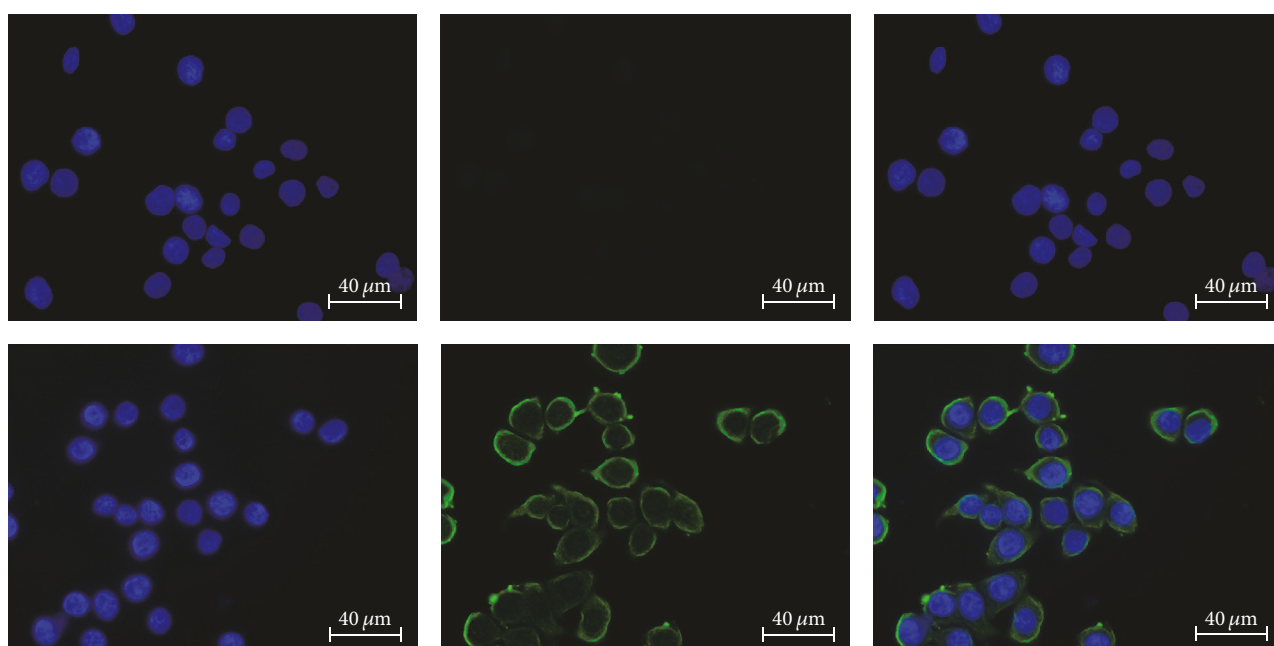


FIGURE 2: Immunofluorescent staining of HT-29 cells; left: DAPI, middle: FITC, right: merge. Upper row: mouse isotype control, lower row: anti-human A<sub>3</sub>AR staining.

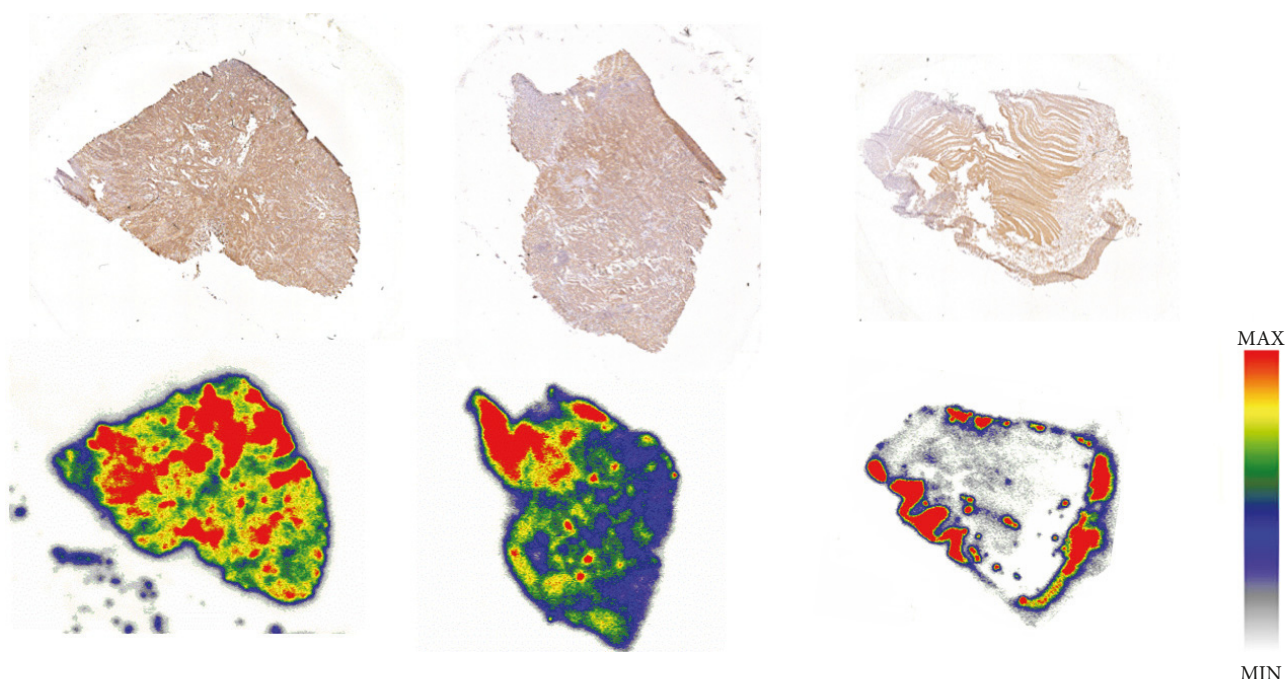


FIGURE 3: Upper row: immunohistochemical staining of hA<sub>3</sub>AR. Lower row: autoradiographic analysis of the corresponding vicinal tissue slices using [<sup>18</sup>F]FE@SUPPY. Left and center: colon cancer tissue, right: healthy colon tissue.

Since tumor uptake in the chosen model was insufficient and not blockable, this phenomenon was not investigated any further.

For a detailed analysis of the pharmacokinetics, volumes of interest were also generated for mouse body liquids including blood, urine, and bile fluid (Figure 7). The radioactivity

in blood was generally low ( $SUV = 1.21 \pm 0.11$ ) compared to the body liquids, urine ( $SUV = 8.86 \pm 3.44$ ), and bile fluid ( $21.85 \pm 10.63$ ), showing the highest accumulation of [<sup>18</sup>F]FE@SUPPY, which is in line with the biodistribution experiments. The mentioned standardized uptake values refer to baseline conditions.



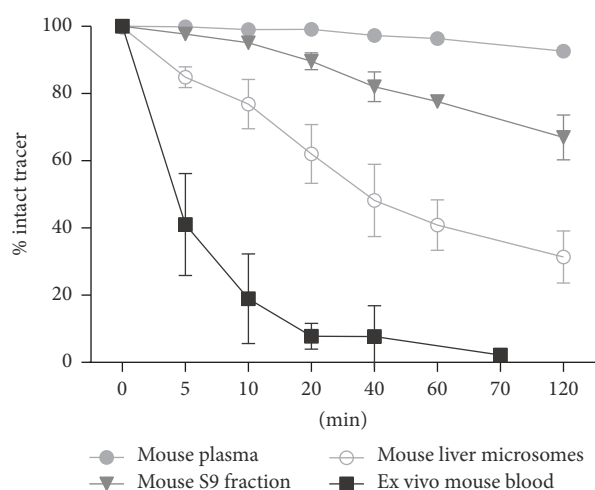


FIGURE 4: *In vitro* stability and *ex vivo* blood stability of [ $^{18}\text{F}$ ]FE@SUPPY.

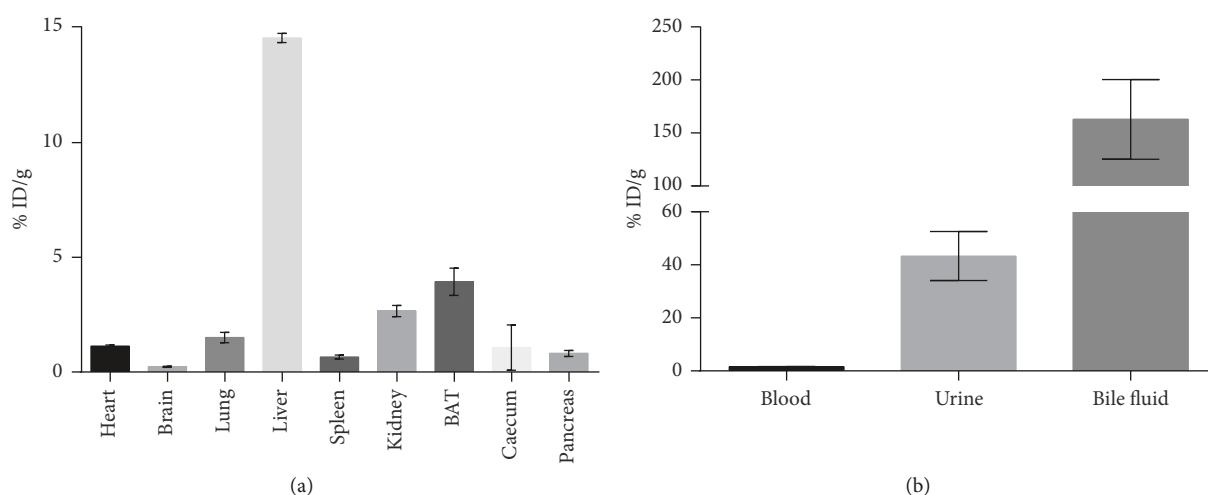


FIGURE 5: Biodistribution of [ $^{18}\text{F}$ ]FE@SUPPY in healthy BALB/c mice ( $n = 3$ ). (a) shows biodistribution in organs. (b) shows accumulation in body liquids.

Adenosine concentrations of  $\sim 0.5 \mu\text{M}$  have been proposed in HT-29 tumors grown as xenografts [4]. Even though adenosine displays only intermediate affinity for the  $\text{A}_3\text{AR}$  ( $\sim 1 \mu\text{M}$  at the rat  $\text{A}_3\text{AR}$  [33]), the PET-tracer would have to compete with the endogenous ligand for  $\text{A}_3\text{AR}$  occupancy. This may decrease accumulation of [ $^{18}\text{F}$ ]FE@SUPPY in the xenografts. However, more importantly, despite the fact that western blot analysis demonstrated  $\text{hA}_3\text{AR}$  expression in HT-29 cells,  $\text{hA}_3\text{AR}$  protein could not be detected in tissue lysates derived from HT-29 xenografts. This indicates that the human receptor is poorly conserved in mice upon tumor graft (Figure 8). To our knowledge, this phenomenon has not been described in literature so far but has tremendous impact on *in vivo* imaging. PET imaging is only feasible if an abundant amount of the target is available, as only nanomolar or even lower concentrations of PET-tracers are applied.

#### 4. Conclusion

We found a favorable binding profile of [ $^{18}\text{F}$ ]FE@SUPPY displaying high affinity for the human  $\text{A}_3\text{AR}$  besides low affinity for the other human adenosine receptor subtypes. Autoradiography showed  $\geq 2.3$ -fold higher uptake in human CRC compared to adjacent healthy colon tissues. First *in vivo* studies using HT-29 xenografts showed insufficient tumor uptake. After initial high expression rates of the  $\text{A}_3\text{AR}$  in the HT-29 cells, tumor masses, derived from HT-29 xenografts, revealed low target expression. The receptor was not conserved in the xenograft, which hampered the PET imaging strategy. An additional drawback of the used mouse model is the unfavorable pharmacokinetics of the PET-tracer [ $^{18}\text{F}$ ]FE@SUPPY in mice. It is questionable how accurate xenograft models in immunocompromised mice are to study the role of human  $\text{A}_3\text{AR}$ s in cancer. Despite all efforts, *in vivo*

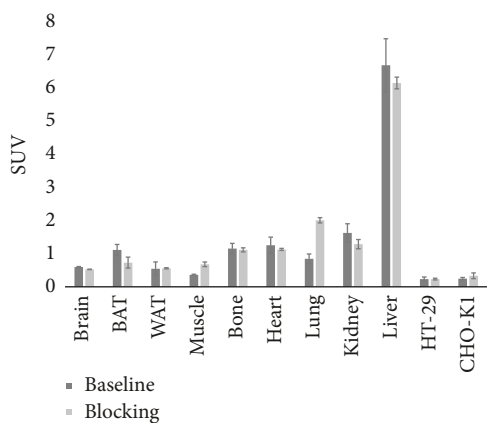


FIGURE 6:  $\mu$ PET-imaging was performed for 60 min. Activity concentration of [ $^{18}\text{F}$ ]FE@SUPPY in organs of interest is expressed as standardized uptake value (SUV). Blocking experiments, shown in the figure, were performed using unlabeled FE@SUPPY. Blocking experiments using MRS1523 provided the same outcome and are not shown in the figure.

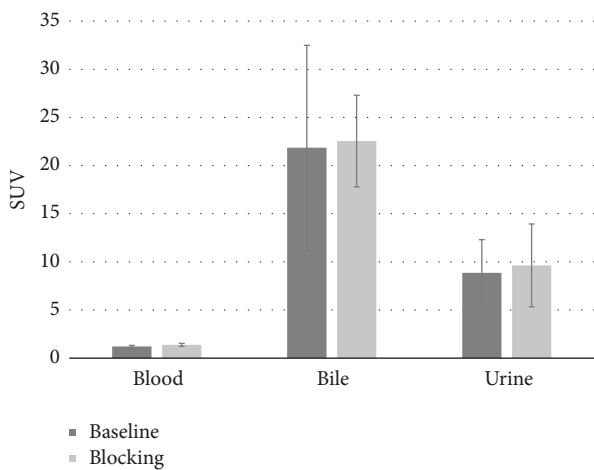


FIGURE 7:  $\mu$ PET-imaging was performed for 60 min. Activity concentration of [ $^{18}\text{F}$ ]FE@SUPPY in body liquids is expressed as standardized uptake value (SUV). Blocking experiments, shown in the figure, were performed using unlabeled FE@SUPPY. Blocking experiments using MRS1523 provided the same outcome and are not shown in the figure.

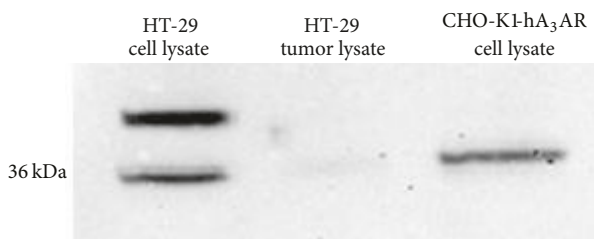


FIGURE 8: Western blot analysis of HT-29 cell lysate and tissue lysate derived from HT-29 xenograft tumors. CHO-K1-hA<sub>3</sub>AR cell lysate was loaded as a positive control. An additional band of unknown identity was detected in HT-29 cell lysate.

visualization of the A<sub>3</sub>AR has not been successful to date and deeper understanding of A<sub>3</sub>AR function is still missing.

### Conflicts of Interest

The authors declare that they have no conflicts of interest.

### Acknowledgments

This work was supported by the Austrian Science Fund (FWF P26502-B24, M. Mitterhauser) and was performed with the support of the Molecular Imaging Cluster of the Medical University of Vienna, Austria. J. Fazekas-Singer was supported by Grant CCHD W1205-B09 awarded to Dr. E. Jensen-Jarolim. The authors want to thank Petra F rlinger for her collaboration in the autoradiography experiments and Markus Zeilinger for his support in statistics.

### Supplementary Materials

Table S1: binding values of FE@SUPPY are expressed as fmol/mm<sup>2</sup> tissue. (*Supplementary Materials*)

### References

- [1] Global Burden of Disease Cancer C, "The global burden of cancer 2013," *JAMA Oncology*, vol. 1, no. 4, pp. 505–527, 2015.
- [2] L. Fass, "Imaging and cancer: a review," *Molecular Oncology*, vol. 2, no. 2, pp. 115–152, 2008.
- [3] B. B. Fredholm, A. P. Ijzerman, K. A. Jacobson, K. Klotz, and J. Linden, "International Union of Pharmacology. XXV. Nomenclature and classification of adenosine receptors," *Pharmacological Reviews*, vol. 53, no. 4, pp. 527–552, 2001.
- [4] J. Blay, T. D. White, and D. W. Hoskin, "The extracellular fluid of solid carcinomas contains immunosuppressive concentrations of adenosine," *Cancer Research*, vol. 57, no. 13, pp. 2602–2605, 1997.
- [5] S. Merighi, P. Mirandola, K. Varani et al., "A glance at adenosine receptors: Novel target for antitumor therapy," *Pharmacology & Therapeutics*, vol. 100, no. 1, pp. 31–48, 2003.
- [6] S. Gessi, S. Merighi, V. Sacchetto, C. Simioni, and P. A. Borea, "Adenosine receptors and cancer," *Biochimica et Biophysica Acta (BBA) - Biomembranes*, vol. 1808, no. 5, pp. 1400–1412, 2011.
- [7] P. A. Borea, S. Gessi, S. Merighi, and K. Varani, "Adenosine as a multi-signalling guardian angel in human diseases: when, where and how does it exert its protective effects?" *Trends in Pharmacological Sciences*, vol. 37, no. 6, pp. 419–434, 2016.
- [8] S. Gessi, K. Varani, S. Merighi et al., "Pharmacological and biochemical characterization of A<sub>3</sub> adenosine receptors in Jurkat T cells," *British Journal of Pharmacology*, vol. 134, no. 1, pp. 116–126, 2001.
- [9] S. Merighi, P. Mirandola, D. Milani et al., "Adenosine receptors as mediators of both cell proliferation and cell death of cultured human melanoma cells," *Journal of Investigative Dermatology*, vol. 119, no. 4, pp. 923–933, 2002.
- [10] S. Merighi, A. Benini, P. Mirandola et al., "A<sub>3</sub> adenosine receptors modulate hypoxia-inducible factor-1 $\alpha$  expression in human A375 melanoma cells," *Neoplasia*, vol. 7, no. 10, pp. 894–903, 2005.

- [11] S. Gessi, K. Varani, S. Merighi et al., "A3 adenosine receptors in human neutrophils and promyelocytic HL60 cells: A pharmacological and biochemical study," *Molecular Pharmacology*, vol. 61, no. 2, pp. 415–424, 2002.
- [12] M. L. Trincavelli, D. Tusciano, M. Marroni et al., "A3 adenosine receptors in human astrocytoma cells: Agonist-mediated desensitization, internalization, and down-regulation," *Molecular Pharmacology*, vol. 62, no. 6, pp. 1373–1384, 2002.
- [13] M. Sakowicz-Burkiewicz, A. Kitowska, M. Grden, I. Maciejewska, A. Szutowicz, and T. Pawelczyk, "Differential effect of adenosine receptors on growth of human colon cancer HCT 116 and HT-29 cell lines," *Archives of Biochemistry and Biophysics*, vol. 533, no. 1–2, pp. 47–54, 2013.
- [14] E. Polycarpou, L. B. Meira, S. Carrington, E. Tyrrell, H. Modjtahedi, and M. A. Carew, "Resveratrol 3-O-d-glucuronide and resveratrol 4'-O-d-glucuronide inhibit colon cancer cell growth: evidence for a role of A3 adenosine receptors, cyclin D1 depletion, and G1 cell cycle arrest," *Molecular Nutrition & Food Research*, vol. 57, no. 10, pp. 1708–1717, 2013.
- [15] S. Gessi, S. Merighi, K. Varani et al., "Adenosine receptors in colon carcinoma tissues and colon tumoral cell lines: focus on the A3 adenosine subtype," *Journal of Cellular Physiology*, vol. 211, no. 3, pp. 826–836, 2007.
- [16] S. Merighi, A. Benini, P. Mirandola et al., "Caffeine inhibits adenosine-induced accumulation of hypoxia-inducible factor-1 $\alpha$ , vascular endothelial growth factor, and interleukin-8 expression in hypoxic human colon cancer cells," *Molecular Pharmacology*, vol. 72, no. 2, pp. 395–406, 2007.
- [17] L. Madi, A. Ochaion, L. Rath-Wolfson et al., "The A3 adenosine receptor is highly expressed in tumor versus normal cells: Potential target for tumor growth inhibition," *Clinical Cancer Research*, vol. 10, no. 13, pp. 4472–4479, 2004.
- [18] S. Gessi, E. Cattabriga, A. Avitabile et al., "Elevated expression of A3 adenosine receptors in human colorectal cancer is reflected in peripheral blood cells," *Clinical Cancer Research*, vol. 10, no. 17, pp. 5895–5901, 2004.
- [19] A. Koussounadis, S. P. Langdon, I. H. Um, D. J. Harrison, and V. A. Smith, "Relationship between differentially expressed mRNA and mRNA-protein correlations in a xenograft model system," *Scientific Reports*, vol. 5, Article ID 10775, 2015.
- [20] W. Wadsak, L.-K. Mien, K. Shanab et al., "Preparation and first evaluation of [18F]FE@SUPPY: a new PET tracer for the adenosine A3 receptor," *Nuclear Medicine and Biology*, vol. 35, no. 1, pp. 61–66, 2008.
- [21] W. Wadsak, L.-K. Mien, K. Shanab et al., "Radiosynthesis of the adenosine A3 receptor ligand 5-(2-[18F]fluoroethyl) 2,4-diethyl-3-(ethylsulfanylcarbonyl)-6-phenylpyridine-5-carboxylate ([18F]FE@SUPPY)," *Radiochimica Acta*, vol. 96, no. 2, pp. 119–124, 2008.
- [22] D. Haeusler, C. Kuntner, L. Nics et al., "[18F]FE@SUPPY: a suitable PET tracer for the adenosine A3 receptor? An in vivo study in rodents," *European Journal of Nuclear Medicine and Molecular Imaging*, vol. 42, no. 5, pp. 741–749, 2015.
- [23] M. Mitterhauser, D. Haeusler, L. Mien et al., "Automatisation and First Evaluation of [18F]FE@SUPPY:2, an Alternative PET-Tracer for the Adenosine A3 Receptor: A Comparison with [18F]FE@SUPPY," *The Open Nuclear Medicine Journal*, vol. 1, no. 1, pp. 15–23, 2009.
- [24] M. Gao, A. C. Gao, M. Wang, and Q.-H. Zheng, "Simple synthesis of new carbon-11-labeled 1,2,4-triazolo[4,3-a]quinoxalin-1-one derivatives for PET imaging of A3 adenosine receptor," *Applied Radiation and Isotopes*, vol. 91, pp. 71–78, 2014.
- [25] D. O. Kiesewetter, L. Lang, Y. Ma et al., "Synthesis and characterization of [76Br]-labeled high-affinity A3 adenosine receptor ligands for positron emission tomography," *Nuclear Medicine and Biology*, vol. 36, no. 1, pp. 3–10, 2009.
- [26] C. Philippe, D. Haeusler, F. Fuchshuber et al., "Comparative autoradiographic in vitro investigation of melanin concentrating hormone receptor 1 ligands in the central nervous system," *European Journal of Pharmacology*, vol. 735, no. 1, pp. 177–183, 2014.
- [27] L. Nics, C. Vraha, M. Hendl, D. Haeusler, K. H. Wagner, K. Shanab et al., "In-vitro stability of [18F]FE@SUPPY and [18F]FE@SUPPY:2 against human liver-microsomes and human plasma," *Nuklearmedizin*, vol. 50, 2011.
- [28] D. Haeusler, L. Nics, L.-K. Mien et al., "[18F]FE@SUPPY and [18F]FE@SUPPY:2 - metabolic considerations," *Nuclear Medicine and Biology*, vol. 37, no. 4, pp. 421–426, 2010.
- [29] A.-H. Li, S. Moro, N. Forsyth, N. Melman, X.-D. Ji, and K. A. Jacobson, "Synthesis, CoMFA analysis, and receptor docking of 3,5-diacetyl-2,4-dialkylpyridine derivatives as selective A3 adenosine receptor antagonists," *Journal of Medicinal Chemistry*, vol. 42, no. 4, pp. 706–721, 1999.
- [30] C. Vraha, L. Nics, K.-H. Wagner, M. Hacker, W. Wadsak, and M. Mitterhauser, "LogP, a yesterday's value?" *Nuclear Medicine and Biology*, vol. 50, pp. 1–10, 2017.
- [31] J. Pan, M. Pourghasian, N. Hundal et al., "2-[18F]Fluoroethanol and 3-[18F]fluoropropanol: Facile preparation, biodistribution in mice, and their application as nucleophiles in the synthesis of [18F]fluoroalkyl aryl ester and ether PET tracers," *Nuclear Medicine and Biology*, vol. 40, no. 6, pp. 850–857, 2013.
- [32] K. Yamano, M. Inoue, S. Masaki, M. Saki, M. Ichimura, and M. Satoh, "Generation of adenosine A3 receptor functionally humanized mice for the evaluation of the human antagonists," *Biochemical Pharmacology*, vol. 71, no. 3, pp. 294–306, 2006.
- [33] K. A. Jacobson, H. O. Kim, S. M. Siddiqi, M. E. Olah, G. L. Stiles, and D. K. J. E. Von Lubitz, "A3-adenosine receptors: Design of selective ligands and therapeutic prospects," *Drugs of the Future*, vol. 20, no. 7, pp. 689–699, 1995.



## **Supplementary**

sample		Colorectal cancer	Healthy colon	P value	ratio
Patient 1	Region 1	7.0 ± 3.6	3.1 ± 0.6	< 0.05	2.3
	Region 2	9.9 ± 1.1	4.1 ± 1.2	< 0.01	2.4
	Region 3	12.2 ± 2.8	4.4 ± 1.2	< 0.01	2.8
	Region 4	7.6 ± 2.3	2.3 ± 0.9	< 0.01	3.3
Patient 2	Region 1	8.6 ± 0.8	3.4 ± 0.2	< 0.01	2.5
	Region 2	8.5 ± 0.9	6.6 ± 1.7	ns	1.3
	Region 3	25.0 ± 2.6	15.6 ± 0.5	< 0.05	1.6

Table S1: Binding values (mean ± SD, n=3-9) of [<sup>18</sup>F]FE@SUPPY are expressed as fmol/mm<sup>2</sup> tissue.



## 3.2 Manuscript #2

**Title:** A new method measuring the interaction of radiotracers with the human P-glycoprotein (P-gp) transporter

**Authors:** Chrysoula Vraka, Monika Dumanic, Teresa Racz, Florian Pichler, Cécile Philippe, **Theresa Balber**, Eva-Maria Klebermass, Karl-Heinz Wagner, Marcus Hacker, Wolfgang Wadsak and Markus Mitterhauser

**Associated Content:** Supplementary information DOI: 10.1016/j.nucmedbio.2018.02.002.

**Rationale and Aim:** In today's world, the prevention and treatment of mental disorders are becoming increasingly important, as society has to face an incident rate of 25% to develop one or more mental or behavioral disorders once in a lifetime. According to the World Health Report on Mental Health, individuals of both sexes at all stages of the life course are affected and mental disorders are not limited to industrialized countries. (177) Concomitantly, there is a rising interest in accurate and early diagnosis of psychiatric and mental diseases. In this context, PET offers a powerful imaging technique enabling the molecular characterization of the underlying dysfunction in neurotransmission while being minimal invasive.

Central tracer uptake and thus blood brain barrier penetration is a prerequisite for a PET-tracer intended for brain imaging. However, 98% of small molecules fail to cross the blood-brain barrier. (34) Therefore, the development of central PET-tracers is very challenging. At the same time, there is a lack of adequate *in vitro* models to test for brain entrance and mostly outdated parameters are used to predict blood brain barrier penetration. (61) One main hindrance for the successful central application of a PET-tracer is its binding to efflux transporters. Brain efflux is often recognized only in pre-clinical *in vivo* studies, when a lot of effort regarding radiochemical preparation and preclinical testing has already been made. Thus, a reliable *in vitro* method for the early prediction of a PET-tracer's interaction with the efflux transporter P-gp is of great importance to the scientific community. Moreover, in accordance with the 3R principle (replace, reduce, refine), animal experiments can be kept to a minimum.

Thus, the establishment of a reliable method for blood brain barrier prediction became a major research goal of our working group. We aimed at the set-up of an easy to handle cell-based method providing straightforward information about the direct interaction of a respective PET-tracer with P-gp.







# A new method measuring the interaction of radiotracers with the human P-glycoprotein (P-gp) transporter<sup>☆</sup>

Chrysoula Vraka<sup>a,b</sup>, Monika Dumanic<sup>a</sup>, Teresa Racz<sup>a</sup>, Florian Pichler<sup>a,c</sup>, Cecile Philippe<sup>a</sup>, Theresa Balber<sup>a,f</sup>, Eva-Maria Klebermass<sup>a</sup>, Karl-Heinz Wagner<sup>b</sup>, Marcus Hacker<sup>a</sup>, Wolfgang Wadsak<sup>a,d,e</sup>, Markus Mitterhauser<sup>a,f,g,\*</sup>

<sup>a</sup> Department of Biomedical Imaging and Image-guided Therapy, Division of Nuclear Medicine, Medical University of Vienna, Vienna, Austria

<sup>b</sup> Department for Nutritional Science, University of Vienna, Vienna, Austria

<sup>c</sup> Department of Engineering, University of Applied Sciences Wiener Neustadt, Austria

<sup>d</sup> Department of Inorganic Chemistry, University of Vienna, Vienna, Austria

<sup>e</sup> CBmed, Graz, Austria

<sup>f</sup> Department of Pharmaceutical Technology and Biopharmaceuticals (PTB), University of Vienna, Vienna, Austria

<sup>g</sup> Ludwig Boltzmann Institute Applied Diagnostics, Vienna, Austria

## ARTICLE INFO

### Article history:

Received 13 November 2017

Received in revised form 17 January 2018

Accepted 6 February 2018

Available online xxxx

### Keywords:

ABCB1

efflux transporter

MDR1

PET tracer

P-gp-substrate

## ABSTRACT

In drug development, biomarkers for cerebral applications have a lower success rate compared to cardiovascular drugs or tumor therapeutics. One reason is the missing blood brain barrier penetration, caused by the tracer's interaction with efflux transporters such as the P-gp (MDR1 or ABCB1). Aim of this study was the development of a reliable model to measure the interaction of radiotracers with the human efflux transporter P-gp in parallel to the radiolabeling process. LigandTracer® Technology was used with the wildtype cell line MDCKII and the equivalent cell line overexpressing human P-gp (MDCKII-hMDR1). The method was evaluated based on established PET tracers with known interaction with the human P-gp transporter and in nanomolar concentration (15 nM). [<sup>11</sup>C]SNAP-7941 and [<sup>18</sup>F]FE@SNAP were used as P-gp substrates by comparing the real-time model with an uptake assay and  $\mu$ PET images. [<sup>11</sup>C]DASB [<sup>11</sup>C]Harmine, [<sup>18</sup>F]FMeNER, [<sup>18</sup>F]FE@SUPPLY and [<sup>11</sup>C]Me@HAPTHI were used as tracers without interactions with P-gp *in vitro*. However, [<sup>11</sup>C]Me@HAPTHI shows a significant increase in SUV levels after blocking with Tariquidar. The developed real-time kinetic model uses directly PET tracers in a compound concentration, which is reflecting the *in vivo* situation. This method may be used at an early stage of radiopharmaceutical development to measure interactions to P-gp before conducting animal experiments.

© 2018 Elsevier Inc. All rights reserved.

## 1. Introduction

According to the World Health Organization, there is an incident rate of ~1:4 to suffer from mental disorders once in a lifetime. Currently, >450 million people worldwide are affected [1]. Still, none of these disorders are fully understood and the underlying neurobiology changes and the pathway of medication are discussed controversially. Positron emission tomography (PET) is currently the most sensitive and specific

imaging technique for the quantification of these biochemical changes of the involved neurotransmitter systems, since it contributes to the elucidation with minimal invasive effort. Therefore, the demand of PET tracers targeting the brain is expanding rapidly. In comparison to drugs targeting cancer or cardiovascular diseases, medications for the central nervous system (CNS) have a lower success rate (<15% in phase III compared to >30%) [2]. Pardridge et al. stated that about ~98% of all small molecules are not crossing the blood brain barrier (BBB) [3]. In addition, central uptake of exogenous compounds is limited by efflux transporters [4,5].

Efflux transporters belong to the ATP binding cassette (ABC) super family and can be found in organs of mammalian species ubiquitously. Furthermore, ABC efflux transporters were found in a plethora of tumor membranes thereby limiting effective therapies with cytotoxic agents and targeted anticancer drugs (multiple drug resistance) [6–9]. Therefore, efflux transporters are significantly involved in drug pharmacokinetics. The most relevant efflux transporter is the permeability glycoprotein (P-gp), also known as MDR1 (genetic name) or ABCB1

Abbreviations: AUC, area under the curve; BCRP, breast cancer resistance protein;  $K_i$ , equilibrium inhibitory constant; hMDR1, human multiple drug resistance 1; MDCKII, Madin-Darby Canine Kidney cell line; MRP-1, multiple drug resistance protein 1; PET, positron emission tomography; TQD, Tariquidar; VERA, Verapamil; WT, wildtype.

<sup>☆</sup> This work was supported by the Austrian Science Fund (FWF P26502-B24, M. Mitterhauser).

\* Corresponding author at: Ludwig Boltzmann Institute Applied Diagnostics, General Hospital of Vienna, Waehringer Guertel 18–20, A-1090 Vienna, Austria.

E-mail address: [markus.mitterhauser@meduniwien.ac.at](mailto:markus.mitterhauser@meduniwien.ac.at) (M. Mitterhauser).

(family name). Interestingly, a wide range of P-gp substrates with different chemical structures and pharmacological functions are known (e.g. anticancer drugs, protease inhibitors, peptides, steroids, calcium channel blockers and antihistamines) [9,10]. Solely based on structure or chemical properties, an upfront identification of P-gp substrates is impossible. For that reason, there is a need for *in vitro* technologies that reliably predict interactions between newly developed drugs and the efflux transporter P-gp already at early stages of PET tracer development.

Objective of the study was to set up a real-time kinetic model to distinguish between P-gp-substrates and biomarkers without any interaction with the human P-gp (hMDR1) transporter.

## 2. Materials & methods

### 2.1. Animal preparation

All procedures and protocols using animals were conducted in compliance and approval by the Institutional Animal Care and Use Committee of the Medical University of Vienna, Austria, as well as by the Austrian Ministry of Science, Research and Economy (BMFWF-66.009/0029-WF/V/3b/2015; BMFWF-66.009/0209-WF/V/3b/2015). The manuscript adheres to the Directive European law (2010/63/EU) and to the ARRIVE guidelines for reporting animal experiments.

### 2.2. Real-time kinetic model

The Madin-Darby Canine Kidney cell line, overexpressing human P-gp, (MDCKII-hMDR1) and the MDCKII-wildtype (MDCKII-WT) cell lines were purchased from the Netherlands Cancer Institute (NKI, Amsterdam, Netherlands). MDCKII-hMDR1 and MDCKII-WT cell lines were cultivated in DMEM GlutaMAX™ (Gibco® 61965-026), 10% FCS (Gibco® 10270-106) and 0.5% Pen/Strep (Gibco® 15140).  $2.5 \times 10^5$  cells were seeded two days before experiments in the oblique plane of a cell culture dish (100/20 mm, Greiner Bio-one, cellstar 664160) to allow attachment to only one side of the dish. After 24 h, the cell culture dishes were positioned horizontally. Prior to experiments, cells were treated with serum free medium to avoid unspecific binding of the tracer to fetal calf serum. For the blocking experiments on the MDCKII-hMDR1 cells ( $\pm$ )-Verapamil hydrochloride purchased from Sigma Aldrich (St. Louis, Missouri, USA) diluted in DMSO was used. To avoid effects of Verapamil, the MDCKII-WT cells were also treated with ( $\pm$ )-Verapamil hydrochloride in DMSO. Blocking concentration was 10  $\mu$ M and concentration of organic solvent was <0.5%. For the assessment of P-gp binding or P-gp mediated transport, real-time kinetics with the PET tracers [ $^{18}$ F]FE@SNAP, [ $^{18}$ F]FE@SUPPLY, [ $^{11}$ C]SNAP-7941, [ $^{18}$ F]FMeNER-D2, [ $^{11}$ C]DASB, [ $^{11}$ C]Harmin and [ $^{11}$ C]Me@HAPTHI were performed using LigandTracer®Yellow and LigandTracer®White technology (Ridgeview Instruments AB, Uppsala, Sweden, for detailed work procedure cf. supplementary information). During one revolution of the petri dish, two positions were measured for 3 s with a delay of 2 s. One of these positions (within the cell pole) serves as signal- and the other (cell free area) as the background measurement. In pre-experiments, appropriate tracer concentrations were tested within the linearity range of the instrument's detector resulting in 0.1–625 nM concentrations (data not shown). 15 nM compound concentrations were used for the final setups and the different tracer kinetics were compared. Calculations and drafting of the kinetics were performed by using GraphPadPrism Version 6.01 © 1992–2012 GraphPad Software, Inc. (CA, USA). Single results are represented as CPS over time, whereas overall mean results are normalized to % signal of the maximum CPS. All measurements of the presented results were performed at least in duplicates on at least 3 different days ( $n \geq 3$ ).

### 2.3. Conventional internalization experiments

MDCKII-WT and MDCKII-hMDR1 cells were cultivated in 6-well plates ( $1 \times 10^5$  cells per well) two days prior to the experiments. One hour before the experiments, cells were washed with DPBS (Gibco® 14,190-094) and serum free medium was added. The cells were incubated with the tracers [ $^{11}$ C]SNAP-7941 or [ $^{18}$ F]FE@SNAP. In an additional setup, both cell lines were treated with 10  $\mu$ M ( $\pm$ )-Verapamil hydrochloride (DMSO <0.5%) for 0.5 h before the respective tracer was added. After tracer incubation for 0.5 h, the medium was removed, the cells were washed with 1 mL DPBS, scratched off and removed from the well with an additional washing step. The cell fraction and the supernatant were counted in the calibrated Gamma-Counter (Perkin Elmer, Waltham, Massachusetts, USA), calibrated for [ $^{18}$ F]fluoride and [ $^{11}$ C]carbon. Furthermore, the internalization protocol for [ $^{11}$ C]SNAP-7941 was performed with additional washing steps with glycine buffer to account for unspecific binding of the tracer at the membrane surface [11]. The data were processed with Microsoft Excel Version 14.00 © Microsoft Cooperation (WA, USA) or GraphPadPrism Version 6.01 © 1992–2012 GraphPad Software, Inc. (CA, USA).

### 2.4. $\mu$ PET imaging

*In vivo* imaging experiments were conducted with a small animal computed tomography (CT) and positron emission tomography (PET) scanner (Siemens Inveon Multimodal  $\mu$ SPECT/CT, dedicated  $\mu$ PET; Siemens Medical Solutions, Knoxville, USA). Twelve to fourteen weeks old male Sprague Dawley rats (HIM:OFA, Himberg, Austria) weighing  $420 \pm 42$  g were kept under controlled laboratory conditions ( $22 \pm 1$  °C; 12 h light/dark cycle) with food and water access *ad libitum*. Anesthetized rats (1.5–2% isoflurane vaporized in oxygen 1–1.5 L/min) were prepared for the imaging experiments and positioned in the center of the field of view. Physiological parameters and the depth of anesthesia were constantly monitored and adapted throughout the experiment. All animals received the P-gp/BCRP inhibitor tariquidar methanesulfonate, hydrate (TQD, HY-10550A, MedChemExpress Europe, Sollentuna, Sweden) (15 mg/kg body weight; 500  $\mu$ L intravenously) or 2.5% glucose solution as vehicle 60 min before the administration (i.v.) of the respective radiotracer ([ $^{11}$ C]SNAP-7941 [12]; [ $^{18}$ F]FE@SNAP,  $46.62 \pm 5.63$  MBq, molar activity:  $210.9 \pm 240.6$  GBq/ $\mu$ mol (range:  $28.2$ – $627.3$  GBq/ $\mu$ mol); [ $^{11}$ C]ME@HAPTHI,  $54.852 \pm 4.89$  MBq, mol. activity:  $43.9 \pm 33.8$  GBq/ $\mu$ mol (range:  $20$ – $87.6$  GBq/ $\mu$ mol)). Once the radioligands were administered through the lateral tail vein, the PET data acquisition took 45 to 60 min to allow tracer kinetics to attain full equilibration. For statistical relevance, experiments were performed in triplicate.

The CT data was corrected for beam-hardening. PET list mode data was sorted into three-dimensional sinograms and reconstructed using an OSEM3D/OP-MAP with scatter and attenuation correction. All relevant corrections (e.g. normalization, dead time, random) for quantitative PET data were performed. Image data analysis was carried out using the Inveon Research Workplace (IRW; Siemens Medical Solutions, Knoxville, USA). Volumes of interest (VOIs), comprising the brain of rats was outlined on the CT and transferred to the PET images. Time-activity curves (TACs) were calculated and expressed as standardized uptake values normalized to the body weight of the animal ( $SUV_{BW}$ ).

### 2.5. Radiosynthesis

[ $^{18}$ F]FE@SNAP, [ $^{18}$ F]FMeNER-D2, [ $^{18}$ F]FE@SUPPLY, [ $^{11}$ C]SNAP-7941, [ $^{11}$ C]Me@HAPTHI, [ $^{11}$ C]DASB and [ $^{11}$ C]Harmin were synthesized following previously published procedures [13–19].

## 3. Results

A general overview of the results is given in Table S1.

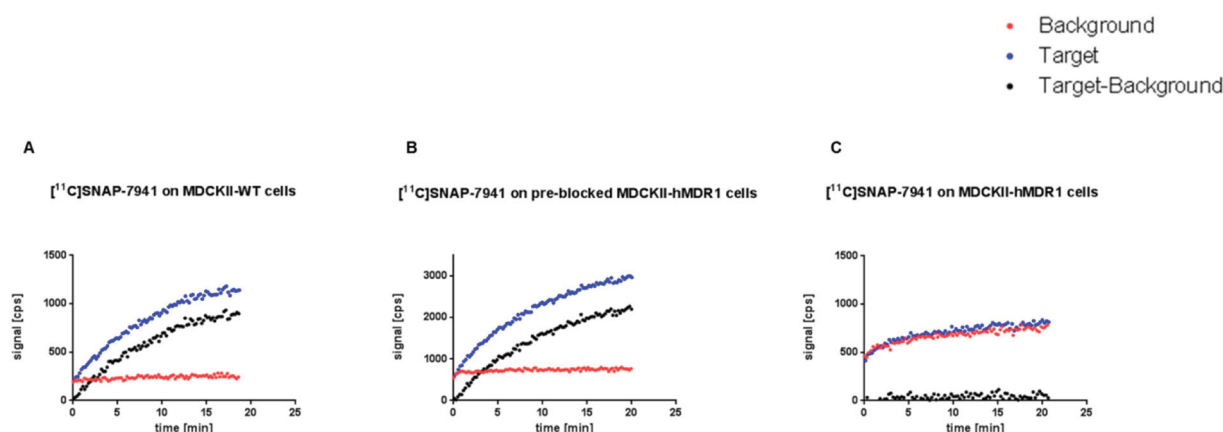


**Fig. 1.** Illustrates the kinetics of [ $^{11}\text{C}$ ]SNAP-7941 (signal in [CPS]). (A) Shows the kinetics on MDCKII-WT cells. (B) Shows the signal on the MDCKII-hMDR1 cells, where the transporter was blocked with ( $\pm$ )-Verapamil. (C) Exemplifies that the signal of the tracer on the P-gp transporter expressing cell line is due to unspecific accumulation. The red signal represents the background measurement (plastic surface of the petri dish) and the blue signal the kinetics of the tracers on the target area (cells), whereas the black signal shows the corrected signal (target minus background).

### 3.1. Real-time kinetic model

Throughout all experiments at all used concentrations (0.1 to 625 nM), qualitative and reproducible results were obtained (uptake or no uptake) for all tested PET tracers. For quantification of the kinetics, only experiments using 15 nM concentration of the respective tracer were taken into account.

### 3.2. P-gp substrates

The direct comparison of the curves shows different uptake behavior for [ $^{18}\text{F}$ ]FE@SNAP and [ $^{11}\text{C}$ ]SNAP-7941 in the three described experimental setups: A clear uptake of the respective tracers was visible in the MDCKII-WT cells. A significant uptake on the cell side was also obtained when MDCKII-hMDR1 cells were treated with ( $\pm$ )-Verapamil (pre-blocking). On the other hand, no cell uptake was measured on untreated MDCKII-hMDR1 cells.

When all results with 15 nM of tracer concentration were superimposed, both compounds exhibited a comparable kinetic on the MDCKII-WT cell line as well as on the MDCKII-hMDR1 cells, where P-gp was inhibited with ( $\pm$ )-Verapamil (Fig. 2A). In contrast, for the MDCKII-hMDR1 cells both PET tracers showed no uptake (diffuse widespread signal, cf. Fig. 2B).

### 3.3. Compounds with no interaction with the P-gp transporter

No difference was observed regarding the kinetics of [ $^{11}\text{C}$ ]Harmine, [ $^{11}\text{C}$ ]DASB, [ $^{11}\text{C}$ ]Me@HAPTHI, [ $^{18}\text{F}$ ]FE@SUPPLY and [ $^{18}\text{F}$ ]FMeNER-D2 (Figs. 3 and 4). In Fig. 3, exemplary curves are presented for [ $^{11}\text{C}$ ]Harmine. An uptake can be observed after background subtraction on both cell lines.

In direct comparison, overall overlaid and normalized results (Fig. 4) show no differences in the uptake behavior or the kinetics of [ $^{11}\text{C}$ ]Harmine, [ $^{11}\text{C}$ ]DASB, [ $^{18}\text{F}$ ]FE@SUPPLY and [ $^{18}\text{F}$ ]FMeNER-D2 (Fig. 4A).

The kinetics of [ $^{11}\text{C}$ ]Me@HAPTHI showed a slower uptake behavior in contrast to the results of [ $^{11}\text{C}$ ]Harmine, [ $^{11}\text{C}$ ]DASB, [ $^{18}\text{F}$ ]FE@SUPPLY and [ $^{18}\text{F}$ ]FMeNER-D2, but a clear uptake on both cell lines.

### 3.4. Conventional internalization experiments

The cell internalization assay with [ $^{11}\text{C}$ ]SNAP-7941 and [ $^{18}\text{F}$ ]FE@SNAP showed an increased uptake in the MDCKII-WT cells in contrast to MDCKII-hMDR1 cells. Same results were observed when P-gp was blocked in MDCKII-hMDR1 cells (Fig. 5). Internalization ratios were calculated for MDCKII-WT/MDCKII-hMDR1 and pre-blocked MDCKII-

hMDR1/MDCKII-hMDR1. No significant differences were found using a multiple comparison test and Sidak correction (Fig. 5B). Unspecific binding measured with two additional washing steps was <5% for each setup and cell line.

### 3.4.1. PET-Imaging

**3.4.1.1. [ $^{18}\text{F}$ ]FE@SNAP in rats.** VOIs comprising the brain were outlined on the images resulting in  $0.31 \pm 0.07$  SUV<sub>BW</sub> for the vehicle group (A) and  $0.75 \pm 0.17$  SUV<sub>BW</sub> for the TQD treated group (B) (cf. Fig. 6A and B).

**3.4.1.2. [ $^{11}\text{C}$ ]SNAP-7941 in rats.** As previously reported, mean brain TACs of [ $^{11}\text{C}$ ]SNAP-7941 in rats were  $0.22 \pm 0.0$  SUV<sub>BW</sub> 55 min after tracer injection. In rats, pre-treated with TQD the SUV increased to  $1.04 \pm 0.1$  SUV<sub>BW</sub> at 55 min after tracer injection (4.72 fold increase) [12].

**3.4.1.3. [ $^{11}\text{C}$ ]Me@HAPTHI in rats.** VOIs comprising the brain were outlined in the images resulting in  $0.19 \pm 0.04$  SUV<sub>BW</sub> for the vehicle group (Fig. 6C) and  $0.56 \pm 0.21$  SUV<sub>BW</sub> for the TQD treated group (cf. Fig. 6D).

**3.4.1.4. [ $^{18}\text{F}$ ]FE@SUPPLY.** In a previously published study it was shown that efflux inhibition with TQD did not change the brain uptake of [ $^{18}\text{F}$ ]FE@SUPPLY. Peak brain activity was similar in the baseline scans ( $1.56 \pm 0.01$  SUV) and the group which was pre-treated with TQD ( $1.53 \pm 0.01$  SUV) [20].

## 4. Discussion

### 4.1. General

It is undisputed that P-gp and associated efflux transporters of the ABC family play an important role for the pharmacokinetics and therapeutic efficiency of drugs. Drug-drug interactions resulting from inhibition or induction of P-gp are a recognized clinical concern and highlighted in the “Food and Drug Administration Concept” of the FDA [21–25]. Consequently, the development of selective efflux transporter inhibitors should be emphasized as an additional medication for tumor therapeutics to avoid multiple drug resistance [9,26]. Hence, it is pivotal to assess any interaction of newly developed drugs with these transporters in the preclinical or even *pre vivo* phase. So far, there are several methods for this purpose, however, none of them directly addressing the pure interaction of the PET tracer with the P-gp. Molecular imaging of the efflux transporters at the BBB, based on PET, has become increasingly interesting in recent years. However, the binding characteristics of the respective tracers to these transporters are

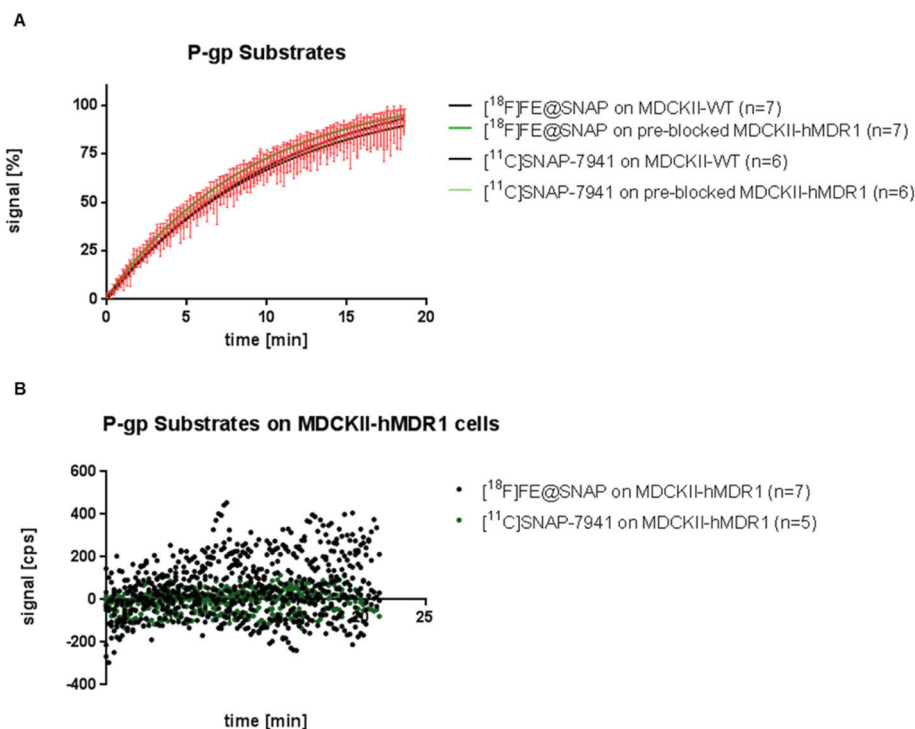


**Fig. 2.** Shows the uptake of  $[^{18}\text{F}]\text{FE@SNAP}$  ( $n = 7$ ) and  $[^{11}\text{C}]\text{SNAP-7941}$  ( $n = 6$ ) on the MDCKII-wildtype and MDCKII-hMDR1 cells pre-blocked with ( $\pm$ )-Verapamil (means of the experiments, normalized to 100% uptake, standard deviations are illustrated with bars (A)) and the non-treated hMDR1 cell line (B). (For interpretation of the references to color in this figure legend, the reader is referred to the web version of this article.)

different and not yet fully understood. These differences can be concentration dependent processes as described for Verapamil: in a nanomolar range, Verapamil is supposed to be a substrate, whereas at micromolar ranges, it becomes an inhibitor [27]. For other tracers, shared (dual) interactions with the transporter variants are known: e.g. Tariquidar binds to P-gp and is transported by BCRP [28,29]. The authors conclude that currently available labeled inhibitors may not be suitable for imaging the efflux transporter density. Therefore, there is a need for optimized PET imaging protocols and for PET tracers with high affinity ( $K_i < 5 \text{ nM}$ ) [30,31]. The present study aimed at the establishment of a general experimental real-time model for the direct quantification of the interactions of PET tracers with the human P-gp transporter in nanomolar concentration.

#### 4.2. Real-time kinetic model

The developed real-time kinetic assay is highly robust, rapid and needs less preparation and experimental time in comparison to the cell internalization assay. Theoretically, the identification of a P-gp substrate can be assessed in a single experiment on P-gp expressing cells, showing high background to target ratio of the labelled molecules. This experiment can be performed on pre-blocked cells (with the disadvantage of a required second setup) or in real-time, where the inhibitor is added after equilibrium of the tracer. In that case, the signal on the cell side increases immediately, if the tracer is a P-gp substrate. For comparison, three setups were chosen: experiments with the MDCKII-WT (I), the MDCKII-hMDR1 cells (II) and latter ones with pre-blocking of the

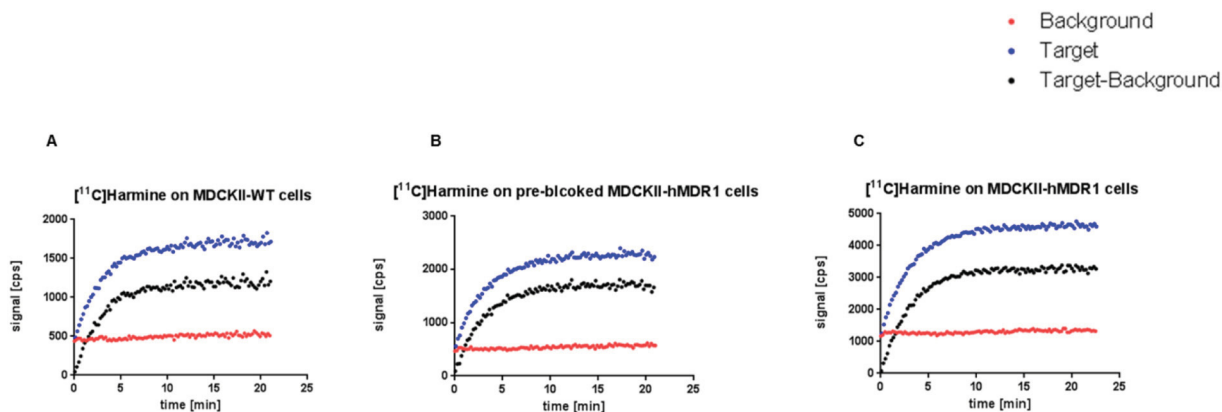


**Fig. 3.** Exemplifies the kinetics of the PET tracer  $[^{11}\text{C}]\text{Harmine}$ , which is known to have no interactions with the P-gp transporter. The red signal represents the background measurement (plastic surface of the petri dish) and the blue signal the kinetics of the tracers on the target area (cells), whereas the black signal shows the corrected signal (target minus background). There are no differences displayed in the kinetics at all examined setups (A–C).



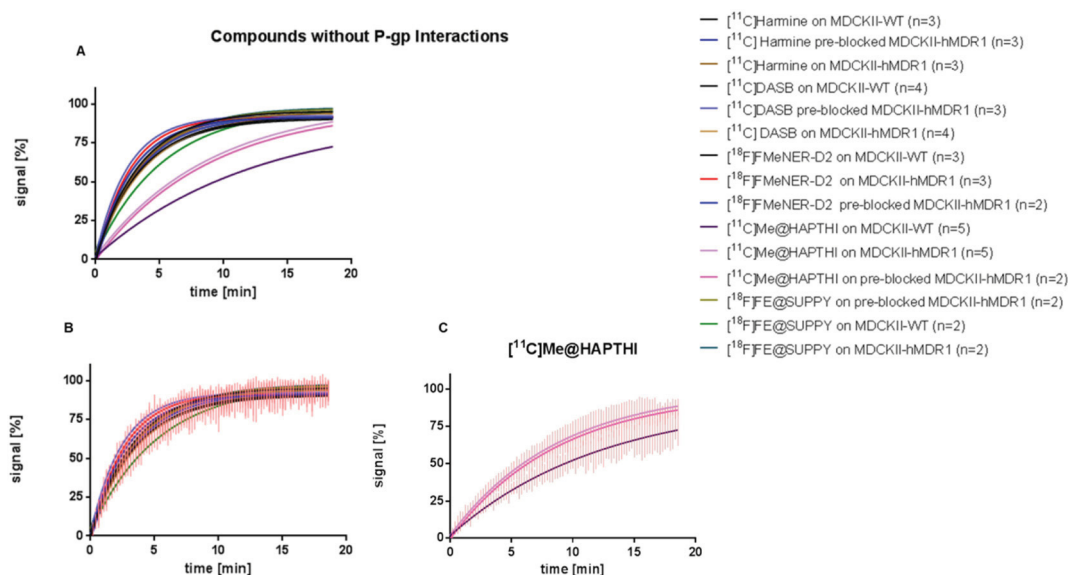


**Fig. 4.** Shows the signal means (colored lines) of all performed experiments with the PET tracers  $[^{11}\text{C}]$ Harimine,  $[^{11}\text{C}]$ DASB,  $[^{18}\text{F}]$ FE@SUPPLY,  $[^{18}\text{F}]$ MeNER-D2 and  $[^{11}\text{C}]$ Me@HAPTHI in all setups (4A). Panels B and C illustrate the curves with standard deviations (red bars), splitted by the different kinetic properties of the respective PET tracer (B:  $[^{11}\text{C}]$ Harimine,  $[^{11}\text{C}]$ DASB,  $[^{18}\text{F}]$ FE@SUPPLY and  $[^{18}\text{F}]$ MeNER-D2 and C:  $[^{11}\text{C}]$ Me@HAPTHI). (For interpretation of the references to color in this figure legend, the reader is referred to the web version of this article.)

P-gp transporter using ( $\pm$ )-Verapamil. In prior experiments and by treatment of the WT, we excluded vehicle effects as well as effects of Verapamil itself on the MDCKII cells. Additionally, vehicle effects were tested for the transfected cell line.

Currently available methods are not efficient, as they are time consuming and require the use of long-lived radionuclides. Other assays, derived from toxicology studies (e.g. calcein-AM assay, rhodamine 123 assay or digoxin assays), indirectly measure the dependence of the toxic effect on the P-gp blockade [32–36].

The established new application for the LigandTracer® Technology directly uses the PET tracer in very small activities. Main advantage of this method is the insight into the kinetic behavior of the uptake process in real-time enabling a direct interpretation of the underlying mechanism such as the affinity towards the P-gp transporter [26] and the distinction between substrates and compounds without any protein interaction. Therefore, it may be used for quantification of the equilibrium inhibitory constant ( $K_i$ ) of newly developed P-gp inhibitors. Furthermore, this method is not limited to the use of high energy gamma detection as for PET and SPECT nuclides, but also applicable for beta emitters.

#### 4.3. P-gp transporter substrates

The two SNAP derivatives  $[^{18}\text{F}]$ FE@SNAP and  $[^{11}\text{C}]$ SNAP-7941 were confirmed to be highly potent P-gp-substrates. The kinetic changes were obvious: no signal could be observed on the P-gp expressing cell line, whereas WT cells and cell lines pre-blocked with ( $\pm$ )-Verapamil exhibited a significantly increased signal with a similar curve shape (cf. Figs. 1 and 2). Further experiments were conducted with the MDCKII-hMDR1 cells treated with non-labeled Verapamil after incubation with the P-gp substrates during the real-time assay. The signal on the cell side increased instantly indicating that P-gp inhibition was also successful while performing the real-time assay.

#### 4.4. Compounds with no interaction with the P-gp transporter

The PET tracers  $[^{11}\text{C}]$ Harimine,  $[^{11}\text{C}]$ DASB and  $[^{18}\text{F}]$ MeNER-D2, which are described to have no interaction with the human P-gp transporter (established brain tracer) showed the same kinetic behavior in all tested setups and all used concentrations (prior-experiments, data

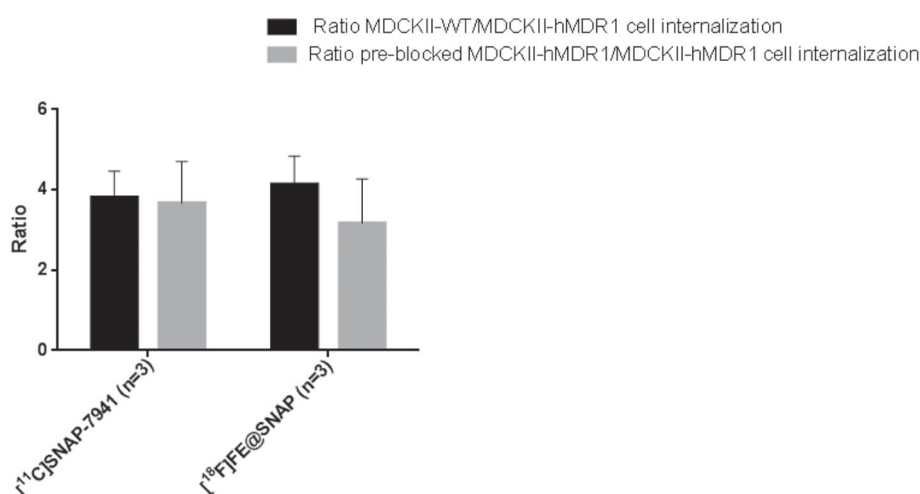


**Fig. 5.** Shows the ratio of tracer internalization of wildtype versus MDR1 cells and blocked MDR1 versus untreated MDR1 cells of  $[^{11}\text{C}]$ SNAP-7941 and  $[^{18}\text{F}]$ FE@SNAP. Standard deviations are illustrated as black bars. There was no significant difference between the ratios (multiple comparison test, Sidak correction).

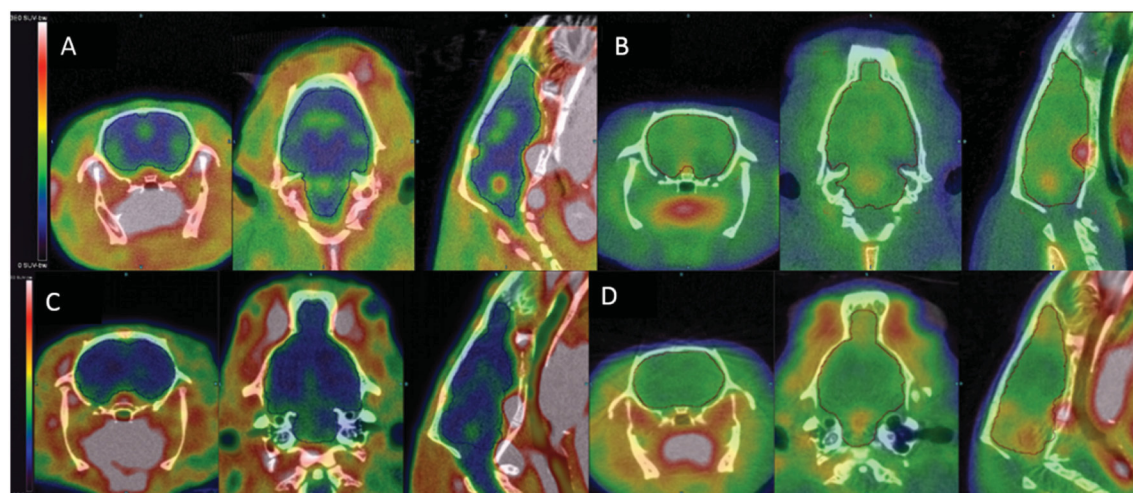


**Fig. 6.** Shows representative  $\mu$ PET/CT images of a rat brain in axial, coronal and sagittal planes of [ $^{18}\text{F}$ ]FE@SNAP (A, B) and [ $^{11}\text{C}$ ]Me@HAPTHI (C, D). The animals received the P-gp/BCRP inhibitor TQD (15 mg/kg body weight; intravenously) (B, D) or the respective vehicle (A, C) 60 min before  $\mu$ PET acquisition.

not shown). Hence, they were classified as non-P-gp-substrates. [ $^{18}\text{F}$ ]FE@SUPPY shows comparable uptake behavior in the real-time assay. In previously published PET data, [ $^{18}\text{F}$ ]FE@SUPPY shows no increasing brain uptake after inhibition with Tariquidar, which is in accordance to the findings of the *in vitro* assay. However, AUC levels were increased after inhibition [20]. In baseline scans with [ $^{11}\text{C}$ ]Me@HAPTHI, we observed a slight brain uptake. At that stage, we hypothesized that the PET tracer could be a P-gp-substrate. This assumption was not proven by *in vitro* experiments (real-time model), since [ $^{11}\text{C}$ ]Me@HAPTHI shows uptake in both cell lines independent of blocking. However, the time to equilibrium was slower for [ $^{11}\text{C}$ ]Me@HAPTHI than of the other non-interacting PET tracers (cf. Fig. 4A and C). We hypothesize that this observed change is due to differences in permeability efficiency, especially bearing in mind, that MDCKII cell lines are a widely used model for the assessment of permeability features of compounds [37,38] and that [ $^{11}\text{C}$ ]Me@HAPTHI may interact with other efflux transporter like BCRP (breast cancer resistance protein), which are also natively expressed in the MDCKII cell lines. The latter becomes conclusive by overlapping the kinetics of SNAP PET tracer and [ $^{11}\text{C}$ ]Me@HAPTHI (Fig. 7C and D) and interpreting the imaging data.

#### 4.5. Conventional internalization experiments

The interactions of [ $^{11}\text{C}$ ]SNAP-7941 and [ $^{18}\text{F}$ ]FE@SNAP with the P-gp transporter were also evaluated using a conventional cell internalization assay. Comparing the real-time assay with the conventional internalization assay, the established real-time model is easy, needs fewer activities and achieves the same results in less time with lower standard deviation. Calculation of the uptake ratio between (1) WT versus non-

treated hMDR1 cell lines and (2) pre-blocked hMDR1 versus untreated hMDR1 cell line of the PET tracers [ $^{18}\text{F}$ ]FE@SNAP and [ $^{11}\text{C}$ ]SNAP-7941 show that the uptake in the WT and the pre-blocked MDCKII-hMDR1 cell line increased by the same factor. Therefore, the results were in the same ratio and did not differ significantly. Hence, the two SNAP derivatives can also be classified as P-gp substrates in this internalization assay.

#### 4.6. PET Imaging

Animal experiments were conducted under baseline (vehicle) and TQD blocking conditions (15 mg/kg bodyweight) in rats. Currently, TQD is the gold standard for *in vivo* inhibition of P-gp in preclinical and clinical settings, but also known as an inhibitor for BCRP (dual inhibitor) [39]. Therefore, *in vivo* PET studies using this inhibitor cannot distinguish between interactions of the PET tracer with BCRP and P-gp. However, conducting animal experiments with ( $\pm$ )-Verapamil is impossible since it is a highly potent calcium channel blocker with a variety of severe cardiovascular and central side-effects. Based on our  $\mu$ PET results with [ $^{18}\text{F}$ ]FE@SNAP and [ $^{11}\text{C}$ ]SNAP-7941, a clear assignment of the efflux effect to human BCRP, P-gp or both, respectively, is not possible. Yet, our *in vitro* assay shows that there is a strong interaction with the human P-gp. In contrast, the imaging results of [ $^{11}\text{C}$ ]Me@HAPTHI show a significant brain uptake after inhibition with TQD, whereas no effect can be seen *in vitro*. This leads to the hypothesis that this PET tracer might be a substrate of BCRP (*in vivo*). An alternative explanation might be species differences as it is described for some other radiotracers showing an efflux in rat brains, but not in human or monkey imaging studies [5].

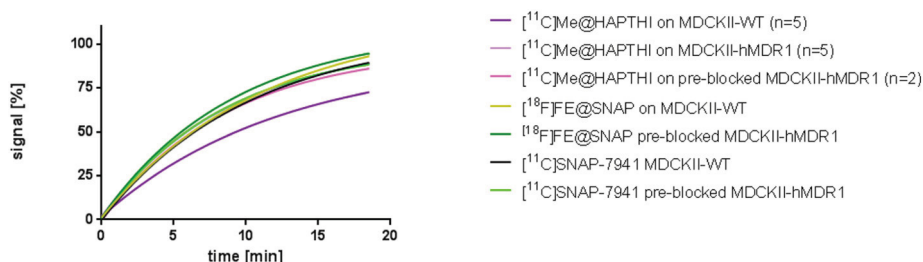


**Fig. 7.** Shows the signal means (colored lines, see legend) of all performed experiments with the PET tracers [ $^{11}\text{C}$ ]SNAP-7941, [ $^{18}\text{F}$ ]FE@SNAP and [ $^{11}\text{C}$ ]Me@HAPTHI using all setups. (For interpretation of the references to color in this figure legend, the reader is referred to the web version of this article.)

#### 4.7. Conclusion and outlook

A rapid *in vitro* real-time kinetic model was developed for a qualitative measurement of P-gp interactions for early stage PET tracer development after candidate selection. These data correlate with *in vivo* PET quantifications. Hence, PET tracers can be clearly categorized into P-gp substrates or substances without P-gp interaction (neither inhibitory effect nor efflux) based on their kinetic behavior.

Subsequent evaluations shall demonstrate the ability of this method to distinguish between strong and weak substrates as well as to measure binding kinetics of newly developed or known inhibitors. Furthermore, this method will be used with different cell lines (e.g. expressing human BCRP) to depict interactions with various efflux transporters.

#### Acknowledgements

We gratefully acknowledge the support of Markus Zeilinger, MSc for his proper expertise in LigandTracer Technologies, Prof Dr. Oliver Langer for fruitful discussions, Dr. Verena Pichler, and Neydher Berroteran, MSc for synthesis of the diverse PET tracers and their support. This work was supported by the Austrian Science Fund (FWF P26502-B24, M. Mitterhauser).

#### Authors contribution

CV, TB, E-MK, TR, CP, FP, MD performed the experiments. MM, CV, WW, MH and K-HW planned the experiments. CV, MM, MD and CP composed the draft. WW, MH, K-HW, and FP reviewed the manuscript. CV, TB, E-MK, TR, FP, MD and MM performed the calculations and analyses.

#### Disclosure/conflict of interest

We have nothing to disclose.

#### Appendix A. Supplementary data

Supplementary data to this article can be found online at <https://doi.org/10.1016/j.nucmedbio.2018.02.002>.

#### References

- [1] World Health Organization. World Health Report. Geneva: 2001.
- [2] Alavijeh MS, Chishty M, Qaiser MZ, Palmer AM. Drug metabolism and pharmacokinetics, the blood-brain barrier, and central nervous system drug discovery. *NeuroRx* 2005;2:554–71. <https://doi.org/10.1602/neurorx.2.4.554>.
- [3] Pardridge WM. Drug transport across the blood–brain barrier. *J Cereb Blood Flow Metab* 2012;32:1959–72. <https://doi.org/10.1038/jcbfm.2012.126>.
- [4] Abbott NJ, Patabendige AAK, Dolman DEM, Yusof SR, Begley DJ. Structure and function of the blood–brain barrier. *Neurobiol Dis* 2010;37:13–25. <https://doi.org/10.1016/j.nbd.2009.07.030>.
- [5] Pike VW. PET radiotracers: crossing the blood–brain barrier and surviving metabolism. *Trends Pharmacol Sci* 2009;30:431–40. <https://doi.org/10.1016/j.tips.2009.05.005>.
- [6] Sharom FJ. ABC multidrug transporters: structure, function and role in chemoresistance. *Pharmacogenomics* 2008;9:105–27. <https://doi.org/10.2217/14622416.9.1.105>.
- [7] Endres CJ, Hsiao P, Chung FS, Unadkat JD. The role of transporters in drug interactions. *Eur J Pharm Sci* 2006;27:501–17. <https://doi.org/10.1016/j.ejps.2005.11.002>.
- [8] Agnani D, Acharya P, Martinez E, Tran TT, Abraham F, Tobin F, et al. Fitting the elementary rate constants of the P-gp transporter network in the hMDR1-MDCK confluent cell monolayer using a particle swarm algorithm. *PLoS One* 2011;6:e25086. <https://doi.org/10.1371/journal.pone.0025086>.
- [9] Chen Z, Shi T, Zhang L, Zhu P, Deng M, Huang C, et al. Mammalian drug efflux transporters of the ATP binding cassette (ABC) family in multidrug resistance: a review of the past decade. *Cancer Lett* 2016;370:153–64. <https://doi.org/10.1016/j.canlet.2015.10.010>.
- [10] Wanek T, Mairinger S, Langer O. Radioligands targeting P-glycoprotein and other drug efflux proteins at the blood–brain barrier. *J Label Compd Radiopharm* 2013;56:68–77. <https://doi.org/10.1002/jlcr.2993>.
- [11] Fischer C, Vomstein S, Mindt T. A bombesin-shepherdin radioconjugate designed for combined extra- and intracellular targeting. *Pharmaceuticals* 2014;7:662–75. <https://doi.org/10.3390/ph7060662>.
- [12] Philippe C, Nics L, Zeilinger M, Kuntner C, Wanek T, Mairinger S, et al. Preclinical *in vitro* & *in vivo* evaluation of [(11C)SNAP-7941 – the first PET tracer for the melanin concentrating hormone receptor 1. *Nucl Med Biol* 2013;40:919–25. <https://doi.org/10.1016/j.nucmedbio.2013.05.010>.
- [13] Rami-Mark C, Zhang M-R, Mitterhauser M, Lanzenberger R, Hacker M, Wadsak W. [18F]FMeNER-D2: reliable fully-automated synthesis for visualization of the norepinephrine transporter. *Nucl Med Biol* 2013;40:1049–54. <https://doi.org/10.1016/j.nucmedbio.2013.08.007>.
- [14] Philippe C, Zeilinger M, Mitterhauser M, Dumanic M, Lanzenberger R, Hacker M, et al. Parameter evaluation and fully-automated radiosynthesis of [11C]harmine for imaging of MAO-A for clinical trials. *Appl Radiat Isot* 2015;97:182–7. <https://doi.org/10.1016/j.apradiso.2015.01.002>.
- [15] Philippe C, Nics L, Zeilinger M, Schirmer E, Spreitzer H, Karanikas G, et al. Preparation and first preclinical evaluation of [18F]FE@SNAP: a potential PET tracer for the melanin-concentrating hormone receptor-1 (MCHR1). *Sci Pharm* 2013;81:625–39. <https://doi.org/10.3797/scipharm.1306-02>.
- [16] Philippe C, Schirmer E, Mitterhauser M, Shanab K, Lanzenberger R, Karanikas G, et al. Radiosynthesis of [11C]SNAP-7941—the first PET-tracer for the melanin concentrating hormone receptor 1 (MCHR1). *Appl Radiat Isot* 2012;70:2287–94. <https://doi.org/10.1016/j.apradiso.2012.07.010>.
- [17] Haeusler D, Mien L-K, Nics L, Ungersboeck J, Philippe C, Lanzenberger RR, et al. Simple and rapid preparation of [11C]DASB with high quality and reliability for routine applications. *Appl Radiat Isot* 2009;67:1654–60. <https://doi.org/10.1016/j.apradiso.2009.03.005>.
- [18] Rami-Mark C, Berroterán-Infante N, Philippe C, Foltin S, Vraha C, Hoepfing A, et al. Radiosynthesis and first preclinical evaluation of the novel norepinephrine transporter pet-ligand [11C]ME@HAPTH. *EJNMMI Res* 2015;5. <https://doi.org/10.1186/s13550-015-0113-3>.
- [19] Wadsak W, Mien L-K, Shanab K, Ettlinger DE, Haeusler D, Sindelar K, et al. Preparation and first evaluation of [18F]FE@SUPPLY: a new PET tracer for the adenosine A3 receptor. *Nucl Med Biol* 2008;35:61–6. <https://doi.org/10.1016/j.nucmedbio.2007.09.004>.
- [20] Haeusler D, Kuntner C, Nics L, Savli M, Zeilinger M, Wanek T, et al. [18F]FE@SUPPLY: a suitable PET tracer for the adenosine A3 receptor? An *in vivo* study in rodents. *Eur J Nucl Med Mol Imaging* 2015;42:741–9. <https://doi.org/10.1007/s00259-014-2976-3>.
- [21] Prueksaritanont T, Chu X, Gibson C, Cui D, Yee KL, Ballard J, et al. Drug–drug interaction studies: regulatory guidance and An industry perspective. *AAPS J* 2013;15: 629–45. <https://doi.org/10.1208/s12248-013-9470-x>.
- [22] Zhang L, Strong JM, Qiu W, Lesko LJ, Huang S-M. Scientific perspectives on drug transporters and their role in drug interactions<sup>1</sup>. *Mol Pharm* 2006;3:62–9. <https://doi.org/10.1021/mp050095h>.
- [23] Brinkmann U, Roots I, Eichelbaum M. Pharmacogenetics of the human drug-transporter gene MDR1: impact of polymorphisms on pharmacotherapy. *Drug Discov Today* 2001;6:835–9.
- [24] Englund G, Hallberg P, Artursson P, Michaëlsson K, Melhus H. Association between the number of coadministered P-glycoprotein inhibitors and serum digoxin levels in patients on therapeutic drug monitoring. *BMC Med* 2004;2. <https://doi.org/10.1186/1741-7015-2-8>.
- [25] Balayssac D, Authier N, Cayre A, Coudore F. Does inhibition of P-glycoprotein lead to drug–drug interactions? *Toxicol Lett* 2005;156:319–29. <https://doi.org/10.1016/j.toxlet.2004.12.008>.
- [26] Zeilinger M, Pichler F, Nics L, Wadsak W, Spreitzer H, Hacker M, et al. New approaches for the reliable *in vitro* assessment of binding affinity based on high-resolution real-time data acquisition of radioligand-receptor binding kinetics. *EJNMMI Res* 2017;7. <https://doi.org/10.1186/s13550-016-0249-9>.
- [27] Römermann K, Wanek T, Bankstahl M, Bankstahl JP, Fedrowitz M, Müller M, et al. [(R)-11C]verapamil is selectively transported by murine and human P-glycoprotein at the blood–brain barrier, and not by MRP1 and BCRP. *Nucl Med Biol* 2013;40:873–8. <https://doi.org/10.1016/j.nucmedbio.2013.05.012>.
- [28] Kannan P, Telu S, Shukla S, Ambudkar SV, Pike VW, Halldin C, et al. The “specific” P-glycoprotein inhibitor tariquidar is also a substrate and an inhibitor for breast cancer resistance protein (BCRP/ABCG2). *ACS Chem Neurosci* 2011;2:82–9. <https://doi.org/10.1021/cn100078a>.
- [29] Weidner LD, Fung KL, Kannan P, Moen JK, Kumar JS, Mulder J, et al. Tariquidar is an inhibitor and not a substrate of human and mouse P-glycoprotein. *Drug Metab Dispos* 2016;44:275–82. <https://doi.org/10.1124/dmd.115.067785>.
- [30] Kannan P, John C, Zoghbi SS, Halldin C, Gottesman MM, Innis RB, et al. Imaging the function of P-glycoprotein with radiotracers: pharmacokinetics and *in vivo* applications. *Clin Pharmacol Ther* 2009;86:368–77. <https://doi.org/10.1038/clpt.2009.138>.
- [31] Kannan P, Pike VW, Halldin C, Langer O, Gottesman MM, Innis RB, et al. Factors that limit positron emission tomography imaging of p-glycoprotein density at the blood–brain barrier. *Mol Pharm* 2013;10:2222–9. <https://doi.org/10.1021/mp400011g>.
- [32] Keogh JP, Kunta JR. Development, validation and utility of an *in vitro* technique for assessment of potential clinical drug–drug interactions involving P-glycoprotein. *Eur J Pharm Sci* 2006;27:543–54. <https://doi.org/10.1016/j.ejps.2005.11.011>.
- [33] Rautio J, Humphreys JE, Webster LO, Balakrishnan A, Keogh JP, Kunta JR, et al. *In vitro* p-glycoprotein inhibition assays for assessment of clinical drug interaction potential of new drug candidates: a recommendation for probe substrates. *Drug Metab Dispos* 2006;34:786–92. <https://doi.org/10.1124/dmd.105.008615>.

- [34] Doan KMM, Humphreys JE, Webster LO, Wring SA, Shampine LJ, Serabjit-Singh CJ, et al. Passive permeability and P-glycoprotein-mediated efflux differentiate central nervous system (CNS) and non-CNS marketed drugs. *J Pharmacol Exp Ther* 2002; 303:1029–37. <https://doi.org/10.1124/jpet.102.039255>.
- [35] Polli JW, Wring SA, Humphreys JE, Huang L, Morgan JB, Webster LO, et al. Rational use of in vitro P-glycoprotein assays in drug discovery. *J Pharmacol Exp Ther* 2001;299:620–8.
- [36] Dörner B, Kuntner C, Bankstahl JP, Wanek T, Bankstahl M, Stanek J, et al. Radiosynthesis and in vivo evaluation of 1-[18F]fluoroelacridar as a positron emission tomography tracer for P-glycoprotein and breast cancer resistance protein. *Bioorg Med Chem* 2011;19:2190–8. <https://doi.org/10.1016/j.bmc.2011.02.039>.
- [37] Di L, Whitney P, Pickett C, Umland JP, Zhang H, Zhang X, Gebhard DF, et al. Development of a new permeability assay using low-efflux MDCKII cells. *J Pharm Sci* 2011; 100:4974–85. <https://doi.org/10.1002/jps.22674>.
- [38] Irvine JD, Takahashi L, Lockhart K, Cheong J, Tolan JW, Selick HE, et al. MDCK (Madin-Darby canine kidney) cells: a tool for membrane permeability screening. *J Pharm Sci* 1999;88:28–33. <https://doi.org/10.1021/js9803205>.
- [39] Bauer M, Karch R, Zeitlinger M, Stanek J, Philippe C, Wadsak W, et al. Interaction of 11C-tarividar and 11C-elacridar with P-glycoprotein and breast cancer resistance protein at the human blood-brain barrier. *J Nucl Med* 2013;54. <https://doi.org/10.2967/jnumed.112.118232>.



## Supplementary information

**Figure S1** Culture plate preparation for LigandTracer® experiments

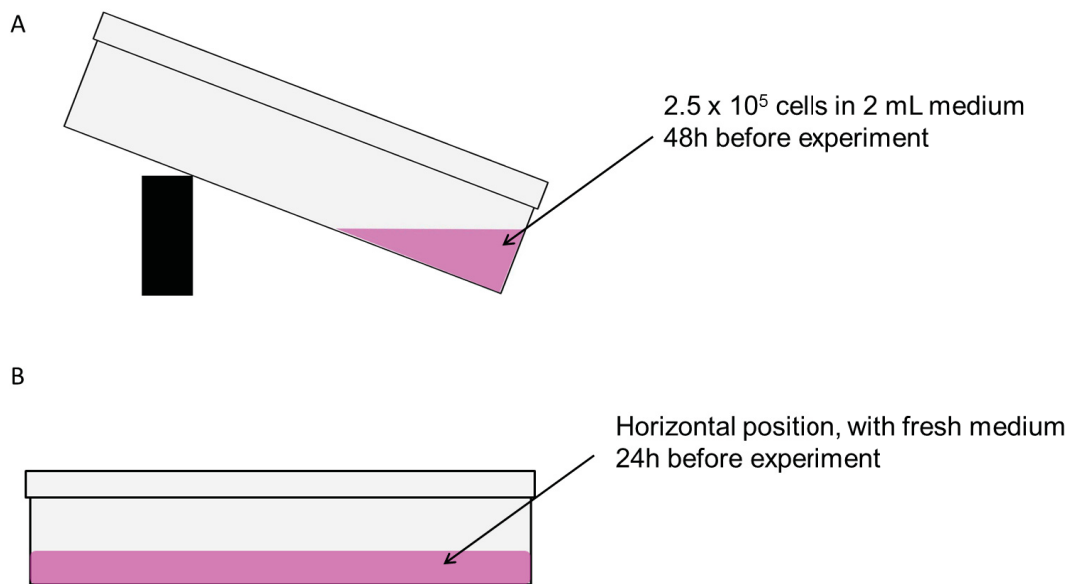


Figure S1 A illustrates the cultivation of the cells in an oblique plane of the culture dish. Therefore, the lid of a cell culture dish can be used in the incubator to stabilize the dish in the oblique position (approximately 30°). Depending on the cell type and their rate of growth  $2.5 \times 10^5$  up to  $1 \times 10^6$  are seeded. After 24 hours of incubation (B), the dish is placed horizontally and fresh cell culture medium is added to completely cover the cell surface. On the next day, cell viability and confluence are examined. According to the experimental protocol, the cells are washed with DPBS, the medium is replaced by serum-free medium (2 mL), and the culture dish is repositioned to an oblique position till the start of experiments. Henceforth, the cells can be treated with the inhibitor or vehicle.

**Figure S2** Principle of LigandTracer® Technology

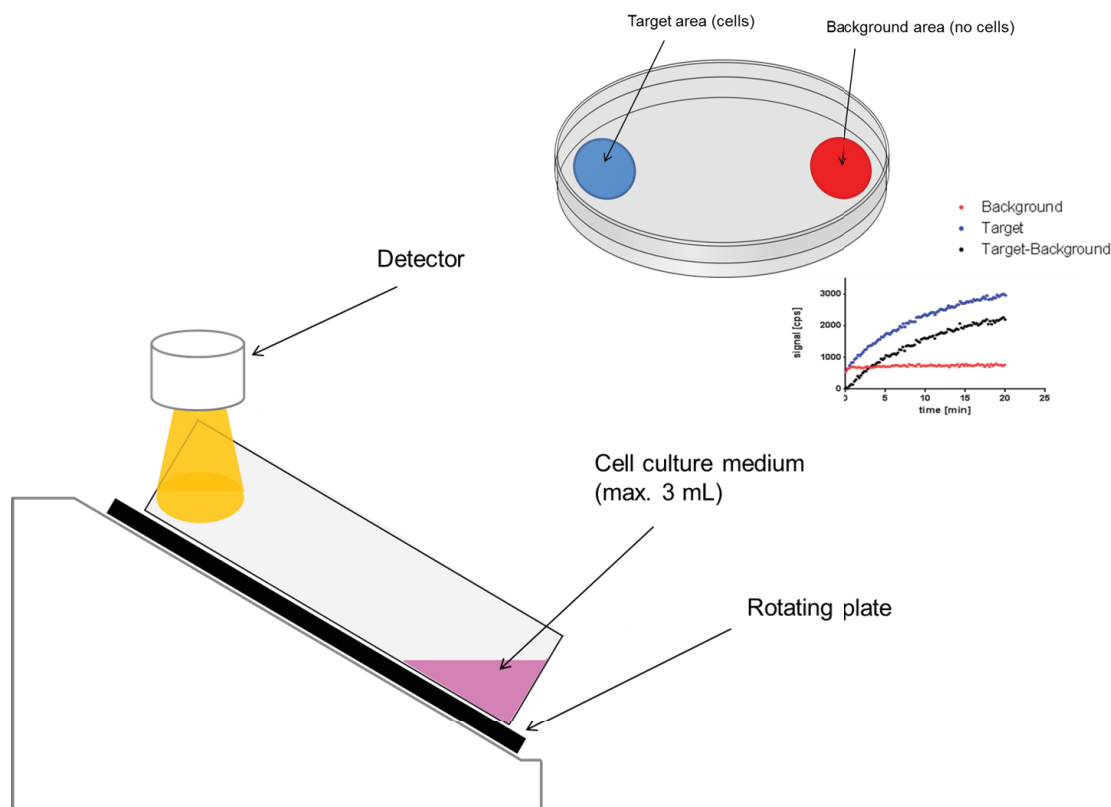


Figure S2 shows a scheme of an open LigandTracer® device (detector is located in the cap). The detector (different types of the diverse LigandTracer® models for low and high energy gamma, fluorescence and beta emitters: green, yellow, grey and white) is counting on the upper side of the cell culture dish while the medium is at the bottom of the rotating dish. The measurements are performed on an open cell culture dish and a maximum of 3 mL medium. The LigandTracer® Control software is user friendly and allows freedom of the measurement time, delay and number of measured points (up to three). The blue area is illustrating the cell pole while the red area on the opposite side is the reference region without cells to count for nonspecific binding and the thin coating of the medium on the surface of the culture dish. Therefore, the red signal represents the background measurement and the blue signal the measured signal on the cells. Additionally, the corrected signal (target minus background) is given as black kinetic.

Table S1 Summary of the used methods and results

Tracer	Real-Time Assay			Well-Plate		In vivo Imaging	
	MDCK II-hMDR1 (pure or treatment with vehicle 30 min before exp.)	MDCK II-hMDR1, 30 min before experiment blocking with 10 μM VERA	MDCK II-WT, 30 min before experiment treatment with 10 μM VERA or vehicle	Uptake Ratio MDCKII WT/MDCK II-hMDR1 cells	Uptake Ratio 10μM VERA MDCKII-hMDR1 /MDCK II-hMDR1 cells	Baseline Scan: Vehicle administration 60 min before tracer application	Scan 2: TQD (15mg/kg bw) 60min before tracer administration
<sup>18</sup> F]FE@SNAP	No cell accumulation	Cell accumulation	Cell accumulation	4.1 ± 0.7	3.2 ± 1	0.31 ± 0.07 SUV <sub>BW</sub>	0.7 5 ± 0.17 SUV <sub>BW</sub>
		Same kinetic		Not significant			
<sup>11</sup> C]SNAP-7941	No cell accumulation	Cell accumulation	Cell accumulation	3.8 ±0.6	3.7 ± 1	0.22 ± 0.0 SUV <sub>BW</sub> [12]	1.04 ± 0.1 SUV <sub>BW</sub> [12]
		Same kinetic		Not significant			
<sup>11</sup> C]Me@HAPTHI	Cell accumulation	Cell accumulation	Cell accumulation			0.19 ± 0.04 SUV <sub>BW</sub>	0.56 ± 0.21 SUV <sub>BW</sub>
	Same kinetic		slower kinetic				
<sup>18</sup> F]FE@SUPPY	Cell accumulation (kinetic)	Cell accumulation (kinetic)	Cell accumulation			1.56 ± 0.01 SUV [20]	1.53 ± 0.01 SUV [20]
	Same kinetic		slightly slower kinetic				
<sup>11</sup> C]DASB, <sup>11</sup> C]Harmine, <sup>18</sup> F]FMeNER	Cell accumulation	Cell accumulation	Cell accumulation	No interactions with P-gp known according to literature			
	Same kinetic						

Table S1 shows the overview of all performed measurements.



## 3.3 Manuscript #3

**Title:** [ $^{18}\text{F}$ ]FEPPA: Improved Automated Radiosynthesis, Binding Affinity, and Preliminary *in Vitro* Evaluation in Colorectal Cancer

**Authors:** Neydher Berroterán-Infante, **Theresa Balber**, Petra Furlinger, Michael Bergmann, Rupert Lanzenberger, Marcus Hacker, Markus Mitterhauser and Wolfgang Wadsak

**Associated Content:** Supporting Information DOI: 10.1021/acsmedchemlett.7b00367

**Rationale and Aim:** Colorectal cancer (CRC) is a major cause of mortality worldwide as it is often diagnosed at a late stage. Early detection of neoplasms drastically improves prognosis; however, endoscopic examinations of the colon and rectum are invasive and inconvenient. (178) Thus, the scientific community agrees that there is a need for new and specific biomarkers, non-invasive diagnostic techniques and early screening programs for CRC. (179-181)

The 18 kDa translocator protein (TSPO) is a well-recognized target involved in microglia activation and serves as an early biomarker for brain injury and inflammation. (126) Besides, increased TSPO binding sites have been demonstrated in colonic adenocarcinoma by means of [ $^3\text{H}$ ]PK11195 binding. (182, 183) There is evidence that TSPO displays a potential therapeutic target in colorectal cancer and that TSPO overexpression is a relevant unfavorable prognostic factor in stage III colorectal cancer. (128, 184) However, preclinical PET imaging strategies employing TSPO ligands for CRC imaging are scarce and a successful imaging strategy is questioned due to basal TSPO expression in human colon. (127, 185) [ $^{18}\text{F}$ ]FEPPA is a 2<sup>nd</sup> generation TSPO PET-tracer and is clinically applied for the detection of neuro-inflammation. (186) Unfortunately, the large inter-individual variability in binding affinity due to the polymorphism within the TSPO gene, impairs quantitative interpretation of [ $^{18}\text{F}$ ]FEPPA PET images. (136)

Our primary aim was the *in vitro* assessment of the feasibility of TSPO PET for CRC imaging. For this purpose, TSPO expression levels were investigated in tumorous and non-neoplastic colon tissues by immunohistochemistry and Western Blot. Moreover, specificity of [ $^{18}\text{F}$ ]FEPPA binding was examined using colorectal cancer tissue sections and human colonic adenocarcinoma cells (HT-29) to evaluate the suitability of [ $^{18}\text{F}$ ]FEPPA for PET imaging in CRC. The second aim was the determination of FEPPA  $K_i$  values towards the three different binding classes (high, low and mixed affinity binders). This detailed characterization of [ $^{18}\text{F}$ ]FEPPA binding behavior fills a knowledge gap and contributes to PET data interpretation.



# [<sup>18</sup>F]FEPPA: Improved Automated Radiosynthesis, Binding Affinity, and Preliminary In Vitro Evaluation in Colorectal Cancer

Neydher Berroterán-Infante,<sup>†,‡</sup> Theresa Balber,<sup>†,§</sup> Petra Furlinger,<sup>†</sup> Michael Bergmann,<sup>||</sup> Rupert Lanzenberger,<sup>⊥</sup> Marcus Hacker,<sup>†</sup> Markus Mitterhauser,<sup>†,§,#</sup> and Wolfgang Wadsak<sup>\*,†,‡,∇</sup>

<sup>†</sup>Division of Nuclear Medicine, Department of Biomedical Imaging and Image-guided Therapy, Medical University of Vienna, Vienna A-1090, Austria

<sup>‡</sup>Department of Inorganic Chemistry, Faculty of Chemistry, University of Vienna, Vienna A-1090, Austria

<sup>§</sup>Department of Pharmaceutical Technology, Faculty of Life Sciences, University of Vienna, Vienna A-1090, Austria

<sup>||</sup>Surgical Research Laboratories, Department of Surgery, Medical University of Vienna, Vienna A-1090, Austria

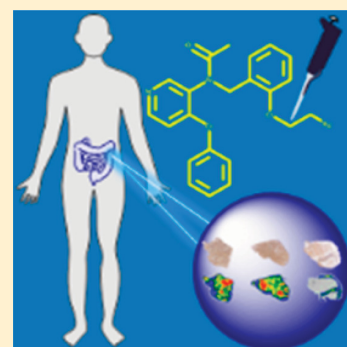
<sup>⊥</sup>Department of Psychiatry and Psychotherapy, Medical University of Vienna, Vienna A-1090, Austria

<sup>#</sup>Ludwig Boltzmann Institute Applied Diagnostics, Vienna A-1090, Austria

<sup>∇</sup>Center for Biomarker Research in Medicine, CBmed GmbH, Graz A-8010, Austria

## Supporting Information

**ABSTRACT:** The overexpression of the translocator protein (TSPO) has been amply reported for a variety of conditions, including neurodegenerative disorders, heart failure, and cancer. Thus, TSPO has been proposed as an excellent imaging biomarker, allowing, in this manner, to obtain an accurate diagnosis and to follow disease progression and therapy response. Accordingly, several radioligands have been developed to accomplish this purpose. In this work, we selected [<sup>18</sup>F]FEPPA, as one of the clinical established tracers, and assessed its in vitro performance in colorectal cancer. Moreover, we setup an improved radiosynthesis method and assessed the in vitro binding affinity of the nonradioactive ligand toward the human TSPO. Our results show an excellent to moderate affinity, in the subnanomolar and nanomolar range, as well as the suitability of [<sup>18</sup>F]FEPPA as an imaging agent for the TSPO in colorectal cancer.



**KEYWORDS:** TSPO, FEPPA, radiosynthesis, affinity, autoradiography, colorectal cancer

The translocator protein (TSPO), previously known as the peripheral benzodiazepine receptor (PBR),<sup>1</sup> has emerged in the last years as an attractive target for diagnosis and treatment of several pathological conditions.<sup>2–5</sup> Its up-regulation has been especially reported in activated microglia of neuroinflammatory disorders such as multiple sclerosis, Parkinson's, Alzheimer's, and Huntington's diseases, as well in some type of cancers, including breast, colon, and glioblastomas.<sup>6–8</sup> Therefore, a variety of ligands have been developed for in vivo visualization, for instance, with positron emission tomography (PET), of the TSPO; including isoquinoline carboxamides, phenoxyphenyl acetamides, pyridazinoindoles, and others.<sup>9–11</sup> The isoquinoline carboxamide [<sup>11</sup>C](R)-PK11195 ((R)-1-(2-chlorophenyl)-N-[<sup>11</sup>C]methyl-N-(1-methylpropyl)-isoquinoline) is one of the first and, until now, the most used ligand for TSPO imaging using PET.<sup>12</sup> However, a high nonspecific binding, due to its high lipophilicity, which ultimately leads to a low signal-to-noise ratio and a problematic radiosynthesis, have been a major drawback for the use of this tracer.<sup>13</sup> To overcome these issues, a second generation of TSPO PET ligands with improved affinity and lipophilicity has arisen over the years. Nevertheless, a single nucleotide

polymorphism (rs6971) in the TSPO gene (Ala147Thr substitution) has hampered the development of such tracers because all these ligands exhibit different binding affinities toward human TSPO from subjects with different genotype. In this regard, three groups have been reported: high-affinity binders (HAB, homozygotes Ala147Ala), mixed-affinity binders (MAB, heterozygotes Ala147Thr), and low-affinity binders (LAB, homozygotes Thr147Thr).<sup>14</sup> Some of those PET tracers are still widely used, although it is common to exclude LAB from clinical studies since low or no uptake of the tracers is observed. The second disadvantage is the interpretation of the data since the difference in the binding affinity must be considered, causing difficulties on the appropriate quantification of the tracer uptake.<sup>15</sup> Among these tracers, the phenoxyphenyl acetamide [<sup>18</sup>F]FEPPA (N-acetyl-N-(2-[<sup>18</sup>F]-fluoroethoxybenzyl)-2-phenoxy-5-pyridinamine) shows out-

**Received:** September 6, 2017

**Accepted:** February 21, 2018

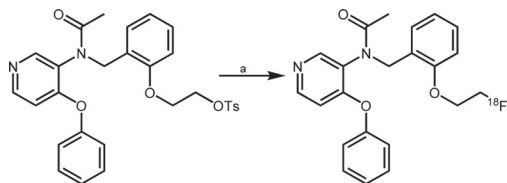
**Published:** February 21, 2018

standing properties regarding affinity, stability, lipophilicity, and radiosynthesis.<sup>16</sup>

[<sup>18</sup>F]FEPPA has been already used in several preclinical and clinical settings;<sup>17,18</sup> however, only the in vivo effect of the polymorphism has been reported.<sup>19</sup> To the best of our knowledge, no binding affinity profile, in terms of the inhibitory constant ( $K_i$ ) toward the human TSPO, nor the evaluation in colorectal cancer have been performed. Hence, starting from the already reported automated radiosynthesis of [<sup>18</sup>F]FEPPA, we first established an improved and reliable method for the tracer production and subsequently assessed the in vitro binding affinity profile regarding the polymorphism rs6971. Furthermore, since the overexpression of TSPO in colorectal cancer is amply described,<sup>20–22</sup> autoradiography experiments with [<sup>18</sup>F]FEPPA, using human colorectal cancer and healthy colon tissues, as well as real-time kinetic experiments utilizing the colorectal cancer cell line HT-29 were conducted.

The TSPO-PET tracer [<sup>18</sup>F]FEPPA was synthesized according to previously published procedures,<sup>16,17</sup> with some minor modifications as outlined in Scheme 1.

#### Scheme 1. Radiosynthesis of [<sup>18</sup>F]FEPPA



<sup>a</sup>[<sup>18</sup>F]KF/K222(dry), ACN, 90 °C, 10 min. Purification: preparative HPLC, SPE.

Briefly, aliphatic nucleophilic substitution was automated in a nuclear interface synthesizer between dried [<sup>18</sup>F]KF/K222 and the tosylate precursor (2-(2-((N-(4-phenoxy-3-pyridin-3-yl)-acetamido)methyl)phenoxy)ethyl 4-methylbenzenesulfonate). After the reaction time, the crude product was transferred to a semipreparative HPLC system, and the fraction containing the product ( $t_R \approx 5$  min) was collected. The solvents were removed by SPE and the product reformulated in ethanol, sodium chloride, and phosphate-buffered saline. The (radio)chemical purity was assessed by means of analytical HPLC and TLC. All other quality control tests (visual inspection, pH, osmolality, radionuclide purity, K222, and residual solvents contents) were performed using regular procedures implemented in the PET Centre of the Vienna General Hospital. Complete details of the radiosynthesis and the quality control can be found in the Supporting Information.

The purity of [<sup>18</sup>F]FEPPA always exceeded 99%, and  $4.2 \pm 0.8$  GBq of the product was afforded, representing a nondecay corrected radiochemical yield of  $38 \pm 3\%$  (based on [<sup>18</sup>F]F<sup>−</sup> at EOB) with a molar radioactivity of  $241 \pm 13$  GBq/μmol<sup>−1</sup> ( $n = 15$ ) in a total synthesis time of 30 min. The quality control was always in accordance to the guidelines of the European Pharmacopeia.<sup>23</sup>

With this new set of conditions, the main outcome was the time reduction of the purification step of the previously published method<sup>17</sup> from 23 to 5 min, which drastically reduces the total synthesis time and affords a small increase in the radiochemical yield.

The affinity toward human TSPO of nonradioactive FEPPA (cold standard, *N*-acetyl-*N*-(2-fluoroethoxybenzyl)-2-phenoxy-

5-pyridinamine) was determined in a competitive binding assay, as reported elsewhere,<sup>24</sup> using [<sup>3</sup>H]PK11195 and a TSPO-expressing platelet membrane, from individuals previously genotyped regarding the polymorphism rs6971 and subsequently identified as HAB, MAB, and LAB (approved by the Ethics Committee of the Medical University of Vienna).

Inhibition constants in the subnanomolar and nanomolar range were obtained for FEPPA (Figure 1).  $K_i$  (HAB) =  $(0.5 \pm$

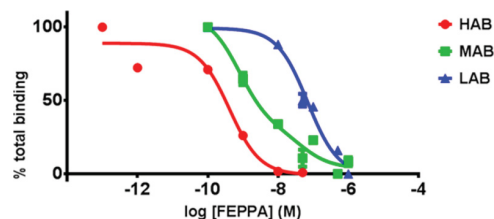


**Figure 1.** Competition binding assays of nonradioactive FEPPA in HAB, MAB, and LAB using [<sup>3</sup>H]PK11195 and a TSPO-expressing platelet membrane.

0.1) nM,  $K_i$  (MAB) =  $(0.6 \pm 0.1)$ ,  $(37 \pm 5)$  nM, and  $K_i$  (LAB) =  $(37 \pm 5)$  nM. As expected, the in vitro binding affinity of FEPPA shows the typical behavior of the second generation of TSPO ligands regarding the TSPO polymorphism rs6971. Moreover, the inhibition constant for LAB shows a moderate binding affinity, which is 70 times lower than for HAB.

Although the up-regulation of TSPO in colorectal cancer is well-known, little research has been performed regarding TSPO imaging in this disease. TSPO-PET research has been more focused on neuroinflammation disorders and glioblastomas, as a consequence of the significant role of TSPO in glial activation.<sup>25</sup> Therefore, we deemed to evaluate the appropriateness of [<sup>18</sup>F]FEPPA as an imaging agent for colorectal cancer in vitro.

First, the expression of the TSPO in colon cancer and healthy mucosa (both obtained directly after tumorectomy with full informed consent from one patient bearing colon cancer and approved by the Ethics Committee of the Medical University of Vienna), as well as in HT-29 cells, was examined by Western blot. The presence of TSPO (above the 15 kDa mark, predicted molecular weight of 18 kDa) in HT-29 cells,<sup>26</sup> as well as in the tumor lysate, was confirmed (Figure 2). Interestingly, TSPO was not detected in healthy tissue lysate, although a moderate expression of TSPO in colon has been reported.<sup>27</sup>

Moreover, in order to ensure the suitability of [<sup>18</sup>F]FEPPA for further evaluations and thus taking into account the polymorphism rs6971, we also conducted a PCR-based genotype assay on the cell line and the patient tissue, which distinguished the HT-29 cells and the patient bearing the tumor within the HAB group.

Accordingly, real-time binding experiments, to assess the tracer kinetics, were planned using HT-29 cells and LigandTracer Technology.<sup>28</sup> In a typical real-time binding experiment, the equilibrium was reached after 20 min, and in pursuance of displacing bonded [<sup>18</sup>F]FEPPA and thereby demonstrating specific binding to the TSPO, solutions of unlabeled FEPPA, PBR28, or PK11195 were used.

As shown in Figure 3, specific binding was observed for [<sup>18</sup>F]FEPPA since the signal decreased after the addition of displacement solutions, i.e., the radioactivity bound to the cells was reduced in all cases. Unlabeled FEPPA achieved a  $(50.2 \pm$



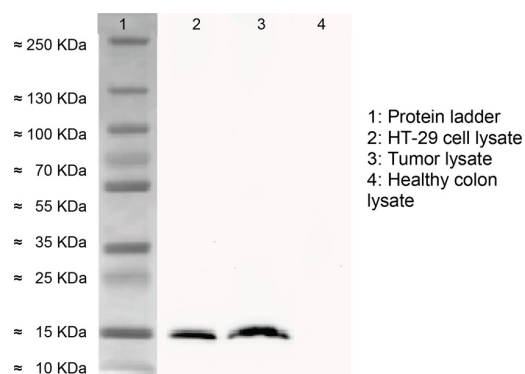


**Figure 2.** Protein bands of ~15 kDa (theoretical molecular weight of TSPO, 18 kDa) were detected via Western blot with a specific anti-TSPO antibody in HT-29 cell and colorectal cancer tissue lysates, however not in healthy colon tissue lysate.

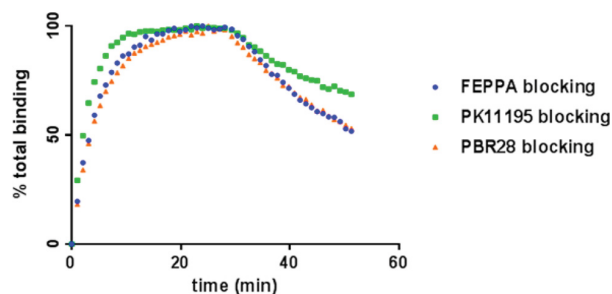


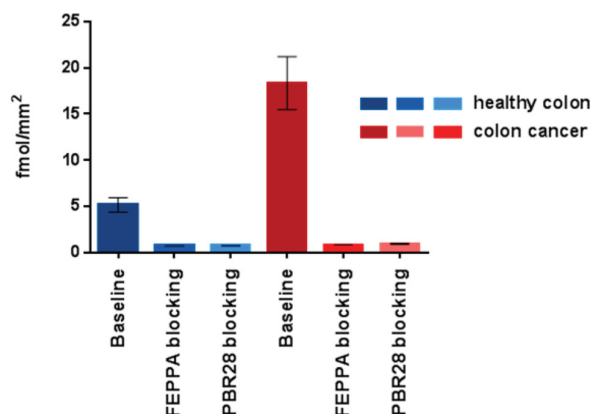
**Figure 3.** Normalized overlay real-time binding kinetics of  $[^{18}\text{F}]$ FEPPA in HT-29 cells using LigandTracer Technology. Association of  $[^{18}\text{F}]$ FEPPA was performed for 30 min, and subsequently, displacing agents (FEPPA, PK11195, or PBR28) were applied. Displacement was examined for additional 30 min.

11.2%) displacement, whereas PBR28 and PK11195 reached ( $48.2 \pm 6.7\%$ ) and ( $32.2 \pm 10.6\%$ ) displacement, respectively. In a similar set of experiments, only DMSO was used as vehicle control.

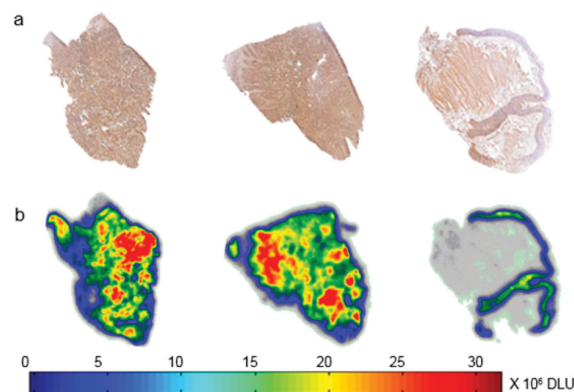
With these results in hand, we proceeded to perform autoradiography experiments with tumor and healthy colon tissues. Tissue slices were incubated with approximately 50 kBq per slice of freshly prepared  $[^{18}\text{F}]$ FEPPA for 1 h. Analogously, blocking experiments were accomplished by coincubating the slices with radiotracer and unlabeled FEPPA or PBR28 ( $10 \mu\text{M}$ ). After exposing the slices to a phosphor screen, radiotracer uptake was analyzed, and the amount of compound ( $\text{fmol}\cdot\text{mm}^{-2}$ ) accumulated in each slice was determined.

Figure 4 shows a significantly higher (three to six times) uptake of the tracer in malignant tissue (baseline red) in comparison with healthy colon tissue (baseline blue), which is in accordance with the already mentioned upregulation of TSPO in colorectal cancer. Moreover, competitive blocking with unlabeled TSPO ligands was significantly observed in all cases.

Furthermore, an immunohistochemical investigation was realized in order to match the TSPO localization and the radiotracer uptake. For this purpose, an anti-TSPO antibody staining was performed using vicinal slices to those used for autoradiography. In Figure 5, a representative staining shows a stronger staining for tumor tissue in comparison to healthy colon. Accordingly, in the autoradiography counterpart, a higher uptake of the tracer in this tissue is observed as well,



**Figure 4.**  $[^{18}\text{F}]$ FEPPA uptake ( $\text{fmol}\cdot\text{mm}^{-2}$ ) in healthy colon compared to colon cancer tissue slices. Specific uptake was confirmed by blocking experiments with cold FEPPA and PBR28.



**Figure 5.**  $[^{18}\text{F}]$ FEPPA accumulation observed in autoradiography corresponded to TSPO expression in the vicinal slices as revealed by immunohistochemistry. (a) TSPO IHC. (b)  $[^{18}\text{F}]$ FEPPA autoradiography. Left/middle, colorectal tumor tissues. Right, healthy colon tissue. DLU, digital light units.

demonstrating once more the high sensitivity of  $[^{18}\text{F}]$ FEPPA for TSPO recognition in colon cancer.

PET imaging of TSPO in colonic diseases seems to be challenging mainly due to the basal expression of this protein in healthy tissues and in less grade due to the availability of several probes with different pharmacological properties, which difficult the comparison of the data. Several reports<sup>29,30</sup> suggest poor specificity of TSPO PET tracers for evaluation of such conditions; meanwhile, some investigations<sup>31–33</sup> support the use of TSPO in inflammatory bowel diseases and colorectal cancer. In view of the high level of specificity demonstrated by our *in vitro* results and also the relatively low uptake of  $[^{18}\text{F}]$ FEPPA *in vivo* in healthy colon and stomach as demonstrated elsewhere,<sup>17</sup> we propose  $[^{18}\text{F}]$ FEPPA as a potentially appropriate probe to be further *in vivo* evaluated as a TSPO PET tracer to evaluate this malignancy.

In summary, we have developed a faster and still reliable method for the radiosynthesis of  $[^{18}\text{F}]$ FEPPA with higher radiochemical yields. Moreover, FEPPA showed similar behavior *in vitro* as other TSPO ligands regarding the polymorphism rs6971; although its affinity in human platelets is very potent in all identified genotypes. Additionally, we present here the first evaluation, to the best of our knowledge,

in colorectal cancer. Our results point toward the suitability of [ $^{18}\text{F}$ ]FEPPA for imaging colorectal cancer with PET.

## ■ ASSOCIATED CONTENT

### Supporting Information

The Supporting Information is available free of charge on the ACS Publications website at DOI: 10.1021/acsmedchemlett.7b00367.

Detailed information about radiosynthetic procedures, binding affinity assays, including genotyping and membrane preparation, cell culture, real-time kinetics, autoradiography, immunohistochemistry, Western blot, and additional results (PDF)

## ■ AUTHOR INFORMATION

### Corresponding Author

\*Tel: +43-1-40400-55330. E-mail: wolfgang.wadsak@meduniwien.ac.at.

### ORCID

Wolfgang Wadsak: 0000-0003-4479-8053

### Author Contributions

N.B.-I. performed all the radiosyntheses, the binding affinity experiments and genotyping assays, and writing of the paper and contributed to autoradiography and real-time binding assays. T.B. performed all immunohistochemistry, Western blot, autoradiography, and real-time binding experiments. P.F. contributed to autoradiography, immunohistochemistry, Western blot, and real-time binding experiments. M.B. performed the tumorectomy and contributed to the design of the study. M.H. and R.L. designed parts of the research and proofread the manuscript. M.M. conceived and supervised the in vitro experiments and proofread the manuscript. W.W. conceived and supervised the radiosyntheses and proofread the manuscript. All authors have given approval to the final version of the manuscript.

### Notes

The authors declare no competing financial interest.

## ■ ACKNOWLEDGMENTS

This scientific project was performed with the support of the Medical Imaging Cluster of the Medical University of Vienna. The authors want to thank Friedrich Girschele for collecting the blood samples for membrane preparation and Stefan Schmitl for his collaboration in the binding affinity profile experiments.

## ■ ABBREVIATIONS

TSPO, translocator protein; PBR, peripheral benzodiazepine receptor; HAB, high-affinity binders; MAB, mixed-affinity binders; LAB, low-affinity binders;  $t_R$ , retention time; ACN, acetonitrile; HPLC, high performance liquid chromatography; SPE, solid phase extraction; TLC, thin layer chromatography; EOB, end of bombardment; PCR, polymerase chain reaction; IHC, immunohistochemistry; DLU, digital light units

## ■ REFERENCES

- (1) Papadopoulos, V.; Baraldi, M.; Guilarte, T. R.; Knudsen, T. B.; Lacapère, J.-J.; Lindemann, P.; Norenberg, M. D.; Nutt, D.; Weizman, A.; Zhang, M.-R.; Gavish, M. Translocator Protein (18 kDa): New Nomenclature for the Peripheral-Type Benzodiazepine Receptor Based on Its Structure and Molecular Function. *Trends Pharmacol. Sci.* **2006**, *27*, 402–409.
- (2) Kim, T.; Pae, A. N. Translocator Protein (TSPO) Ligands for the Diagnosis or Treatment of Neurodegenerative Diseases: A Patent Review (2010–2015; Part 1). *Expert Opin. Ther. Pat.* **2016**, *26*, 1325–1351.
- (3) Kim, T.; Pae, A. N. Translocator Protein (TSPO) Ligands for the Diagnosis or Treatment of Neurodegenerative Diseases: A Patent Review (2010 – 2015; Part 2). *Expert Opin. Ther. Pat.* **2016**, *26*, 1353–1366.
- (4) Rupprecht, R.; Papadopoulos, V.; Rammes, G.; Baghai, T. C.; Fan, J.; Akula, N.; Grover, G.; Adams, D.; Schumacher, M. Translocator Protein (18 kDa) (TSPO) as a Therapeutic Target for Neurological and Psychiatric Disorders. *Nat. Rev. Drug Discovery* **2010**, *9*, 971–988.
- (5) Mukherjee, S.; Das, S. K. Translocator Protein (TSPO) in Breast Cancer. *Curr. Mol. Med.* **2012**, *12*, 443–457.
- (6) Dupont, A.-C.; Largeau, B.; Santiago Ribeiro, M. J.; Guilloteau, D.; Tronel, C.; Arlicot, N. Translocator Protein-18 kDa (TSPO) Positron Emission Tomography (PET) Imaging and Its Clinical Impact in Neurodegenerative Diseases. *Int. J. Mol. Sci.* **2017**, *18*, 785.
- (7) Roncaroli, F.; Su, Z.; Herholz, K.; Gerhard, A.; Turkheimer, F. E. TSPO Expression in Brain Tumours: Is TSPO a Target for Brain Tumour Imaging? *Clin. Transl. Imaging* **2016**, *4*, 145–156.
- (8) Mendonça-Torres, M. C.; Roberts, S. S. The Translocator Protein (TSPO) Ligand PK11195 Induces Apoptosis and Cell Cycle Arrest and Sensitizes to Chemotherapy Treatment in Pre- and Post-Relapse Neuroblastoma Cell Lines. *Cancer Biol. Ther.* **2013**, *14*, 319–326.
- (9) Camsonne, R.; Crouzel, C.; Comar, D.; Mazière, M.; Prenant, C.; Sastre, J.; Moulin, M.; Syrota, A. Synthesis of N-(11C) Methyl, N-(Methyl-1 Propyl), (Chloro-2 Phenyl)-1 Isoquinoline Carboxamide-3 (PK 11195): A New Ligand for Peripheral Benzodiazepine Receptors. *J. Labelled Compd. Radiopharm.* **1984**, *21*, 985–991.
- (10) Briard, E.; Zoghbi, S. S.; Imaizumi, M.; Gourley, J. P.; Shetty, H. U.; Hong, J.; Cropley, V.; Fujita, M.; Innis, R. B.; Pike, V. W. Synthesis and Evaluation in Monkey of Two Sensitive 11C-Labeled Aryloxanilide Ligands for Imaging Brain Peripheral Benzodiazepine Receptors In Vivo. *J. Med. Chem.* **2008**, *51*, 17–30.
- (11) Cheung, Y.-Y.; Nickels, M. L.; Tang, D.; Buck, J. R.; Manning, H. C. Facile Synthesis of SSR180575 and Discovery of 7-Chloro-N,N,5-Trimethyl-4-Oxo-3(6-[ $^{18}\text{F}$ ]Fluoropyridin-2-Yl)-3,5-Dihydro-4H-Pyridazino[4,5-b]Indole-1-Acetamide, a Potent Pyridazinoindole Ligand for PET Imaging of TSPO in Cancer. *Bioorg. Med. Chem. Lett.* **2014**, *24*, 4466–4471.
- (12) Guilarte, T. R. 13.31 - Molecular Imaging: The New Frontier in Neurotoxicology A2. In *Comprehensive Toxicology*, 2nd ed.; McQueen, C. A., Ed.; Elsevier: Oxford, 2010; pp 537–551.
- (13) Boutin, H.; Prenant, C.; Maroy, R.; Galea, J.; Greenhalgh, A. D.; Smigova, A.; Cawthorne, C.; Julyan, P.; Wilkinson, S. M.; Banister, S. D.; Brown, G.; Herholz, K.; Kassioti, M.; Rothwell, N. J. [ $^{18}\text{F}$ ]DPA-714: Direct Comparison with [ $^{11}\text{C}$ ]PK11195 in a Model of Cerebral Ischemia in Rats. *PLoS One* **2013**, *8*, e56441.
- (14) Owen, D. R.; Yeo, A. J.; Gunn, R. N.; Song, K.; Wadsworth, G.; Lewis, A.; Rhodes, C.; Pulford, D. J.; Bennacef, I.; Parker, C. A.; StJean, P. L.; Cardon, L. R.; Mooser, V. E.; Matthews, P. M.; Rabiner, E. A.; Rubio, J. P. An 18-KDa Translocator Protein (TSPO) Polymorphism Explains Differences in Binding Affinity of the PET Radioligand PBR28. *J. Cereb. Blood Flow Metab.* **2012**, *32*, 1–5.
- (15) Owen, D. R.; Guo, Q.; Rabiner, E. A.; Gunn, R. N. The Impact of the Rs6971 Polymorphism in TSPO for Quantification and Study Design. *Clin. Transl. Imaging* **2015**, *3*, 417–422.
- (16) Wilson, A. A.; Garcia, A.; Parkes, J.; McCormick, P.; Stephenson, K. A.; Houle, S.; Vasdev, N. Radiosynthesis and Initial Evaluation of [ $^{18}\text{F}$ ]FEPPA for PET Imaging of Peripheral Benzodiazepine Receptors. *Nucl. Med. Biol.* **2008**, *35*, 305–314.
- (17) Vasdev, N.; Green, D. E.; Vines, D. C.; McLarty, K.; McCormick, P. N.; Moran, M. D.; Houle, S.; Wilson, A. A.; Reilly, R. M. Positron-Emission Tomography Imaging of the TSPO with [ $^{18}\text{F}$ ]FEPPA in a Preclinical Breast Cancer Model. *Cancer Biother. Radiopharm.* **2013**, *28*, 254–259.

- (18) Setiawan, E.; Wilson, A. A.; Mizrahi, R.; et al. Role of Translocator Protein Density, a Marker of Neuroinflammation, in the Brain during Major Depressive Episodes. *JAMA Psychiatry* **2015**, *72*, 268–275.
- (19) Mizrahi, R.; Rusjan, P. M.; Kennedy, J.; Pollock, B.; Mulsant, B.; Suridjan, I.; De Luca, V.; Wilson, A. A.; Houle, S. Translocator Protein (18 KDa) Polymorphism (Rs6971) Explains in-Vivo Brain Binding Affinity of the PET Radioligand [18F]-FEPPA. *J. Cereb. Blood Flow Metab.* **2012**, *32*, 968–972.
- (20) Katz, Y.; Eitan, A.; Amiri, Z.; Gavish, M. Dramatic Increase in Peripheral Benzodiazepine Binding Sites in Human Colonic Adenocarcinoma as Compared to Normal Colon. *Eur. J. Pharmacol.* **1988**, *148*, 483–484.
- (21) Katz, Y.; Eitan, A.; Gavish, M. Increase in Peripheral Benzodiazepine Binding Sites in Colonic Adenocarcinoma. *Oncology* **2004**, *47*, 139–142.
- (22) Han, Z.; Slack, R. S.; Li, W.; Papadopoulos, V. Expression of Peripheral Benzodiazepine Receptor (PBR) in Human Tumors: Relationship to Breast, Colorectal, and Prostate Tumor Progression. *J. Recept. Signal Transduction Res.* **2003**, *23*, 225–238.
- (23) Council of Europe. *Europäisches Arzneibuch (European Pharmacopoeia)*, 8th ed; Verlag Österreich GmbH: Vienna, 2008; pp 995.
- (24) Owen, D. R. J.; Gunn, R. N.; Rabiner, E. A.; Bennacef, I.; Fujita, M.; Kreisl, W. C.; Innis, R. B.; Pike, V. W.; Reynolds, R.; Matthews, P. M.; Parker, C. A. Mixed-Affinity Binding in Humans with 18-KDa Translocator Protein Ligands. *J. Nucl. Med.* **2011**, *52*, 24–32.
- (25) Tronel, C.; Largeau, B.; Santiago Ribeiro, M. J.; Guilloteau, D.; Dupont, A.-C.; Arlicot, N. Molecular Targets for PET Imaging of Activated Microglia: The Current Situation and Future Expectations. *Int. J. Mol. Sci.* **2017**, *18*, 802.
- (26) Ostuni, M.; Ducroc, R.; Péranski, G.; Tonon, M.-C.; Papadopoulos, V.; Lacapère, J.-J. Translocator Protein (18 kDa) Ligand PK 11195 Induces Transient Mitochondrial Ca<sup>2+</sup> Release Leading to Transepithelial Cl<sup>-</sup> Secretion in HT-29 Human Colon Cancer Cells. *Biology of the Cell* **2007**, *99*, 639–647.
- (27) Tang, D.; Li, J.; Buck, J. R.; Tantawy, M. N.; Xia, Y.; Harp, J. M.; Nickels, M. L.; Meiler, J.; Manning, H. C. Evaluation of TSPO PET Ligands [18F]VUIIS1009A and [18F]VUIIS1009B: Tracers for Cancer Imaging. *Mol. Imaging Biol.* **2017**, *19*, 578–588.
- (28) Zeilinger, M.; Pichler, F.; Nics, L.; Wadsak, W.; Spreitzer, H.; Hacker, M.; Mitterhauser, M. New Approaches for the Reliable in Vitro Assessment of Binding Affinity Based on High-Resolution Real-Time Data Acquisition of Radioligand-Receptor Binding Kinetics. *EJNMMI Res.* **2017**, *7*, 22.
- (29) Takano, A.; Gulyás, B.; Varrone, A.; Karlsson, P.; Sjöholm, N.; Larsson, S.; Jonsson, C.; Odh, R.; Sparks, R.; Al Tawil, N.; Hoffmann, A.; Zimmermann, T.; Thiele, A.; Halldin, C. Biodistribution and Radiation Dosimetry of the 18 KDa Translocator Protein (TSPO) Radioligand [18F]FEDAA1106: A Human Whole-Body PET Study. *Eur. J. Nucl. Med. Mol. Imaging* **2011**, *38* (11), 2058–2065.
- (30) Wu, C.; Yue, X.; Lang, L.; Kiesewetter, D. O.; Li, F.; Zhu, Z.; Niu, G.; Chen, X. Longitudinal PET Imaging of Muscular Inflammation Using 18F-DPA-714 and 18F-Alfatide II and Differentiation with Tumors. *Theranostics* **2014**, *4* (5), 546–555.
- (31) Bernards, N.; Pottier, G.; Thézé, B.; Dollé, F.; Boisgard, R. In Vivo Evaluation of Inflammatory Bowel Disease with the Aid of MPET and the Translocator Protein 18 KDa Radioligand [18F]DPA-714. *Mol. Imaging Biol.* **2015**, *17* (1), 67–75.
- (32) Kurtys, E.; Doorduyn, J.; Eisel, U. L. M.; Dierckx, R. A. J. O.; de Vries, E. F. J. Evaluating [11C]PBR28 PET for Monitoring Gut and Brain Inflammation in a Rat Model of Chemically Induced Colitis. *Mol. Imaging Biol.* **2017**, *19* (1), 68–76.
- (33) Powell, A. E.; Vlachich, G.; Zhao, Z.-Y.; McKinley, E. T.; Washington, M. K.; Manning, H. C.; Coffey, R. J. Inducible Loss of One Apc Allele in Lrig1-Expressing Progenitor Cells Results in Multiple Distal Colonic Tumors with Features of Familial Adenomatous Polyposis. *Am. J. Physiol. - Gastrointest. Liver Physiol.* **2014**, *307* (1), G16–G23.



# **[<sup>18</sup>F]FEPPA: Improved Automated Radiosynthesis, Binding Affinity Profile and Preliminary in Vitro Evaluation in Colorectal Cancer**

Neydher Berroterán-Infante,<sup>†,‡</sup> Theresa Balber,<sup>†,¶</sup> Petra Förlinger,<sup>†</sup> Michael Bergmann,<sup>⊥</sup>  
Rupert Lanzenbeger,<sup>⊥</sup> Marcus Hacker,<sup>†</sup> Markus Mitterhauser,<sup>†, ¶,⊥</sup> Wolfgang Wadsak<sup>†,‡,§</sup>

<sup>†</sup> Division of Nuclear Medicine, Department of Biomedical Imaging and Image-guided Therapy, Medical University of Vienna, Vienna, Austria.

<sup>‡</sup> Department of Inorganic Chemistry, Faculty of Chemistry, University of Vienna, Vienna, Austria.

<sup>¶</sup> Department of Pharmaceutical Technology, Faculty of Life Sciences, University of Vienna, Vienna, Austria.

<sup>⊥</sup> Surgical Research Laboratories, Department of Surgery, Medical University of Vienna, Vienna, Austria.

<sup>⊥</sup> Department of Psychiatry and Psychotherapy, Medical University of Vienna, Vienna, Austria

<sup>‡</sup> Ludwig Boltzmann Institute Applied Diagnostics, Vienna, Austria.

<sup>§</sup> Center for Biomarker Research in Medicine, CBmed GmbH, Graz, Austria.

## **Supporting Information**

## 1. Material and Methods

Caution:  $^{18}\text{F}$  is a  $\beta^+$  emitter (511 keV) with a half-life of 109.77 min.  $^3\text{H}$  is a  $\beta^-$  emitter (18.6 keV) with a half-life of 12.32 years. All reactions and experiments involving  $^{18}\text{F}$  and/or  $^3\text{H}$  were performed in a laboratory approved for the handling of radionuclides, and appropriate safety procedures were followed at all times to prevent radioactive contamination

### 1.1. Materials

FEPPA tosylate precursor (2-(2-((*N*-(4-phenoxy-pyridin-3-yl)acetamido)methyl)phenoxy)ethyl 4-methylbenzenesulfonate), FEPPA reference standard (*N*-Acetyl-*N*-(2-fluoroethoxybenzyl)-2-phenoxy-5-pyridinamine), (*R*)-PK11195 ((*R*)-1-(2-chlorophenyl)-*N*-methyl-*N*-(1-methylpropyl)-isoquinoline-3-carboxamide), PBR28 (*N*-Acetyl-*N*-(2-methoxybenzyl)-2-phenoxy-5-pyridinamine) and PS- $\text{HCO}_3$  cartridges (45 mg) were obtained from ABX Advanced Biochemical Compounds (Radeberg, Germany). Acetonitrile (for DNA synthesis and HPLC grade), Kryptofix  $\text{K}_{2.2.2}$  (4,7,13,16,21,24-hexaoxa-1,10-diazabicyclo[8.8.8]hexacosane for synthesis >99%), potassium carbonate ( $\geq 99\%$ ), potassium chloride ( $\geq 99.5\%$ ), anhydrous calcium chloride ( $\geq 98\%$ ), anhydrous magnesium chloride ( $\geq 98\%$ ), ethanol (absolute), hydrochloric acid 1 M, haematoxylin, *n*-butyl acetate, 10X RIPA lysis buffer concentrate and silica gel 60 F254S plates were purchased from Merck (Darmstadt, Germany). Tris base (ACS reagent,  $\geq 99.8\%$ ), ammonium formate ( $\geq 99.995\%$ ), sodium chloride ( $\geq 99\%$ ), anhydrous dimethyl sulfoxide ( $\geq 99.9\%$ ), Triton X-100 (0.2%), 2-methylbutane ( $\geq 99\%$ ), bovine serum albumin, protease inhibitor and aqueous polyethylene imine (50% w/v) were obtained from Sigma Aldrich (Vienna, Austria). C18 plus SepPak<sup>®</sup> cartridges were purchased from Waters (Milford, USA). For formulation of the radiotracer, 0.9% sodium chloride solution from B. Braun (Melsungen, Germany) and a sterile phosphate-buffered saline solution from the Vienna General Hospital's Pharmacy (Vienna, Austria) were used. Mini-PROTEAN<sup>®</sup> TGX<sup>™</sup> precast gels were acquired from BIO-RAD (Hercules, USA) and Amersham Protran<sup>™</sup> Premium 0.2  $\mu\text{m}$  NC nitrocellulose blotting membranes from GE Healthcare Life Sciences (Little Chalfont, United Kingdom). For immunochemistry assays, 10X phosphate-buffered saline concentrate was obtained from Morphisto (Frankfurt am Main, Germany) and diluted to obtain 1X PBS solution. Bloxall<sup>™</sup> blocking solution and Vectastain<sup>®</sup> ABC Kit (PK-4001) were purchased from Vector Laboratories (Burlingame, USA). Avidin/Biotin blocking kit and PureLink<sup>®</sup> Genomic DNA extraction kit, Taqman<sup>®</sup> Genotyping Assay C\_2512465\_20, Taqman<sup>®</sup> PCR Master Mix, nuclease-free water, SuperSignal<sup>™</sup> West Pico chemiluminescent substrate kit, Menzel Superfrost<sup>®</sup> Plus positively charged microscope slides as well as purified rabbit IgG (1 mg.mL<sup>-1</sup>) and Pierce<sup>™</sup> BCA Protein Assay kit were acquired from ThermoFisher Scientific (Waltham, USA). Rabbit monoclonal anti-TSPO antibody (ab109497) and DAB-Substrate kit were purchased from Abcam (Cambridge, United Kingdom). Histofluor<sup>®</sup> mounting medium was obtained from Paul Marienfeld (Lauda-Königshofen, Germany). Low-protein binding Millex<sup>®</sup> GS 0.22  $\mu\text{m}$  sterile filters were obtained from Millipore (Bedford, USA).  $\text{H}_2^{18}\text{O}$  (> 98%) was purchased from Rotem Europe (Leipzig, Germany). All cell culture media and supplements were purchased from ThermoFisher Scientific (Waltham, USA). [ $^3\text{H}$ ]PK11195 (3,149 TBq.mmol<sup>-1</sup>), Ultima Gold<sup>™</sup> liquid scintillation cocktail and multisensitive phosphor screens all three from Perkin Elmer (Waltham, USA) and Whatman<sup>®</sup> GF/B glass fiber paper from Brandel (Gaithersburg, USA) were used. All chemicals and solvents were used without further purification.

## 1.2. Instrumentation

[<sup>18</sup>F]Fluoride was produced in a GE PET trace cyclotron (PETtrace 860, GE Medical Systems, Uppsala, Sweden) and the [<sup>18</sup>F]FEPPA radiosynthesis was performed using a Nuclear Interface synthesizer (GE Healthcare, Uppsala, Sweden); remotely controlled by a laptop with the dedicated software GINA (Elysia-Raytest, Straubenhardt, Germany). Purification of [<sup>18</sup>F]FEPPA was performed by semi-preparative reversed phase HPLC using the synthesizer-integrated system equipped with a radioactivity-, and UV-detector (Linear Instruments Model 200 Detector UV/VIS) and a S1122 HPLC pump (Sykam, Fürstfeldbruck, Germany).

For quality control and molar radioactivity determination of [<sup>18</sup>F]FEPPA, an Agilent 1260 system (Agilent Technologies GmbH, Austria) equipped with a quaternary pump (G1311B), a multi wavelength UV-detector (G1365D), and a NaI (TI) detector from Berthold Technologies (Bad Wildbad, Germany), controlled with the GINA Star software (Elysia-Raytest, Straubenhardt, Germany) was used. The osmolality of the tracer was measured with a Wescor osmometer Vapro<sup>®</sup> 5600 (Sanova Medical Systems, Vienna, Austria) and the pH was controlled using a WTW inoLab 740 pH meter (WTW, Weilheim, Germany). Gas chromatography analysis for solvents residual content was performed with a Bruker Gas Chromatography System 430-GC. Analyses of radio-TLC plates were performed using a Canberra-Packard Instant Imager (Perkin Elmer, Waltham, USA).

Gel electrophoresis, semi-dry transfer and chemiluminescence imaging were performed using a MINI-PROTEAN<sup>®</sup> Tetra Cell - PowerPac<sup>™</sup> Basic Power Supply system, a Trans-Blot<sup>®</sup> SD Semi-dry Transfer Cell and a VersaDoc<sup>™</sup> Imaging system, all three from Bio-Rad (Hercules, California), respectively. Tissues were sliced using a microcryotome Microm HM 560 (Thermo Fisher Scientific, Waltham, USA) and imaged in a TissueFAXS scanner (Tissue Gnostics, Vienna, Austria). The autoradiography screens were processed using a cyclone plus phosphor imager (Perkin Elmer, Waltham, USA). DNA concentration was determined using a Nanodrop<sup>™</sup> 1000 spectrophotometer (ThermoFisher Scientific, Waltham, USA) and PCR, for genotyping assay, was performed using a real-time PCR system OnePlus (Applied Biosystems, ThermoFisher Scientific, Waltham, USA). Total protein concentration of the membranes and lysates was measured in a Synergy HTX plate multimode reader (Biotek, Winooski, USA). For binding affinity experiments, a Hidex 300SL beta counter (Hidex, Turku, Finland) was used. For real-time binding kinetics, cells were counted with a Scepter<sup>™</sup> 2.0 cell counter (Merck, Darmstadt, Germany) and the experiments were performed using LigandTracer<sup>®</sup> Yellow (Ridgeview Instruments AB, Uppsala, Sweden).

## 1.3. Methods

### 1.3.1. Radiochemistry

The synthesis of [<sup>18</sup>F]FEPPA was conducted according to previously published procedures<sup>1,2</sup> with some modifications. For the radiosynthesis, cyclotron-produced [<sup>18</sup>F]fluoride (<sup>18</sup>O(p,n)<sup>18</sup>F-) was transferred to the synthesizer module and fixed on a PS-HCO<sub>3</sub> cartridge. In order to start the labeling reaction, the activity was eluted with 0.8 mL of a potassium carbonate (4.5 mg.mL<sup>-1</sup>) and Kriptofix (22 mg.mL<sup>-1</sup>) solution in acetonitrile/water

80/20 from the cartridge and transferred to the reactor with vacuum. The complex was azeotropically dried at 100 °C by addition of 0.6 mL of acetonitrile. After complete drying, 0.5 mL of a 6.25 mg.mL<sup>-1</sup> solution of the FEPPA tosylate precursor in acetonitrile was added to the activated and dried [<sup>18</sup>F]fluoride/K<sub>2.2.2</sub> complex and the reaction vessel was heated at 90 °C. After 10 min, the reaction was quenched with 2 mL of water and the crude product was transferred to a semi-preparative HPLC column (Phenomenex Onyx™ Monolithic Semi-PREP C18 Column 100x10 mm) and eluted with a solution of 60% 10 mM ammonium formate adjusted at pH 7.2 and 40% acetonitrile (flow at 4 mL.min<sup>-1</sup>). The fraction containing the product was collected and dissolved in 60 mL of water. Subsequently, the solvents were removed by solid-phase extraction using a pre-conditioned (10 mL ethanol and 20 mL water) C18plus SepPak cartridge. The cartridge was washed with water and the product ([<sup>18</sup>F]FEPPA) was eluted with ethanol (1.5 mL) and formulated with sodium chloride (10 mL) and phosphate-buffered saline (6 mL). Finally, the (radio)chemical purity was assessed via HPLC using a column (Phenomenex Onyx™ Monolithic C18 Column 100x4.6 mm) as stationary phase and a solution of 70% 10 mM ammonium formate and 30% acetonitrile (flow at 3 mL.min<sup>-1</sup>) as the mobile phase.

### 1.3.2. Western Blot

#### 1.3.2.1. Preparation of the tissue lysate

The tissue was homogenized in enough volume of RIPA lysis buffer using an Ultra-Turrax®. The resulting suspension was transferred into a reaction tube and protease inhibitor was added. The tube was gently shaken at 4 °C for 30 min and afterwards centrifuged at 4 °C for 20 min (12000 rpm). The pellet was discarded and the supernatant aliquoted and stored at -80 °C. The total protein concentration of the lysate was measured reading the absorbance at 562 nm, following the instructions of the BCA kit.

#### 1.3.2.2. Gel electrophoresis and western blot

Lysate samples were diluted with Laemmli buffer and heated to 95 °C for 5 min. 20 µg protein per well were loaded onto the gel and gel electrophoresis was performed at 200 V for 28 min using conventional page buffer (25 mM tris base, 193 mM glycine and 3.5 mM SDS). Semi-dry transfer to nitrocellulose blotting membrane was performed at 80 mA per gel for 1 h. Membranes were blocked for 1 h at room temperature using 5% dry milk powder in TBS-T (tris buffered saline containing 0.1% Tween-20). Incubation with primary antibody (rabbit monoclonal anti-PBR, 1:10,000) was performed for 2 h at room temperature. After washing the membrane three times with TBS-T, incubation with secondary antibody (goat anti rabbit IgG, HRP- conjugate, 1:2500) was conducted under the same conditions. Detection was performed using the dedicated chemiluminescent kit.

### 1.3.3. Genotyping

Venous blood (≈2 mL) was obtained from healthy volunteers in EDTA-containing tubes. Genomic DNA (gDNA) was extracted from blood, the HT-29 cells and the colon cancer tissue using the PureLink Genomic DNA Kit, according to the instructions manual. Subsequently, the gDNA concentration (A<sub>260</sub>) and purity (A<sub>260</sub>/A<sub>280</sub>) was determined by means of NanoDrop® spectrophotometry. 20 ng of the gDNA were placed in a 96-well fast plate



and dried. Subsequently, 10  $\mu$ L of a 50/5/45 v/v mixture, containing the Taqman<sup>®</sup> Master Mix (2X), the Taqman<sup>®</sup> Assay (20X) and nuclease-free water, were added. After centrifugation, to spin down the contents and to eliminate the air bubbles from the plate, the PCR was performed using the thermal cycling conditions specified in the table 1. A final post-PCR fluorescence-read revealed the corresponding genotype: homozygous for one of the alleles (HAB or LAB) or heterozygous (MAB).

Table 1. Thermal conditions for PCR

Step	Temperature (°C)	Duration (s)	Cycles
<b>AmpliTaqGold<sup>®</sup>, UP, Enzyme activation</b>	95	600	HOLD
<b>Denaturation</b>	95	15	40
<b>Annealing / Extension</b>	60	60	40

#### 1.3.4. Binding affinity profile

The affinity of FEPPA was determined in a TSPO-expressing membrane binding protocol, according to Owen et al.<sup>3</sup> The membranes were prepared following already described procedures.<sup>4</sup> In detail, venous blood ( $\approx$ 80 mL) was obtained in EDTA-containing tubes from previously genotyped healthy volunteers, i.e. the volunteers were identified as HAB, MAB and LAB. The whole blood was centrifuged at room temperature for 15 min (180 g). The resulting platelet-rich plasma was re-centrifuged at room temperature for 15 min (1800 g), to obtain a platelet pellet. Subsequently, the pellet was homogenized with buffer 1 (0.32 mM sucrose, 5 mM tris base, 1 mM MgCl<sub>2</sub>, pH 7.4, 4 °C). Homogenates were centrifuged at 4 °C for 15 min (48000 g), followed by removal of the supernatant. The pellet was re-homogenized in 10 times w/v buffer 2 (50 mM tris base, 1 mM MgCl<sub>2</sub>, pH 7.4, 4 °C) and re-centrifuged two times under the same conditions, with an intermediate resuspension step with buffer 2. The resulting membrane was mixed with approximately 4 mL of buffer 2 and aliquots were stored at -80 °C until use. The total protein concentration of the membrane was measured reading the absorbance at 562 nm, following the instructions manual of the BCA kit.

The competitive binding experiments were performed in test tubes, filled with 250  $\mu$ L of non-radioactive reference compound (FEPPA) dissolved in assay buffer (50 mM tris base, 140 mM NaCl, 1.5 mM MgCl<sub>2</sub>, 5 mM KCl, 1.5 mM CaCl<sub>2</sub>, pH 7.4, 37 °C, 2% DMSO), 200  $\mu$ L of the membrane suspension (250  $\mu$ g.mL<sup>-1</sup>) and 50  $\mu$ L of a 10 nM [<sup>3</sup>H]PK11195 solution. For determining non-specific binding, 20  $\mu$ M PK11195 was used; and for total binding, only [<sup>3</sup>H]PK11195 and membrane suspension were incubated. All dilutions were performed in assay buffer, whereby the final concentration of DMSO never exceeded 1%. After incubation time, binding was quenched with ice cold wash buffer (50 mM tris base, 1.4 mM MgCl<sub>2</sub>, pH 7.4, 4 °C) and membrane bound radioactivity was recovered by rapid filtration through GF/B glass fiber filters presoaked in assay buffer containing 0.05% polyethylene imine. Filters were washed 3 times with 1 mL wash buffer and transferred into  $\beta$ -counting vials. 4 mL of  $\beta$ -scintillation cocktail were added and finally the tubes were counted. Data from the competition plots

(from three independent experiments, performed in triplicate) were analyzed and successively IC<sub>50</sub> and K<sub>i</sub> values were calculated using a dissociation constant of 29.25 nM for [<sup>3</sup>H]PK11195 and GraphPad Prism<sup>®</sup> software.

### 1.3.5. Real-time kinetics

#### 1.3.5.1. Cell Culture

Human colorectal adenocarcinoma cell line, HT-29 were purchased from ATCC (Manassas, USA) and were grown and maintained at 37 °C and 5% CO<sub>2</sub> in a cell incubator. HT-29 cells were cultivated using RPMI medium supplemented with 10% fetal bovine serum (FBS), 2 mM L-glutamine and 10 µg.mL<sup>-1</sup> gentamicin sulfate. 1x10<sup>6</sup> cells were seeded in a 100/20 mm cell culture dish two days prior to the experiment. The cell culture dishes were slightly tilted and the cells were incubated for 24 h in this position to allow adherence at only one side of the petri dish (Figure 1a). On the next day, the medium was discarded and the dishes were evenly incubated in 10 mL medium to obtain a confluent cell layer (Figure 1b).

#### 1.3.5.2. Real-time kinetics measurements

Real-time kinetics measurements were performed using a LigandTracer<sup>®</sup> Yellow device (Figure 1c). First, a background measurement was performed for 5 min. Growth medium was replaced by 2 mL of supplement-free medium and the dishes were placed in the LigandTracer<sup>®</sup> device. Taking into account the molar radioactivity of the [<sup>18</sup>F]FEPPA batches, a small volume of the freshly prepared radiotracer was added to the cells, to reach a final concentration of 15 – 30 nM. After the equilibrium was reached, the measurement was paused and 1 µL of a solution of non-labeled TSPO ligand (FEPPA, PK11195 or PBR28) in DMSO was added and the measurement was re-started (final concentration of TSPO ligand 1.5 µM, DMSO content never exceeded 0.5%).<sup>5</sup>

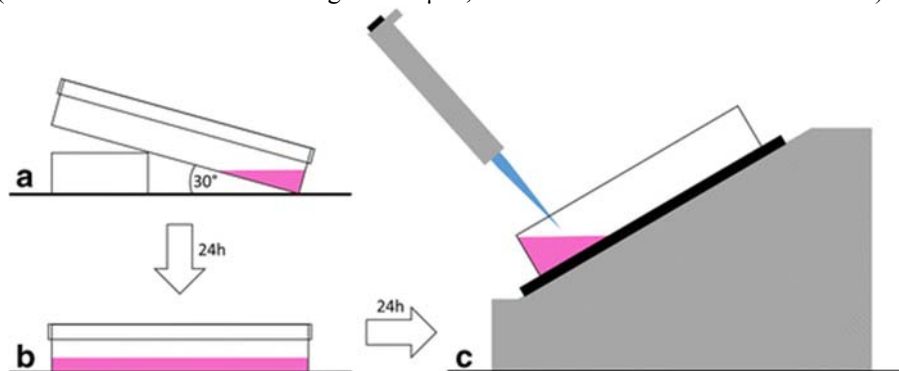


Figure 1. Cultivation of cells for real-time kinetics measurements (Adapted from Zeitlinger et al)<sup>5</sup>

### 1.3.6. Immunohistochemistry and autoradiography

#### 1.3.6.1. Tissue preparation

Healthy mucosa and tumor tissues were obtained directly after tumorectomy from the Department of Surgery at the Medical University Vienna and quickly frozen in 2-methylbutane at -40 °C and subsequently stored at -80 °C until further processing. Tissue blocks were thawed within 12 h to -20 °C and cut using a microcryotome into 10 µm thick slices. Slices were mounted onto positively charged glass slides and stored at -80 °C until use.

#### 1.3.6.2. Immunohistochemistry

Cryoslices were fixed in 96% ethanol for 10 min at room temperature. Permeabilization was performed with 0.2% Triton X-100 in PBS for 5 min. Tissue slices were surrounded with a Barrier-Pen and endogenous peroxidases were blocked by incubating the slices with 2 drops of Bloxall™ blocking solution for 10 min in a humid, dark chamber. Endogenous avidin and biotin were blocked using the dedicated kit, following the instructions of the user manual. Additionally, slices were incubated for 20 min with goat serum (1:10, PBS) to reduce non-specific binding. Primary antibody incubation was performed for 1 h in a humid, dark chamber (1:100; 0.1% BSA in PBS). Purified rabbit IgG was used as an isotype control. Slices were washed with PBS containing 0.1% Tween-20 and incubated for 30 min under same conditions with a biotinylated anti-rabbit IgG antibody provided by the Vectastain® kit (1:200, 5% goat serum in PBS). Subsequently, slices were washed three times for 5 min at room temperature using 0.1% Tween-20 in PBS. The preparation of the avidin/biotin-complex solution, provided by the Vectastain® ABC kit, was prepared and used according to the manufacturer's instructions. After filtered a washing step, a freshly prepared 1:50 dilution of DAB reagent was incubated for 1 minute and the following washing step was achieved with tap water. Haematoxylin (1:7, deionized water) was filtrated onto the slices and incubated for 3 min. Development of the staining was accomplished in tap water. Slices were dehydrated using increasing concentrations of ethanol and n-butyl acetate. Finally, the slides were embedded in Histofluid® mounting medium and ulteriorly scanned.

#### 1.3.6.3. Autoradiography

Tissue sections were allowed to thaw to room temperature until disappearing of condense water residues and pre-incubated with assay buffer (50 mM tris-HCl in deionized water, pH 7.4) at room temperature for 30 min in a Coplin jar. After careful removal of buffer, tissue slices were promptly incubated for 60 min with 100 µL of the freshly prepared radioligand [<sup>18</sup>F]FEPPA in assay buffer (≈50 kBq per slice). For blocking experiments, non-labeled FEPPA and PBR28 were co-incubated at different concentrations. After the incubation time, the radioactive solution was cautiously discarded and the slides were washed twice for 5 min in a jar with ice-cold assay buffer, then with water and ultimately dried under an air stream and exposed to a phosphor screen until the next day. Tracer uptake was expressed as fmol of FEPPA.mm<sup>-2</sup> of tissue.

#### 1.4. Statistical analysis

Quantitative data are reported as arithmetic mean ± standard deviation. For the determination of significance, a Tukey's multiple comparison test ( $\alpha=0.99$ ) was performed using GraphPad Prism® software.

## 2. Results

### 2.1. Preparative HPLC purification

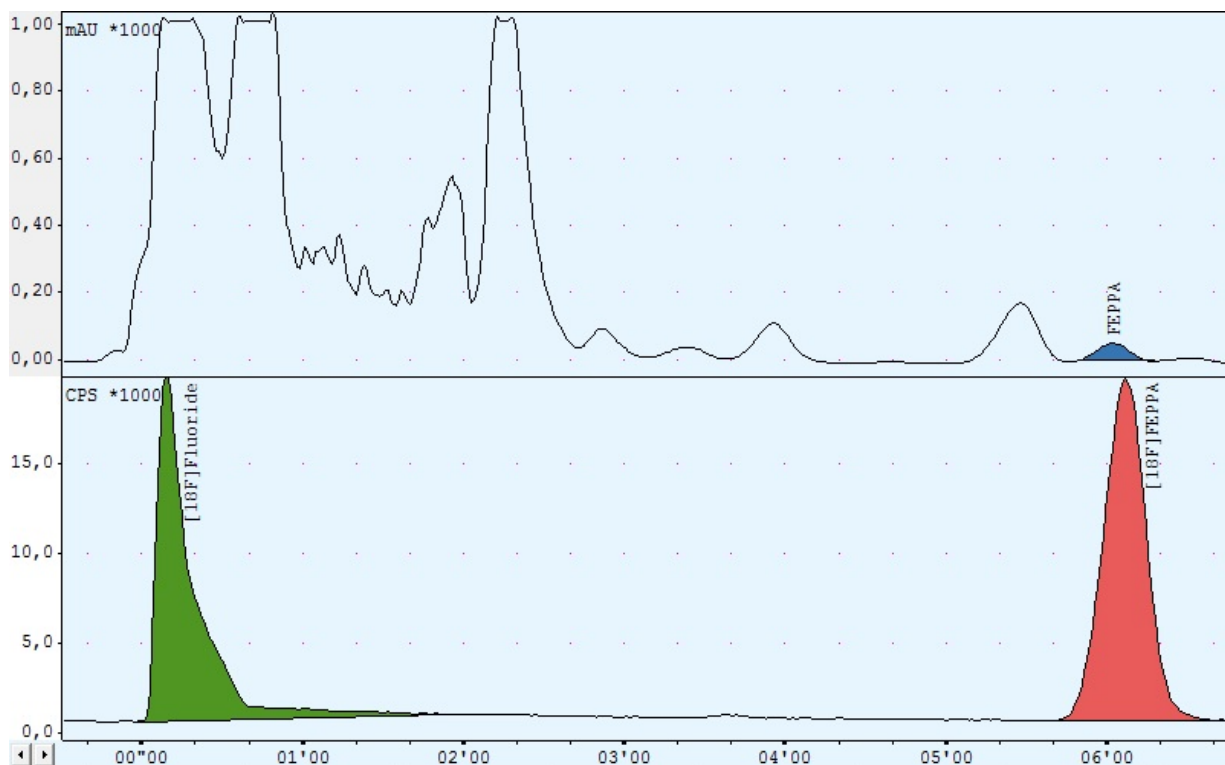


Figure 2. Representative preparative chromatogram for  $[^{18}\text{F}]$ FEPPA purification

### 2.2. Quality control

Table 2. Quality control assessment of  $[^{18}\text{F}]$ FEPPA

Test	Acceptance criteria	Result
Vial contents	Clear, colorless, particle free	Pass
pH	4.5 – 8.5	7.5
Radiochemical purity	$\geq 95\%$	$\geq 99\%$
Chemical (non-radioactive) impurities detected by HPLC (UV channel)	$< 1\%$	$< 0.1\%$
Radionuclidic purity	Half-life: $(109 \pm 10)$ min	$(112 \pm 5)$ min
	$\gamma$ -Spectrum: 511 keV	$(505 \pm 4)$ keV
Ethanol content	$\leq 100000$ ppm	$\leq 85000$ ppm
Acetonitrile content	$\leq 400$ ppm	$\leq 214$ ppm
Kryptofix content	$\leq 50 \mu\text{g.mL}^{-1}$	$\leq 20 \mu\text{g.mL}^{-1}$

A typical analytical chromatogram is shown in Figure 3. In order to determine the amount of cold FEPPA present in the radiotracer formulation, FEPPA standards were injected in the analytical HPLC using the same conditions for the quality control of [ $^{18}\text{F}$ ]FEPPA. Accordingly, a calibration curve was prepared to calculate the corresponding amount.

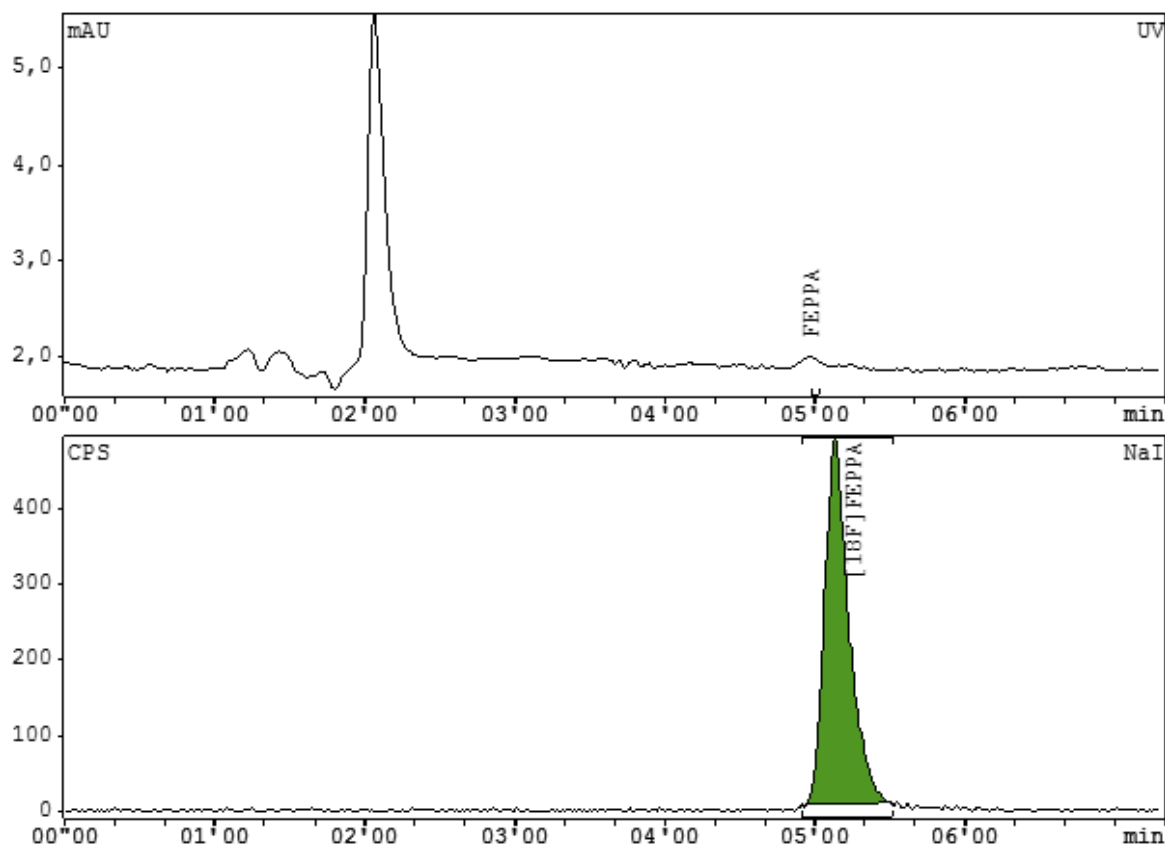


Figure 3. Representative analytical HPLC chromatogram

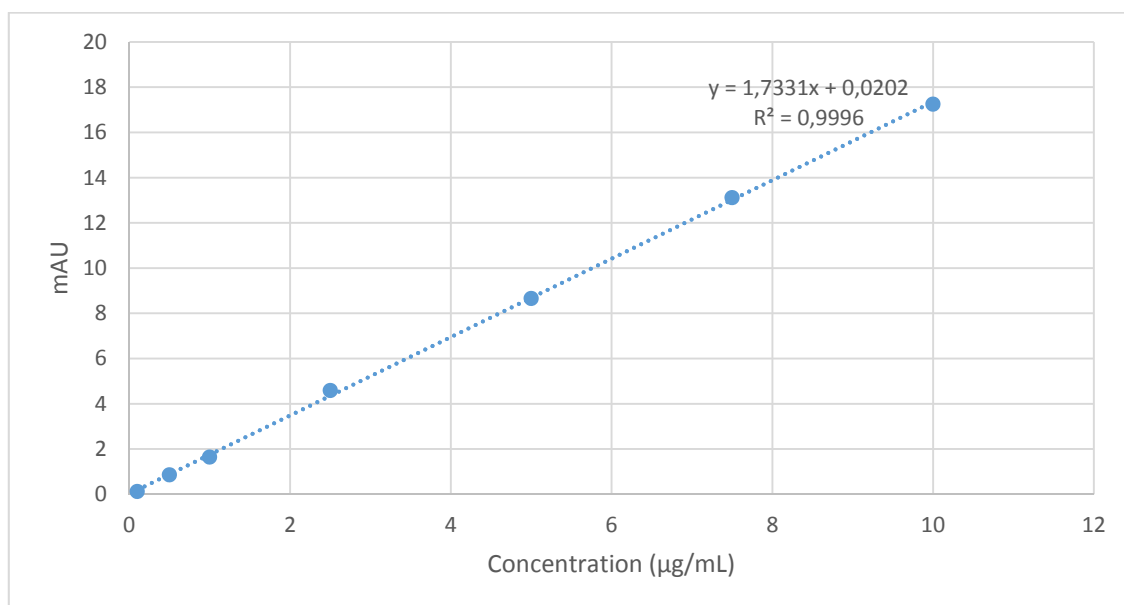


Figure 4. Calibration curve of FEPPA

### 2.3. Genotyping

A typical allelic discrimination plot is shown in Figure 5. Three different clusters can be observed, representing the three different genotypes: homozygous (red; Allele 1/Allele 1; Thr147Thr; LAB); homozygous (blue; Allele 2/Allele 2; Ala147Ala) and heterozygous (green; Allele 1/Allele 2; Ala147Thr; MAB).

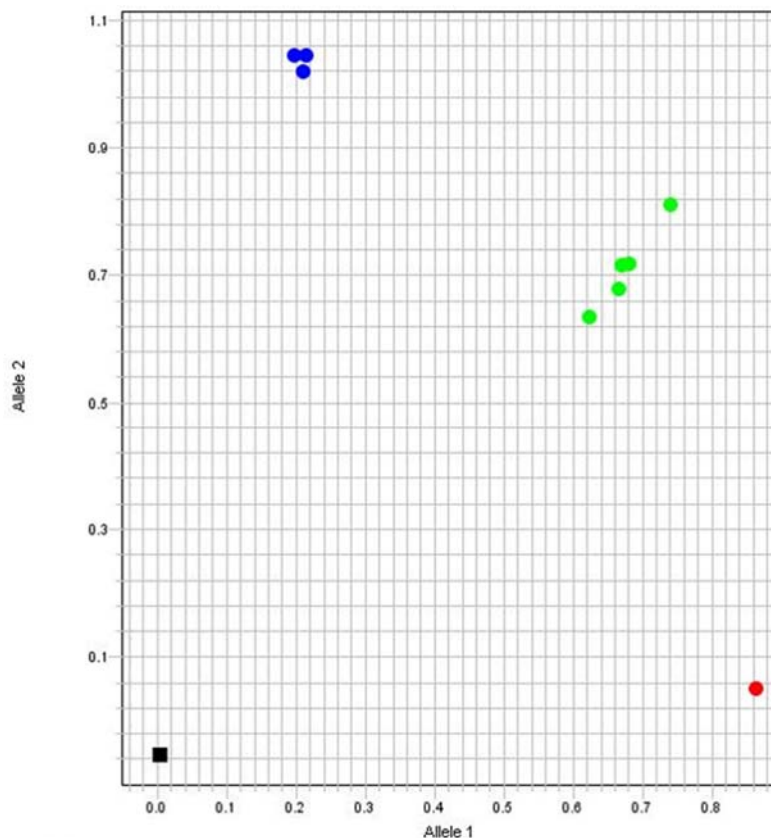


Figure 5. Allelic discrimination plot

### 2.4. Real-time kinetics

In Figure 6, a vehicle control indicates no effect in the signal after the addition of DMSO.

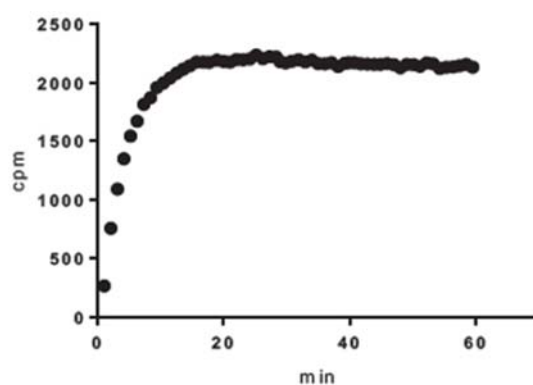


Figure 6. Vehicle controls in real-time kinetics measurements

### 3. References

- (1) Wilson, A. A.; Garcia, A.; Parkes, J.; McCormick, P.; Stephenson, K. A.; Houle, S.; Vasdev, N. Radiosynthesis and Initial Evaluation of [18F]-FEPPA for PET Imaging of Peripheral Benzodiazepine Receptors. *Nucl. Med. Biol.* **2008**, *35* (3), 305–314.
- (2) Vasdev, N.; Green, D. E.; Vines, D. C.; McLarty, K.; McCormick, P. N.; Moran, M. D.; Houle, S.; Wilson, A. A.; Reilly, R. M. Positron-Emission Tomography Imaging of the TSPO with [18F]FEPPA in a Preclinical Breast Cancer Model. *Cancer Biother. Radiopharm.* **2013**, *28* (3), 254–259.
- (3) Owen, D. R. J.; Gunn, R. N.; Rabiner, E. A.; Bennacef, I.; Fujita, M.; Kreisl, W. C.; Innis, R. B.; Pike, V. W.; Reynolds, R.; Matthews, P. M.; Parker, C. A. Mixed-Affinity Binding in Humans with 18-KDa Translocator Protein Ligands. *J. Nucl. Med.* **2011**, *52* (1), 24–32.
- (4) Owen, D. R.; Yeo, A. J.; Gunn, R. N.; Song, K.; Wadsworth, G.; Lewis, A.; Rhodes, C.; Pulford, D. J.; Bennacef, I.; Parker, C. A.; StJean, P. L.; Cardon, L. R.; Mooser, V. E.; Matthews, P. M.; Rabiner, E. A.; Rubio, J. P. An 18-KDa Translocator Protein (TSPO) Polymorphism Explains Differences in Binding Affinity of the PET Radioligand PBR28. *J. Cereb. Blood Flow Metab.* **2012**, *32* (1), 1–5.
- (5) Zeilinger, M.; Pichler, F.; Nics, L.; Wadsak, W.; Spreitzer, H.; Hacker, M.; Mitterhauser, M. New Approaches for the Reliable in Vitro Assessment of Binding Affinity Based on High-Resolution Real-Time Data Acquisition of Radioligand-Receptor Binding Kinetics. *EJNMMI Res.* **2017**, *7*, 22.
- (6) Mizrahi, R.; Rusjan, P. M.; Kennedy, J.; Pollock, B.; Mulsant, B.; Suridjan, I.; De Luca, V.; Wilson, A. A.; Houle, S. Translocator Protein (18 KDa) Polymorphism (Rs6971) Explains in-Vivo Brain Binding Affinity of the PET Radioligand [18F]-FEPPA. *J. Cereb. Blood Flow Metab.* **2012**, *32* (6), 968–972.





## 3.4 Manuscript #4

**Title:** SNAPshots of the MCHR1: a Comparison Between the PET-Tracers [ $^{18}\text{F}$ ]FE@SNAP and [ $^{11}\text{C}$ ]SNAP-7941

**Authors:** Cécile Philippe, Markus Zeilinger, Monika Dumanic, Florian Pichler, Lukas Fetty, Chrysoula Vraka, **Theresa Balber**, Wolfgang Wadsak, Katharina Pallitsch, Helmut Spreitzer, Rupert Lanzenberger, Marcus Hacker and Markus Mitterhauser

**Associated Content:** None DOI: 10.1007/s11307-018-1212-0

**Rationale and Aim:** The development of a successful PET-tracer for the MCHR1 emerged as a central research objective in our group for several reasons: The involvement of the melanin-concentrating hormone system in the central control of appetite and food intake, which is fundamental to the most prevalent metabolic disorders – obesity and diabetes –, makes the MCHR1 a target worth to image. Moreover, molecular imaging quantifying MCHR1 expression *in vivo* would significantly enhance the knowledge about MCH neurotransmission.


Our imaging strategy was based on the selection of the MCHR1 antagonist SNAP-7941 for radio-labeling. (163) Accordingly, [ $^{11}\text{C}$ ]SNAP-7941 was presented as the first PET-tracer for MCHR1 imaging. (166, 170) Due to the short half-life of carbon-11, a radio-fluorinated PET-tracer was developed. Modification of SNAP-7941 yielded the fluoro-ethyl derivative FE@SNAP and [ $^{18}\text{F}$ ]FE@SNAP was proposed as an alternative PET-tracer later on. (165, 171) First preclinical testing revealed promising results regarding a potential application in neuro-imaging though preliminary data do not yet permit the decision upon the selection of the optimum tracer.

The overall goal is the application of MCHR1 PET for human use. This manuscript provides a detailed *in vitro* and *in vivo* evaluation of the MCHR1 PET-tracers [ $^{18}\text{F}$ ]FE@SNAP and [ $^{11}\text{C}$ ]SNAP-7941 in order to identify the adequate tracer for future human use. The two MCHR1 PET tracers were thus compared with regard to affinity, selectivity, metabolic stability and suitability for subsequent PET imaging.



## RESEARCH ARTICLE

# SNAPshots of the MCHR1: a Comparison Between the PET-Tracers [ $^{18}\text{F}$ ]FE@SNAP and [ $^{11}\text{C}$ ]SNAP-7941

Cécile Philippe,<sup>1,2</sup> Markus Zeilinger,<sup>1,3</sup> Monika Dumanic,<sup>1</sup> Florian Pichler,<sup>1,3</sup> Lukas Fetty,<sup>1,4</sup> Chrysoula Vraka,<sup>1</sup> Theresa Balber,<sup>1</sup> Wolfgang Wadsak,<sup>1,5,6</sup> Katharina Pallitsch,<sup>7</sup> Helmut Spreitzer,<sup>8</sup> Rupert Lanzenberger,<sup>9</sup> Marcus Hacker,<sup>1</sup> Markus Mitterhauser<sup>1,2,10</sup> 

<sup>1</sup>Department of Biomedical Imaging and Image-guided Therapy, Division of Nuclear Medicine, Medical University of Vienna, Waehringer Guertel 18-20, 1090, Vienna, Austria

<sup>2</sup>Department of Pharmaceutical Technology and Biopharmaceutics, University of Vienna, Vienna, Austria

<sup>3</sup>Faculty of Engineering, University of Applied Sciences Wiener Neustadt, Neustadt, Austria

<sup>4</sup>Department of Radiotherapy, Division of Medical Physics, Medical University of Vienna, Vienna, Austria

<sup>5</sup>Department of Inorganic Chemistry, University of Vienna, Vienna, Austria

<sup>6</sup>CBmed, Graz, Austria

<sup>7</sup>Department of Organic Chemistry, University of Vienna, Vienna, Austria

<sup>8</sup>Department of Pharmaceutical Chemistry, University of Vienna, Vienna, Austria

<sup>9</sup>Department of Psychiatry and Psychotherapy, Medical University of Vienna, Vienna, Austria

<sup>10</sup>Ludwig Boltzmann Institute Applied Diagnostics, Vienna, Austria

### Abstract

**Purpose:** The melanin-concentrating hormone receptor 1 (MCHR1) has become an important pharmacological target, since it may be involved in various diseases, such as diabetes, insulin resistance, and obesity. Hence, a suitable positron emission tomography radiotracer for the *in vivo* assessment of the MCHR1 pharmacology is imperative. The current paper contrasts the extensive *in vitro*, *in vivo*, and *ex vivo* assessments of the radiotracers [ $^{18}\text{F}$ ]FE@SNAP and [ $^{11}\text{C}$ ]SNAP-7941 and provides comprehensive information about their biological and physico-chemical properties. Furthermore, it examines their suitability for first-in-man imaging studies.

**Procedures:** Kinetic real-time cell-binding studies with [ $^{18}\text{F}$ ]FE@SNAP and [ $^{11}\text{C}$ ]SNAP-7941 were conducted on adherent Chinese hamster ovary (CHO-K1) cells stably expressing the human MCHR1 and MCHR2. Small animal imaging studies on mice and rats were performed under displacement and baseline conditions, as well as after pretreatment with the P-glycoprotein/breast cancer resistant protein inhibitor tariquidar. After the imaging studies, detailed analyses of the *ex vivo* biodistribution were performed. *Ex vivo* metabolism was determined in rat blood and brain and analyzed at various time points using a quantitative radio-HPLC assay.

Cécile Philippe and Markus Zeilinger contributed equally to this work.

Correspondence to: Markus Mitterhauser; e-mail: markus.mitterhauser@meduniwien.ac.at

Published online: 13 June 2018

**Results:** [<sup>11</sup>C]SNAP-7941 demonstrates high uptake on CHO-K1-hMCHR1 cells, whereas no uptake was detected for the CHO-K1-hMCHR2 cells. In contrast, [<sup>18</sup>F]FE@SNAP evinced binding to CHO-K1-hMCHR1 and CHO-K1-hMCHR2 cells. Imaging studies with [<sup>18</sup>F]FE@SNAP and [<sup>11</sup>C]SNAP-7941 showed an increased brain uptake after tariquidar pretreatment in mice, as well as in rats, and exhibited a significant difference between the time-activity curves of the baseline and blocking groups. Biodistribution of both tracers demonstrated a decreased uptake after displacement. [<sup>11</sup>C]SNAP-7941 revealed a high metabolic stability in rats, whereas [<sup>18</sup>F]FE@SNAP was rapidly metabolized.

**Conclusions:** Both radiotracers demonstrate appropriate imaging properties for the MCHR1. However, the pronounced metabolic stability as well as superior selectivity and affinity of [<sup>11</sup>C]SNAP-7941 underlines the decisive superiority over [<sup>18</sup>F]FE@SNAP.

**Key Words:** [<sup>11</sup>C]SNAP-7941, [<sup>18</sup>F]FE@SNAP, MCHR1, PET, Small animal imaging, *In vitro*, *In vivo*, *Ex vivo*

## Introduction

The mammalian melanin-concentrating hormone (MCH), a cyclic 19 amino acid long polypeptide, is primarily produced by neurons in the lateral hypothalamic area (LHA), the incerto-hypothalamic area (IH<sub>y</sub>), and zona incerta (ZI) [1]. Furthermore, the MCH is also expressed in peripheral organs and tissues, such as the β-cells of the pancreas [2], colonic epithelial cells [3], or adipocytes [4, 5]. The biological function of MCH is mediated by two G-protein coupled receptors (GPCRs): MCH receptor 1 (MCHR1) [6–9] and MCH receptor 2 (MCHR2) [10–13]. The latter has only been found functional in primates, dogs, ferrets, and humans [10, 11]. MCH is playing a key role in the up- and down-regulation of energy homeostasis and body weight. Moreover, MCH/MCHR1 is considered to be involved not only in a variety of pathologies, such as diabetes, insulin resistance, gut inflammation, colitis, and obesity [14–21], but also in a variety of psychiatric disorders, such as depression and anxiety [22]. Furthermore, the MCHR1 is also expressed in the ependymal cells of the ventricular system [23–25], where it acts as an important regulator of cerebrospinal fluid (CSF) flow and cilia beat frequency. As observed in MCHR1 knockout mice, a lack of MCHR1 provokes an increase in ventricular size and could eventually lead to a hydrocephalus [23, 24]. Due to its involvement in a plethora of classical lifestyle diseases, MCHR1 has become a very interesting pharmacological target for clinical medicine, as well as for biomedical research [6–9]. Considering the expression of MCH and MCHR1, the ventricular system, LHA, IH<sub>y</sub>, ZI, adipose tissue, lung, pancreas, spleen, colon, eyes, as well as muscle tissue are considered primary target regions [2, 3, 6, 11, 23, 24, 26–28]. In the last decade, several MCHR1 antagonists were presented; some have entered clinical trials for the treatment of obesity [29] or are discussed to become anti-diabetic drugs [30]. For quantitative *in vivo* assessment of the MCHR1, a suitable positron emission tomography (PET) tracer is indispensable. A PET tracer would also facilitate preclinical to clinical translation. The specific MCHR1

antagonist SNAP-7941 ((+)-methyl(4S)-3-{[(3-{4-[3-(acetylamino)phenyl]-1-piperidinyl}propyl)amino]carbonyl}-4-(3,4-difluorophenyl)-6-(methoxymethyl)-2-oxo-1,2,3,4-tetrahydro-5-pyrimidenecarboxylate hydrochloride) [31] served as model for the first MCHR1 PET tracers: [<sup>11</sup>C]SNAP-7941 (Fig. 1a), which is the radiolabeled analog of SNAP-7941 and [<sup>18</sup>F]FE@SNAP, a [<sup>18</sup>F]fluoroethylated derivative (Fig. 1b) [32–38].

The current paper contrasts novel and previously attained *in vitro*, *in vivo*, and *ex vivo* assessments of [<sup>11</sup>C]SNAP-7941 and [<sup>18</sup>F]FE@SNAP to determine the superior radioligand with respect to its biological and physicochemical properties. A comprehensive illustration of the applied *in vitro*, *in vivo*, and *ex vivo* experiments is shown in Fig. 1c.

## Materials and Methods

### Chemical Compounds

The racemic mixture of SNAP-7941 ((±)-SNAP-7941), the fluoroethylated analog (±)-(2-fluoroethyl)-3-{[(3-{4-[3-(acetylamino)phenyl]-1-piperidinyl}propyl)amin]carbonyl}-4-(3,4-difluorophenyl)-6-(methoxymethyl)-2-oxo-1,2,3,4-tetrahydro-5-pyrimidenecarboxylate (FE@SNAP), as well as the precursor compounds (±)-3-{[(3-{4-[3-(acetylamino)phenyl]-1-piperidinyl}propyl)amino]carbonyl}-4-(3,4-difluorophenyl)-6-(methoxymethyl)-2-oxo-1,2,3,4-tetrahydro-5-pyrimidenecarboxylate acid (SNAP-acid), and (±)-2-(tosyloxy)ethyl-3-{[(3-{4-[3-(acetylamino)phenyl]-1-piperidinyl}propyl)amino]carbonyl}-4-(3,4-difluorophenyl)-6-(methoxymethyl)-2-oxo-1,2,3,4-tetrahydro-5-pyrimidenecarboxylate acid (Tos@SNAP) were provided by the Department of Pharmaceutical Chemistry and the Department Organic Chemistry of the University of Vienna (Vienna, Austria) [33]. Tariquidar methanesulfonate (TQD) was purchased from MedChem Express (Princeton, NJ, USA). All other chemicals were purchased from commercial sources and used without further purification.

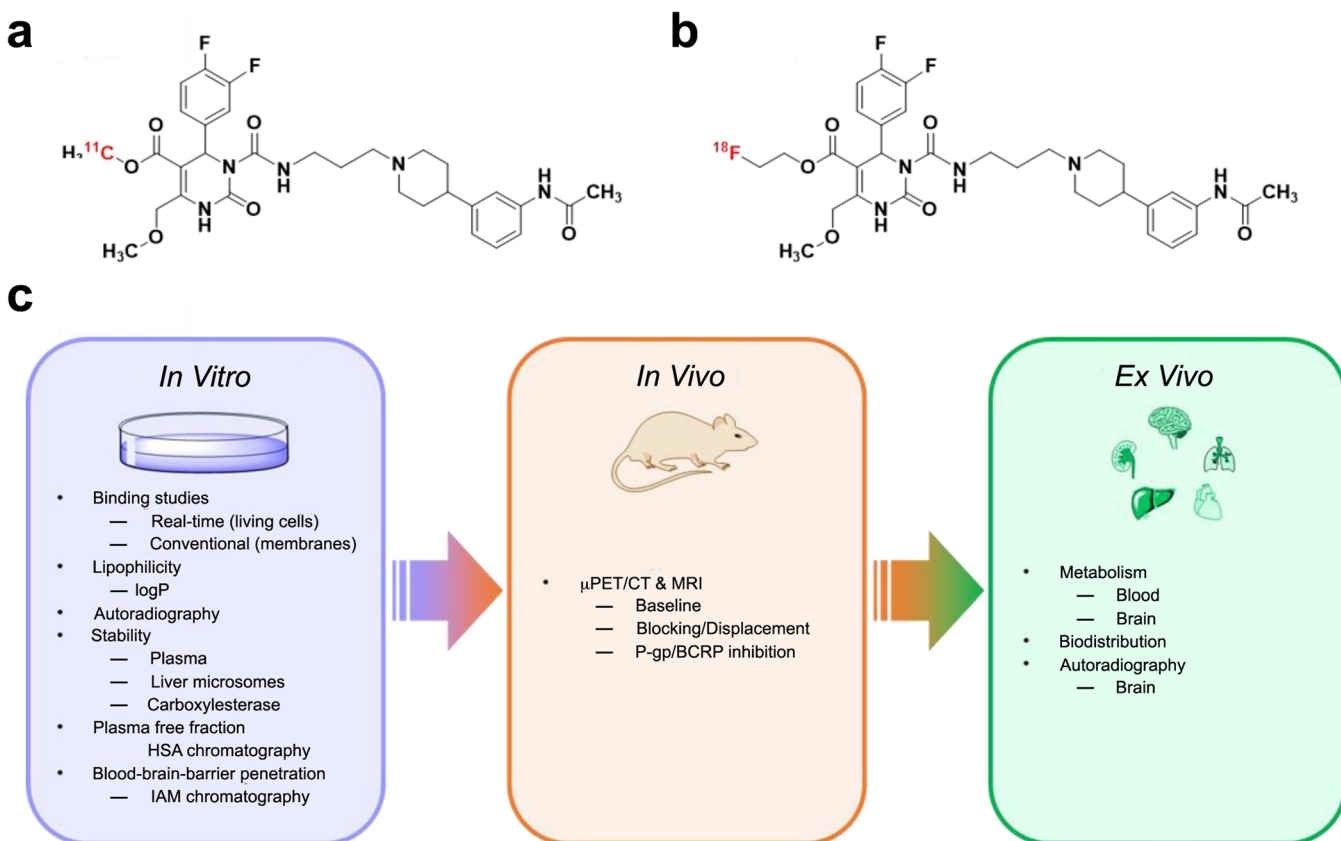


**Fig. 1** Chemical structures of **a** [ $^{11}\text{C}$ ]SNAP-7941 and **b** [ $^{18}\text{F}$ ]FE@SNAP and **c** corresponding *in vitro*, *in vivo*, and *ex vivo* experiments. IAM: immobilized artificial membrane; HAS: human serum albumin; P-gp: P-glycoprotein; BCRP: breast cancer resistance protein.

### Tracer Preparation

The radiosynthesis of [ $^{11}\text{C}$ ]SNAP-7941, the radiolabeled analog of ( $\pm$ )-SNAP-7941, was performed in a fully automated synthesizer (TRACERlab<sup>TM</sup> FX C Pro, GE Healthcare, Germany) as previously reported [30, 33]. Radiosynthesis of [ $^{18}\text{F}$ ]FE@SNAP was performed in a microfluidic device (Advion NanoTek<sup>®</sup>, Ithaca, NY, USA) as described elsewhere [37], followed by purification in a conventional synthesizer unit (Nuclear Interface<sup>®</sup>, GE Medical Systems, Uppsala, Sweden) [36, 38]. Radiochemical purity and molar activity of [ $^{11}\text{C}$ ]SNAP-7941 and [ $^{18}\text{F}$ ]FE@SNAP were determined by analytical high-performance liquid chromatography (HPLC) (Agilent Technologies, Santa Clara, CA, USA).

### Kinetic Real-Time Cell-Binding Studies

Kinetic real-time cell-binding studies were performed on adherent Chinese hamster ovary (CHO-K1) cells (negative control) and CHO-K1 cells stably expressing the human MCHR1 or MCHR2 (PerkinElmer®; Waltham, MA, USA) with [<sup>11</sup>C]SNAP-7941 and [<sup>18</sup>F]FE@SNAP as previously reported [37]. The cells were cultured in Ham's F-12 medium (Gibco®, Life Technologies) with additives (1 %

penicillin-streptomycin-glutamine (PSG), 10 % fetal bovine serum (FBS), and 300- $\mu$ g/m Geneticin (G-418)) and incubated in a humidified 5 % CO<sub>2</sub> atmosphere at 37 °C. For the preparation of the binding experiment, approximately 10<sup>6</sup> cells were seeded as a monolayer on the bottom of a tilted cell culture dish (100 mm  $\times$  20 mm, CELLSTAR®, Greiner Bio-One) and incubated with 2-ml medium for 24 h to avoid a spreading of the cells over the whole Petri dish. In the next step, the medium was discarded and the Petri dish was placed in a horizontal position with 10-ml medium for additional 24 h. Afterwards, the binding experiment was performed at ambient temperature with LigandTracer® Yellow (Ridgeview Instruments AB, Uppsala, Sweden) using 3-ml fresh medium (Ham's F-12, serum-free). Unspecific radiotracer uptake was determined with native CHO-K1 cells. The experiments were initiated with baseline measurements for 10–15 min followed by radioligand incubation of [<sup>11</sup>C]SNAP-7941 and [<sup>18</sup>F]FE@SNAP. Binding to the seeded cells was ensured by adding different concentrations of the radiotracer (0.05–1000 nM). Association-time curves were monitored in real-time until the binding equilibrium was achieved. The observed rate constant of the association reaction ( $k_{\text{obs}}$ ) was determined using non-linear regression curve fitting algorithms implemented in GraphPad Prism 6.0 (GraphPad Software, Inc., San Diego, CA, USA), as previously reported [39, 40]. Cell survival was continuously

examined using the perimeter trace (signal vs. dish position) of the LigandTracer® 1.0.1 software (Ridgeview Instruments AB, Uppsala, Sweden).

### Plasma Protein Binding Using Bioaffinity Chromatography

The binding of ( $\pm$ )-SNAP-7941 and FE@SNAP to human serum albumin (HSA) was examined by bioaffinity chromatography according to a previously published manuscript [40]. In short, the analytes were diluted in 2-propanol and ammonium acetate buffer (0.5 mg/ml) and injected on the CHIRALPAK®HSA stationary phase ( $50 \times 3$  mm, 5  $\mu\text{m}$  pore size, column-batch: H13L-2405, Daicel Chemical Industries, West Chester, PA, USA). Prior the experiments, the column was calibrated with reference standards, and the resulting regression equation was used to convert the logarithmic capacity factors ( $\log(k')$ ) to the percent of plasma protein binding (%PPB). The calibration curves, as well as the experiments, were performed by triplicate injections and at least three times.

### Animals

Ten-week-old male rats ( $412 \pm 58$  g, Sprague-Dawley, HIM:OFA,  $n=30$ ) and 12-week-old male mice ( $24 \pm 6$  g, BALB/cAnNRj,  $n=7$ ) were purchased from the Division of Laboratory Animal Science and Genetics, Himberg, Austria. Animals were kept under conventional housing conditions ( $22 \pm 1$  °C; 40–70 % humidity) with food and water supply *ad libitum* and 12-h day/night cycle. All animals were treated according to the European Union rules on animal care and respective animal experiments were approved by the Austrian Ministry of Sciences, Research and Economy (BMWFW-66.009/0029-WF/V/3b/20159). For *in vivo* imaging, animals were anesthetized using 1.5–2 % isoflurane mixed with oxygen (1.5–2 l/min) to avoid movement during the examination. Anesthesia as well as vital parameters were monitored during the time interval of PET acquisition. Radioligands and non-labeled compounds were administered intravenously *via* the lateral tail vein.

### Small Animal Imaging

Anesthetized rats and mice were immobilized in a multimodal animal carrier unit (MACU; medres®—medical research GmbH, Cologne, Germany). The body temperature was preserved at 37 °C throughout the whole experiment. Rats received either [ $^{11}\text{C}$ ]SNAP-7941 or [ $^{18}\text{F}$ ]FE@SNAP, followed by an injection of ( $\pm$ )-SNAP-7941 (15-mg/kg body weight; displacement study;  $n=4$  for each radiotracer) or the respective solvent serving as the vehicle (baseline condition;  $n=4$  for each radiotracer). The MCHR1 antagonist, ( $\pm$ )-SNAP-7941, and the vehicle were administered either 15

([ $^{11}\text{C}$ ]SNAP-7941) or 20 min ([ $^{18}\text{F}$ ]FE@SNAP) after the radiotracer application *via* the lateral tail vein. To investigate a potential binding to the P-glycoprotein (P-gp) and/or breast cancer resistance protein (BCRP) brain efflux transporter system, rats as well as mice were pretreated either with the P-gp/BCRP inhibitor TQD (15 mg/kg body weight; P-gp/BCRP inhibition group; rats:  $n=4$  for each radiotracer; mice:  $n=4$  for [ $^{18}\text{F}$ ]FE@SNAP) or the respective solvent (baseline condition; rats:  $n=3$  for each radiotracer; mice:  $n=3$  for [ $^{18}\text{F}$ ]FE@SNAP)). Mice received the P-gp/BCRP inhibitor 30 min and rats 60 min before the radiotracer application. Experiments were initiated with a 7-min cone beam attenuation CT (CBCT) of the brain (full rotation, 360 projections; binning  $4 \times 4$ ; 80 kV; 500  $\mu\text{A}$ ; 200-ms exposure time) using a small animal cone beam computed tomography (CBCT) scanner (Siemens Inveon microSPECT/CT, Siemens Medical Solutions, Knoxville, USA). Subsequently, the animals were positioned in the Siemens Inveon microPET scanner (Siemens Medical Solution, Knoxville, USA). The radiotracers were injected intravenously, and dynamic PET imaging was performed for 45 min (rats) in case of [ $^{11}\text{C}$ ]SNAP-7941 ( $77.46 \pm 5.41$  MBq; molar activity  $76.66 \pm 23.58$  GBq/ $\mu\text{mol}$ ; radiochemical purity > 99 %) and 30 min (mice)—60 min (rats) for [ $^{18}\text{F}$ ]FE@SNAP ( $47.08 \pm 6.24$  MBq; molar activity  $22.18 \pm 9.72$  GBq/ $\mu\text{mol}$ ; radiochemical purity > 90 %).

### Image Reconstruction and Data Post-Processing

Image reconstruction of the CT raw data was performed with a Feldkamp algorithm using a ramp filter followed by standard rat beam-hardening correction and noise reduction (matrix size  $1024 \times 1024$ ; effective pixel size: 97.56  $\mu\text{m}$ ). All CT image data was calibrated to Hounsfield units (HU). PET list mode data were sorted into three-dimensional sinograms according to the following frame sequences, [ $^{11}\text{C}$ ]SNAP-7941:  $1 \times 3$  s,  $3 \times 2$  s,  $1 \times 6$  s,  $1 \times 15$  s,  $1 \times 35$  s,  $1 \times 145$  s,  $1 \times 270$  s,  $1 \times 285$  s,  $1 \times 165$  s,  $3 \times 30$  s,  $1 \times 120$  s,  $1 \times 240$  s,  $1 \times 420$  s,  $1 \times 900$  s and for [ $^{18}\text{F}$ ]FE@SNAP:  $1 \times 2$  s,  $1 \times 3$  s,  $1 \times 5$  s,  $3 \times 10$  s,  $1 \times 20$  s,  $1 \times 60$  s,  $1 \times 120$  s,  $4 \times 240$  s,  $4 \times 600$  s. PET image reconstruction were performed using an OSEM 3D/OP-MAP with scatter correction and a ramp filter (matrix size  $128 \times 128$ ). Image data were normalized and corrected for random events, dead time, and radioactive decay. A calibration factor was applied to convert the activity information into absolute concentration units. Multimodal image registration and data post-processing was performed using the biomedical image analysis software PMOD 3.8 (PMOD Technologies Ltd., Zurich, Switzerland) and the Inveon Research Workplace (IRW; Siemens Medical Solutions, Knoxville, USA). Volumes of interest (VOIs) were outlined on the CT images and transferred to the PET data set. Time-activity curves (TACs) were calculated, normalized to dose and weight and expressed as standardized uptake values (SUV; g/ml).



## Ex Vivo Biodistribution

After the imaging studies, the animals were sacrificed by decapitation; blood and tissues were removed and collected in tubes, weighed, and subjected to radioactivity measurements in a Gamma Counter (2480 WIZARD<sup>2</sup>, PerkinElmer, Waltham, MA, USA). Values were normalized to the applied dose, the organ, and body weight and expressed as the standardized uptake value (SUV [g/ml]).

## Ex Vivo Metabolites

For the analysis of potential radiometabolites, blood samples (50–80  $\mu\text{l}$ ) from rats were withdrawn at 10 and 45 min for [ $^{11}\text{C}$ ]SNAP-7941 and at 10, 30, and 60 min for [ $^{18}\text{F}$ ]FE@SNAP and immediately subjected to the equivalent amount of acetonitrile, homogenized, and stored on ice before processing. Additionally, [ $^{18}\text{F}$ ]FE@SNAP was administered to three rats, which were sacrificed after 45 min. Whole brains were harvested and homogenized with equivalent amounts (500–800  $\mu\text{l}$ ) of acetonitrile and 0.9 % saline solution using an ULTRA-TURRAX® (T25 basic, IKA Laboratory Equipment, Staufen, Germany). Subsequently, blood and brain were centrifuged (23,000  $\times g$ , 4 min, 4 °C; Hettich Universal 30RF, Tuttlingen, Germany), and the obtained supernatant was analyzed by an analytical HPLC equipped with a radioactivity detector (radio-HPLC) (stationary phase: Chromolith® Performance RP-18e, 100–4.6 mm; precolumn: Chromolith® Guard Cartridge RP-18e, 5–4.6 mm; Merck, Darmstadt, Germany), mobile phase: (water/acetic acid 97.5/2.5 v/v; 2.5 g/l ammonium acetate; pH 3.5)/acetonitrile 70/30 v/v; flow: 1 ml/min,  $\lambda=254$  nm). The ratio between metabolite and intact radiotracer was calculated using quantitative HPLC analysis.

## Statistical Analysis

Experimental data are expressed as mean  $\pm$  SEM of independent experiments ( $n \geq 3$ ) with different lots of radiolabeled and non-labeled compounds. Statistical testing was performed using GraphPad Prism 7.0 (GraphPad Software, Inc., San Diego, CA). Differences among groups and conditions were determined using either a two-tailed, unpaired Student's *t* test with Welch's correction or a two-tailed parametric paired *t* test. Post hoc testing for multiple comparisons was performed using either ordinary one-way ANOVA with Tukey's correction or ordinary two-way ANOVA with Sidak's correction. Values of  $P < 0.05$  were considered as statistically significant.

## Results

### Kinetic Real-Time Cell-Binding Studies

Kinetic real-time cell-binding studies were performed in a reliable manner with high temporal resolution as shown in Fig. 2. [ $^{18}\text{F}$ ]FE@SNAP and [ $^{11}\text{C}$ ]SNAP-7941 demonstrate high accumulation on CHO-K1-hMCHR1 cells, whereas negligible accumulation was detected for the native CHO-K1 cells. The observed association time courses between [ $^{18}\text{F}$ ]FE@SNAP ( $k_{\text{obs}} = 0.0859 \pm 0.0028 \text{ min}^{-1}$ ) and [ $^{11}\text{C}$ ]SNAP-7941 ( $k_{\text{obs}} = 0.0629 \pm 0.0020 \text{ min}^{-1}$ ) on CHO-K1-hMCHR1 cells showed no significant differences ( $P = 0.9$ ). High statistical significance was observed for the accumulation of both radiotracers on the native CHO-K1 cells compared to the CHO-K1-hMCHR1 cells ( $P < 0.0001$ , Fig. 2a). In contrast, a significant difference in the binding kinetics was observed for the CHO-K1-hMCHR2 cells. The observed association rate constants were significantly different for [ $^{18}\text{F}$ ]FE@SNAP ( $k_{\text{obs}} = 0.0918 \pm 0.0031 \text{ min}^{-1}$ ) compared to [ $^{11}\text{C}$ ]SNAP-7941. No significant difference in the binding pattern was determined for [ $^{11}\text{C}$ ]SNAP-7941 on the native CHO-K1 cells compared to the CHO-K1-hMCHR2 cells, which indicates negligible accumulation to these two cell lines (Fig. 2b).

### Plasma Protein Binding Using Bioaffinity Chromatography

The PPB analysis of ( $\pm$ )-SNAP-7941 resulted in  $80 \pm 0.9 \%$  ( $n > 3$ ) and  $77 \pm 0.2 \%$  ( $n = 3$ ) for FE@SNAP.

### Small Animal Imaging

[ $^{18}\text{F}$ ]FE@SNAP imaging experiments in mice showed a 1.93-fold increased brain uptake in the TQD blocking group. As illustrated in Fig. 3a, the differences between the TACs of the vehicle and blocking groups were statistically significant ( $P < 0.0001$ ). Furthermore, both radiotracers showed an increased brain uptake for the TQD blocking group in rats. Brain uptake was increased 2.45-times for [ $^{18}\text{F}$ ]FE@SNAP (Fig. 3b) and 3.04-times for [ $^{11}\text{C}$ ]SNAP-7941 (Fig. 3c), respectively. Both radiotracers exhibited a significant difference between the TACs of the vehicle and blocking groups ( $P < 0.0001$ ).

TACs of selected regions were analyzed before and after displacement with 15 mg/kg ( $\pm$ )-SNAP-7941. A clear difference in the binding pattern was observed for both tracers, [ $^{18}\text{F}$ ]FE@SNAP and [ $^{11}\text{C}$ ]SNAP-7941, for the brown adipose tissue (BAT), brain, and lung. Corresponding TACs are depicted in Fig. 4b–d. The associated blood input curve for both radiotracers is presented in Fig. 4a, showing no significant difference in the uptake behavior ( $P = 0.3117$ ). Differences in the binding profiles before and after displacement with 15 mg/kg ( $\pm$ )-SNAP-7941 in all other regions of

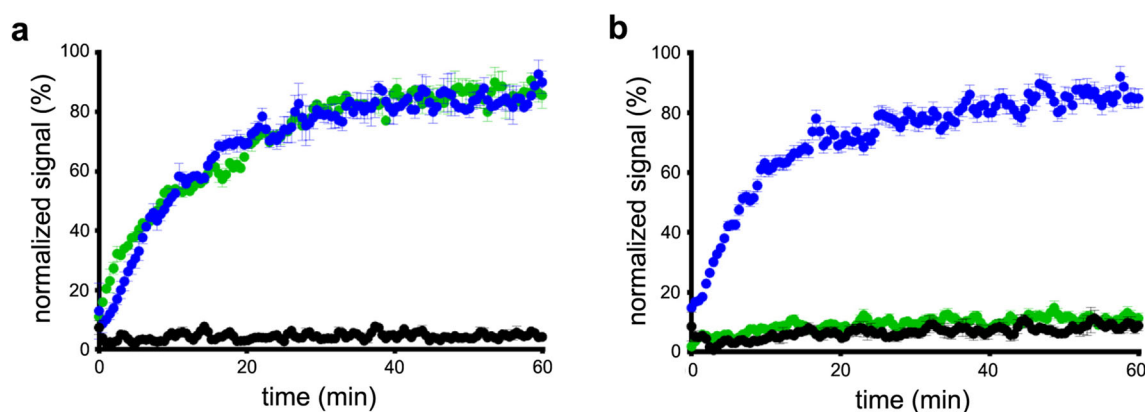


**Fig. 2** Depiction of the association kinetics of [ $^{11}\text{C}$ ]SNAP-7941 (green) and [ $^{18}\text{F}$ ]FE@SNAP (blue) on adherent **a** CHO-K1-hMCHR1 and **b** CHO-K1-hMCHR2 cells. The black curve indicates the accumulation of both tracers to native CHO-K1 cells. Data are displayed as mean  $\pm$  SEM from independent experiments ( $n \geq 3$ , each performed as a quadruplicate, 0.05–1000 nM).

interest were not statistically significant, for both [ $^{18}\text{F}$ ]FE@SNAP and [ $^{11}\text{C}$ ]SNAP-7941.

### Ex Vivo Biodistribution

The overall biodistribution for both radiotracers demonstrated a decreased uptake in the target regions after displacement with 15 mg/kg ( $\pm$ )-SNAP-7941 (Fig. 5a; [ $^{18}\text{F}$ ]FE@SNAP (blue); [ $^{11}\text{C}$ ]SNAP-7941 (green); displacement (red)). A detailed statistical analysis was performed for selected target regions (Fig. 5b–g). Statistically significant differences between the vehicle and displacement groups were determined for [ $^{11}\text{C}$ ]SNAP-7941 for the colon ( $P = 0.0175$ ; Fig. 5c), pancreas ( $P = 0.0010$ ; Fig. 5e), and eye ( $P < 0.0001$ ; Fig. 5g). In contrast, the colon showed no statistically significant difference for [ $^{18}\text{F}$ ]FE@SNAP between the vehicle and displacement groups ( $P = 0.7730$ ; Fig. 5b), whereas the pancreas ( $P = 0.0414$ ; Fig. 5d) and eye ( $P = 0.0037$ ; Fig. 5f) showed significant differences.

### Ex Vivo Metabolites

Ten minutes after the radiotracer application,  $38.40 \pm 2.3$  % of intact [ $^{18}\text{F}$ ]FE@SNAP was present in rat whole blood; at 30 min after administration,  $31.59 \pm 4.0$  % was left and  $14.42 \pm 3.3$  % at 60 min. Moreover, the formation of a radioactive hydrophilic metabolite was observed. On the contrary, [ $^{11}\text{C}$ ]SNAP-7941 evinced a high metabolic stability in rat whole blood, resulting in  $93.52 \pm 0.1$  % of intact tracer at 10 min and  $93.74 \pm 6.2$  % at 45 min (Fig. 6). The investigation of brain metabolites evinced a strong degradation of the parent compound at 45 min ( $22.37 \pm 5.8$  % of intact tracer) for [ $^{18}\text{F}$ ]FE@SNAP.

## Discussion

To quantify the biomolecular mechanisms of the MCHR1 *in vivo*, a selective PET radioligand is indispensable. Hence,

a specific MCHR1 PET-tracer would provide deeper insights on the receptor's involvement in lifestyle diseases, such as obesity and diabetes, and promote drug development for related pathologies. Nevertheless, only three PET radioligands for the visualization of the MCHR1 have been developed [32, 36, 41, 42]. This paper focuses on the first MCHR1 PET ligands, [ $^{18}\text{F}$ ]FE@SNAP and [ $^{11}\text{C}$ ]SNAP-7941, and contrasts their advantages and disadvantages. Table 1 gives an overview of the results, which are discussed in this section.

Regarding the synthesis of these two tracers, [ $^{11}\text{C}$ ]SNAP-7941 is the more reliable compound, due to its higher yields ( $2.9 \pm 1.6$  GBq vs.  $374 \pm 202$  MBq for [ $^{18}\text{F}$ ]FE@SNAP) and fewer preparation steps. Moreover, its radiosynthesis is faster (40 min) compared to [ $^{18}\text{F}$ ]FE@SNAP (100 min), which has to be synthesized *via* a microfluidic device [35, 36].

Since MCHR2 is not expressed in rodents, additional kinetic real-time cell-binding studies were performed to substantiate the target selectivity. In this context, both radiotracers demonstrated a specific accumulation profile on the CHO-K1-hMCHR1 cells and negligible accumulation on the native CHO-K1 cells (Fig. 2a). While [ $^{11}\text{C}$ ]SNAP-7941 evinced selective binding to the CHO-K1-hMCHR1 cells, which is in good agreement with previously published data [32], [ $^{18}\text{F}$ ]FE@SNAP additionally exhibited accumulation to the CHO-K1-hMCHR2 cells (Fig. 2b). This phenomenon contradicts previously elaborated findings on CHO-K1-hMCHR2 membranes [34] and might be explained by the difference in the biochemical approach (competition experiments with the unlabeled ligand vs. direct binding with the radiolabeled ligand) and the experimental setup (membranes vs. living cells). In this context, it has to be highlighted that experiments on living cells, as performed in the present study, enhance the understanding of the complex interplay between the radiotracer and the dedicated biological target [39]. Moreover, previous experiments revealed higher binding affinity for ( $\pm$ )-SNAP-7941 ( $K_i = 3.91 \pm 0.74$  nM) compared to FE@SNAP ( $K_i = 9.98 \pm$



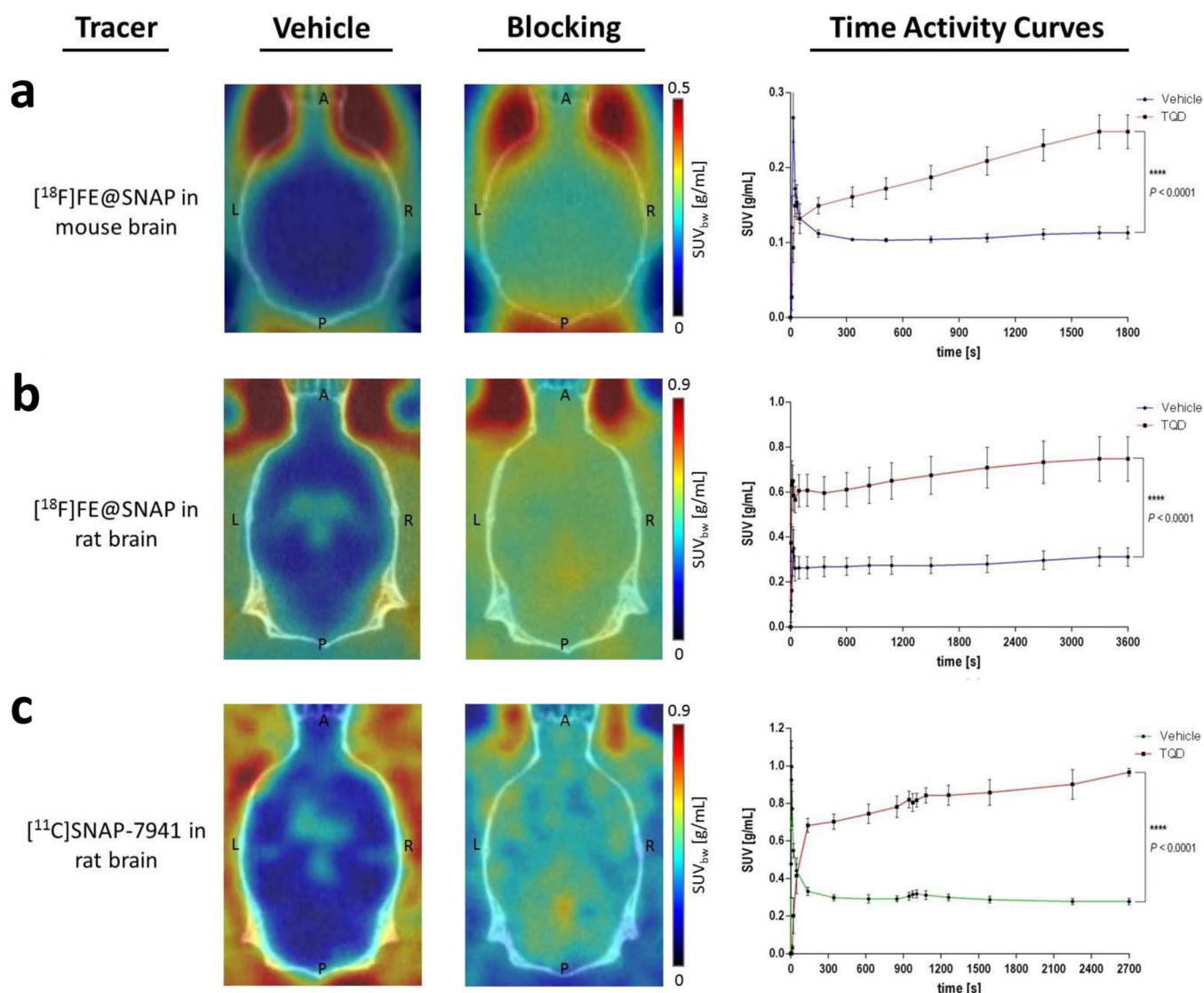


**Fig. 3** Representation of axial planes of mouse (**a**) and rat (**b**, **c**) brains under vehicle and blocking conditions with the P-gp/BCRP inhibitor TQD for [ $^{18}\text{F}$ ]FE@SNAP (**a**, **b**) and [ $^{11}\text{C}$ ]SNAP-7941 (**c**). Respective TACs are presented on the right-hand side of each illustration for the dedicated radiotracers [ $^{18}\text{F}$ ]FE@SNAP (blue), [ $^{11}\text{C}$ ]SNAP-7941 (green) under vehicle conditions, and in combination with 15-mg/kg TQD (red). Data are displayed as mean  $\pm$  SEM from independent experiments ( $n \geq 3$ ). Differences among groups were tested using a repeated measures ANOVA (\*\*\*\* =  $P < 0.0001$ ). If not visible, error bars are within the margin of the symbols.

1.12 nM) [25]. Based on current and previous results, [ $^{11}\text{C}$ ]SNAP-7941 exhibits an improved target affinity and superior selectivity.

Considering the *in vivo* pharmacology, it has been demonstrated in preceding [32, 43] and recent experiments that [ $^{11}\text{C}$ ]SNAP-7941 is a P-gp/BCRP substrate, as confirmed in small animal imaging studies of rat brains (3.04-times higher uptake after TQD pretreatment, Fig. 3c). A similar behavior was observed for [ $^{18}\text{F}$ ]FE@SNAP (2.45-times higher uptake after TQD pretreatment, Fig. 3b). Additionally, no species differences in P-gp/BCRP inhibition between mouse and rat were found as shown in small animal imaging studies of mouse brains with [ $^{18}\text{F}$ ]FE@SNAP, revealing also an increased brain uptake

after TQD pretreatment (Fig. 3a). Detailed quantitative assessment of the whole brain uptake evinced a more distinct difference between the vehicle and TQD-treated groups for [ $^{11}\text{C}$ ]SNAP-7941 unlike [ $^{18}\text{F}$ ]FE@SNAP. These variations result from the already higher brain uptake in the vehicle group of [ $^{18}\text{F}$ ]FE@SNAP, which presumably originates from a higher unspecific binding. This stands in line with the physicochemical parameters already determined in previous studies showing a lower  $\log D$  ( $3.29 \pm 0.01$ ) for [ $^{11}\text{C}$ ]SNAP-7941 compared to [ $^{18}\text{F}$ ]FE@SNAP ( $\log D = 3.83 \pm 0.1$ ). In previous studies, plasma free fractions of  $12.6 \pm 0.2$  % were reported for [ $^{18}\text{F}$ ]FE@SNAP and of  $20.96 \pm 1$  % for [ $^{11}\text{C}$ ]SNAP-7941 using an ultrafiltration method with human pooled plasma [32, 36]. For ( $\pm$ )-SNAP-

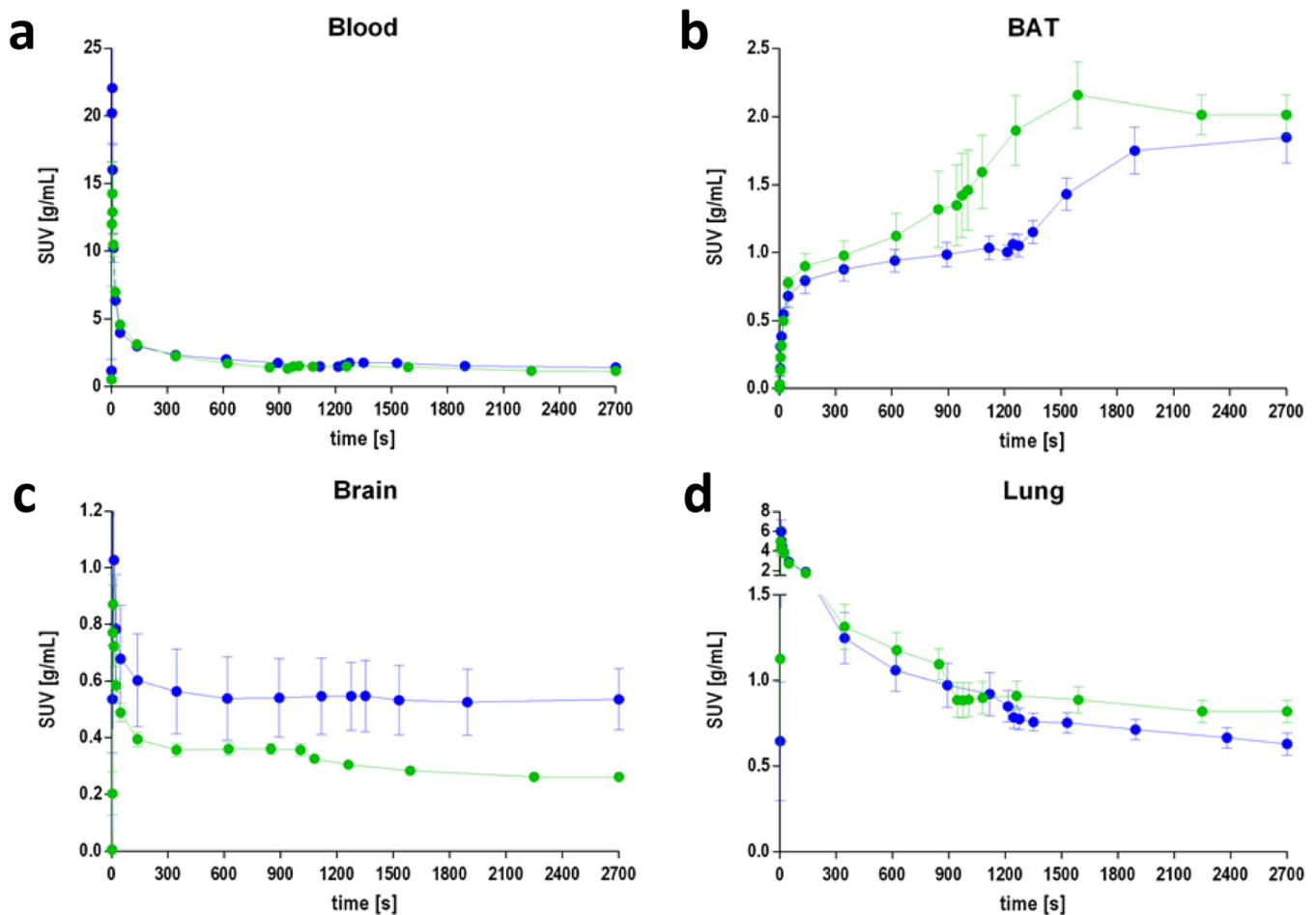


Fig. 4 TACs for [ $^{18}\text{F}$ ]FE@SNAP (blue) and [ $^{11}\text{C}$ ]SNAP-7941 (green) before and after displacement with 15 mg/kg ( $\pm$ )-SNAP-7941 in **a** blood, **b** BAT, **c** brain, and **d** lung, after 900 or 1200 s, respectively. Data are displayed as mean  $\pm$  SEM from independent experiments ( $n \geq 3$ ). If not visible, error bars are within the margin of the symbols.

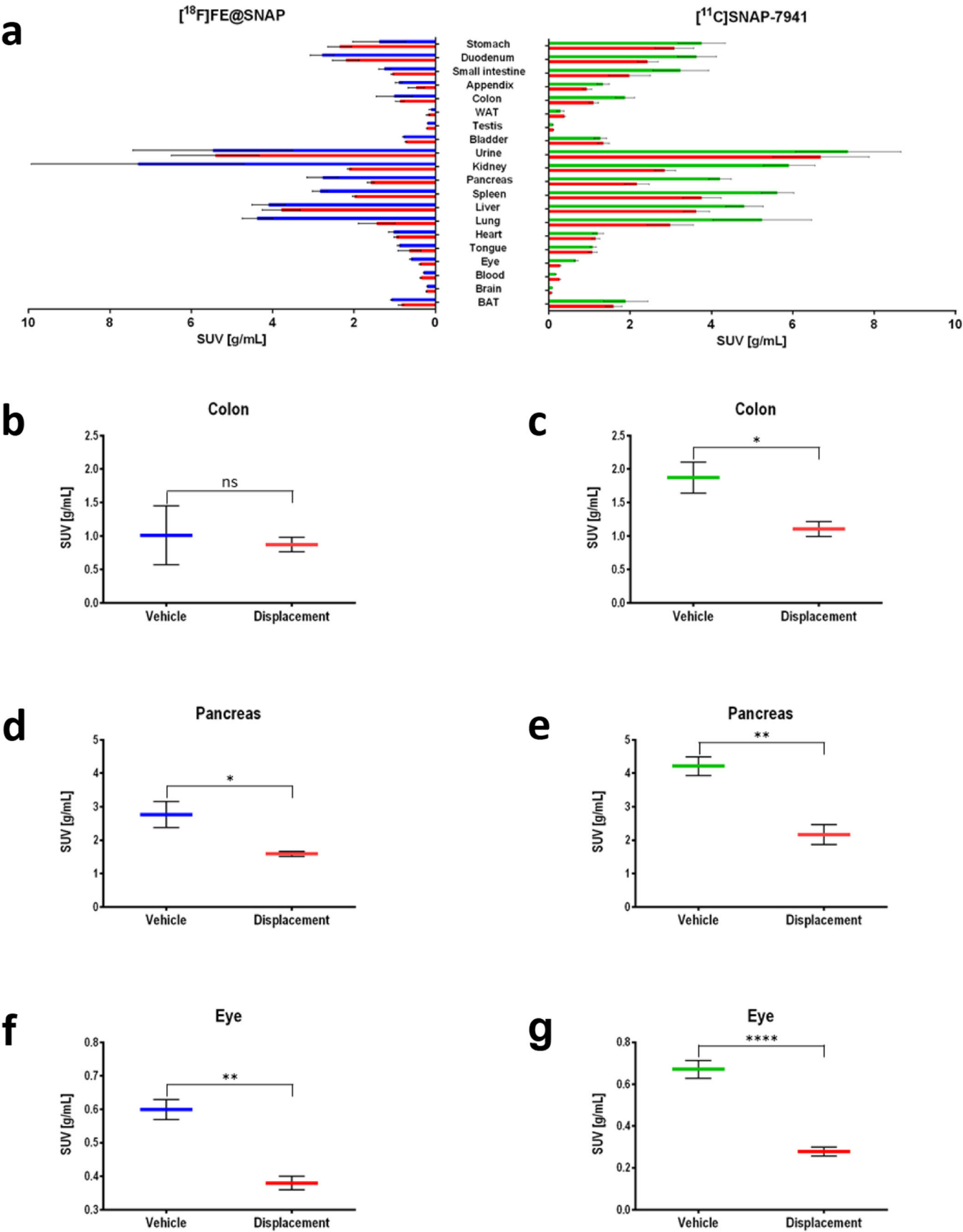
7941, these results were in accordance with the bioaffinity chromatography outcome, indicating that ( $\pm$ )-SNAP-7941 utterly binds to serum albumin. Whereas, the results for FE@SNAP diverged around 10 % when applying the chromatographic method. One reason might be that FE@SNAP also binds to other plasma components, such as alpha1-acid glycoprotein or diverse lipoproteins.

Furthermore, the higher brain uptake of [ $^{18}\text{F}$ ]FE@SNAP compared to [ $^{11}\text{C}$ ]SNAP-7941 results from the formation of radiometabolites (*e.g.*, [ $^{18}\text{F}$ ]fluoroethanol) supported by the findings from the *ex vivo* metabolism studies in rat whole blood (Fig. 6), which underlines the superior imaging contrast of [ $^{11}\text{C}$ ]SNAP-7941 in the brain.

Considering the vehicle and displacement groups, the analysis of the whole brain resulted in a clear displacement for [ $^{11}\text{C}$ ]SNAP-7941, whereas for [ $^{18}\text{F}$ ]FE@SNAP a displacement could not be detected (Fig. 4c). This finding is supported by previously conducted experiments [25] and is likely a result of the high unspecific binding and metabolic degradation of [ $^{18}\text{F}$ ]FE@SNAP. Furthermore, a drop in the TAC of both radiotracers after displacement with 15 mg/kg ( $\pm$ )-SNAP-7941 could be detected for the lung (Fig. 4d). The

detailed analysis of the TACs of other target regions, such as tongue, pancreas, and colon, was not possible due to the limited field of view of the imaging modality and spillover effects of the surrounding tissue. Interestingly, the TAC of the BAT depicts an increased uptake for both tracers after the administration of ( $\pm$ )-SNAP-7941 (Fig. 4b), which indicates a potential involvement of the MCHergic system and a further interaction of important regulatory pathways. The representative TAC of the blood pool confirms the proper administration and further bioavailability of both radiotracers (Fig. 4a).

**Fig. 5** **a** Representative *ex vivo* rat biodistribution of [ $^{11}\text{C}$ ]SNAP-7941 and [ $^{18}\text{F}$ ]FE@SNAP and **b–g** selected target regions of both radiotracers [ $^{18}\text{F}$ ]FE@SNAP (blue) and [ $^{11}\text{C}$ ]SNAP-7941 (green) under vehicle conditions and after displacement with 15 mg/kg ( $\pm$ )-SNAP-7941 (red). Data are displayed as mean  $\pm$  SEM from independent experiments ( $n \geq 3$ ). Differences among groups were tested using a two-tailed parametric paired *t* test ( $ns = P > 0.05$ ;  $* = P < 0.05$ ;  $** = P < 0.01$ ;  $**** = P < 0.0001$ ). If not visible, error bars are within the margin of the symbols.



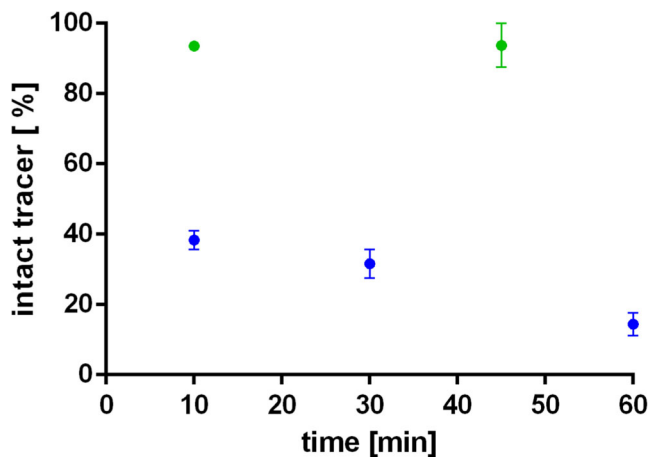


Fig. 6 *Ex vivo* metabolic stability of [ $^{18}\text{F}$ ]FE@SNAP (blue) and [ $^{11}\text{C}$ ]SNAP-7941 (green) in rat whole blood over time. Data are displayed as mean  $\pm$  SEM from independent experiments ( $n \geq 3$ ). If not visible, error bars are within the margin of the symbols.

Global analysis of the *ex vivo* biodistribution depicts reduced tracer uptake after displacement with ( $\pm$ )-SNAP-7941 for both radiotracers (Fig. 5a). This finding is highlighted by previously conducted studies [38] and confirmed by tissue-to-blood analyses [32]. The reduced uptake in BAT stands in contrast to the enhanced uptake shown in the TAC (Fig. 4b). This phenomenon may be explained by the differences in the experimental setup due to the high biodiversity when using different animals as used in biodistribution studies. In contrast, the *in vivo* displacement analysis of the TACs was performed within the same animal. The involvement of the MCHR1 in BAT is part of ongoing investigations.

Regional analysis of selected target regions (colon, pancreas, eye) contrasts the higher suitability of [ $^{11}\text{C}$ ]SNAP-7941. Even if both radiotracers demonstrate a significant decrease in uptake in the pancreas and eye after displacement with ( $\pm$ )-SNAP-7941, [ $^{11}\text{C}$ ]SNAP-7941 revealed a more pronounced difference. However, a significant displacement in the colon was only observed for [ $^{11}\text{C}$ ]SNAP-7941 (Fig. 5b–g); a possible explanation might be the fast and high metabolic degradation of [ $^{18}\text{F}$ ]FE@SNAP, which hampered the assessment of the as

due to the high metabolic degradation of [ $^{18}\text{F}$ ]FE@SNAP no significant displacement.

Furthermore, [ $^{11}\text{C}$ ]SNAP-7941 evinced a high metabolic stability in rat whole blood, whereas [ $^{18}\text{F}$ ]FE@SNAP was rapidly metabolized (Fig. 6), which was validated by previous *in vitro* as well as *in vivo* studies. A detailed analysis of the brain metabolism demonstrated an extensive degradation of [ $^{18}\text{F}$ ]FE@SNAP, while [ $^{11}\text{C}$ ]SNAP-7941 remained metabolically stable [32, 36, 38].

Even though both tracers exhibit suitable properties for the imaging of the MCHR1, [ $^{11}\text{C}$ ]SNAP-7941 clearly demonstrated superior imaging properties due to its higher selectivity, affinity, and metabolic stability. Based on the combined data, we recommend [ $^{11}\text{C}$ ]SNAP-7941 as the tracer of choice for the imaging of MCHR1.

## Conclusions

The MCHR1 has become an interesting pharmacological target for clinical medicine, as well as for biomedical research, since it may be involved in a plethora of lifestyle diseases. In this context, the availability of a suitable PET radiotracer is a crucial step for the quantitative *in vivo* assessment of MCHR1 pharmacology. Extensive *in vitro*, *in vivo*, and *ex vivo* assessments of [ $^{18}\text{F}$ ]FE@SNAP and [ $^{11}\text{C}$ ]SNAP-7941 demonstrate appropriate imaging properties for the MCHR1. Yet, some physiological processes influenced by the MCH system, as for instance its contribution to BAT stimulation, remain unclear and demand further elucidation.

However, the pronounced metabolic stability as well as superior affinity and selectivity of [ $^{11}\text{C}$ ]SNAP-7941 reveal the decisive superiority over [ $^{18}\text{F}$ ]FE@SNAP. Since humans express both the MCHR1 and MCHR2, tracer selectivity is essential for prospective first-in-man imaging studies. Therefore, [ $^{11}\text{C}$ ]SNAP-7941 is the ideal candidate for initial clinical trials, addressing the imaging of endocrinological and psychiatric disorders.

**Funding Information.** Open access funding provided by Medical University of Vienna. This scientific project was performed with the support of the Medical Imaging Cluster of the Medical University of Vienna. This research was part of a study funded by the Austrian Science Fund (FWF P20977-B09; P.I.: Markus Mitterhauser).

Table 1.. Overview of discussed results

		[ $^{11}\text{C}$ ]SNAP-7941		[ $^{18}\text{F}$ ]FE@SNAP	
<i>In vitro</i>	Radiosynthesis	$2.9 \pm 1.6$ GBq	[33]	$374 \pm 202$ MBq	[34]
	Affinity to MCHR1 ( $K_i$ )	$3.91 \pm 0.74$	[25]	$9.98 \pm 1.12$	[25]
	Selectivity over MCHR2	Yes		No	
	Lipophilicity ( $\log D$ )	$3.29 \pm 0.01$	[30]	$3.83 \pm 0.1$	[34]
	Plasma free fraction (human)	$20.96 \pm 1$ %	[30]	$12.6 \pm 0.2$ %	[34]
	Binding to human serum albumin	$80 \pm 0.9$ %		$77 \pm 0.2$ %	
<i>In vivo</i>	Autoradiography	✓	[32]	✓	[32]
	Small animal PET	✓		✓	
<i>Ex vivo</i>	Biodistribution	✓		✓	
	Metabolism in rat blood	Stable		Rapidly metabolized	
	Metabolism in rat brain	Stable		Rapidly metabolized	



## Compliance with Ethical Standards

## Conflict of Interest

The authors declare that there is no conflict of interest.

**Open Access** This article is distributed under the terms of the Creative Commons Attribution 4.0 International License (<http://creativecommons.org/licenses/by/4.0/>), which permits unrestricted use, distribution, and reproduction in any medium, provided you give appropriate credit to the original author(s) and the source, provide a link to the Creative Commons license, and indicate if changes were made.

## References

- Bittencourt JC (2011) Anatomical organization of the melanin-concentrating hormone peptide family in the mammalian brain. *Gen Comp Endocrinol* 172:185–197
- Tadayyon M, Welters HJ, Haynes AC, Cluderay JE, Hervieu G (2000) Expression of melanin-concentrating hormone receptors in insulin-producing cells: MCH stimulates insulin release in RINm5F and CRI-G1 cell-lines. *Biochem Biophys Res Commun* 275:709–712
- Kokkotou E, Moss AC, Torres D, Karagiannides I, Cheifetz A, Liu S, O'Brien M, Maratos-Flier E, Pothoulakis C (2008) Melanin-concentrating hormone as a mediator of intestinal inflammation. *Proc Natl Acad Sci U S A* 105:10613–10618
- Bradley RL, Kokkotou EG, Maratos-Flier E, Cheatham B (2000) Melanin-concentrating hormone regulates leptin synthesis and secretion in rat adipocytes. *Diabetes* 49:1073–1077
- Bradley RL, Mansfield JPR, Maratos-Flier E, Cheatham B (2002) Melanin-concentrating hormone activates signaling pathways in 3T3-L1 adipocytes. *Am J Physiol Endocrinol Metab* 283:E584–E592
- Saito Y, Nothacker H-P, Wang Z, Lin SHS, Leslie F, Civelli O (1999) Molecular characterization of the melanin-concentrating-hormone receptor. *Nature* 400:265–269
- Shimomura Y, Mori M, Sugo T, Ishibashi Y, Abe M, Kurokawa T, Onda H, Nishimura O, Sumino Y, Fujino M (1999) Isolation and identification of melanin-concentrating hormone as the endogenous ligand of the SLC-1 receptor. *Biochem Biophys Res Commun* 261:622–626
- Chambers J, Ames RS, Bergsma D, Muir A, Fitzgerald LR, Hervieu G, Dytko GM, Foley JJ, Martin J, Liu WS, Park J, Ellis C, Ganguly S, Konchar S, Cluderay J, Leslie R, Wilson S, Sarau HM (1999) Melanin-concentrating hormone is the cognate ligand for the orphan G-protein-coupled receptor SLC-1. *Nature* 400:261–265
- Lembo PMC, Grazzini E, Cao J, Hubatsch DA, Pelletier M, Hoffert C, St-Onge S, Pou C, Labrecque J, Groblewski T, O'Donnell D, Payza K, Ahmad S, Walker P (1999) The receptor for the orexigenic peptide melanin-concentrating hormone is a G-protein-coupled receptor. *Nat Cell Biol* 1:267–271
- Sailer AW, Sano H, Zeng Z, McDonald TP, Pan J, Pong SS, Feighner SD, Tan CP, Fukami T, Iwaasa H, Hreniuk DL, Morin NR, Sadowski SJ, Ito M, Ito M, Bansal A, Ky B, Figueroa DJ, Jiang Q, Austin CP, MacNeil DJ, Ishihara A, Ihara M, Kanatani A, van der Ploeg LHT, Howard AD, Liu Q (2001) Identification and characterization of a second melanin-concentrating hormone receptor, MCH-2R. *Proc Natl Acad Sci U S A* 98:7564–7569
- Hill J, Duckworth M, Murdock P, Rennie G, Sabido-David C, Ames RS, Szekeres P, Wilson S, Bergsma DJ, Gloger IS, Levy DS, Chambers JK, Muir AI (2001) Molecular cloning and functional characterization of MCH2, a novel human MCH receptor. *J Biol Chem* 276:20125–20129
- Wang S, Behan J, O'Neill K et al (2001) Identification and pharmacological characterization of a novel human melanin-concentrating hormone receptor, MCH-R2. *J Biol Chem* 276:34664–34670
- An S, Cutler G, Zhao JJ, Huang SG, Tian H, Li W, Liang L, Rich M, Bakleh A, du J, Chen JL, Dai K (2001) Identification and characterization of a melanin-concentrating hormone receptor. *Proc Natl Acad Sci U S A* 98:7576–7581
- Casatti CA, Elias CF, Sita LV, Frigo L, Furlani VCG, Bauer JA, Bittencourt JC (2002) Distribution of melanin-concentrating hormone neurons projecting to the medial mammillary nucleus. *Neuroscience* 115:899–915
- Marsh DJ, Weingarth DT, Novi DE, Chen HY, Trumbauer ME, Chen AS, Guan XM, Jiang MM, Feng Y, Camacho RE, Shen Z, Frazier EG, Yu H, Metzger JM, Kuca SJ, Shearman LP, Gopal-Truter S, MacNeil DJ, Strack AM, MacIntyre DE, van der Ploeg LHT, Qian S (2002) Melanin-concentrating hormone 1 receptor-deficient mice are lean, hyperactive, and hyperphagic and have altered metabolism. *Proc Natl Acad Sci* 99:3240–3245
- Ito M, Gomori A, Ishihara A, Oda Z, Mashiko S, Matsushita H, Yumoto M, Ito M, Sano H, Tokita S, Moriya M, Iwaasa H, Kanatani A (2003) Characterization of MCH-mediated obesity in mice. *Am J Physiol—Endocrinol Metab* 284:E940–E945
- Ito M, Ishihara A, Gomori A, Egashira S, Matsushita H, Mashiko S, Ito J, Ito M, Nakase K, Haga Y, Iwaasa H, Suzuki T, Ohtake N, Moriya M, Sato N, MacNeil DJ, Takenaga N, Tokita S, Kanatani A (2009) Melanin-concentrating hormone 1-receptor antagonist suppresses body weight gain correlated with high receptor occupancy levels in diet-induced obesity mice. *Eur J Pharmacol* 624:77–83
- Elliott JC, Harrold JA, Brodin P, Enquist K, Bäckman A, Byström M, Lindgren K, King P, Williams G (2004) Increases in melanin-concentrating hormone and MCH receptor levels in the hypothalamus of dietary-obese rats. *Mol Brain Res* 128:150–159
- Schwartz MW, Woods SC, Porte D, Seeley RJ, Baskin DG (2000) Central nervous system control of food intake. *Nature* 404:661–671
- Pereira-da-Silva M, De Souza CT, Gasparetti AL et al (2005) Melanin-concentrating hormone induces insulin resistance through a mechanism independent of body weight gain. *J Endocrinol* 186:193–201
- Philippe C, Mitterhauser M (2017) The potential role of the MCHR1 in diagnostic facts and trends imaging. In: Blumenberg M (ed) *InTech: Melanin*. pp 27–38
- Smith DG, Davis RJ, Rorick-Kehn L et al (2005) Melanin-concentrating hormone-1 receptor modulates neuroendocrine, behavioral, and corticolic neurochemical stress responses in mice. *Neuropsychopharmacology* 31:1135–1145
- Conductier G, Brau F, Viola A, Langlet F, Ramkumar N, Dehouck B, Lemaire T, Chapot R, Lucas L, Rovère C, Maitre P, Hosseiny S, Petit-Paillet A, Adamantidis A, Lakaye B, Risold PY, Prévot V, Meste O, Nahon JL, Guyon A (2013) Melanin-concentrating hormone regulates beat frequency of ependymal cilia and ventricular volume. *Nat Neurosci* 16:845–847
- Conductier G, Martin AO, Risold P-Y et al (2013) Control of ventricular ciliary beating by the melanin concentrating hormone-expressing neurons of the lateral hypothalamus: a functional imaging survey. *Front Endocrinol* 4:182
- Zeilinger M, Dumanic M, Pichler F, Budinsky L, Wadsak W, Pallitsch K, Spreitzer H, Lanzenberger R, Hacker M, Mitterhauser M, Philippe C (2017) In vivo evaluation of radiotracers targeting the melanin-concentrating hormone receptor 1: [<sup>11</sup>C]SNAP-7941 and [<sup>18</sup>F]FE@SNAP reveal specific uptake in the ventricular system. *Sci Rep* 7:8054
- Kokkotou EG, Tritos NA, Mastaitis JW, Slieker L, Maratos-Flier E (2001) Melanin-concentrating hormone receptor is a target of leptin action in the mouse brain. *Endocrinology* 142:680–686
- Verlaet M, Adamantidis A, Coumans B, Chanas G, Zorzi W, Heinen E, Grisar T, Lakaye B (2002) Human immune cells express ppMCH mRNA and functional MCHR1 receptor. *FEBS Lett* 527:205–210
- Coumans B, Grisar T, Nahon JL, Lakaye B (2007) Effect of ppMCH derived peptides on PBMC proliferation and cytokine expression. *Regul Pept* 143:104–108
- Luthin DR (2007) Anti-obesity effects of small molecule melanin-concentrating hormone receptor1 (MCHR1) antagonists. *Life Sci* 81:423–440
- Gattrell WT, Sambrook Smith CP, Smith AJ (2012) An example of designed multiple ligands spanning protein classes: dual MCH-1R antagonists/DPP-IV inhibitors. *Bioorg Med Chem Lett* 22:2464–2469
- Borowsky B, Durkin MM, Ogozalek K, Marzabadi MR, DeLeon J, Lagu B, Heurich R, Lichtblau H, Shaposhnik Z, Daniewska I, Blackburn TP, Branchek TA, Gerald C, Vaysse PJ, Forray C (2002) Antidepressant, anxiolytic and anorectic effects of a melanin-concentrating hormone-1 receptor antagonist. *Nat Med* 8:825–830
- Philippe C, Nics L, Zeilinger M, Kuntner C, Wanek T, Mairinger S, Shanab K, Spreitzer H, Viernstein H, Wadsak W, Mitterhauser M

- (2013) Preclinical in vitro & in vivo evaluation of [<sup>11</sup>C]SNAP-7941—the first PET tracer for the melanin concentrating hormone receptor 1. *Nucl Med Biol* 40:919–925
33. Schirmer E, Shanab K, Datterl B, Neudorfer C, Mitterhauser M, Wadsak W, Philippe C, Spreitzer H (2013) Syntheses of precursors and reference compounds of the melanin-concentrating hormone receptor 1 (MCHR1) tracers [<sup>11</sup>C]SNAP-7941 and [<sup>18</sup>F]FE@SNAP for positron emission tomography. *Molecules* 18:12119–12143
34. Philippe C, Haeusler D, Fuchshuber F, Spreitzer H, Viernstein H, Hacker M, Wadsak W, Mitterhauser M (2014) Comparative autoradiographic in vitro investigation of melanin concentrating hormone receptor 1 ligands in the central nervous system. *Eur J Pharmacol* 735:177–183
35. Philippe C, Schirmer E, Mitterhauser M, Shanab K, Lanzenberger R, Karanikas G, Spreitzer H, Viernstein H, Wadsak W (2012) Radiosynthesis of [<sup>11</sup>C]SNAP-7941—the first PET-tracer for the melanin concentrating hormone receptor 1 (MCHR1). *Appl Radiat Isot* 70:2287–2294
36. Philippe C, Nics L, Zeilinger M, Schirmer E, Spreitzer H, Karanikas G, Lanzenberger R, Viernstein H, Wadsak W, Mitterhauser M (2013) Preparation and first preclinical evaluation of [<sup>18</sup>F]FE@SNAP: a potential PET tracer for the melanin-concentrating hormone receptor-1 (MCHR1). *Sci Pharm* 81:625–639
37. Philippe C, Ungersboeck J, Schirmer E, Zdravkovic M, Nics L, Zeilinger M, Shanab K, Lanzenberger R, Karanikas G, Spreitzer H, Viernstein H, Mitterhauser M, Wadsak W (2012) FE@SNAP—a new PET tracer for the melanin concentrating hormone receptor 1 (MCHR1): microfluidic and vessel-based approaches. *Bioorganic Med Chem* 20:5936–5940
38. Philippe C, Haeusler D, Scherer T, Fürnsinn C, Zeilinger M, Wadsak W, Shanab K, Spreitzer H, Hacker M, Mitterhauser M (2016) [<sup>18</sup>F]FE@SNAP—a specific PET tracer for melanin-concentrating hormone receptor 1 imaging? *EJNMMI Res* 6:31
39. Zeilinger M, Pichler F, Nics L, Wadsak W, Spreitzer H, Hacker M, Mitterhauser M (2017) New approaches for the reliable in vitro assessment of binding affinity based on high-resolution real-time data acquisition of radioligand-receptor binding kinetics. *EJNMMI Res* 7:22
40. Guo D, van Dorp EJH, Mulder-Krieger T et al (2012) Dual-point competition association assay. *J Biomol Screen* 18:309–320
41. Igawa H, Stepanov V, Tari L, Okuda S, Yamamoto S, Kasai S, Nagisa Y, Haggkvist J, Svedberg M, Toth M, Takano A, Halldin C (2017) Development of a novel carbon-11 labeled PET radioligand for melanin-concentrating hormone receptor 1. *Curr Radiopharm* 10:35–40
42. Kawata Y, Okuda S, Hotta N, Igawa H, Takahashi M, Ikoma M, Kasai S, Ando A, Satomi Y, Nishida M, Nakayama M, Yamamoto S, Nagisa Y, Takekawa S (2017) A novel and selective melanin-concentrating hormone receptor 1 antagonist ameliorates obesity and hepatic steatosis in diet-induced obese rodent models. *Eur J Pharmacol* 796:45–53
43. Vranka C, Dumanic M, Racz T, et al. (2018) A model for the prediction of the interaction of radiotracers with the P-glycoprotein (P-gp) transporter. *Nucl Med Biol.* submitted

## 3.5 Manuscript #5

Title: First Radiopharmaceutical Evidence for MCHR1 Expression in Brown Adipose Tissue

Authors: Theresa Balber, Katarína Benčurová, Florian Werner Kiefer, Oana Cristina Hedesan, Karl-Heinz Wagner, Helmut Viernstein, Katharina Pallitsch, Helmut Spreitzer, Marcus Hacker, Wolfgang Wadsak, Markus Mitterhauser and Cécile Philippe

Manuscript #5 is currently under revision in *Frontiers in Endocrinology* (submitted August 2018).

Associated Content: None

**Rationale and Aim:** We previously uncovered accumulation of MCHR1 PET-tracers in brown adipose tissue of naïve rats (cf. Manuscript #4), whereby *in vivo* data obtained from blocking and displacement experiments was inconclusive. Depending on the experimental setting, two different phenomena were observed: When biodistribution experiments were performed in alert animals, significant blocking of [<sup>18</sup>F]FE@SNAP in brown adipose tissue was achieved upon pre-blocking using unlabeled reference compound. (68) Whereas, when animals were anesthetized and subjected to  $\mu$ PET acquisition, binding enhancement of both [<sup>18</sup>F]FE@SNAP and [<sup>11</sup>C]SNAP-7941 was observed upon administration of SNAP-7941 (Manuscript #4). The substantial difference in the experimental setup was the use of anesthesia, which is indispensable for small animal imaging. Effects of isoflurane, which was used as volatile anesthesia during  $\mu$ PET acquisition, on brown adipose tissue are still uncertain.

Due to the observed discrepancy and the fact that the target (MCHR1) was not reported in brown adipose tissue so far, selectivity of the MCHR1 PET-tracers was doubted and potential off-target binding (i.e. binding to adrenergic beta-3 receptors) was considered. Moreover, a brown adipose tissue activating effect of pharmacological doses of the MCHR1 antagonist SNAP-7941, which would explain the observed binding enhancement, was proposed.

Manuscript #5 builds on our prior study and aims at determining (i) affinity of FE@SNAP and SNAP-7941 towards adrenergic beta-3 receptors and thus selectivity towards MCHR1, (ii) specificity of [<sup>11</sup>C]SNAP binding to brown adipocytes and (iii) effects of MCHR1 ligands on brown adipose tissue activation. *In vivo* blocking experiments are common to investigate specificity of PET-tracer uptake. In this case, we decided to follow an *in vitro* approach, as pure target-ligand interactions can be studied without possible interference of anesthesia.





## In vitro radiopharmaceutical evidence for MCHR1 binding sites in murine brown adipocytes

Balber T<sup>1,2</sup>, Benčurová K<sup>1,3</sup>, Kiefer FW<sup>4</sup>, Hedesan OC<sup>1,4</sup>, Klebermass EM<sup>1,2</sup>, Wagner KH<sup>3</sup>, Viernstein H<sup>2</sup>, Pallitsch K<sup>5</sup>, Spreitzer H<sup>6</sup>, Hacker M<sup>1</sup>, Wadsak W<sup>1,7</sup>, Mitterhauser M<sup>1,8\*</sup>, Philippe C<sup>1,2</sup>

<sup>1</sup>Biomedical Imaging and Image-Guided Therapy, Division of Nuclear Medicine, Medical University of Vienna, Vienna, AUSTRIA

<sup>2</sup>Department of Pharmaceutical Technology and Biopharmaceutics, Faculty of Life Sciences, University of Vienna, Vienna, AUSTRIA

<sup>3</sup>Department of Nutritional Sciences, Faculty of Life Sciences, University of Vienna, Vienna, AUSTRIA

<sup>4</sup>Division of Endocrinology and Metabolism, Department of Medicine III, Medical University of Vienna, Vienna, AUSTRIA

<sup>5</sup>Institute of Organic Chemistry, University of Vienna, Vienna, AUSTRIA

<sup>6</sup>Department of Pharmaceutical Chemistry, Faculty of Life Sciences, University of Vienna, Vienna, AUSTRIA

<sup>7</sup>Center for Biomarker Research in Medicine - CBmed GmbH, Graz, AUSTRIA

<sup>8</sup>Ludwig Boltzmann Institute Applied Diagnostics, Vienna, AUSTRIA

### \* Correspondence:

Mag. Dr. Markus Mitterhauser  
markus.mitterhauser@meduniwien.ac.at

**Keywords: Melanin-concentrating hormone receptor 1, MCHR1, brown adipocytes, BAT, adrenergic beta-3 receptor, [<sup>18</sup>F]FE@SNAP, [<sup>11</sup>C]SNAP-7941, PET**

### Abstract

[<sup>11</sup>C]SNAP-7941 and its radiofluorinated, fluoro-ethyl derivative [<sup>18</sup>F]FE@SNAP have been developed as the first positron emission tomography tracers for melanin-concentrating hormone receptor 1 (MCHR1) imaging. Accumulation of these MCHR1 PET-tracers in rat brown adipose tissue (BAT) *in vivo* provided first indication of MCHR1 expression in rodent BAT. To rule out off-target binding, affinity of both MCHR1 ligands towards adrenergic beta-3 receptors (ADRB3) was examined. Further, specific binding of [<sup>11</sup>C]SNAP-7941 to brown adipocytes and effects of MCHR1

ligands on brown adipocyte activation were investigated. SNAP-7941 and FE@SNAP evinced to be highly selective towards MCHR1. [ $^{11}\text{C}$ ]SNAP-7941 binding to brown adipocytes was shown to be mainly MCHR1-specific. This data strongly indicates MCHR1 expression in rodent BAT and moreover, a peripheral, anti-obesity effect of MCHR1 antagonists directly exerted in BAT is proposed. Moreover, MCHR1 expression in murine brown adipocytes was confirmed by protein analysis. We conclude that MCHR1 PET imaging contributes to basic research in endocrinology by elucidating the involvement of the MCH system in peripheral tissues, such as BAT.

## 1 Introduction

Although the physiological relevance of brown adipose tissue (BAT) was underestimated for long time, it nowadays attracts scientific interest as a therapeutic target for obesity and related metabolic diseases such as type 2 diabetes. (1-3) The groundbreaking discovery of functional BAT depots in adult humans contributed significantly to the re-introduction of BAT in metabolic research and was enabled by positron emission tomography (PET) using the glucose analogue 2- $^{18}\text{F}$ fluoro-2-deoxy-D-glucose ( $^{18}\text{F}$ FDG) combined with computer tomography (CT). The fact that BAT activity, quantified as  $^{18}\text{F}$ FDG uptake, was negatively correlated to body mass index and percent body fat indicated a potential role of BAT in energy expenditure in humans. (4-6) PET is a sensitive and non-invasive *in vivo* imaging technique that directly visualizes different molecular interactions or metabolic processes depending on the used radiolabeled tracer in a target tissue. Thus, besides  $^{18}\text{F}$ FDG, also other PET-tracers were investigated to study BAT function, namely [ $^{11}\text{C}$ ]meta-hydroxyephedrine, [ $^{11}\text{C}$ ]acetate, 14- $^{18}\text{F}$ fluoro-6-thiaheptadecanoic acid and (S,S)-O-[methyl- $^{11}\text{C}$ ]methylreboxetine thereby enhancing the understanding of BAT activation, control and metabolism. (7-9)

Evolutionary, BAT functions as an energy dissipating organ by exerting non-shivering thermogenesis and thus maintaining body temperature during cold exposure. This heat-producing process is controlled by the sympathetic nervous system leading to noradrenaline release followed by activation of adrenergic beta-3 receptors (ADRB3) in brown adipocytes. Subsequent lipolysis or increased uptake of glucose and its conversion into fatty acids finally lead to the uncoupling of ATP synthesis *via* uncoupling protein 1 (UCP-1) resulting in increased fatty acid oxidation and dissipation of excess energy as heat. Thereby, BAT regulates fuel metabolism by increasing glucose and triglyceride uptake, decreasing blood glucose and lipids and by serving as glycogen storage. (1, 10-14)

Obesity results from a chronic energy imbalance, when food intake exceeds total body energy expenditure. (15) The melanin-concentrating hormone, a neuropeptide predominantly expressed in the lateral hypothalamus and zona incerta, is involved in the control of appetite and food intake. (16, 17) In fact, upregulated MCH expression was found in the hypothalamus of obese and leptin-deficient mice and is moreover induced by fasting in wild-type mice. (16) Accordingly, MCH-deficient mice are lean due to hypophagia and have an increased metabolic rate. (18) Besides, MCH was shown to stimulate leptin secretion in rat white adipocytes and MCH was detected in rat plasma. (19) In rodents, MCH exerts its effects solely by stimulation of the melanin-concentrating hormone receptor 1 (MCHR1), as rodents do not express melanin-concentrating hormone receptor 2 (MCHR2). Several centrally active MCHR1 antagonists have been developed for the treatment of obesity. (20) In a diet-induced obesity mouse model it was shown that the anti-obesity effects of the tested MCHR1 antagonist are not only due to suppression of feeding, but also to a stimulation of energy expenditure. A significantly increased body temperature in MCHR1 antagonist-treated mice suggested a potential involvement of the MCH system in the regulation of energy expenditure *via* BAT. (21) It was reported that a large proportion of neurons in the lateral hypothalamus projecting to BAT contain MCH. (22) Thus, a central effect of the MCHR1 antagonist and subsequent transmission to BAT was presumed, as a direct effect on BAT could not be shown. (21)

[<sup>11</sup>C]SNAP-7941 and its fluoro-ethylated analogue [<sup>18</sup>F]FE@SNAP – both MCHR1 antagonists – have been developed as the first PET-tracers for MCHR1 imaging in our group. (23-28) Recent  $\mu$ PET experiments in naïve rats showed uptake of [<sup>18</sup>F]FE@SNAP and [<sup>11</sup>C]SNAP-7941 in BAT, though MCHR1 expression has previously not been reported in this tissue. Surprisingly, administration of a pharmacological dose (15 mg/kg BW) of unlabeled SNAP-7941 for displacement purposes caused uptake enhancement of both MCHR1 PET-tracers in interscapular BAT depots. (29) These observations suggest activation of BAT by MCHR1 antagonists. However, they were contradictory to earlier performed biodistribution experiments in conscious rats, when animals received a pharmacological dose of SNAP-7941 (15 mg/kg BW) or vehicle 30 min prior to [<sup>18</sup>F]FE@SNAP application *via* a jugular vein catheter. *Ex vivo* autoradiography and *ex vivo* biodistribution demonstrated significant blocking of [<sup>18</sup>F]FE@SNAP uptake in BAT of conscious rats, indicating specific [<sup>18</sup>F]FE@SNAP binding. (30) The discrepancy in anesthetized and conscious rats suggests a potential influence of the applied anesthesia on  $\mu$ PET acquisition.

Based on these *in vivo* findings, MCHR1-selectivity of FE@SNAP and SNAP-7941 has to be proven to avoid misleading interpretation of PET imaging data. To evade molecular alterations caused by anesthesia, we decided in favor of an *in vitro* approach. Therefore, in this preclinical *in vitro* study, affinity of both ligands towards the ADRB3, which is the receptor predominantly involved in BAT activation, was determined. Moreover, the potential involvement of the MCHR1 in BAT was investigated using brown adipocytes and the respective PET-tracer [<sup>11</sup>C]SNAP-7941 and additionally, [<sup>18</sup>F]FDG as a surrogate marker for brown adipocyte activity. Within the scope of this *in vitro* study, we aimed at applying conventional binding assays and kinetic radioligand binding measurements to cover binding interactions with single receptor sites as well as whole cell binding studies.

## 2 Methods

### 2.1 General

2-[<sup>18</sup>F]fluoro-2-deoxy-D-glucose ([<sup>18</sup>F]FDG) was prepared in-house using a fully automated cassette-based synthesizer (FASTlab, GE Healthcare, Uppsala, Sweden) within the clinical routine production at the General Hospital of Vienna, Austria. [<sup>11</sup>C]SNAP-7941 was synthesized as reported elsewhere using an automated module (TRACERlab FC X Pro, GE Healthcare, Uppsala, Sweden). (25) All PET-tracers were physiologically formulated and quality-controlled prior to administration. The adrenergic receptor beta ligands carazolol, pindolol and (S)-propranolol hydrochloride were purchased from Sigma-Aldrich (St. Louis, USA). The ADRB3 agonist CL 316,243 was purchased from Tocris Bioscience (Bristol, UK). The unlabeled compounds FE@SNAP and SNAP-7941 were synthesized at the Department of Pharmaceutical Chemistry and at the Department of Organic Chemistry (University of Vienna, Austria). The radioligands 5,7-[<sup>3</sup>H](−)CGP-12177 and [<sup>125</sup>I](−)Iodocyanopindolol were purchased from PerkinElmer, Inc. (Waltham, USA). All other reagents and cell culture supplies were purchased from standard commercial sources.

### 2.2 Cell culture

Cells were maintained under standard conditions in a humidified incubator (37°C, 5% CO<sub>2</sub>). CHO-K1 cells expressing the human adrenergic beta-3 receptor (CHO-K1-ADRB3) were purchased from PerkinElmer (ValiScreen® ES-035-C). CHO-K1-ADRB3 were grown using Ham's F12 (Nut Mix) supplemented with 10% FCS, 2 mM L-glutamine, penicillin (100 Units/mL), streptomycin (100 µg/mL) and 0.4 mg/mL geneticin. CHO-K1 cells were a generous gift from Prof. Karl Norbert

Klotz (University Würzburg, Germany) and cultured likewise without selection antibiotics. Immortalized murine brown pre-adipocytes were provided by the Department of Medicine III (Medical University of Vienna, Austria) and cultured in high glucose Dulbecco's Modified Eagle's Medium (DMEM) supplemented with 10% FBS, 1 mM pyruvate, penicillin (100 Units/mL) and streptomycin (100 µg/mL). When cells were confluent, differentiation to brown adipocytes was induced for 48 h using 1.72 µM insulin (human recombinant), 1 nM thyroid hormone (T3), 0.5 mM 3-isobutyl-1-methylxanthine (IBMX), 125 nM indomethacin and 1 µM dexamethasone. After induction, the medium was changed to post-differentiation medium (high glucose DMEM) supplemented with 10% FBS, 1 mM pyruvate, penicillin (100 Units/mL), streptomycin (100 µg/mL), 1.72 µM insulin and 1 nM T3. The post-differentiation medium was replenished every second day. Brown adipocytes were used for experimental investigations 4 to 6 days after induction. Oil Red O staining was performed according to the manufacturer's instructions. Counterstaining was performed using haematoxylin.

### 2.3 Cell membrane preparation

CHO-K1-ADRB3 cell membranes were prepared from 175 cm<sup>2</sup> cell culture flasks, when 80% confluence was reached. All procedures were performed at 4°C. Cells were scraped off using ice-cold lysis buffer (10 mM Tris-HCl pH 7.4, 1 mM EDTA) and protease inhibitor cocktail was added according to the manufacturer's instructions (Sigma-Aldrich, St.Louis, USA). The cell suspension was homogenized using cannulas (29 G) and centrifuged for 10 min at 1,000 × g. The obtained supernatant was centrifuged for 30 min at 100,000 × g. Subsequently, the pellet was suspended using 50 mM Tris-HCl pH 7.4 and aliquoted. Aliquots were shock-frozen in liquid nitrogen and stored at -80°C until usage. Protein concentration of the cell membrane suspension was determined using BCA Protein Assay Kit (Thermo Scientific, Waltham, USA).

### 2.4 Competitive binding studies: Affinity determination

All stated concentrations refer to the final assay volume of 500 µL buffer (25 mM HEPES pH 7.4, 1 mM EDTA, 0.5% BSA). Competitive binding assays were performed using 13.6 ng/µL ADRB3 expressing CHO-K1 cell membrane suspension (cf. 2.3) and 5 nM [<sup>3</sup>H]CGP-12177 as the respective radioligand. Test compounds (carazolol, pindolol, (S)-propranolol, FE@SNAP, SNAP-7941) were added in rising concentrations, whereby the concentration of solvent (ethanol or dimethyl sulfoxide (DMSO)) in the final assay volume remained always 1%. Nonspecific binding was determined using

10  $\mu$ M carazolol. Total binding was determined in the presence of 1% respective solvent. Incubation was performed for 90 min at 27°C. Filtration through GF/B filters (Whatman®, presoaked in 0.05% PEI) was performed using a cell harvester (Brandel®, Gaithersburg, MD, USA) and was followed by two washing steps using ice-cold wash buffer (10 mM HEPES, 500 mM NaCl, pH 7.4). Filter pieces containing receptor-bound radioactivity were shaken for 30 min in scintillation cocktail (Ultima Gold™, PerkinElmer, Waltham, USA) before liquid scintillation counting (Hidex 300 SL, Turku, Finland). IC<sub>50</sub> fitted binding curves were generated using the GraphPad Software 5.0 (La Jolla, CA, USA) using nonlinear regression. K<sub>i</sub> values were calculated using the Cheng & Prusoff equation assuming a K<sub>d</sub> value of 109.2 nM for [<sup>3</sup>H]CGP-12177 according to the literature. (31)

## 2.5 Kinetic measurements: Displacement of [<sup>125</sup>I]Iodocyanopindolol binding

2.5 x 10<sup>5</sup> cells (CHO-K1, CHO-K1-ADRB3) per cell culture dish were seeded 2 days prior to the experiment and incubated in an inclined position to allow an adherent cell pole at one side of the cell dish. Cell dish preparation was performed as previously described. (32, 33) Real-time kinetic radioligand binding measurements were performed using a dedicated device for low energy gamma radiation (LigandTracer® Grey Technology, Ridgeview, Sweden). The assay protocol comprised consecutive radioactivity measurements of the target region (cell pole) and of the opposite pole of the petri dish, where no cells were seeded (background signal). Radioactivity was counted in each region for 3 seconds with a delay of 2 seconds over the time course of the experiment. Raw counts per second (cps) of the target region were corrected for background signal and for radioactive decay. Displacement of [<sup>125</sup>I]Iodocyanopindolol binding was conducted after 1 h association phase of radioligand binding by consecutively applying rising concentrations of SNAP-7941 and FE@SNAP. The same volume of ethanol was added as vehicle control. Experiments were performed on at least three different days.

## 2.6 Kinetic measurements: Glycolytic activity

Kinetic measurements of [<sup>18</sup>F]FDG uptake were performed in pre-adipocytes and differentiated brown adipocytes to investigate metabolic activity. Cell seeding and the assay protocol followed a standard procedure described above (cf. 2.5). One hour prior to the experiment, post-differentiation medium was discarded and unsupplemented, glucose-free DMEM was added, followed by incubation with [<sup>18</sup>F]FDG (150 kBq per dish) for another 50 min. As glucose concentration is high in cell culture

media thus interfering with [ $^{18}\text{F}$ ]FDG uptake, cells were starved to achieve reasonable signal. Experiments were performed on at least three different days.

## 2.7 [ $^{18}\text{F}$ ]FDG uptake experiments: Effects of MCHR1 ligands on brown adipocyte activation

Brown pre-adipocytes were seeded, grown to confluence and differentiated in 6-well plates as described in section 2.1. Cell starving was performed for 1 h using unsupplemented, glucose-free DMEM. 30 min prior to [ $^{18}\text{F}$ ]FDG incubation, cells were pre-treated with the adrenergic beta-3 agonist (2  $\mu\text{M}$  CL 316,243), adrenergic beta antagonist (2  $\mu\text{M}$  (S)-propranolol), the MCHR1 ligands (20  $\mu\text{M}$  SNAP-7941 or FE@SNAP) or vehicle (baseline). [ $^{18}\text{F}$ ]FDG uptake was performed for 50 min at 37°C (humidified atmosphere, 5%  $\text{CO}_2$ ). Supernatant was taken off, cells were washed with ice-cold PBS and finally trypsinized. Radioactive cell fractions were gamma counted (2480 Wizard<sup>2</sup>, PerkinElmer) and normalized to percentage uptake per well. [ $^{18}\text{F}$ ]FDG uptake under baseline conditions refers to 100% uptake. Three independent experiments were performed in triplicates. Statistical analysis was performed using an unpaired, two-tailed *t*-test.

## 2.8 Investigation of specific [ $^{11}\text{C}$ ]SNAP-7941 binding to brown adipocytes

Brown pre-adipocytes were seeded, grown to confluence and differentiated in 6-well plates as described above. 30 min prior to the experiment, maintenance medium (cf. 2.1) was discarded and replaced with respective serum- and additive-free medium to avoid plasma protein binding of the PET-tracer. Cell starving, as performed for [ $^{18}\text{F}$ ]FDG uptake measurements, was not indicated for [ $^{11}\text{C}$ ]SNAP-7941 binding experiments. Cells were pre-treated for 30 min with ADRB3 ligands (CL 316,243, (S)-propranolol, 2  $\mu\text{M}$  each) or MCHR1 ligands (SNAP-7941, FE@SNAP, 2  $\mu\text{M}$  each). Baseline was determined using DMSO or ethanol, respectively. Sample processing, data analysis and statistical testing were performed as described in 2.7.

## 2.9 MCHR1 Western Blot

Cell lysates were prepared from immortalized murine brown adipocytes (cf. 2.2) using either a dedicated protein extraction kit for cultured adipocytes (Minute<sup>TM</sup>, Invent Biotechnologies, Inc.) (lysate# 1) or using commercially available radioimmunoprecipitation assay (RIPA) buffer (lysate# 2). Protease inhibitor cocktail was added according to the manufacturer's instructions. Separation of the water-oil emulsion was achieved by freezing at -20°C and subsequent centrifugation through filter cartridges (Minute<sup>TM</sup> extraction kit). In case of the extraction method

using RIPA buffer, three centrifugation steps (12000 rpm, 4°C) were required to obtain a lipid-free protein fraction. Tissue lysates of mouse tongue (positive control) and mouse spleen (negative control) were used as respective references. Both control tissues (non-fat tissues) were extracted using RIPA buffer and a standard extraction protocol including one centrifugation step. Protein concentration was determined using a bicinchoninic acid kit (BCA kit, Thermo Scientific) and 20 µg protein was loaded each. After gel electrophoreses (TGX™ precast gels, Bio-Rad, Laboratories, Inc.) and subsequent semi-dry blotting, nitrocellulose membranes (Amersham™ Protran™, GE Healthcare Life Science) were incubated with 5% dry milk powder for 90 min. Primary antibody incubation (rabbit polyclonal anti-MCHR1, 1:1000, Thermo Fisher Scientific) was performed overnight at 4°C. Membranes were further incubated with goat anti-rabbit IgG HRP conjugate (1:2500, 1 h, RT), followed by chemiluminescence imaging using a substrate detection kit and a dedicated device (Bio-Rad ChemiDoc™ Imaging System).

### 3 Results

#### 3.1 Competitive binding studies: Affinity determination

The two MCHR1 ligands displayed intermediate affinity towards ADRB3, as  $K_i$  values in µM-range were obtained (SNAP-7941:  $14.5 \pm 0.3$  µM and FE@SNAP:  $65.1 \pm 2.9$  µM,  $n=3$  in triplicates). However, both ligands demonstrated high selectivity towards MCHR1. For comparability, the assay was also performed using the ADRB3 ligands carazolol, pindolol and (S)-propranolol as standard compounds (Table 1).

#### 3.2 Kinetic measurements: Displacement of [<sup>125</sup>I]Iodocyanopindolol binding

Additionally to the conventional affinity determination using cell membrane preparations, displacement experiments using [<sup>125</sup>I]Iodocyanopindolol as the ADRB3 model ligand were performed. No binding kinetics was observed for parental CHO-K1 cells (data not shown). Application of 20 µM non-radioactive compound (either SNAP-7941 or FE@SNAP) after 60 min [<sup>125</sup>I]Iodocyanopindolol association phase did not affect binding to CHO-K1-ADRB3 cells. A second application of 20 µM MCHR1 ligand after 120 min led to a decrease in cell-associated radioactive signal, which was more pronounced after a third addition of unlabeled compound (Figure 1). Thus, for displacement of [<sup>125</sup>I]Iodocyanopindolol binding, excess of unlabeled MCHR1 ligand was required pointing at the intermediate affinity of SNAP-7941 and FE@SNAP towards ADRB3.



Vehicle control (ethanol) showed no effect on [ $^{125}$ I]Iodocyanopindolol binding to CHO-K1-ADRB3 cells.

### 3.3 Histological staining and metabolic activity of brown adipocytes

Morphological characterization of brown adipocytes was performed *via* Oil Red O staining. Mature brown adipocytes were obtained 4 to 6 days after induction. Fully differentiated brown adipocytes showed typical morphologic characteristics (spherical shape, multilocular lipid vesicles, central nucleus, Figure 2) and were thus visually distinguishable from pre-adipocytes (fibroblast-like shape). Glycolytic activity of brown adipocytes was demonstrated by means of kinetic [ $^{18}$ F]FDG uptake measurements. [ $^{18}$ F]FDG uptake by pre-adipocytes was negligible (Figure 3).

### 3.4 [ $^{18}$ F]FDG uptake experiments: Effects of MCHR1 ligands on brown adipocyte activation

Pharmacological effects of MCHR1 antagonists and ADRB3 ligands on brown adipocyte activation were measured using [ $^{18}$ F]FDG as a surrogate marker. The ADRB3 agonist CL 316,243 significantly ( $P < 0.05$ ) enhanced [ $^{18}$ F]FDG uptake to  $137.7 \pm 12.2\%$  referring to baseline, whereas the non-selective adrenergic beta receptor antagonist (S)-propranolol did not alter [ $^{18}$ F]FDG uptake. The opposite effect was observed for MCHR1 ligands, as [ $^{18}$ F]FDG uptake was significantly reduced, when SNAP-7941 ( $63.24 \pm 2.6\%$ ) or FE@SNAP ( $73.03 \pm 13.6\%$ ) were applied (Figure 4).

### 3.5 Investigation of specific [ $^{11}$ C]SNAP-7941 binding to brown adipocytes

Competitive binding experiments were performed to investigate specificity of [ $^{11}$ C]SNAP-7941 binding to brown adipocytes. Application of 2  $\mu$ M unlabeled SNAP-7941 significantly reduced cell-associated radioactive signal of [ $^{11}$ C]SNAP-7941 to  $77.1 \pm 5.0\%$  binding per well referring to baseline ( $P < 0.01$ ). Moreover, competition of [ $^{11}$ C]SNAP-7941 using ADRB3 ligands resulted in  $95.8 \pm 8.6\%$  binding/well for (S)-propranolol (not significant) and  $91.1 \pm 3.6\%$  binding/well for CL 316,243, respectively (Figure 5).

### 3.6 MCHR1 protein expression in murine brown adipocytes

In addition to radioligand binding, MCHR1 protein was detected in murine brown adipocytes. In brown adipocytes, an additional protein band, which was not detected in mouse tongue (MCHR1-positive control tissue), was found. Interestingly, depending on the used protein extraction method, the band was differently pronounced (Figure 6).

## 4 Discussion

For affinity determination towards ADRB3, a competitive binding assay using CHO-K1-ADRB3 cell membranes was established and tested using known ADRB3 ligands. The obtained  $K_i$  values for (S)-propranolol and pindolol differed slightly from literature due to different experimental settings (applied radioligand, whole cells *versus* membranes, etc.), which emphasizes the importance of testing reference compounds for distinct experimental settings. Obtained  $K_i$  values for FE@SNAP and SNAP-7941 suggested intermediate affinity towards ADRB3 and thus potential ADRB3 mediated effects when pharmacological doses of unlabeled compounds are applied (e.g. *in vivo* blocking/displacement experiments). However, the affinity of both ligands towards MCHR1 is several thousand times higher than towards ADRB3. Due to the applied trace amounts of PET ligands (usually nanomolar range or lower), we conclude that [ $^{18}\text{F}$ ]FE@SNAP and [ $^{11}\text{C}$ ]SNAP-7941 are selective PET-tracers for MCHR1 imaging. Additionally performed real-time kinetic measurements using CHO-K1-ADRB3 cells and the yet rarely employed LigandTracer® technology provide a cell binding technique which is closer to *in vivo* imaging techniques like PET, as high resolution time-activity curves are generated by applying a single tracer concentration. Displacement of [ $^{125}\text{I}$ ]Iodocyanopindolol binding to CHO-K1-ADRB3 was achieved when concentrations  $\geq 40 \mu\text{M}$  of unlabeled MCHR1 ligands were applied. This finding is in accordance with the  $K_i$  values in double digit  $\mu\text{M}$ -range obtained from competitive binding studies using cell membrane preparations and [ $^3\text{H}$ ]CGP-12177 as the respective radioligand.

Furthermore, whole cell binding experiments using mature brown adipocytes were performed to investigate the complexity of binding interactions apart from binding to a single receptor site, as in membrane preparations of CHO-K1-ADRB3 cells. Generally, experiments using whole cells account for unspecific processes including diffusion, nonspecific and off-target binding - processes that are often overlooked when applying cell membranes. Thus, pre-adipocytes were cultivated and differentiated to mature brown adipocytes. Morphologic (histological staining of lipids) and metabolic ([ $^{18}\text{F}$ ]FDG uptake measurements) characteristics of the BAT phenotype were achieved 4 to 6 days after induction, thus, experiments using brown adipocytes were performed in this time frame. [ $^{18}\text{F}$ ]FDG uptake by mature brown adipocytes followed linear kinetics mirroring the unique trapping mechanism of [ $^{18}\text{F}$ ]FDG: it is transported *via* glucose transporters and intracellularly phosphorylated by hexokinase leading to trapping of the respective metabolite [ $^{18}\text{F}$ ]FDG-6-phosphate, as further

metabolism is hindered. (34-36) [ $^{18}\text{F}$ ]FDG uptake by undifferentiated pre-adipocytes was only minor indicating fibroblast-like functionality.

ADRB3 stimulation by the agonist CL 316,243 in brown adipocytes led to enhanced [ $^{18}\text{F}$ ]FDG uptake demonstrating brown adipocyte activation. This experiment served as the positive control, as this phenomenon is well described for brown adipose tissue in rodents. (37, 38) Accordingly, the adrenergic beta receptor antagonist (S)-propranolol exerted no BAT activating effect. These results prove the expression of functional ADRB3 on the cultivated brown adipocytes used within this study. Interestingly, opposite effects (significant decrease in [ $^{18}\text{F}$ ]FDG uptake) are observed for pharmacological doses of SNAP-7941 and FE@SNAP. The role of MCHR1 in brown adipose tissue, especially the involvement in glycolytic activity and glucose transporter expression is yet unexplored.

As accumulation of the MCHR1 PET-tracers were found in brown adipose tissue of naïve rats, specific binding to brown adipocytes was investigated *in vitro*. In competition binding experiments, the MCHR1 antagonist led to ~23% blocking of [ $^{11}\text{C}$ ]SNAP-7941 accumulation evincing specific binding to brown adipocytes. This finding points at MCHR1 expression in brown adipocytes and a subsequent involvement of the melanin-concentrating hormone system in brown fat depots. Western Blot analysis proved the expression of the MCHR1 in murine brown adipocytes. In this respect, our findings support the initial theory of Ito *et al.* assuming that the anti-obesity effect of MCHR1 antagonists is not limited to a central action, but MCHR1 antagonists may also act peripherally in BAT. (21) Expression of functional MCHR1 in rat white adipocytes has previously been demonstrated and a peripheral role for MCH in adipocytes in addition to its centrally mediated effects was already proposed by Bradley *et al.* (19, 39) [ $^{11}\text{C}$ ]SNAP-7941 binding to brown adipocytes was blocked to a minor proportion by both the selective ADRB3 agonist CL 316,243 and the non-selective antagonist (S)-propranolol, demonstrating the superior affinity of [ $^{11}\text{C}$ ]SNAP-7941 towards MCHR1 compared to ADRB3. As (S)-propranolol displays even higher affinity for the adrenergic beta-1 and beta-2 receptor, [ $^{11}\text{C}$ ]SNAP-7941 binding to adrenergic beta receptor subtypes other than beta-3 can additionally be excluded. (40) However, relatively high non-displaceable binding was found, which may be due to unspecific accumulation in lipids within brown adipocytes.

Moreover, these *in vitro* results are in accordance with the previously performed *in vivo* experiments administering [ $^{18}\text{F}$ ]FE@SNAP to conscious animals without the use of anesthesia, where significant blocking was achieved by a pharmacological dose SNAP-7941. (30) Contradictory results were

obtained from  $\mu$ PET imaging, where binding enhancement of [ $^{11}\text{C}$ ]SNAP-7941 in BAT was shown after administration of a pharmacological dose of the unlabeled compound. PET imaging in small animals requires anesthesia in order to prevent laboratory animals from moving during the examination. However, anesthesia bears the disadvantage of possible molecular alterations, which may affect the examination's outcome, as it is already well-established for brain PET imaging. (41) Effects of isoflurane, the used anesthetic agent within the mentioned *in vivo* study, on ADRB3 and/or MCHR1 expression are not described, though potential effects cannot be excluded.

Investigation of specific binding to brown adipocytes was solely performed for [ $^{11}\text{C}$ ]SNAP-7941, as extensive *in vitro* and *in vivo* investigations evinced the superior properties of [ $^{11}\text{C}$ ]SNAP-7941 compared to the fluoro-ethylated analogue regarding radiochemical yield, metabolic stability, target affinity, selectivity and imaging contrast. (29) Thus, [ $^{18}\text{F}$ ]FE@SNAP was not further evaluated in this context.

The value of PET for BAT research was ultimately recognized when the radiolabeled glucose-analogue, [ $^{18}\text{F}$ ]FDG was introduced for imaging and quantification of BAT activation. Although primarily perceived as a clinical tool, PET employing specific tracers can also add to basic research. In this way, MCHR1 PET imaging provided first evidence for MCHR1 expression in BAT and will contribute to the elucidation of the MCHR1 axis in BAT.

## 5 Conclusion

The present study aimed at enhancing the understanding of the interplay between MCHR1 ligands and the pharmacologically complex brown adipose tissue. Uptake of [ $^{11}\text{C}$ ]SNAP-7941 and [ $^{18}\text{F}$ ]FE@SNAP in rat BAT gave the initial hint for MCHR1 expression in BAT. The herein performed *in vitro* binding studies, demonstrating specific [ $^{11}\text{C}$ ]SNAP-7941 binding to brown adipocytes and superior selectivity towards MCHR1 compared to ADRB3, provide first evidence for a direct involvement of the MCH/MCHR1 system in brown adipose tissue.

## Author Contributions Statement

TB, CP and MM conceived the study and designed the experiments. TB and KB performed all the experiments. CP performed the radiosyntheses of [ $^{11}\text{C}$ ]SNAP-7941 and [ $^{18}\text{F}$ ]FE@SNAP. OCH and FWK provided brown pre-adipocytes and established the induction protocol. KP and HS synthesized precursor compounds for radiolabeling and standard compounds. TB and CP analyzed the data and

composed the draft. MM, KHW, WW, MH and HV helped with outcome interpretation and reviewed the manuscript. All authors have given approval to the final version of the manuscript.

### Conflict of Interest Statement

The authors declare that the research was conducted in the absence of any commercial or financial relationships that could be construed as a potential conflict of interest.

### Acknowledgements

The authors want to thank the production team of the General Hospital in Vienna for providing [ $^{18}\text{F}$ ]FDG. Verena Pichler, Thomas Zenz and Andreas Krcal are gratefully acknowledged for their organizational and technical support.

### References

- Chondronikola M, Volpi E, Borsheim E, Porter C, Annamalai P, Enerback S, et al. Brown adipose tissue improves whole-body glucose homeostasis and insulin sensitivity in humans. *Diabetes*. 2014;63(12):4089-99.
- Sammons MF, Price DA. Modulation of adipose tissue thermogenesis as a method for increasing energy expenditure. *Bioorganic & Medicinal Chemistry Letters*. 2014;24(2):425-9.
- Kiefer FW. The significance of beige and brown fat in humans. *Endocrine Connections*. 2017;6(5):R70-r9.
- Cypess AM, Lehman S, Williams G, Tal I, Rodman D, Goldfine AB, et al. Identification and importance of brown adipose tissue in adult humans. *The New England Journal of Medicine*. 2009;360(15):1509-17.
- van Marken Lichtenbelt WD, Vanhommerig JW, Smulders NM, Drossaerts JM, Kemerink GJ, Bouvy ND, et al. Cold-activated brown adipose tissue in healthy men. *The New England Journal of Medicine*. 2009;360(15):1500-8.
- Virtanen KA, Lidell ME, Orava J, Heglind M, Westergren R, Niemi T, et al. Functional brown adipose tissue in healthy adults. *The New England Journal of Medicine*. 2009;360(15):1518-25.
- Ouellet V, Labbé SM, Blondin DP, Phoenix S, Guérin B, Haman F, et al. Brown adipose tissue oxidative metabolism contributes to energy expenditure during acute cold exposure in humans. *The Journal of Clinical Investigation*. 2012;122(2):545-52.

- 384 8. Quarta C, Lodi F, Mazza R, Giannone F, Boschi L, Nanni C, et al. (11)C-meta-  
385 hydroxyephedrine PET/CT imaging allows in vivo study of adaptive thermogenesis and white-to-  
386 brown fat conversion. *Molecular Metabolism*. 2013;2(3):153-60.
- 387 9. Lin S-f, Fan X, Yeckel CW, Weinzimmer D, Mulnix T, Gallezot J-D, et al. Ex vivo and in  
388 vivo Evaluation of the Norepinephrine Transporter Ligand [(11)C]MRB for Brown Adipose Tissue  
389 Imaging. *Nuclear Medicine and Biology*. 2012;39(7):1081-6.
- 390 10. Hankir MK, Cowley MA, Fenske WK. A BAT-Centric Approach to the Treatment of  
391 Diabetes: Turn on the Brain. *Cell Metabolism*. 2016;24(1):31-40.
- 392 11. Cannon B, Nedergaard J. Brown adipose tissue: function and physiological significance.  
393 *Physiological Reviews*. 2004;84(1):277-359.
- 394 12. Fenzl A, Kiefer Florian W. Brown adipose tissue and thermogenesis. *Hormone Molecular*  
395 *Biology and Clinical Investigation*. 2014;19(1):25-37.
- 396 13. Nicholls DG. The hunt for the molecular mechanism of brown fat thermogenesis. *Biochimie*.  
397 2017;134:9-18.
- 398 14. Labbé SM, Caron A, Bakan I, Laplante M, Carpentier AC, Lecomte R, et al. In vivo  
399 measurement of energy substrate contribution to cold-induced brown adipose tissue thermogenesis.  
400 *The FASEB Journal*. 2015;29(5):2046-58.
- 401 15. Spiegelman BM, Flier JS. Obesity and the regulation of energy balance. *Cell*.  
402 2001;104(4):531-43.
- 403 16. Qu D, Ludwig DS, Gammeltoft S, Piper M, Pelleymounter MA, Cullen MJ, et al. A role for  
404 melanin-concentrating hormone in the central regulation of feeding behaviour. *Nature*.  
405 1996;380(6571):243-7.
- 406 17. Nahon JL. The melanocortins and melanin-concentrating hormone in the central regulation of  
407 feeding behavior and energy homeostasis. *Comptes Rendus biologies*. 2006;329(8):623-38;  
408 discussion 53-5.
- 409 18. Shimada M, Tritos NA, Lowell BB, Flier JS, Maratos-Flier E. Mice lacking melanin-  
410 concentrating hormone are hypophagic and lean. *Nature*. 1998;396(6712):670-4.
- 411 19. Bradley RL, Kokkotou EG, Maratos-Flier E, Cheatham B. Melanin-concentrating hormone  
412 regulates leptin synthesis and secretion in rat adipocytes. *Diabetes*. 2000;49(7):1073.
- 413 20. Szalai KK, Beke G, Eles J, Kitka T, Kovacs P, Nagy J, et al. Recent patents on novel MCH1  
414 receptor antagonists as potential anti-obesity drugs. *Recent patents on CNS drug discovery*.  
415 2014;9(2):122-40.

- 416 21. Ito M, Ishihara A, Gomori A, Matsushita H, Ito M, Metzger JM, et al. Mechanism of the anti-  
417 obesity effects induced by a novel melanin-concentrating hormone 1-receptor antagonist in mice.  
418 British Journal of Pharmacology. 2010;159(2):374-83.
- 419 22. Oldfield BJ, Giles ME, Watson A, Anderson C, Colvill LM, McKinley MJ. The  
420 neurochemical characterisation of hypothalamic pathways projecting polysynaptically to brown  
421 adipose tissue in the rat. Neuroscience. 2002;110(3):515-26.
- 422 23. Philippe C, Nics L, Zeilinger M, Kuntner C, Wanek T, Mairinger S, et al. Preclinical in vitro  
423 &in vivo evaluation of [11C]SNAP-7941 - the first PET tracer for the melanin concentrating  
424 hormone receptor 1. Nuclear medicine and biology. 2013;40(7):919-25.
- 425 24. Philippe C, Nics L, Zeilinger M, Schirmer E, Spreitzer H, Karanikas G, et al. Preparation and  
426 First Preclinical Evaluation of [18F]FE@SNAP: A Potential PET Tracer for the Melanin-  
427 Concentrating Hormone Receptor-1 (MCHR1). Scientia Pharmaceutica. 2013;81(3):625-39.
- 428 25. Philippe C, Schirmer E, Mitterhauser M, Shanab K, Lanzenberger R, Karanikas G, et al.  
429 Radiosynthesis of [11C]SNAP-7941-the first PET-tracer for the melanin concentrating hormone  
430 receptor 1 (MCHR1). Applied Radiation and Isotopes. 2012;70(10):2287-94.
- 431 26. Philippe C, Ungersboeck J, Schirmer E, Zdravkovic M, Nics L, Zeilinger M, et al.  
432 [18F]FE@SNAP-A new PET tracer for the melanin concentrating hormone receptor 1 (MCHR1):  
433 microfluidic and vessel-based approaches. Bioorganic & Medicinal Chemistry. 2012;20(19):5936-40.
- 434 27. Philippe C, Haeusler D, Fuchshuber F, Spreitzer H, Viernstein H, Hacker M, et al.  
435 Comparative autoradiographic in vitro investigation of melanin concentrating hormone receptor 1  
436 ligands in the central nervous system. European journal of pharmacology. 2014;735(Supplement  
437 C):177-83.
- 438 28. Zeilinger M, Dumanic M, Pichler F, Budinsky L, Wadsak W, Pallitsch K, et al. In vivo  
439 evaluation of radiotracers targeting the melanin-concentrating hormone receptor 1: [(11)C]SNAP-  
440 7941 and [(18)F]FE@SNAP reveal specific uptake in the ventricular system. Scientific Reports.  
441 2017;7(1):8054.
- 442 29. Philippe C, Zeilinger M, Dumanic M, Pichler F, Fetty L, Vranka C, et al. SNAPshots of the  
443 MCHR1: a Comparison Between the PET-Tracers [18F]FE@SNAP and [11C]SNAP-7941.  
444 Molecular Imaging and Biology. 2018.
- 445 30. Philippe C, Zeilinger M, Scherer T, Fürnsinn C, Dumanic M, Pilz J, Wadsak W, Hacker M,  
446 Mitterhauser M. MCHR1: a potential indicator for BAT activity. Nuklearmedizin. 2016;55(2):A78.
- 447 31. Baker JG. The selectivity of  $\beta$ -adrenoceptor agonists at human  $\beta(1)$ -,  $\beta(2)$ - and  $\beta(3)$ -  
448 adrenoceptors. British Journal of Pharmacology. 2010;160(5):1048-61.
- 449 32. Zeilinger M, Pichler F, Nics L, Wadsak W, Spreitzer H, Hacker M, et al. New approaches for  
450 the reliable in vitro assessment of binding affinity based on high-resolution real-time data acquisition

- of radioligand-receptor binding kinetics. *European Journal of Nuclear Medicine and Molecular Imaging Research*. 2017;7(1):22.
33. Vranka C, Dumanic M, Racz T, Pichler F, Philippe C, Balber T, et al. A new method measuring the interaction of radiotracers with the human P-glycoprotein (P-gp) transporter. *Nuclear Medicine and Biology*. 2018;60:29-36.
34. Wadsak W, Mitterhauser M. Basics and principles of radiopharmaceuticals for PET/CT. *European Journal of Radiology*. 2010;73(3):461-9.
35. Mitterhauser M, Wadsak W. Imaging biomarkers or biomarker imaging? *Pharmaceuticals*. 2014;7(7):765-78.
36. Schade KN, Baranwal A, Liang C, Mirbolooki MR, Mukherjee J. Preliminary evaluation of beta3-adrenoceptor agonist-induced 18F-FDG metabolic activity of brown adipose tissue in obese Zucker rat. *Nuclear Medicine and Biology*. 2015;42(8):691-4.
37. Mirbolooki MR, Upadhyay SK, Constantinescu CC, Pan ML, Mukherjee J. Adrenergic pathway activation enhances brown adipose tissue metabolism: a [18F]FDG PET/CT study in mice. *Nuclear Medicine and Biology*. 2014;41(1):10-6.
38. Mirbolooki MR, Constantinescu CC, Pan ML, Mukherjee J. Quantitative assessment of brown adipose tissue metabolic activity and volume using 18F-FDG PET/CT and beta3-adrenergic receptor activation. *European Journal of Nuclear Medicine and Molecular Imaging Research*. 2011;1(1):30.
39. Bradley RL, Mansfield JP, Maratos-Flier E, Cheatham B. Melanin-concentrating hormone activates signaling pathways in 3T3-L1 adipocytes. *American Journal of Physiology Endocrinology and Metabolism*. 2002;283(3):E584-92.
40. Hoffmann C, Leitz M, Oberdorf-Maass S, Lohse M, Klotz K-N. Comparative pharmacology of human  $\beta$ -adrenergic receptor subtypes—characterization of stably transfected receptors in CHO cells. *Naunyn-Schmiedeberg's archives of pharmacology*. 2004;369(2):151-9.
41. Alstrup AK, Smith DF. Anaesthesia for positron emission tomography scanning of animal brains. *Laboratory Animals*. 2013;47(1):12-8.
42. Méjean A, Guillaume J-L, Strosberg AD. Carazolol: a potent, selective  $\beta$ 3-adrenoceptor agonist. *European Journal of Pharmacology: Molecular Pharmacology*. 1995;291(3):359-66.
43. Blin N, Camoin L, Maigret B, Strosberg AD. Structural and conformational features determining selective signal transduction in the beta 3-adrenergic receptor. *Molecular Pharmacology*. 1993;44(6):1094-104.
44. Emorine LJ, Marullo S, Briand-Sutren MM, Patey G, Tate K, Delavie-Klutchko C, et al. Molecular characterization of the human beta 3-adrenergic receptor. *Science*. 1989;245(4922):1118-21.



Figures and Tables

Table 1:  $K_i$  values are given in nM or  $\mu$ M, respectively and were obtained from three independent experiments performed in triplicates. Reference values for standard compounds were taken from literature. (40, 42-44)  $K_i$  values for SNAP-7941 and FE@SNAP towards MCHR1 were previously described. (28) (n.a.: not available, n.d.: not determined)

compound	ADRB3 experimental	ADRB3 reference	MCHR1	ADRB3/MCHR1
carazolol	$2.0 \pm 0.3$ nM	2.0 nM	n.d.	n.d.
pindolol	$44.5 \pm 11.8$ nM	44.1 nM and 11 nM	n.d.	n.d.
(S)-propranolol	$67.4 \pm 14.4$ nM	186 nM and 145nM	n.d.	n.d.
SNAP-7941	$14.5 \pm 0.3$ $\mu$ M	n.a.	$3.91 \pm 0.74$ nM	$\sim 3708$
FE@SNAP	$65.1 \pm 2.9$ $\mu$ M	n.a.	$9.98 \pm 1.12$ nM	$\sim 6523$

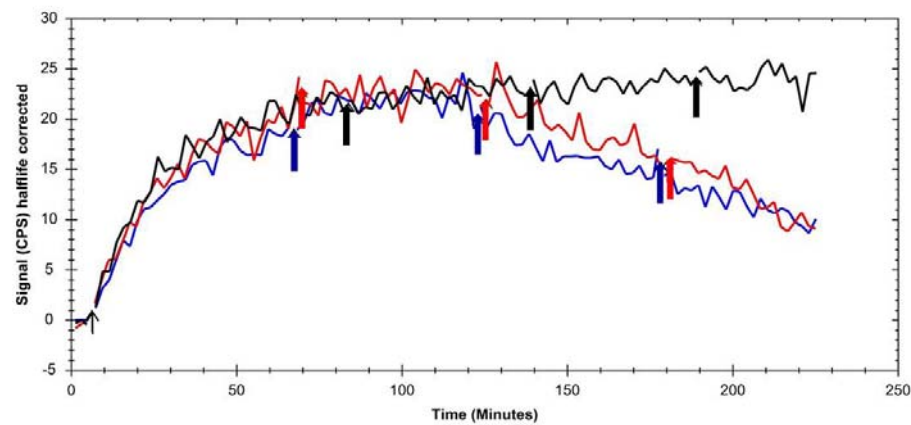


Figure 1: Overlay of kinetic binding towards CHO-K1-ADRB3 and displacement curves of [ $^{125}$ I]iodocyanopindolol using the MCHR1 ligands SNAP-7941 (red line) and FE@SNAP (blue line) and ethanol (black line) as the respective vehicle control. Arrows indicate the addition time points of the MCHR1 ligands and vehicle, respectively.

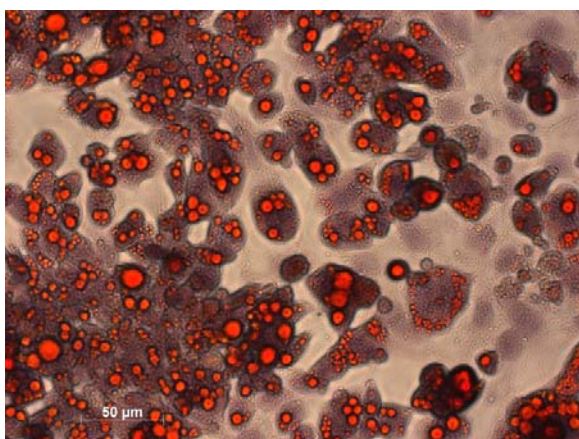


Figure 2: Histological staining of lipids in mature brown adipocytes was performed using Oil Red O and haematoxylin for counterstaining. Lipids appear in red and chromatin in bluish.

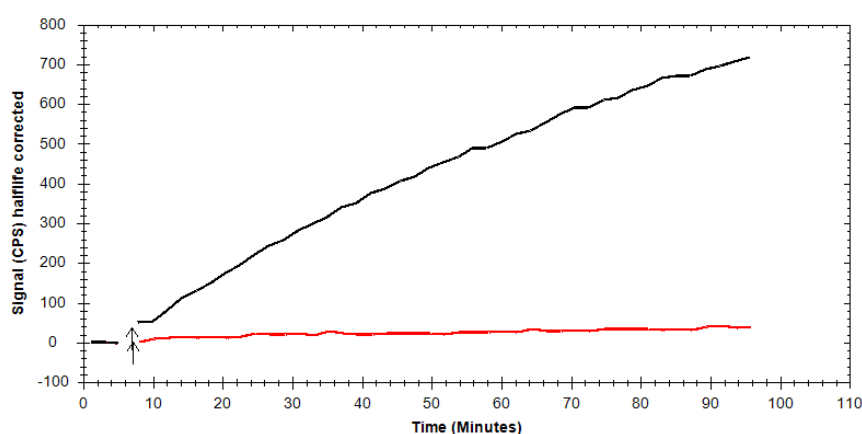


Figure 3: Representative, background-corrected time-activity curves of [ $^{18}\text{F}$ ]FDG uptake by mature brown adipocytes (black) and pre-adipocytes (red) are shown as overlay.

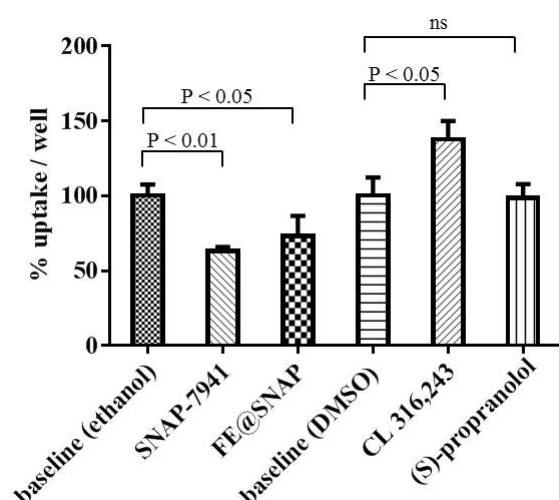


Figure 4: Baseline refers to 60 min [ $^{18}\text{F}$ ]FDG uptake in the presence of vehicle control and was normalized to 100% uptake/well. Data is presented as mean  $\pm$  standard deviation (SD) from at least three independent experiments.

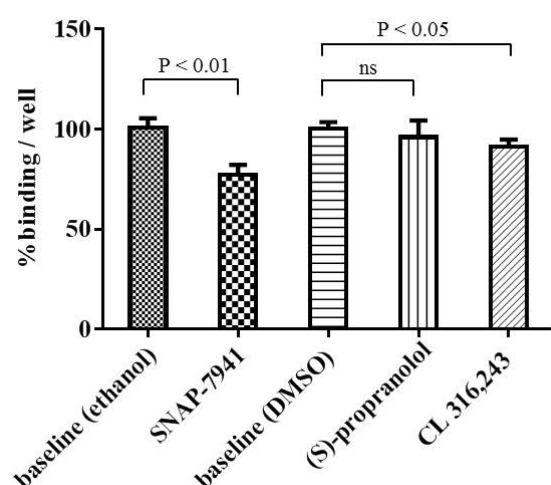
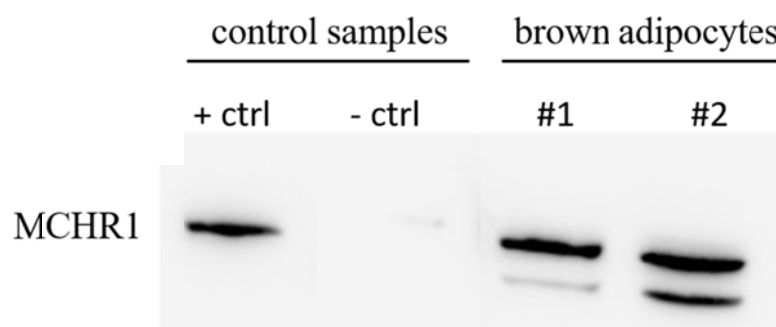


Figure 5: [ $^{11}\text{C}$ ]SNAP-7941 binding to brown adipocytes in the presence of vehicle control (ethanol or DMSO) represents baseline (100% binding/well). SNAP-7941 (2  $\mu\text{M}$ ) significantly reduced [ $^{11}\text{C}$ ]SNAP-7941 binding by  $22.9 \pm 5.0\%$ . The effect of the ADRB3 agonist CL 316,243 was less pronounced and the non-selective adrenergic receptor beta antagonist propranolol did not alter [ $^{11}\text{C}$ ]SNAP-7941 binding. Data is presented as mean  $\pm$  standard deviation (SD) from at least three independent experiments.

518



519

520 Figure 6: Western Blot analysis of MCHR1 expression in murine brown adipocyte lysates: brown  
 521 adipocytes were either lysed using a dedicated kit (lysate #1) or using RIPA buffer (lysate #2).  
 522 Mouse tongue was used as MCHR1-positive sample (+ ctrl) and mouse spleen as MCHR1-negative  
 523 control (- ctrl). Both control samples were extracted using RIPA buffer. Data is presented as cropped  
 524 image format.

## 4. UNPUBLISHED RESULTS

---

The presented, unpublished experimental results are related to the project “**The Adenosine A3 Receptor in Oncology – A completely new Target for PET Imaging**”, which was funded by the Austrian Science Fund (FWF P26502-B24, awarded to Dr. Markus Mitterhauser).

### 4.1. *Ex vivo* tumor autoradiography

CB17-SCID beige mice were inoculated with  $2 \times 10^6$  HT-29 and  $2 \times 10^6$  CHO-K1 cells (cf. Manuscript #1 Tumor Grafting). After [ $^{18}\text{F}$ ]FE@SUPPY  $\mu\text{PET}$  acquisition, animals were sacrificed, and organs were removed. Tumors, obtained from the same mouse (right and left flank, respectively), were quick-frozen ( $-40^\circ\text{C}$ , 2-methylbutane), cryo-sectioned and incubated on the same phosphor storage screen in a dedicated lead shielded cassette overnight. After exposure, read-out of the plate was performed using a Cyclone Phosphor Imager (Perkin Elmer, Waltham, USA) and whole tumor sections were determined as regions of interest. Digital light units per  $\text{mm}^2$  (DLU/ $\text{mm}^2$ ) were obtained for HT-29 tumor sections and CHO-K1 sections, whereby the light intensity of the stored energy is proportional to the radioactivity in the respective tissue section. Accordingly, mean DLU/ $\text{mm}^2$  (CHO-K1  $62,129 \pm 39,977$  versus HT-29  $126,099 \pm 21,733$ ) pointed at a 2-fold increased accumulation of [ $^{18}\text{F}$ ]FE@SUPPY in HT-29 tumors (target region) compared to CHO-K1 tumor grafts (Figure 6).

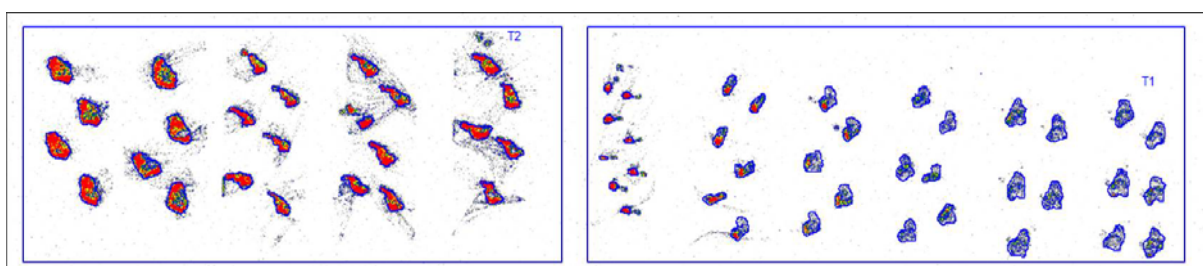


**Figure 6:** *Ex vivo* autoradiography of HT-29 tumor sections (left panel) and CHO-K1 tumor sections (right panel): representative whole phosphor storage screen shown.

### 4.2. [ $^{18}\text{F}$ ]FE@SUPPY uptake in mouse brain

Additionally to the uptake of [ $^{18}\text{F}$ ]FE@SUPPY (standardized uptake value, SUV) in different organs (cf. Manuscript#1, section: *In Vivo* Imaging), [ $^{18}\text{F}$ ]FE@SUPPY uptake was investigated in specific brain regions applying an atlas-based segmentation method using Pmod Software 3.8 (PMOD Technologies LLC). Brain accumulation was low ( $\text{SUV} < 1$ ), but there was a trend towards specific binding

in all investigated brain regions (Figure 7). However, blocking using the A<sub>3</sub>AR antagonist MRS1523 was not significant, partly due to the small sample size.

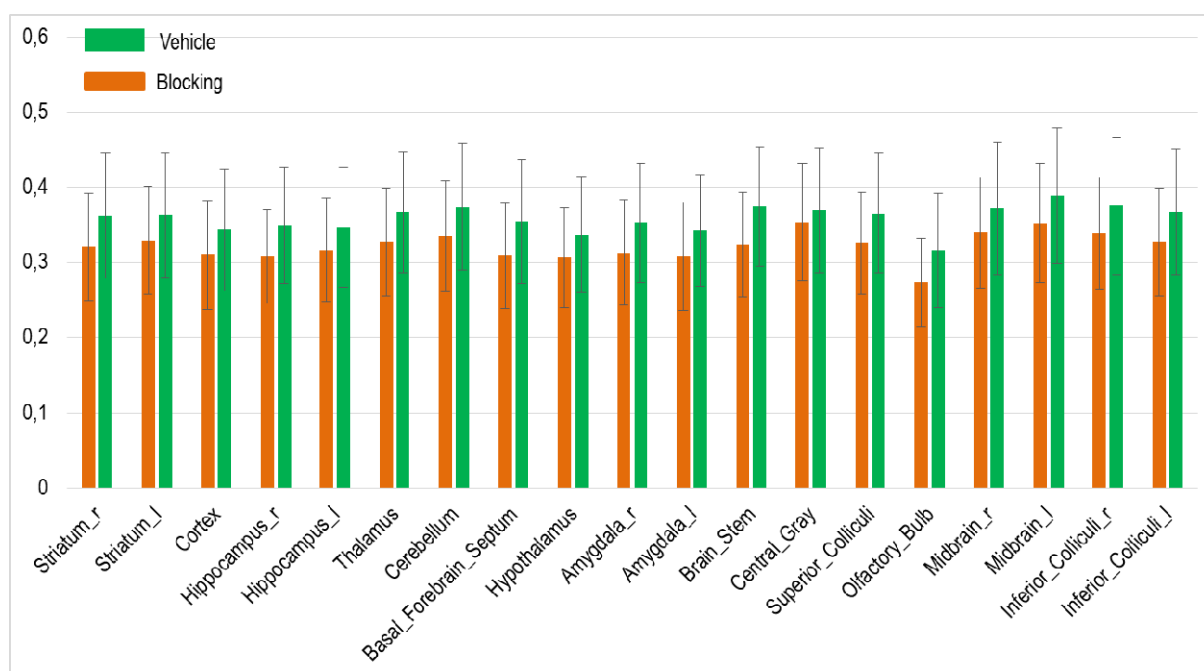


**Figure 7:** Body weighted standardized uptake values under baseline (vehicle) and blocking (MRS1523) conditions are plotted for different brain regions (mean ± SD, n=3).

### 4.3 *Ex vivo* metabolic stability

Six BALB/c mice were injected with ~ 10 MBq [<sup>18</sup>F]FE@SUPPY and sacrificed after 2, 5 and 10 min post injection. Blood and A<sub>3</sub>AR expressing organs (lung, brain, heart) were harvested, immediately subjected to equivalent amounts of methanol:acetonitrile (1:10) and 0.9% saline on ice for precipitation and homogenized using an electric tissue grinder (Ultra-Turrax® IKA laboratory equipment, Germany). Blood and tissue homogenates were centrifuged (23,000 x g, 4°C) until a clear supernatant was obtained. The supernatant was subjected to HPLC coupled to a radioactivity detector (cf. Manuscript #1, section: *Ex Vivo* Blood Stability). Percentage of intact parent compound ([<sup>18</sup>F]FE@SUPPY) was determined in blood, lung, brain and heart for the following time points: 2, 5 and 10 min post injection (Figure 8). [<sup>18</sup>F]FE@SUPPY was rapidly degraded in blood, as high amounts of hydrophilic metabolites were observed, resulting in only 12% intact tracer after 10 min. Approximately 70% intact tracer were determined in lung and heart after 10 min, whereas [<sup>18</sup>F]FE@SUPPY remained largely unchanged in brain.

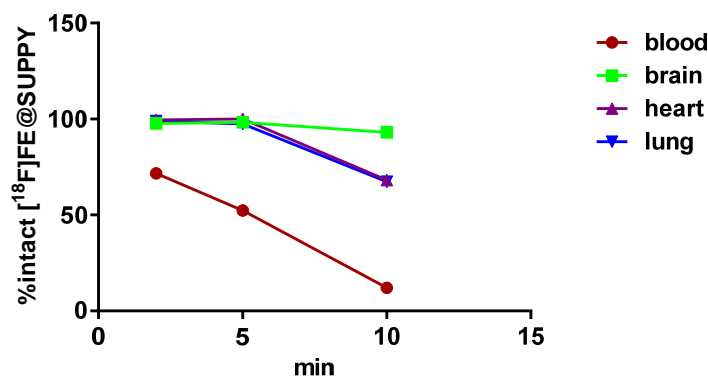


**Figure 8:** Mean values of percentage of intact (unmetabolized) PET-tracer are plotted for 2, 5 and 10 min p.i (n=2 for each organ and time point).

## 4.4 Cell binding and internalization studies

[<sup>125</sup>I]-AB-MECA, an A<sub>3</sub>AR agonist, serves as a well-characterized radioligand for the A<sub>3</sub>AR. Moreover, receptor-internalization is a well described phenomenon for most G-protein coupled receptors as well as for the A<sub>3</sub>AR. (107) Binding of [<sup>125</sup>I]-AB-MECA to A<sub>3</sub>ARs and internalization rates were investigated using CHO-K1 cells transfected with the human A<sub>3</sub>AR (positive control). Parent CHO-K1 served as the respective negative control (no target expression). To this, cells were grown in 6-well plates and incubated with 2.4 kBq [<sup>125</sup>I]-AB-MECA per well for 1 h at 37°C. After radioligand incubation, supernatants, containing free radioligand, were collected. Cells were washed with phosphate buffered saline, followed by an acidic glycine wash (membrane-bound fraction). Finally, cells were lysed using sodium hydroxide (internalized fraction).

First, potential solvent effects on the internalization rate of [<sup>125</sup>I]-AB-MECA were determined. Thus, radioligand incubation was performed in the absence or presence of 0.1% dimethyl sulfoxide (DMSO). Despite the low DMSO concentration, a significant decrease in the receptor-bound fraction and an increase in the internalized fraction by approximately the same amount were observed. No significant membrane-binding and internalization rates were determined in the control cell line (parent CHO-K1) indicating negligible unspecific membrane-binding of [<sup>125</sup>I]-AB-MECA (Figure 9). Evidently, DMSO increases cell membrane permeability and thereby internalization rates of [<sup>125</sup>I]-AB-MECA in CHO-K1-hA<sub>3</sub>AR cells.

Blocking experiments were performed as described above in the presence of 1 μM FE@SUPPLY using DMSO as vehicle (final DMSO concentration was 0.1% in an assay volume of 1 mL). Therefore, baseline was assessed in the presence of 0.1% DMSO. FE@SUPPLY reduced hA<sub>3</sub>AR receptor-binding of [<sup>125</sup>I]-AB-MECA and almost quantitatively blocked the internalization of [<sup>125</sup>I]-AB-MECA in

CHO-K1-hA<sub>3</sub>AR cells (Figure 10). This data indicates specific binding of FE@SUPPY and competitive antagonism for hA<sub>3</sub>AR occupancy.

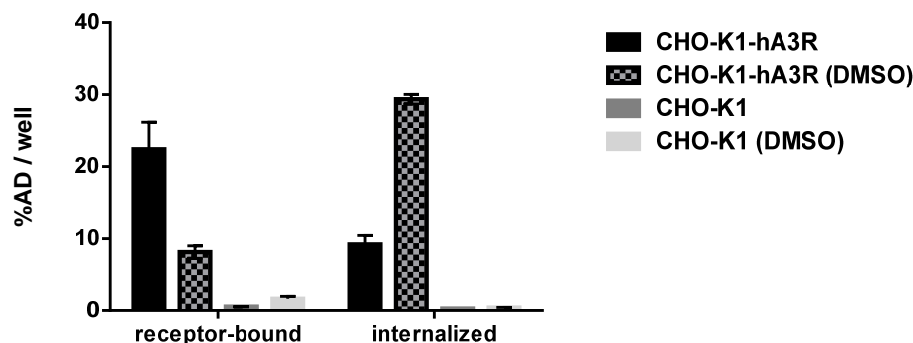


**Figure 9:** Effect of dimethyl sulfoxide on the internalization rate of [<sup>125</sup>I]-AB-MECA. Percentage of applied dose per well (%AD / well) is plotted as mean values  $\pm$  SD (experiment performed in triplicates).

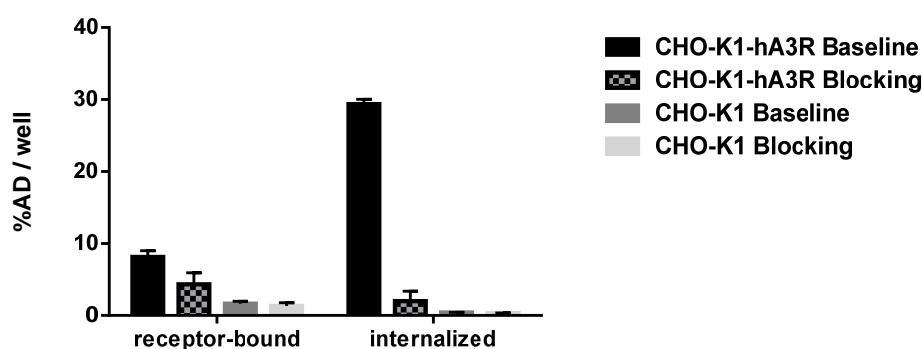


**Figure 10:** Blocking was performed using 1  $\mu$ M FE@SUPPY. Baseline was conducted in the presence of 0.1% DMSO. Mean values of %AD / well  $\pm$  SD from two independent experiments performed in triplicates are plotted.

Additionally to the model cell lines, [<sup>125</sup>I]-AB-MECA binding to hA<sub>3</sub>ARs and internalization rates were determined for human cancer cell lines (HT-29 and PC-3). [<sup>125</sup>I]-AB-MECA receptor-binding to HT-29 and PC-3 cells was minor and comparable to the hA<sub>3</sub>AR-nonexpressing CHO-K1 cell line (Figure 11). This data indicates a lack of hA<sub>3</sub>AR expression in the investigated tumor cell lines.



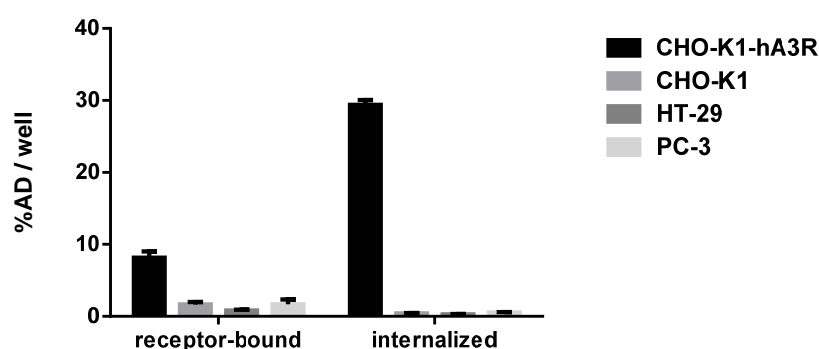


**Figure 11:** [ $^{125}$ I]I-AB-MECA receptor-binding to tumor cells (HT-29, PC3) and respective internalization rates (mean values of %AD / well  $\pm$  SD, n=2 in triplicates) .

## 4.5 Characterization of A<sub>3</sub>AR expression in multicellular spheroids

Stable and uniform HT-29 spheroids were obtained within four days using the hanging drop method (500 cells per 10  $\mu$ L). HT-29 spheroids were subsequently transferred to non-cell culture treated 96-well plates and maintained in growth medium. HCT-116 spheroid formation was achieved within 24 h using pellet culture in round bottomed 96-well plates coated with 1.5% agarose (5,000 cells per well).

HT-29 and HCT-116 spheroids were grown to a size of 600  $\mu$ m and fixed using 4% paraformaldehyde for 1 h, followed by 20% sucrose solution. Spheroids were embedded in mounting medium (Tissue-Tek® O.C.T™) prior to frozen sectioning using a cryotom (Microm HM 560, Thermo Scientific). 10  $\mu$ m sections were mounted on positively charged glass slides (Menzel Gläser Superfrost® Plus) and stored at -80°C until processing. Haematoxylin and eosin staining of spheroid sections was performed according to a standard protocol to investigate cell morphology in multicellular tumor spheroids (Figure 12). Nuclear staining was less pronounced in the spheroid core indicating cell damage.

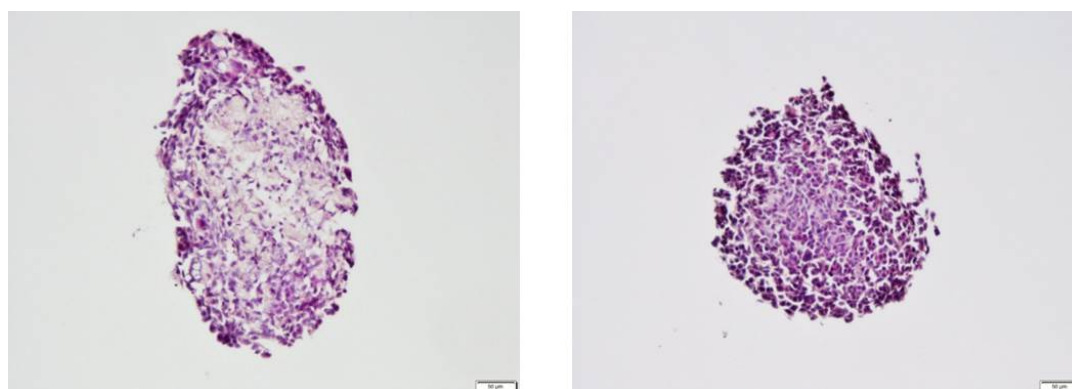


**Figure 12:** Haematoxylin (purple, nuclei) and Eosin (pink, cytoplasm) staining of HCT-116 tumor spheroid (left panel) and HT-29 tumor spheroid (right panel). Scale bar refers to 50  $\mu$ m.

To investigate changes in A<sub>3</sub>AR protein expression, cell monolayers and spheroids of different size (300  $\mu$ m, 500  $\mu$ m, 800  $\mu$ m) were lysed using radioimmunoprecipitation assay (RIPA) buffer and protease inhibitors. Samples were shaken at 4°C for 30 min and subsequently centrifuged (12,000 rpm, 20 min). Protein concentrations of cell and spheroid extracts were determined using the bicinchoninic acid (BCA) assay. Gel electrophoresis (20  $\mu$ g protein per well) was performed under reducing conditions (Laemmli buffer containing mercaptoethanol). After semi-dry transfer, nitrocellulose blotting membranes were blocked with 5% dry milk powder at room temperature, followed by primary antibody incubation at 4°C overnight (polyclonal rabbit anti human A<sub>3</sub>AR, 1:750, sc-13938, Santa Cruz Biotechnology). Secondary antibody incubation was performed for 1 h at room temperature (goat anti rabbit IgG, horse radish peroxidase (HRP) conjugate, 1:2500). The A<sub>3</sub>AR expression pattern differed between the two colorectal cancer cell lines: A<sub>3</sub>AR protein expression was minor in HCT-116 cell monolayers, but increased with spheroid size. Whereas, highest amounts of A<sub>3</sub>AR protein were detected in cell lysates and protein expression varied in spheroids of different size.

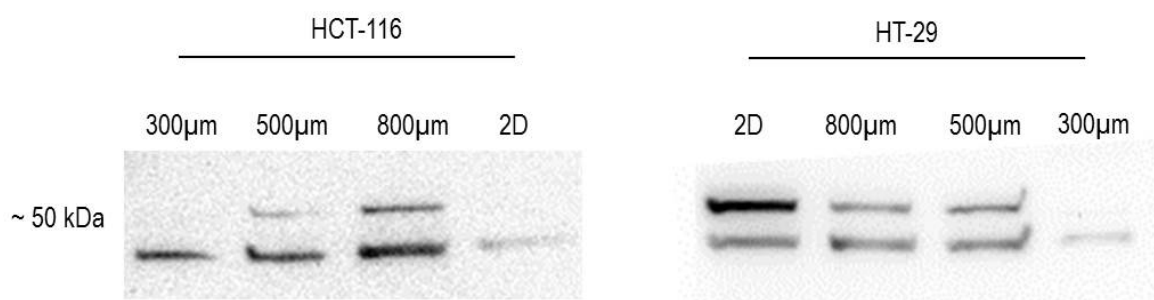


**Figure 13:** Relative A<sub>3</sub>AR protein expression analysis of HCT-116 and HT-29 cell lysates and respective lysates derived from spheroids of different size (300  $\mu$ m, 500  $\mu$ m and 800  $\mu$ m). The expected molecular weight of the A<sub>3</sub>AR is 36 kDa. An additional band of higher molecular weight was detected in some samples and is probably indicating a post-translational modified A<sub>3</sub>AR protein.

## 5. DISCUSSION

---

### 5.1 Characterization of the Target

Target expression on a protein level is one main prerequisite for a successful imaging strategy. However, elevated mRNA levels do not necessarily correspond to increased protein concentration. The regulation of translation is complex, and the synthesis rate of proteins not only depends on the amount of mRNA present but also on environmental factors such as nutrient deprivation, stress and cell growth. For example, to maintain homeostasis and rapidly adapt to physiological changes, the cell may compensate for increased transcription by regressing protein synthesis. (50, 187, 188) Due to the described discrepancy between mRNA and protein levels, solely biochemical methods determining protein expression were used for target characterization during the course of this thesis and gene expression analyses such as polymerase chain reaction (PCR) were refrained.

TSPO expression was demonstrated in colorectal cancer specimens by means of immunohistochemistry (IHC) and Western Blot (WB) analyses (Manuscript #3). The comparison with healthy specimens from the same patients (n=2), respectively, showed minor (IHC) to absent (WB) TSPO expression, which strongly suggests TSPO as a suitable imaging biomarker in colorectal cancer. TSPO expression was additionally detected in the colon adenocarcinoma cell line HT-29 by means of Western Blot, which provided an appropriate tool for studying [ $^{18}\text{F}$ ]FEPPA binding to colorectal cancer cells.

The thorough characterization of a target to the best knowledge may be decisive in the understanding and interpretation of PET imaging data. This is especially true for TSPO, as a mutation within the TSPO gene results in two different binding sites with either high or low binding affinity. (135) Thus, this polymorphism exerts tremendous impact on TSPO PET-tracer binding and has to be considered (cf. target-ligand-interactions).

A<sub>3</sub>AR protein expression was investigated in detail in HT-29 cells by several biochemical techniques (Manuscript #1). Western Blot and fluorescence-activating cell sorting (FACS) analysis demonstrated high A<sub>3</sub>AR protein expression in HT-29 cells. Interestingly, an additional band (higher than the predicted molecular weight of 36 kDa) was detected in HT-29 cells, but not found in CHO-K1 cells transfected with the human A<sub>3</sub>AR transcript. This data proposes a post-translational modified version of the A<sub>3</sub>AR in cancer cells. Fluorescence staining and subsequent microscopy provided insights into

the cellular localization of the A<sub>3</sub>AR: A pronounced staining of the cell membrane was observed, demonstrating expression of the A<sub>3</sub>AR on the cell surface, which is a typical feature of GPCRs. For that reason, HT-29 cell line was subsequently chosen for tumor graft. However, even a thorough characterization ultimately fails when targets are not sufficiently conserved upon tumor cell transplantation in animals. This is one of the main limitations of the chosen animal model (cf. characterization of the target-ligand interaction). Moreover, target expression in cancer cell monolayers (two-dimensional cell culture) may differ from those in three-dimensional tumor grafts. Therefore, A<sub>3</sub>AR protein expression was later on investigated in multicellular tumor spheroids derived from HT-29 and HCT116 cells (Figure 12), providing insights into varying protein expression between two- and three-dimensional cell growth (Figure 13).

In general, the applied antibody-based biochemical techniques display semi-quantitative methods. Thus, only relative estimations about target protein amounts can be made. However, high target abundance is significant to deliver sufficient PET signal. Regarding [<sup>18</sup>F]FDG, the detection limit of PET is in the magnitude of 10<sup>5</sup> to 10<sup>6</sup> malignant cells depending on the metabolic rate of the specific cancer and provided that the minimum [<sup>18</sup>F]FDG uptake corresponds to an activity of approximately 50 Bq/mL. (189) Unfortunately, there is little data on receptor-targeted PET-tracers, and the target quantity which must be expressed per cell to yield in a detectable PET signal is largely unknown.

## 5.2 Characterization of the Radioligand

A radioligand is characterized by its physicochemical and pharmacokinetic properties, which directs drug delivery. Unfavorable pharmacokinetics and extensive metabolism hamper a successful imaging strategy and thus, have to be investigated to ensure sufficient PET-tracer delivery to the target tissue. *In vitro* stability tests usually do not account for the metabolic extent, a PET-tracer undergoes *in vivo*. Accordingly, significantly reduced metabolic stability of [<sup>18</sup>F]FE@SUPPY was found in mouse blood *in vivo* compared to *in vitro* incubation with mouse plasma and liver microsomes (Manuscript #1).

Moreover, interactions with efflux transporters are a crucial issue regarding the successful delivery of a PET-tracer to its target tissue. High densities of multi drug resistance protein 1 (para glycoprotein, P-gp) are described for brain and various tumors which are of great importance in the development of PET-tracers for central and oncologic applications. Within this thesis, a new kinetic model for the reliable identification of P-gp substrates, P-gp inhibitors and PET-tracers not interacting with P-gp was presented (Manuscript #2). The distinct experimental approaches using MDCKII-WT or pre-blocked MDCKII-hMDR1 cells resulted in the same main outcome (classification of [<sup>11</sup>C]SNAP-7941 and [<sup>18</sup>F]FE@SNAP as potent P-gp substrates), supporting the versatility of this new *in vitro* method. Proof of concept was demonstrated by conventional internalization assays and by  $\mu$ PET imaging in rodents using tariquidar as efflux inhibitor. As canine kidney cells transfected with the human MDR1 (P-gp) protein are used, the translational value regarding the prediction of the PET-tracer's performance in humans is high. However, species differences regarding efflux transporters are described for humans and rodents. (53) Thus, binding to human P-gp does not necessarily correlate with the outcome in small animal experiments, as it was observed for [<sup>11</sup>C]Me@HAPTHI. Limitations of the *in vitro* method may also include the disregard of heterogeneity in P-gp distribution, which is described for the rat brain: Regional differences in brain uptake – based on differences in P-gp expression – are not considered. (190) One advantage of the presented kinetic model is the direct application of the PET-tracer in nanomolar concentration mimicking *in vivo* conditions similar to the real conditions in PET acquisition. The further development of this kinetic model as an indirect (competitive) binding assay would be favorable, as unlabeled compounds could be tested. This would enhance the significance of this new *in vitro* method for central drug development in general. Moreover, the proposed method bears a significant application potential as cell lines transfected with other efflux transporters of the ATP-binding cassette (ABC) transporter family can be applied in the same manner as described for MDCKII-hMDR1 cells.

## 5.3 Characterization of the Target-Ligand-Interaction

Competitive binding studies using cell membrane preparations were applied for:

- (i) selectivity tests of FE@SUPPY on human adenosine receptor subtypes,
- (ii) the characterization of FEPPA binding behavior towards the three distinct TSPO phenotypes (HAB, MAB, LAB), and
- (iii) affinity tests of SNAP-7941 and FE@SNAP towards adrenergic beta-3 receptors.

Unlike adenosine receptor expressing CHO-K1 cell membranes, which are commercially available, adrenergic beta-3 receptor expressing membranes had to be prepared from respective CHO-K1 cells, as commercially available ones showed insufficient protein expression. Due to the polymorphism within the TSPO gene, platelet membranes had to be prepared in-house from blood samples after subject genotyping. This procedure is laborious and time consuming. However, human blood sampling was essential to investigate the different binding phenotypes. Generally, competitive binding studies display an indirect method thereby delivering  $K_i$  values and relying on a radioligand that competitively binds the same receptor site (binding pocket). Moreover, in contrast to intact cells, cell membranes allow for studying pure receptor-ligand interactions without the involvement of passive diffusion or active transportation. We conclude that competitive binding studies are useful for pure affinity determinations and bear the advantage to test unlabeled compounds, which is crucial in early phases of PET-tracer development.

Binding studies performed on whole cells also involve diffusion and transportation as well as specific retention processes as internalization or metabolic trapping. Internalization experiments using the  $A_3AR$  model ligand [ $^{125}I$ ]-AB-MECA and CHO-K1-h $A_3AR$  cells revealed tremendous solvent effects on internalization rate (Figure 9). Surprisingly, binding and internalization of [ $^{125}I$ ]-AB-MECA was minor using cancer cells. This fact would be interpreted as no or minor target expression (Figure 11). This data is contradictory to those obtained by biochemical techniques that demonstrated  $A_3AR$  expression in HT-29 cells. There is a discrepancy between antibody-based detection methods and ligand binding techniques mainly investigating binding sites. Michel M.C. *et al.* recently claimed that *"lack of selectivity appears to be the rule rather than the exception for antibodies against GPCRs"*. (191) One more possible explanation may be that the h $A_3AR$  transcript used for transfection (CHO-K1-h $A_3AR$ ) differs in protein sequence or post-translational modifications from the  $A_3AR$  protein expressed in cancer cells.

Recently, a new technology has been developed that enables kinetic binding studies by using a single radioligand concentration (LigandTracer®technology). In this way, association and dissociation

phases can be observed in real-time with minimal effort. This technique was applied for exploring [ $^{18}\text{F}$ ]FEPPA association and displacement kinetics demonstrating binding specificity to colon cancer cells (Manuscript #3). Moreover, binding of [ $^{18}\text{F}$ ]FE@SNAP and [ $^{11}\text{C}$ ]SNAP-7941 to CHO-K1 (unspecific binding) and CHO-K1 cells expressing either MCHR1 (specific binding) or MCHR2 (unselective binding) was investigated (Manuscript #4). Since humans express both melanin-concentrating hormone receptors (MCHR1 and MCHR2), determination of tracer selectivity is essential for potential first-in-man use. Moreover, glucose turnover of brown adipocytes was investigated by tracing [ $^{18}\text{F}$ ]FDG uptake and subsequent trapping, which was also mirrored in linear uptake and trapping kinetics (Manuscript #5). Additionally, a completely new approach, investigating binding to efflux transporters was established using this LigandTracer® technology (Manuscript #2, cf. characterization of the radioligand). Kinetic cell binding measurements provide time-activity-curves, which are more informative than simple single time-point uptake experiments. However, using LigandTracer®, only cell-associated radioactivity is measured. The radioactive signal thus comprises receptor-bound and intracellular radioactive fractions as well as unspecific membrane binding and diffusion. Displacement conditions are of necessity to subsequently prove specific binding.

To investigate radioligand binding in cell-connection, tissue autoradiography is one of the most useful techniques, which is characterized by its high sensitivity. Insignificant (barely visible and quantifiable) [ $^{18}\text{F}$ ]FE@SUPPLY uptake in tumor tissue and no differentiation between HT-29 cells (colon cancer cells) and CHO-K1 control cells were detected by  $\mu\text{PET}$  *in vivo*. Subsequent *ex vivo* autoradiography of the harvested tumor specimens evinced 2-fold higher accumulation of [ $^{18}\text{F}$ ]FE@SUPPLY in HT-29 tumor mass compared to CHO-K1 cell mass. Nevertheless, target protein expression in HT-29 tumor grafts is too low to pursue an *in vivo* PET imaging strategy. As a conclusion, due to the high sensitivity, *ex vivo* autoradiography might still deliver quantitative data of radiotracer binding, if the target density or expression is too low for *in vivo*  $\mu\text{PET}$  imaging.

*In vitro* binding techniques using cells omit complex tissue-specific interactions and signaling processes that are taking place in the living organism. To assess *in vivo* molecular mechanisms including blood flow, drug delivery and metabolism, PET imaging in small animals is indispensable.  $\mu\text{PET}$  can detail the complex *in vivo* interactions, but this technique is prone to pitfalls:

Immobilization of animals during scanning is essential to avoid motion artefacts and mostly requires anesthesia. Many anesthetic drugs are administered intravenously. Due to allowed maximum injection volumes of 10 mL/kg body weight for mice and 5 mL/kg for rats (192), intravenous administrations in addition to the i.v. injection of the PET-tracer (and/or inhibitor) are limited. Thus, volatile anesthesia (i.e. isoflurane), as routinely applied in  $\mu\text{PET}$  experiments, is preferable. However, we ob-

served significant differences in MCHR1 PET-tracer uptake in brown adipose tissue between anesthetized and alert rats. This phenomenon may be directly or indirectly caused by anesthesia. Isoflurane is suspected to have a direct pharmacological effect on brown adipose tissue activation, probably by stimulating either alpha or beta adrenergic receptors. Apart from that, general anesthesia bears the risk of hypothermia. For this reason, torpid animals subjected to  $\mu$ PET imaging are warmed from the outside (e.g. using an external heat source such as warming pads) to keep the animal's body temperature constant during the measurement. (192) Normally, maintenance of core body temperature in mammals in response to skin cooling is regulated through the central nervous system leading to an increase in brown adipose tissue thermogenesis (BAT activation). In contrast, inverted thermoregulatory reflexes appear to be involved during hibernation and torpor. BAT thermogenesis is inhibited during cold exposure to allow for low core body temperature and minimal metabolism. Accordingly, skin (re)warming activates thermogenesis to return to normal body temperature. (193) Regarding BAT imaging, the issue of thermoregulation is maybe most crucial to be considered, as rodents rely heavily on BAT for adaptive thermogenesis. With that in mind, the observed discrepancy may be indirectly caused by anesthesia due to different heat regulation in actively moving or torpid animals. The performance of biodistribution experiments using [ $^{18}\text{F}$ ]FE@SNAP in alert rats was thus eye-opening as a completely different uptake behavior was observed upon blocking. Moreover, the translation of an experimental result from torpid animals to humans, who are generally not anesthetized during PET imaging, is scarce. We thus highly encourage the development of new approaches for  $\mu$ PET imaging in conscious animals without physical restraint. Pioneer work has already been performed in motion tracking and compensation in freely moving small animals and in the development of a portable miniature PET device. (194-196)

Generally, the total mass of injected PET-tracer is very low, provided that non-carrier added tracer preparations are used. Thus, biological processes are usually not perturbed by mass effects in humans. However, considering PET imaging in small animals, which differ in body weight up to 2500-fold (mice) from humans, mass effects need to be considered carefully. This is especially important when measuring saturable systems such as low-density receptors. (197, 198) It is undisputed that masses of injected radiotracer, which show no pharmacological effect in humans, can be beyond the pharmacodynamical threshold in small animals. Apart from the chemical quantity of the injected PET-tracer, pharmacological interventions (as blocking or displacement studies) have to be applied with caution. Blocking interventions applying high doses to small animals are common practice to prove specificity of PET-tracers, though possible molecular alterations are often overlooked. In this way, [ $^{11}\text{C}$ ]SNAP-7941 and [ $^{18}\text{F}$ ]FE@SNAP proved to be selective MCHR1 imaging agents, as PET employs only tracer amounts (picogram to nanogram) of radiolabeled compounds (Manuscript #5).



However, pharmacological doses of the respective unlabeled compounds may also cause pharmacological off-target effects and thus may mislead functional imaging data interpretation.

In general, the decision for an animal model should be made considering target (and ligand) species differences. Regarding the melanin-concentrating hormone system, the endogenous ligand structure (MCH) is identical in human, rat and mouse. (152) Moreover, the human MCHR1 is highly conserved in rodents, as human and rat share 96% and human and mouse 95% identity. Rodent models are thus considered adequate to investigate MCHR1 PET imaging strategies. In contrast, rodent models are challenging in terms of A<sub>3</sub>AR imaging. The translational value of rodent models is considered rather low, as there is low sequence homology between the rat and human A<sub>3</sub>AR and species differences in ligand affinities have been observed. This fact has already been recognized by other groups and led to the development of A<sub>3</sub>AR functionally humanized mice. (199, 200)

Moreover, disease models should be chosen carefully, especially regarding oncologic imaging: Heterotopic xenograft models are generated by subcutaneous implantation of human cancer cells into immunocompromised mice leading to an externally formed tumor. These subcutaneously formed tumors can be accurately growth-monitored and easily resected after euthanasia for further histological or biochemical processing. However, the translational value of heterotopic murine models is limited, as human cancer progression is not mimicked adequately due to the extra-anatomical location of the tumor. (201) Subcutaneous xenografts grow faster and lack the formation of metastases. Moreover, implantation of tumor cells into animals suffering from T-cell deficiency or even severe combined immunodeficiency may be misleading when exploring microenvironment-related targets or immune checkpoints. Compared to the human situation, tumor size is far greater at the time of tracer administration. For that reason, necrosis is more pronounced in murine models and could potentially lead to low tumor uptake owing to a lack in cell viability.



## 6. CONCLUSION AND FUTURE CONSIDERATIONS

---

In conclusion, it has to be stated that the predictive and translational value of *in vitro* methods might be limited. A translational gap between *in vitro* studies using cell monolayers and *in vivo* tumor grafts was observed. We propose three-dimensional multicellular spheroids as an *in vitro* technique to characterize target expression and study target-ligand interactions. Compared to two-dimensional models, spheroids contribute significantly to the understanding of the functional and complex interactions in cell aggregates.

The availability of transfected cell lines overexpressing P-gp and a dedicated detection device (LigandTracer®) enabled the establishment of a new *in vitro* method measuring interactions with efflux transporters in our laboratory in real time (Manuscript #2). We conclude that the presented new kinetic *in vitro* model is straightforward and beneficial to drug delivery investigations, as it requires minimal cell culture effort, it uses a technically undemanding device, which is easy to handle for the operator, and it enables an immediate data interpretation based on real-time kinetics providing a prompt qualitative statement about the PET-tracer's interaction with P-gp. We thus suggest the herein presented method as a powerful screening tool in PET-tracer development.

[<sup>18</sup>F]FE@SUPPY was developed as the first PET-tracer for human A<sub>3</sub>AR imaging in 2008 and was extensively probed during the last ten years by our group. (55, 119, 174-176, 202) Unfortunately, [<sup>18</sup>F]FE@SUPPY evinced as a highly lipophilic compound and showed unspecific binding, unfavorable pharmacokinetics and low *in vivo* stability when it was first evaluated in a mouse model (Manuscript #1). We conclude that – in its given form – [<sup>18</sup>F]FE@SUPPY is inadequate to serve as a PET-tracer for A<sub>3</sub>AR imaging. Thus, a new imaging strategy is envisaged. 2-CI-IB-MECA is a highly affine and selective A<sub>3</sub>AR agonist, which has been tested in an open label phase I/II dose escalation study for the treatment of hepatocellular carcinoma. It was shown that this compound is toxicologically safe and a potent drug candidate by inducing apoptosis of hepatocellular carcinoma cells. (111, 203) However, it is well described that the A<sub>3</sub>AR is internalized and may even be down-regulated after agonist exposure (107). The successful conversion of 2-CI-IB-MECA into a selective antagonist by the simple introduction of a second methyl group within the uronamide moiety was reported (Figure 14). (204)

The binding affinity ( $K_i$ ) towards the human  $A_3AR$  of the respective *N,N*-dimethyl derivative (MRS3771) was shown to be 29 nM in a competitive binding assay using [ $^{125}I$ ]-AB-MECA and binding was demonstrated to be more than 200-fold selective with regard to the other adenosine receptor subtypes. Moreover, lower but still intermediate affinity for the rat  $A_3AR$  was reported, which is beneficial for future animal experiments in rodents. (204) We hypothesize that  $A_3AR$  ligands based on nucleoside-like structures display superior pharmacokinetic properties than phenyl pyridine ligands such as FE@SUPPY due to their increased hydrophilicity (MRS3771 CLogP 1.69 *versus* FE@SUPPY CLogP 6.11).

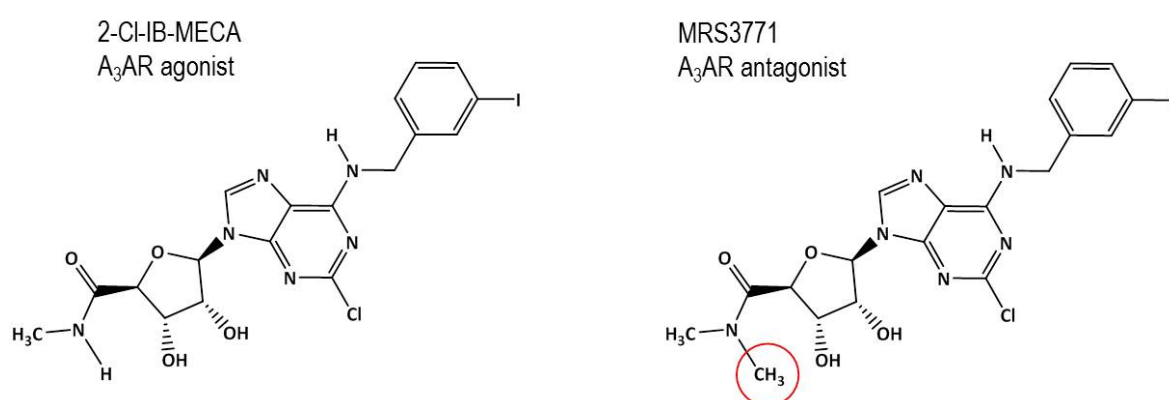


**Figure 14:** The highly affine and selective  $A_3AR$  agonist 2-Cl-IB-MECA ( $K_i$ = 1.4 nM) was converted into an  $A_3AR$  antagonist by appending a second *N*-methyl group at the 5'-uronamide position (MRS3771, 2-Cl-IB-ME<sub>2</sub>CA). (204)

The well-established TSPO PET-tracer [ $^{18}F$ ]FEPPA, which is currently in clinical use for microglia activation imaging, was evaluated *in vitro* for colorectal cancer imaging for the first time. Preliminary testing showed promising results regarding the specificity of [ $^{18}F$ ]FEPPA binding to colon cancer tissue and cells. The development of multiple distal colonic tumors in a mouse model of familial adenomatous polyposis was successfully monitored by TSPO PET applying a radiofluorinated pyrazolopyrimidine ([ $^{18}F$ ]VUIIS1008). (185) This study supports our findings and the feasibility of this imaging strategy. However, elevated TSPO expression was also found in enterocytes of chronic inflammatory diseases of the colon. (205) Thus, differentiation from inflammatory bowel disease may not be feasible using a TSPO imaging strategy, which has to be investigated using dedicated animal disease models in the future.

Moreover,  $K_i$  values of FEPPA were determined for the three different binding phenotypes (HAB, LAB and MAB), which contributes to an accurate quantification of TSPO expression using PET (Manuscript #3). However, the potential of TSPO PET imaging using [ $^{18}F$ ]FEPPA still has to be proven as polymorphism rs6971 genotyping is crucial before statistical analysis of PET imaging data

when using [ $^{18}\text{F}$ ]FEPPA or any other 2<sup>nd</sup> generation TSPO PET-tracer. This leads to a “screen out procedure” to ensure that all subjects included in a clinical study are from the same binding class. In my opinion, TSPO imaging using the 2<sup>nd</sup> generation PET-tracers provides only a temporary solution until a PET-tracer is developed, which binds with equal affinity to TSPO in all patient subjects. First attempts by our group to develop a suitable and universally applicable TSPO PET-tracer included the syntheses of carbon-11 labeled and fluorine-18 labeled PK11195 analogues ([ $^{11}\text{C}$ ]Me@NEBIQUINIDE and [ $^{18}\text{F}$ ]NEBIFQUINIDE, respectively). (206, 207)

Feasibility of the MCHR1 PET imaging strategy using [ $^{11}\text{C}$ ]SNAP-7941 and [ $^{18}\text{F}$ ]FE@SNAP was demonstrated recently. (167, 168, 170) From the detailed *in vitro* and *in vivo* evaluation of the MCHR1 PET-tracers, [ $^{11}\text{C}$ ]SNAP-7941 emerged as the superior tracer for future human use considering affinity, selectivity, metabolic stability and quality of PET imaging data (Manuscript #4). In a further study, special emphasis was placed on the evaluation of [ $^{11}\text{C}$ ]SNAP-7941 for brown adipose tissue imaging, as preliminary data indicated MCHR1 expression in BAT. Specific uptake of [ $^{11}\text{C}$ ]SNAP-7941 to brown adipocytes was demonstrated, supporting a role of MCHR1 in brown adipose tissue metabolism (Manuscript #5). In conclusion, brown adipose tissue imaging using MCHR1 PET enhances the understanding of this complex and unique metabolic organ. Thus, besides a clinical application of [ $^{11}\text{C}$ ]SNAP-7941 in mental and neurologic disorders, an application in metabolic related diseases is becoming more and more realistic.



# Bibliography

1. Mankoff DA. A definition of molecular imaging. *Journal of Nuclear Medicine*. 2007;48(6):18n-21n.
2. Pysz MA, Gambhir SS, Willmann JK. Molecular imaging: current status and emerging strategies. *Clinical Radiology*. 2010;65(7):500-16.
3. Townsend DW. Physical principles and technology of clinical PET imaging. *Annals of the Academy of Medicine, Singapore*. 2004;33(2):133-45.
4. Ametamey SM, Honer M, Schubiger PA. Molecular Imaging with PET. *Chemical Reviews*. 2008;108(5):1501-16.
5. Cherry SR. Fundamentals of positron emission tomography and applications in preclinical drug development. *Journal of Clinical Pharmacology*. 2001;41(5):482-91.
6. Phelps ME. Positron emission tomography provides molecular imaging of biological processes. *Proceedings of the National Academy of Sciences of the United States of America*. 2000;97(16):9226-33.
7. Drevets WC, Frank E, Price JC, Kupfer DJ, Holt D, Greer PJ, Huang Y, Gautier C, Mathis C. Pet imaging of serotonin 1A receptor binding in depression. *Biological Psychiatry*. 1999;46(10):1375-87.
8. Hammes J, Drzezga A, van Eimeren T. The Role of Tau Imaging in Parkinsonian Disorders. *Current Neurology and Neuroscience Reports*. 2018;18:86.
9. Saint-Aubert L, Lemoine L, Chiotis K, Leuzy A, Rodriguez-Vieitez E, Nordberg A. Tau PET imaging: present and future directions. *Molecular Neurodegeneration*. 2017;12:19.
10. Nasrallah I, Dubroff J. An Overview of PET Neuroimaging. *Seminars in Nuclear Medicine*. 2013;43(6):449-61.
11. Quigley H, Colloby SJ, O'Brien JT. PET imaging of brain amyloid in dementia: a review. *International Journal of Geriatric Psychiatry*. 2011;26(10):991-9.
12. Pretze M, Wangler C, Wangler B. 6-[<sup>18</sup>F]fluoro-L-DOPA: a well-established neurotracer with expanding application spectrum and strongly improved radiosyntheses. *BioMed Research International*. 2014;2014:674063.
13. Fass L. Imaging and cancer: a review. *Molecular Oncology*. 2008;2(2):115-52.
14. McDermott S, Kilcoyne A. Molecular imaging-its current role in cancer. *QJM : monthly journal of the Association of Physicians*. 2016;109(5):295-9.
15. Pichler BJ, Judenhofer MS, Pfannenberger C. Multimodal Imaging Approaches: PET/CT and PET/MRI. In: Semmler W, Schwaiger M, editors. *Molecular Imaging I*. Berlin, Heidelberg: Springer Berlin Heidelberg; 2008. p. 109-32.
16. Nolting DD, Nickels ML, Guo N, Pham W. Molecular imaging probe development: a chemistry perspective. *American Journal of Nuclear Medicine and Molecular Imaging*. 2012;2(3):273-306.
17. Herrmann K, Larson SM, Weber WA. Theranostic Concepts: More Than Just a Fashion Trend—Introduction and Overview. *Journal of Nuclear Medicine*. 2017;58(Supplement 2):1S-2S.

18. Ghasemi M, Nabipour I, Omrani A, Alipour Z, Assadi M. Precision medicine and molecular imaging: new targeted approaches toward cancer therapeutic and diagnosis. *American Journal of Nuclear Medicine and Molecular Imaging*. 2016;6(6):310-27.
19. Matthews PM, Rabiner EA, Passchier J, Gunn RN. Positron emission tomography molecular imaging for drug development. *British Journal of Clinical Pharmacology*. 2012;73(2):175-86.
20. Bergstrom M, Grahnen A, Langstrom B. Positron emission tomography microdosing: a new concept with application in tracer and early clinical drug development. *European Journal of Clinical Pharmacology*. 2003;59(5-6):357-66.
21. World Health O. World health report 2001: Mental health: New understanding, new hope: World Health Organization; 2001.
22. Hany TF, Gharehpapagh E, Kamel EM, Buck A, Himms-Hagen J, von Schulthess GK. Brown adipose tissue: a factor to consider in symmetrical tracer uptake in the neck and upper chest region. *European Journal of Nuclear Medicine and Molecular Imaging*. 2002;29(10):1393-8.
23. Cohade C, Osman M, Pannu HK, Wahl RL. Uptake in supraclavicular area fat ("USA-Fat"): Description on 18F-FDG PET/CT. *The Journal of Nuclear Medicine*. 2003;44(2):170.
24. Cypess AM, Lehman S, Williams G, Tal I, Rodman D, Goldfine AB, Kuo FC, Palmer EL, Tseng YH, Doria A, Kolodny GM, Kahn CR. Identification and importance of brown adipose tissue in adult humans. *The New England Journal of Medicine*. 2009;360(15):1509-17.
25. Wadsak W, Mitterhauser M. Basics and principles of radiopharmaceuticals for PET/CT. *European Journal of Radiology*. 2010;73(3):461-9.
26. Miller PW, Long NJ, Vilar R, Gee AD. Synthesis of <sup>11</sup>C, <sup>18</sup>F, <sup>15</sup>O, and <sup>13</sup>N Radiolabels for Positron Emission Tomography. *Angewandte Chemie International Edition*. 2008;47(47):8998-9033.
27. Pichler V, Berroteran-Infante N, Philippe C, Vraka C, Klebermass EM, Balber T, Pfaff S, Nics L, Mitterhauser M, Wadsak W. An Overview of PET Radiochemistry, Part 1: The Covalent Labels <sup>18</sup>F, <sup>11</sup>C, and <sup>13</sup>N. *Journal of Nuclear Medicine*. 2018;59(9):1350-4.
28. Qaim SM. The present and future of medical radionuclide production. *Radiochimica Acta*. 2012;100(8-9):635-51.
29. Currie GM, Wheat JM, Davidson R, Kiat H. Radionuclide production. *Radiographer*. 2011;58(3):46-52.
30. Brandt M, Cardinale J, Aulsebrook ML, Gasser G, Mindt TL. An Overview of PET Radiochemistry, Part 2: Radiometals. *Journal of Nuclear Medicine*. 2018;59(10):1500-6.
31. Schlyer DJ. PET tracers and radiochemistry. *Annals of the Academy of Medicine, Singapore*. 2004;33(2):146-54.
32. Serdons K, Verbruggen A, Bormans GM. Developing new molecular imaging probes for PET. *Methods*. 2009;48(2):104-11.
33. Serdons K, Verbruggen A, Bormans G. The presence of ethanol in radiopharmaceutical injections. *Journal of Nuclear Medicine*. 2008;49(12):2071.
34. Pardridge WM. The blood-brain barrier: bottleneck in brain drug development. *NeuroRx : The Journal of the American Society for Experimental NeuroTherapeutics*. 2005;2(1):3-14.



35. Marcus CS. How Should the FDA Review Diagnostic Radiopharmaceuticals? *Journal of Nuclear Medicine*. 2018;59(6):868-70.
36. AGENCY IAE. Quality Control in the Production of Radiopharmaceuticals. Vienna: INTERNATIONAL ATOMIC ENERGY AGENCY; 2018.
37. Briner WH. Radiopharmaceuticals are drugs. *Modern Hospital*. 1960;95:110-4.
38. Schwarz SW, Dick D, VanBrocklin HF, Hoffman JM. Regulatory Requirements for PET Drug Production. *Journal of Nuclear Medicine*. 2014;55(7):1132-7.
39. Coenen HH, Gee AD, Adam M, Antoni G, Cutler CS, Fujibayashi Y, Jeong JM, Mach RH, Mindt TL, Pike VW, Windhorst AD. Consensus nomenclature rules for radiopharmaceutical chemistry — Setting the record straight. *Nuclear Medicine and Biology*. 2017;55:v-xi.
40. Pichler V, Zenz T, Philippe C, Vracka C, Berrot ran-Infante N, Pfaff S, Nics L, Ozenil M, Langer O, Willeit M, Traub-Weidinger T, Lanzenberger R, Mitterhauser M, Hacker M, Wadsak W. Molar activity – the keystone in 11C-radiochemistry: an explorative study using the gas phase method. *Nuclear Medicine and Biology*. 2018;67:21-26
41. Zhuang H, Codreanu I. Growing applications of FDG PET-CT imaging in non-oncologic conditions. *Journal of Biomedical Research*. 2015;29(3):189-202.
42. Culverwell AD, Scarsbrook AF, Chowdhury FU. False-positive uptake on 2-[18F]-fluoro-2-deoxy-d-glucose (FDG) positron-emission tomography/computed tomography (PET/CT) in oncological imaging. *Clinical Radiology*. 2011;66(4):366-82.
43. Jadvar H. Imaging evaluation of prostate cancer with 18F-fluorodeoxyglucose PET/CT: utility and limitations. *European Journal of Nuclear Medicine and Molecular Imaging*. 2013;40 Suppl 1:S5-10.
44. Hanahan D, Weinberg RA. The Hallmarks of Cancer. *Cell*. 2000;100(1):57-70.
45. Rosenkrantz AB, Friedman K, Chandarana H, Melsaether A, Moy L, Ding YS, Jhaveri K, Beltran L, Jain R. Current Status of Hybrid PET/MRI in Oncologic Imaging. *American Journal of Roentgenology*. 2015;206(1):162-72.
46. Hicks RJ, Dorow D, Roselt P. PET tracer development—a tale of mice and men. *Cancer Imaging*. 2006;6(Spec No A):S102-S6.
47. Mitterhauser M, Wadsak W. Imaging biomarkers or biomarker imaging? *Pharmaceuticals*. 2014;7(7):765-78.
48. Ludwig JA, Weinstein JN. Biomarkers in Cancer Staging, Prognosis and Treatment Selection. *Nature Reviews Cancer*. 2005;5:845-56.
49. Rosenbaum DM, Rasmussen SG, Kobilka BK. The structure and function of G-protein-coupled receptors. *Nature*. 2009;459(7245):356-63.
50. Vogel C, Marcotte EM. Insights into the regulation of protein abundance from proteomic and transcriptomic analyses. *Nature Reviews Genetics*. 2012;13:227.
51. Koussounadis A, Langdon SP, Um IH, Harrison DJ, Smith VA. Relationship between differentially expressed mRNA and mRNA-protein correlations in a xenograft model system. *Scientific reports*. 2015;5:10775.
52. Nordberg M, Duffus J, Templeton DM. Glossary of terms used in toxicokinetics (IUPAC Recommendations 2003). *Pure and Applied Chemistry*. 2004;76(5):1033-1082.

53. Pike VW. PET radiotracers: crossing the blood–brain barrier and surviving metabolism. *Trends in Pharmacological Sciences*. 2009;30(8):431-40.
54. Ettlinger DE, Wadsak W, Mien LK, Machek M, Wabnegger L, Rendl G, Karanikas G, Viernstein H, Kletter K, Dudczak R, Mitterhauser M. [18F]FETO: metabolic considerations. *European Journal of Nuclear Medicine and Molecular Imaging*. 2006;33(8):928-31.
55. Haeusler D, Nics L, Mien LK, Ungersboeck J, Lanzenberger RR, Shanab K, Spreitzer H, Sindelar KM, Viernstein H, Wagner KH, Dudczak R, Kletter K, Wadsak W, Mitterhauser M. [18F]FE@SUPPY and [18F]FE@SUPPY:2 – metabolic considerations. *Nuclear Medicine and Biology*. 2010;37(4):421-6.
56. Rami-Mark C, Eberherr N, Berroteran-Infante N, Vanicek T, Nics L, Lanzenberger R, Hacker M, Wadsak W, Mitterhauser M. [18F]FMeNER-D2: A systematic in vitro analysis of radio-metabolism. *Nuclear Medicine and Biology*. 2016;43(8):490-5.
57. Maeda H, Wu J, Sawa T, Matsumura Y, Hori K. Tumor vascular permeability and the EPR effect in macromolecular therapeutics: a review. *Journal of Controlled Release*. 2000;65(1):271-84.
58. Heneweer C, Holland JP, Divilov V, Carlin S, Lewis JS. Magnitude of enhanced permeability and retention effect in tumors with different phenotypes: 89Zr-albumin as a model system. *Journal of Nuclear Medicine*. 2011;52(4):625-33.
59. Vranka C, Mijailovic S, Frohlich V, Zeilinger M, Klebermass EM, Wadsak W, Wagner KH, Hacker M, Mitterhauser M. Expanding LogP: Present possibilities. *Nuclear Medicine and Biology*. 2018;58:20-32.
60. Valko K, Nunhuck S, Bevan C, Abraham MH, Reynolds DP. Fast gradient HPLC method to determine compounds binding to human serum albumin. Relationships with octanol/water and immobilized artificial membrane lipophilicity. *Journal of Pharmaceutical Sciences*. 2003;92(11):2236-48.
61. Vranka C, Nics L, Wagner K-H, Hacker M, Wadsak W, Mitterhauser M. LogP, a yesterday's value? *Nuclear Medicine and Biology*. 2017;50:1-10.
62. Donovan SF, Pescatore MC. Method for measuring the logarithm of the octanol–water partition coefficient by using short octadecyl–poly(vinyl alcohol) high-performance liquid chromatography columns. *Journal of Chromatography A*. 2002;952(1):47-61.
63. De Vrieze M, Lynen F, Chen K, Szucs R, Sandra P. Predicting drug penetration across the blood–brain barrier: comparison of micellar liquid chromatography and immobilized artificial membrane liquid chromatography. *Analytical and Bioanalytical Chemistry*. 2013;405(18):6029-41.
64. Giaginis C, Tsantili-Kakoulidou A. Alternative measures of lipophilicity: from octanol-water partitioning to IAM retention. *Journal of Pharmaceutical Sciences*. 2008;97(8):2984-3004.
65. Pardridge WM. Drug transport across the blood-brain barrier. *Journal of Cerebral Blood Flow and Metabolism*. 2012;32(11):1959-72.
66. Tavares AA, Lewsey J, Dewar D, Pimlott SL. Radiotracer properties determined by high performance liquid chromatography: a potential tool for brain radiotracer discovery. *Nuclear Medicine and Biology*. 2012;39(1):127-35.
67. Vranka C, Mitterhauser M. Reconsider logP! *Nuclear Medicine and Biology*. 2017;54:42.
68. Philippe C, Zeilinger M, Scherer T, Fürnsinn C, Dumanic M, Pilz J, Wadsak W, Hacker M, Mitterhauser M. MCHR1: a potential indicator for BAT activity. *Nuklearmedizin*. 2016. 2016;55(2):A78.

69. Kathawala RJ, Gupta P, Ashby CR, Chen Z-S. The modulation of ABC transporter-mediated multi-drug resistance in cancer: A review of the past decade. *Drug Resistance Updates*. 2015;18:1-17.
70. Cheng Y, Prusoff WH. Relationship between the inhibition constant ( $K_1$ ) and the concentration of inhibitor which causes 50 per cent inhibition ( $I_{50}$ ) of an enzymatic reaction. *Biochemical Pharmacology*. 1973;22(23):3099-108.
71. Lancelot S, Zimmer L. Small-animal positron emission tomography as a tool for neuropharmacology. *Trends Pharmacol Sci*. 2010;31(9):411-7.
72. Oume M. Overview of ligand-receptor binding techniques. In: *Receptor Binding Techniques. Methods in Molecular Biology Volume 106*; Springer; 1999. p. 3-23.
73. Zeilinger M, Pichler F, Nics L, Wadsak W, Spreitzer H, Hacker M, Mitterhauser M. New approaches for the reliable in vitro assessment of binding affinity based on high-resolution real-time data acquisition of radioligand-receptor binding kinetics. *European Journal of Nuclear Medicine and Molecular Imaging*. 2017;7(1):22.
74. Kluba CA, Bauman A, Valverde IE, Vomstein S, Mindt TL. Dual-targeting conjugates designed to improve the efficacy of radiolabeled peptides. *Organic and Biomolecular Chemistry*. 2012;10(37):7594-602.
75. Sutherland RM. Importance of critical metabolites and cellular interactions in the biology of microregions of tumors. *Cancer*. 1986;58(8):1668-80.
76. Yamada KM, Clark K. Survival in three dimensions. *Nature*. 2002;419:790.
77. Mueller-Klieser W. Tumor biology and experimental therapeutics. *Critical Reviews in Oncology/Hematology*. 2000;36(2):123-39.
78. Santini MT, Rainaldi G. Three-dimensional spheroid model in tumor biology. *Pathobiology*. 1999;67(3):148-57.
79. Sutherland RM, Eddy HA, Bareham B, Reich K, Vanantwerp D. Resistance to adriamycin in multicellular spheroids. *International Journal of Radiation Oncology, Biology, Physics*. 1979;5(8):1225-30.
80. Sakata K, Kwok TT, Gordon GR, Waleh NS, Sutherland RM. Resistance to verapamil sensitization of multidrug-resistant cells grown as multicellular spheroids. *International Journal of Cancer*. 1994;59(2):282-6.
81. Sutherland RM, Durand RE. Radiation response of multicell spheroids – an in vitro tumour model. *Current Topics in Radiation Research Quarterly*. 1976;11(1):87-139.
82. Monazzam A, Razifar P, Simonsson M, Qvarnstrom F, Josephsson R, Blomqvist C, Langstrom B, Bergstrom M. Multicellular tumour spheroid as a model for evaluation of [ $^{18}\text{F}$ ]FDG as biomarker for breast cancer treatment monitoring. *Cancer Cell International*. 2006;6:6.
83. Monazzam A, Josephsson R, Blomqvist C, Carlsson J, Langstrom B, Bergstrom M. Application of the multicellular tumour spheroid model to screen PET tracers for analysis of early response of chemotherapy in breast cancer. *Breast Cancer Research*. 2007;9(4):R45.
84. Pichler V, Litos L, Frey T, Klebermass EM, Balber T, Hacker M, Mitterhauser M, Wadsak W. Radiopharmakon, quo vadis? Transportsysteme in multizellulären Tumorsphäroiden. 56. Jahrestagung Der Deutschen Gesellschaft für Nuklearmedizin. *Nuklearmedizin*. 2018;57(02):A1-A95.

85. Haeusler Daniela. Preclinical tools in PET-tracer development: automatisisation and biopharmaceutical evaluation with special emphasis on the adenosine A3 receptor. PhD Thesis, Faculty of Life Sciences, University of Vienna. 2010.
86. Fueger BJ, Czernin J, Hildebrandt I, Tran C, Halpern BS, Stout D, Phelps ME, Weber WA. Impact of animal handling on the results of 18F-FDG PET studies in mice. *Journal of Nuclear Medicine*. 2006;47(6):999-1006.
87. Alstrup AK, Smith DF. Anaesthesia for positron emission tomography scanning of animal brains. *Laboratory Animals*. 2013;47(1):12-8.
88. Chauveau F, Boutin H, Van Camp N, Dollé F, Tavitian B. Nuclear imaging of neuroinflammation: a comprehensive review of [11C]PK11195 challengers. *European Journal of Nuclear Medicine and Molecular Imaging*. 2008;35(12):2304-19.
89. Poulsen SA, Quinn RJ. Adenosine receptors: new opportunities for future drugs. *Bioorganic and Medicinal Chemistry*. 1998;6(6):619-41.
90. Fredholm BB, IJzerman AP, Jacobson KA, Klotz K-N, Linden J. International Union of Pharmacology. XXV. Nomenclature and Classification of Adenosine Receptors. *Pharmacological Reviews*. 2001;53(4):527-52.
91. Zimmermann H. Extracellular metabolism of ATP and other nucleotides. *Naunyn-Schmiedeberg's Archives of Pharmacology*. 2000;362(4-5):299-309.
92. Antonioli L, Yegutkin GG, Pacher P, Blandizzi C, Hasko G. Anti-CD73 in cancer immunotherapy: awakening new opportunities. *Trends in Cancer*. 2016;2(2):95-109.
93. Jacobson KA. Introduction to adenosine receptors as therapeutic targets. In: *Adenosine receptors in health and disease*: Springer; 2009. p. 1-24.
94. Gessi S, Merighi S, Sacchetto V, Simioni C, Borea PA. Adenosine receptors and cancer. *Biochimica et Biophysica Acta*. 2011;1808(5):1400-12.
95. Borea PA, Gessi S, Merighi S, Varani K. Adenosine as a Multi-Signalling Guardian Angel in Human Diseases: When, Where and How Does it Exert its Protective Effects? *Trends in Pharmacological Sciences*. 2016;37(6):419-34.
96. Bowser JL, Lee JW, Yuan X, Eltzschig HK. The hypoxia-adenosine link during inflammation. *Journal of Applied Physiology*. 2017;123(5):1303-20.
97. Blay J, White TD, Hoskin DW. The Extracellular Fluid of Solid Carcinomas Contains Immunosuppressive Concentrations of Adenosine. *Cancer Research*. 1997;57(13):2602-5.
98. Antonioli L, Blandizzi C, Pacher P, Hasko G. Immunity, inflammation and cancer: a leading role for adenosine. *Nature Reviews Cancer*. 2013;13(12):842-57.
99. Allard B, Beavis PA, Darcy PK, Stagg J. Immunosuppressive activities of adenosine in cancer. *Current Opinion in Pharmacology*. 2016;29:7-16.
100. Sitkovsky M, Ohta A. Targeting the hypoxia-adenosinergic signaling pathway to improve the adoptive immunotherapy of cancer. *Journal of Molecular Medicine*. 2013;91(2):147-55.
101. Hoskin DW, Mader JS, Furlong SJ, Conrad DM, Blay J. Inhibition of T cell and natural killer cell function by adenosine and its contribution to immune evasion by tumor cells (Review). *International Journal of Oncology*. 2008;32(3):527-35.

102. Antonioli L, Hasko G, Fornai M, Colucci R, Blandizzi C. Adenosine pathway and cancer: where do we go from here? *Expert Opinion on Therapeutic Targets*. 2014;18(9):973-7.
103. Hoskin DW, Butler JJ, Drapeau D, Haeryfar SMM, Blay J. Adenosine acts through an A3 receptor to prevent the induction of murine anti-CD3-activated killer T cells. *International Journal of Cancer*. 2002;99(3):386-95.
104. Gessi S, Varani K, Merighi S, Morelli A, Ferrari D, Leung E, Baraldi PG, Spalluto G, Borea PA. Pharmacological and biochemical characterization of A3 adenosine receptors in Jurkat T cells. *British Journal of Pharmacology*. 2001;134(1):116-26.
105. Gessi S, Varani K, Merighi S, Cattabriga E, Iannotta V, Leung E, Baraldi PG, Borea PA. A3 Adenosine Receptors in Human Neutrophils and Promyelocytic HL60 Cells: A Pharmacological and Biochemical Study. *Molecular Pharmacology*. 2002;61(2):415-24.
106. Merighi S, Varani K, Gessi S, Cattabriga E, Iannotta V, Ulouglu C, Leung E, Borea PA. Pharmacological and biochemical characterization of adenosine receptors in the human malignant melanoma A375 cell line. *British Journal of Pharmacology*. 2001;134(6):1215-26.
107. Trincavelli ML, Tuscano D, Marroni M, Falleni A, Gremigni V, Ceruti S, Abbracchio MP, Jacobson KA, Cattabeni F, Martini C. A3 Adenosine Receptors in Human Astrocytoma Cells: Agonist-Mediated Desensitization, Internalization, and Down-Regulation. *Molecular Pharmacology*. 2002;62(6):1373-84.
108. Fishman P, Bar-Yehuda S, Ardon E, Rath-Wolfson L, Barrer F, Ochaion A, Madi L. Targeting the A3 adenosine receptor for cancer therapy: inhibition of prostate carcinoma cell growth by A3AR agonist. *Anticancer Research*. 2003;23(3a):2077-83.
109. Ohana G, Bar-Yehuda S, Arich A, Madi L, Drennick Z, Rath-Wolfson L, Silberman D, Slosman G, Fishman P. Inhibition of primary colon carcinoma growth and liver metastasis by the A3 adenosine receptor agonist CF101. *British Journal of Cancer*. 2003;89(8):1552-8.
110. Gessi S, Merighi S, Varani K, Cattabriga E, Benini A, Mirandola P, Leung E, Mac Lennan S, Feo C, Baraldi S, Borea PA. Adenosine receptors in colon carcinoma tissues and colon tumoral cell lines: Focus on the A3 adenosine subtype. *Journal of Cellular Physiology*. 2007;211(3):826-36.
111. Bar-Yehuda S, Stemmer SM, Madi L, Castel D, Ochaion A, Cohen S, Barer F, Zabutti A, Perez-Liz G, Del Valle L, Fishman P. The A3 adenosine receptor agonist CF102 induces apoptosis of hepatocellular carcinoma via de-regulation of the Wnt and NF-kappaB signal transduction pathways. *International Journal of Oncology*. 2008;33(2):287-95.
112. Madi L, Ochaion A, Rath-Wolfson L, Bar-Yehuda S, Erlanger A, Ohana G, Harish A, Merimski O, Barer F, Fishman P. The A3 adenosine receptor is highly expressed in tumor versus normal cells: potential target for tumor growth inhibition. *Clinical Cancer Research*. 2004;10(13):4472-9.
113. Fishman P, Bar-Yehuda S, Madi L, Cohn I. A3 adenosine receptor as a target for cancer therapy. *Anti-Cancer Drugs*. 2002;13(5):437-43.
114. Ochaion A, Bar-Yehuda S, Cohen S, Barer F, Patoka R, Amital H, Reitblat T, Reitblat A, Ophir J, Konfino I, Chowers Y, Ben-Horin S, Fishman P. The anti-inflammatory target A3 adenosine receptor is over-expressed in rheumatoid arthritis, psoriasis and Crohn's disease. *Cellular Immunology*. 2009;258(2):115-22.
115. Varani K, Caramori G, Vincenzi F, Adcock I, Casolari P, Leung E, MacLennan S, Gessi S, Morello S, Barnes PJ, Ito K, Chung KF, Cavallero G, Azzena G, Papi A, Borea PA. Alteration of adenosine receptors in patients with chronic obstructive pulmonary disease. *American Journal of Respiratory and Critical Care Medicine*. 2006;173(4):398-406.

116. Borea PA, Varani K, Vincenzi F, Baraldi PG, Tabrizi MA, Merighi S, Gessi S. The A3 adenosine receptor: history and perspectives. *Pharmacological Reviews*. 2015;67(1):74-102.
117. Salvatore CA, Jacobson MA, Taylor HE, Linden J, Johnson RG. Molecular cloning and characterization of the human A3 adenosine receptor. *Proceedings of the National Academy of Sciences of the United States of America*. 1993;90(21):10365-9.
118. Li A-H, Moro S, Forsyth N, Melman N, Ji X-d, Jacobson KA. Synthesis, CoMFA Analysis, and Receptor Docking of 3,5-Diacyl-2,4-Dialkylpyridine Derivatives as Selective A3 Adenosine Receptor Antagonists. *Journal of Medicinal Chemistry*. 1999;42(4):706-21.
119. Wadsak W, Mien L-K, Shanab K, Weber K, Schmidt B, Sindelar KM, Ettlinger Dagmar E, Haeusler D, Spreitzer H, Keppler BK, Viernstein H, Dudczak R, Kletter K, Mitterhauser M. Radiosynthesis of the adenosine A3 receptor ligand 5-(2-[18F]fluoroethyl) 2,4-diethyl-3-(ethylsulfanylcarbonyl)-6-phenylpyridine-5-carboxylate ([18F]FE@SUPPY). *Radiochimica Acta*. 2008;96(2):119-124.
120. Mitterhauser M, Haeusler D, Mien L-K, Ungersboeck J, Nics L, Lanzenberger RR, Sindelar K, Viernstein H, Dudczak R, Kletter K. Automatisierung und erste Evaluation von [18F]FE@SUPPY:2, ein alternativer PET-Tracer für den Adenosin A3-Rezeptor: ein Vergleich mit [18F]FE@SUPPY. *The Open Nuclear Medicine Journal*. 2009;1:15-23.
121. Kiesewetter DO, Lang L, Ma Y, Bhattacharjee AK, Gao Z-G, Joshi BV, Melman A, de Castro S, Jacobson KA. Synthesis and characterization of [76Br]-labeled high-affinity A3 adenosine receptor ligands for positron emission tomography. *Nuclear Medicine and Biology*. 2009;36(1):3-10.
122. Gao M, Gao AC, Wang M, Zheng Q-H. Simple synthesis of new carbon-11-labeled 1,2,4-triazolo [4,3-a]quinoxalin-1-one derivatives for PET imaging of A3 adenosine receptor. *Applied Radiation and Isotopes*. 2014;91(Supplement C):71-8.
123. Papadopoulos V, Baraldi M, Guilarte TR, Knudsen TB, Lacapère J-J, Lindemann P, Norenberg MD, Nutt D, Weizman A, Zhang M-R, Gavish M. Translocator protein (18kDa): new nomenclature for the peripheral-type benzodiazepine receptor based on its structure and molecular function. *Trends in Pharmacological Sciences*. 2006;27(8):402-9.
124. Batareah A, Papadopoulos V. Regulation of Translocator Protein 18 kDa (TSPO) Expression in Health and Disease States. *Molecular and Cellular Endocrinology*. 2010;327(1-2):1-12.
125. Liu G-J, Middleton RJ, Hatty CR, Kam WW-Y, Chan R, Pham T, Harrison-Brown M, Dodson E, Veale K, Banati RB. The 18 kDa Translocator Protein, Microglia and Neuroinflammation. *Brain Pathology*. 2014;24(6):631-53.
126. Guilarte TR. TSPO in diverse CNS pathologies and psychiatric disease: A critical review and a way forward. *Pharmacology and Therapeutics*. 2018.
127. Bribes E, Carriere D, Goubet C, Galiegue S, Casellas P, Simony-Lafontaine J. Immunohistochemical assessment of the peripheral benzodiazepine receptor in human tissues. *Journal of Histochemistry and Cytochemistry*. 2004;52(1):19-28.
128. Maaser K, Grabowski P, Sutter AP, Hopfner M, Foss HD, Stein H, Berger G, Gavish M, Zeitz M, Scherubl H. Overexpression of the peripheral benzodiazepine receptor is a relevant prognostic factor in stage III colorectal cancer. *Clinical Cancer Research*. 2002;8(10):3205-9.
129. Hardwick M, Fertikh D, Culty M, Li H, Vidic B, Papadopoulos V. Peripheral-Type Benzodiazepine Receptor (PBR) in Human Breast Cancer. *Cancer Research*. 1999;59(4):831.

130. Han Z, Slack RS, Li W, Papadopoulos V. Expression of Peripheral Benzodiazepine Receptor (PBR) in Human Tumors: Relationship to Breast, Colorectal, and Prostate Tumor Progression. *Journal of Receptors and Signal Transduction*. 2003;23(2-3):225-38.
131. Vlodavsky E, Soustiel JF. Immunohistochemical expression of peripheral benzodiazepine receptors in human astrocytomas and its correlation with grade of malignancy, proliferation, apoptosis and survival. *Journal of Neuro-Oncology*. 2007;81(1):1-7.
132. Katz Y, Ben-Baruch G, Kloog Y, Menczer J, Gavish M. Increased density of peripheral benzodiazepine-binding sites in ovarian carcinomas as compared with benign ovarian tumours and normal ovaries. *Clinical Science*. 1990;78(2):155-8.
133. Wilson AA, Garcia A, Parkes J, McCormick P, Stephenson KA, Houle S, Vasdev N. Radiosynthesis and initial evaluation of [18F]-FEPPA for PET imaging of peripheral benzodiazepine receptors. *Nuclear Medicine and Biology*. 2008;35(3):305-14.
134. Mizrahi R, Rusjan PM, Vitcu I, Ng A, Wilson AA, Houle S, Bloomfield PM. Whole body biodistribution and radiation dosimetry in humans of a new PET ligand, [18F]-FEPPA, to image translocator protein (18 kDa). *Molecular Imaging and Biology*. 2013;15(3):353-9.
135. Owen DR, Yeo AJ, Gunn RN, Song K, Wadsworth G, Lewis A, Rhodes C, Pulford DJ, Bennacef I, Parker CA, StJean PL, Cardon LR, Mooser VE, Matthews PM, Rabiner EA, Rubio JP. An 18-kDa translocator protein (TSPO) polymorphism explains differences in binding affinity of the PET radioligand PBR28. *Journal of Cerebral Blood Flow & Metabolism*. 2012;32(1):1-5.
136. Mizrahi R, Rusjan PM, Kennedy J, Pollock B, Mulsant B, Suridjan I, De Luca V, Wilson AA, Houle S. Translocator Protein (18 kDa) Polymorphism (rs6971) Explains in-vivo Brain Binding Affinity of the PET Radioligand [18F]-FEPPA. *Journal of Cerebral Blood Flow & Metabolism*. 2012;32(6):968-72.
137. Presse F, Nahon J-L, Fischer WH, Vale W. Structure of the Human Melanin Concentrating Hormone mRNA. *Molecular Endocrinology*. 1990;4(4):632-7.
138. Saito Y, Nothacker H-P, Civelli O. Melanin-concentrating Hormone Receptor: An Orphan Receptor Fits the Key. *Trends in Endocrinology & Metabolism*. 2000;11(8):299-303.
139. Hill J, Duckworth M, Murdock P, Rennie G, Sabido-David C, Ames RS, Szekeres P, Wilson S, Bergsma DJ, Gloger IS. Molecular cloning and functional characterization of MCH2, a novel human MCH receptor. *Journal of Biological Chemistry*. 2001;276(23):20125-9.
140. Tan CP, Sano H, Iwaasa H, Pan J, Sailer AW, Hreniuk DL, Feighner SD, Palyha OC, Pong S-S, Figueroa DJ, Austin CP, Jiang MM, Yu H, Ito J, Ito M, Ito M, Guan XM, MacNeil DJ, Kanatani A, Van der Ploeg LHT, Howard AD. Melanin-Concentrating Hormone Receptor Subtypes 1 and 2: Species-Specific Gene Expression. *Genomics*. 2002;79(6):785-92.
141. Griffond B, Baker BI. Cell and Molecular Cell Biology of Melanin-Concentrating Hormone. *International Review of Cytology*. 2002;213:233-77.
142. Bittencourt JC, Presse F, Arias C, Peto C, Vaughan J, Nahon JL, Vale W, Sawchenko PE. The melanin-concentrating hormone system of the rat brain: an immuno- and hybridization histochemical characterization. *The Journal of Comparative Neurology*. 1992;319(2):218-45.
143. Qu D, Ludwig DS, Gammeltoft S, Piper M, Pelleymounter MA, Cullen MJ, Mathes WF, Przypek R, Kanarek R, Maratos-Flier E. A role for melanin-concentrating hormone in the central regulation of feeding behaviour. *Nature*. 1996;380(6571):243-7.
144. Shimada M, Tritos NA, Lowell BB, Flier JS, Maratos-Flier E. Mice lacking melanin-concentrating hormone are hypophagic and lean. *Nature*. 1998;396(6712):670-4.

145. Ludwig DS, Tritos NA, Mastaitis JW, Kulkarni R, Kokkotou E, Elmquist J, Lowell B, Flier JS, Maratos-Flier E. Melanin-concentrating hormone overexpression in transgenic mice leads to obesity and insulin resistance. *Journal of Clinical Investigation*. 2001;107(3):379-86.
146. Ito M, Gomori A, Ishihara A, Oda Z, Mashiko S, Matsushita H, Yumoto M, Ito M, Sano H, Tokita S, Moriya M, Iwaasa H, Kanatani A. Characterization of MCH-mediated obesity in mice. *American Journal of Physiology- Endocrinology and Metabolism*. 2003;284(5):E940-5.
147. Conductier G, Brau F, Viola A, Langlet F, Ramkumar N, Dehouck B, Lemaire T, Chapot R, Lucas L, Rovere C, Maitre P, Hosseiny S, Petit-Paitel A, Adamantidis A, Lakaye B, Risold PY, Prevot V, Messte O, Nahon JL, Guyon A. Melanin-concentrating hormone regulates beat frequency of ependymal cilia and ventricular volume. *Nature Neuroscience*. 2013;16(7):845-7.
148. Conductier G, Martin A, Risold P-Y, Jégo S, Lavoie R, Lafont C, Mollard P, Adamantidis A, Nahon J-L. Control of Ventricular Ciliary Beating by the Melanin Concentrating Hormone-Expressing Neurons of the Lateral Hypothalamus: A Functional Imaging Survey. *Frontiers in Endocrinology*. 2013;4(182).
149. Torterolo P, Scorza C, Lagos P, Urbanavicius J, Benedetto L, Pascovich C, López-Hill X, Chase MH, Monti JM. Melanin-Concentrating Hormone (MCH): Role in REM Sleep and Depression. *Frontiers in Neuroscience*. 2015;9(475).
150. Bradley RL, Kokkotou EG, Maratos-Flier E, Cheatham B. Melanin-concentrating hormone regulates leptin synthesis and secretion in rat adipocytes. *Diabetes*. 2000;49(7):1073.
151. Naufahu J, Alzaid F, Fiuza Brito M, Doslikova B, Valencia T, Cunliffe A, Murray JF. Melanin-concentrating hormone in peripheral circulation in the human. *The Journal of Endocrinology*. 2017;232(3):513-23.
152. Pissios P, Ozcan U, Kokkotou E, Okada T, Liew CW, Liu S, Peters JN, Dahlgren G, Karamchandani J, Kudva YC, Kurpad AJ, Kennedy RT, Maratos-Flier E, Kulkarni RN. Melanin concentrating hormone is a novel regulator of islet function and growth. *Diabetes*. 2007;56(2):311-9.
153. Kokkotou E, Moss AC, Torres D, Karagiannides I, Cheifetz A, Liu S, O'Brien M, Maratos-Flier E, Pothoulakis C. Melanin-concentrating hormone as a mediator of intestinal inflammation. *Proceedings of the National Academy of Sciences of the United States of America*. 2008;105(30):10613-8.
154. MacNeil D. The Role of Melanin-Concentrating Hormone and Its Receptors in Energy Homeostasis. *Frontiers in Endocrinology*. 2013;4(49).
155. Luthin DR. Anti-obesity effects of small molecule melanin-concentrating hormone receptor 1 (MCHR1) antagonists. *Life Sciences*. 2007;81(6):423-40.
156. Bednarek MA, Hreniuk DL, Tan C, Palyha OC, MacNeil DJ, Van der Ploeg LH, Howard AD, Feighner SD. Synthesis and biological evaluation in vitro of selective, high affinity peptide antagonists of human melanin-concentrating hormone action at human melanin-concentrating hormone receptor 1. *Biochemistry*. 2002;41(20):6383-90.
157. Macdonald D, Murgolo N, Zhang R, Durkin JP, Yao X, Strader CD, Graziano MP. Molecular characterization of the melanin-concentrating hormone/receptor complex: identification of critical residues involved in binding and activation. *Molecular Pharmacology*. 2000;58(1):217-25.
158. Eric Hu X, Wos JA, Dowty ME, Suchanek PM, Ji W, Chambers JB, Benoit SC, Clegg DJ, Reizes O. Small-molecule melanin-concentrating hormone-1 receptor antagonists require brain penetration for inhibition of food intake and reduction in body weight. *The Journal of Pharmacology and Experimental Therapeutics*. 2008;324(1):206-13.



159. Takekawa S, Asami A, Ishihara Y, Terauchi J, Kato K, Shimomura Y, Mori M, Murakoshi H, Kato K, Suzuki N, Nishimura O, Fujino M. T-226296: a novel, orally active and selective melanin-concentrating hormone receptor antagonist. *European Journal of Pharmacology*. 2002;438(3):129-35.
160. Kanuma K, Omodera K, Nishiguchi M, Funakoshi T, Chaki S, Semple G, Tran T-A, Kramer B, Hsu D, Casper M, Thomsen B, Beeley N, Sekiguchi Y. Discovery of 4-(dimethylamino)quinazolines as potent and selective antagonists for the melanin-concentrating hormone receptor 1. *Bioorganic & Medicinal Chemistry Letters*. 2005;15(10):2565-9.
161. Carpenter AJ, Hertzog DL. Melanin-concentrating hormone receptor antagonists as potential anti-obesity agents. *Expert Opinion on Therapeutic Patents*. 2002;12(11):1639-46.
162. Andersen D, Storz T, Liu P, Wang X, Li L, Fan P, Chen X, Allgeier A, Burgos A, Tedrow J, Baum J, Chen Y, Crockett R, Huang L, Syed R, Larsen RD, Martinelli M. Stereoselective Synthesis of a MCHR1 Antagonist. *The Journal of Organic Chemistry*. 2007;72(25):9648-55.
163. Borowsky B, Durkin MM, Ogozalek K, Marzabadi MR, DeLeon J, Lagu B, Heurich R, Lichtblau H, Shaposhnik Z, Daniewska I, Blackburn TP, Branchek TA, Gerald C, Vaysse PJ, Forray C. Antidepressant, anxiolytic and anorectic effects of a melanin-concentrating hormone-1 receptor antagonist. *Nature Medicine*. 2002;8(8):825-30.
164. Philippe C, Mitterhauser M. The Potential Role of the MCHR1 in Diagnostic Imaging: Facts and Trends. In: *Melanin*, Intech Open; 2017.
165. Philippe C, Ungersboeck J, Schirmer E, Zdravkovic M, Nics L, Zeilinger M, Shanab K, Lanzenberger R, Karanikas G, Spreitzer H, Viernstein H, Mitterhauser M, Wadsak W. [18F]FE@SNAP-A new PET tracer for the melanin concentrating hormone receptor 1 (MCHR1): microfluidic and vessel-based approaches. *Bioorganic and Medicinal Chemistry*. 2012;20(19):5936-40.
166. Philippe C, Schirmer E, Mitterhauser M, Shanab K, Lanzenberger R, Karanikas G, Spreitzer H, Viernstein H, Wadsak W. Radiosynthesis of [11C]SNAP-7941--the first PET-tracer for the melanin concentrating hormone receptor 1 (MCHR1). *Applied Radiation and Isotopes*. 2012;70(10):2287-94.
167. Zeilinger M, Dumanic M, Pichler F, Budinsky L, Wadsak W, Pallitsch K, Spreitzer H, Lanzenberger R, Hacker M, Mitterhauser M, Philippe C. In vivo evaluation of radiotracers targeting the melanin-concentrating hormone receptor 1: [11C]SNAP-7941 and [18F]FE@SNAP reveal specific uptake in the ventricular system. *Scientific Reports*. 2017;7(1):8054.
168. Philippe C, Haeusler D, Scherer T, Furnsinn C, Zeilinger M, Wadsak W, Shanab K, Spreitzer H, Hacker M, Mitterhauser M. [(18)F]FE@SNAP-a specific PET tracer for melanin-concentrating hormone receptor 1 imaging? *European Journal of Nuclear Medicine and Molecular Imaging Research*. 2016;6(1):31.
169. Philippe C, Haeusler D, Fuchshuber F, Spreitzer H, Viernstein H, Hacker M, Wadsak W, Mitterhauser M. Comparative autoradiographic in vitro investigation of melanin concentrating hormone receptor 1 ligands in the central nervous system. *European Journal of Pharmacology*. 2014;735(Supplement C):177-83.
170. Philippe C, Nics L, Zeilinger M, Kuntner C, Wanek T, Mairinger S, Shanab K, Spreitzer H, Viernstein H, Wadsak W, Mitterhauser M. Preclinical in vitro & in vivo evaluation of [11C]SNAP-7941 - the first PET tracer for the melanin concentrating hormone receptor 1. *Nuclear Medicine and Biology*. 2013;40(7):919-25.
171. Philippe C, Nics L, Zeilinger M, Schirmer E, Spreitzer H, Karanikas G, Lanzenberger R, Viernstein H, Wadsak W, Mitterhauser M. Preparation and First Preclinical Evaluation of [18F]FE@SNAP: A Po-

- tential PET Tracer for the Melanin-Concentrating Hormone Receptor-1 (MCHR1). *Scientia Pharmaceutica*. 2013;81(3):625-39.
172. Igawa H, Stepanov V, Tari L, Okuda S, Yamamoto S, Kasai S, Nagisa Y, Haggkvist J, Svedberg M, Toth M, Takano A, Halldin C. Development of a Novel Carbon-11 Labeled PET Radioligand for Melanin-Concentrating Hormone Receptor 1. *Current Radiopharmaceuticals*. 2017;10(1):35-40.
  173. Gessi S, Cattabriga E, Avitabile A, Gafa R, Lanza G, Cavazzini L, Bianchi N, Gambari R, Feo C, Liboni A, Gullini S, Leung E, Mac-Lennan S, Borea PA. Elevated expression of A3 adenosine receptors in human colorectal cancer is reflected in peripheral blood cells. *Clinical Cancer Research*. 2004;10(17):5895-901.
  174. Wadsak W, Mien LK, Shanab K, Ettlinger DE, Haeusler D, Sindelar K, Lanzenberger RR, Spreitzer H, Viernstein H, Keppler BK, Dudczak R, Kletter K, Mitterhauser M. Preparation and first evaluation of [18F]FE@SUPPY: a new PET tracer for the adenosine A3 receptor. *Nuclear Medicine and Biology*. 2008;35(1):61-6.
  175. Haeusler D, Grassinger L, Fuchshuber F, Horleinsberger WJ, Hoftberger R, Leisser I, Girschele F, Shanab K, Spreitzer H, Gerdenitsch W, Hacker M, Wadsak W, Mitterhauser M. Hide and seek: a comparative autoradiographic in vitro investigation of the adenosine A3 receptor. *European Journal of Nuclear Medicine and Molecular Imaging*. 2015;42(6):928-39.
  176. Haeusler D, Kuntner C, Nics L, Savli M, Zeilinger M, Wanek T, Karagiannis P, Lanzenberger RR, Langer O, Shanab K, Spreitzer H, Wadsak W, Hacker M, Mitterhauser M. [18F]FE@SUPPY: a suitable PET tracer for the adenosine A3 receptor? An in vivo study in rodents. *European Journal of Nuclear Medicine and Molecular Imaging*. 2015;42(5):741-9.
  177. World Health O. Burden of mental and behavioral disorders. *The world health report*. 2001;2.
  178. Siegel RL, Miller KD, Jemal A. Cancer statistics, 2017. *CA: A Cancer Journal for Clinicians*. 2017;67(1):7-30.
  179. Ward DG, Suggett N, Cheng Y, Wei W, Johnson H, Billingham LJ, Ismail T, Wakelam MJO, Johnson PJ, Martin A. Identification of serum biomarkers for colon cancer by proteomic analysis. *British Journal of Cancer*. 2006;94:1898.
  180. Link A, Balaguer F, Shen Y, Nagasaka T, Lozano JJ, Boland CR, Goel A. Fecal MicroRNAs as novel biomarkers for colon cancer screening. *Cancer Epidemiology, Biomarkers and Prevention*. 2010;19(7)
  181. Issa IA, Noureddine M. Colorectal cancer screening: An updated review of the available options. *World Journal of Gastroenterology*. 2017;23(28):5086-96.
  182. Katz Y, Eitan A, Amiri Z, Gavish M. Dramatic increase in peripheral benzodiazepine binding sites in human colonic adenocarcinoma as compared to normal colon. *European Journal of Pharmacology*. 1988;148(3):483-4.
  183. Katz Y, Eitan A, Gavish M. Increase in peripheral benzodiazepine binding sites in colonic adenocarcinoma. *Oncology*. 1990;47(2):139-42.
  184. Maaser K, Höpfner M, Jansen A, Weisinger G, Gavish M, Kozikowski AP, Weizman A, Carayon P, Riecken EO, Zeitz M, Scherübl H. Specific ligands of the peripheral benzodiazepine receptor induce apoptosis and cell cycle arrest in human colorectal cancer cells. *British Journal of Cancer*. 2001;85(11):1771-80.
  185. Powell AE, Vlacich G, Zhao Z-Y, McKinley ET, Washington MK, Manning HC, Coffey RJ. Inducible loss of one Apc allele in Lrig1-expressing progenitor cells results in multiple distal colonic tumors with

- features of familial adenomatous polyposis. *American Journal of Physiology-Gastrointestinal and Liver Physiology*. 2014;307(1):G16-G23.
186. Suridjan I, Pollock BG, Verhoeff NP, Voineskos AN, Chow T, Rusjan PM, Lobaugh NJ, Houle S, Mulsant BH, Mizrahi R. In-vivo imaging of grey and white matter neuroinflammation in Alzheimer's disease: a positron emission tomography study with a novel radioligand, [18F]-FEPPA. *Molecular Psychiatry*. 2015;20(12):1579-87.
  187. Sonenberg N, Hinnebusch AG. Regulation of Translation Initiation in Eukaryotes: Mechanisms and Biological Targets. *Cell*. 2009;136(4):731-45.
  188. de Sousa Abreu R, Penalva LO, Marcotte EM, Vogel C. Global signatures of protein and mRNA expression levels. *Molecular BioSystems*. 2009;5(12):1512-26.
  189. Fischer BM, Olsen MW, Ley CD, Klausen TL, Mortensen J, Hojgaard L, Kristjansen PE. How few cancer cells can be detected by positron emission tomography? A frequent question addressed by an in vitro study. *European Journal of Nuclear Medicine and Molecular Imaging*. 2006;33(6):697-702.
  190. Lacan G, Plenevaux A, Rubins DJ, Way BM, Defraiteur C, Lemaire C, Aerts J, Luxen A, Cherry SR, Melega WP. Cyclosporine, a P-glycoprotein modulator, increases [18F]MPPF uptake in rat brain and peripheral tissues: microPET and ex vivo studies. *European Journal of Nuclear Medicine and Molecular Imaging*. 2008;35(12):2256-66.
  191. Michel MC, Wieland T, Tsujimoto G. How reliable are G-protein-coupled receptor antibodies? *Naunyn-Schmiedeberg's Archives of Pharmacology*. 2009;379(4):385-8.
  192. Workman P, Aboagye EO, Balkwill F, Balmain A, Bruder G, Chaplin DJ, Double JA, Everitt J, Farningham DAH, Glennie MJ, Kelland LR, Robinson V, Stratford IJ, Tozer GM, Watson S, Wedge SR, Eccles SA, An ad hoc committee of the National Cancer Research I. Guidelines for the welfare and use of animals in cancer research. *British Journal of Cancer*. 2010;102:1555.
  193. Tupone D, Cano G, Morrison SF. Thermoregulatory inversion: a novel thermoregulatory paradigm. *American Journal of Physiology- Regulatory, Integrative and Comparative Physiology*. 2017;312(5):R779-r86.
  194. Kyme AZ, Zhou VW, Meikle SR, Baldock C, Fulton RR. Optimised motion tracking for positron emission tomography studies of brain function in awake rats. *Public Library of Science One*. 2011;6(7):e21727.
  195. Schulz D, Southekal S, Junnarkar SS, Pratte J-F, Purschke ML, Stoll SP, Ravindranath B, Maramraju SH, Krishnamoorthy S, Henn FA, O'Connor P, Woody CL, Schlyer DJ, Vaska P. Simultaneous assessment of rodent behavior and neurochemistry using a miniature positron emission tomograph. *Nature Methods*. 2011;8:347.
  196. Spangler-Bickell MG, de Laat B, Fulton R, Bormans G, Nuyts J. The effect of isoflurane on (18)F-FDG uptake in the rat brain: a fully conscious dynamic PET study using motion compensation. *European Journal of Nuclear Medicine and Molecular Imaging Research*. 2016;6:86.
  197. Jagoda EM, Vaquero JJ, Seidel J, Green MV, Eckelman WC. Experiment assessment of mass effects in the rat: implications for small animal PET imaging. *Nuclear Medicine and Biology*. 2004;31(6):771-9.
  198. Kung M-P, Kung HF. Mass effect of injected dose in small rodent imaging by SPECT and PET. *Nuclear Medicine and Biology*. 2005;32(7):673-8.

199. Yamano K, Inoue M, Masaki S, Saki M, Ichimura M, Satoh M. Generation of adenosine A3 receptor functionally humanized mice for the evaluation of the human antagonists. *Biochemical Pharmacology*. 2006;71(3):294-306.
200. Yaar R, Jones MR, Chen J-F, Ravid K. Animal models for the study of adenosine receptor function. *Journal of Cellular Physiology*. 2005;202(1):9-20.
201. Mittal VK, Bhullar JS, Jayant K. Animal models of human colorectal cancer: Current status, uses and limitations. *World Journal of Gastroenterology*. 2015;21(41):11854-61.
202. Nics L, Vranka C, Hendl M, Haeusler D, Wagner KH, Shanab K, Spreitzer H, Dudczak R, Wadsak W, Mitterhauser M. In-vitro stability of [18F]FE@SUPPPY and [18F]FE@SUPPY:2 against human liver-microsomes and human plasma. *Nuklearmedizin*. 2011;50:A 176.
203. Stemmer SM, Benjaminov O, Medalia G, Ciuraru NB, Silverman MH, Bar-Yehuda S, Fishman S, Harpaz Z, Farbstein M, Cohen S, Patoka R, Singer B, Kerns WD, Fishman P. CF102 for the Treatment of Hepatocellular Carcinoma: A Phase I/II, Open-Label, Dose-Escalation Study. *The Oncologist*. 2013;18(1):25-6.
204. Gao ZG, Joshi BV, Klutz AM, Kim SK, Lee HW, Kim HO, Jeong LS, Jacobson KA. Conversion of A3 adenosine receptor agonists into selective antagonists by modification of the 5'-ribofuran-uronamide moiety. *Bioorganic & medicinal chemistry letters*. 2006;16(3):596-601.
205. Ostuni MA, Issop L, Peranzi G, Walker F, Fasseu M, Elbim C, Papadopoulos V, Lacapere JJ. Over-expression of translocator protein in inflammatory bowel disease: potential diagnostic and treatment value. *Inflammatory Bowel Disease*. 2010;16(9):1476-87.
206. Berroterán-Infante N, Schmitt S, Kalina T, Spreitzer H, Hacker M, Mitterhauser M, Pallitsch K, Wadsak W. [11C]Me@NEBIQUINIDE: A Real Third Generation TSPO PET Tracer? EP-0246 Annual Congress of the European Association of Nuclear Medicine. *European Journal of Nuclear Medicine and Molecular Imaging*. 2017;44(Suppl 2):S534.
207. Berroterán-Infante N, Fetty L, Hacker M, Haug A, Wadsak W, Mitterhauser M. [18F]NEBIQUINIDE: First in vivo experiences of a new third generation TSPO PET tracer. OP-646 Annual Congress of the European Association of Nuclear Medicine: October 13 – 17, 2018 Düsseldorf, Germany. *European Journal of Nuclear Medicine and Molecular Imaging*. 2018;45(1):S207.

# List of Figures

Figure 1: Principles of Positron Emission Tomography (PET).....	4
Figure 2: [ <sup>18</sup> F]FET PET/MRI.....	6
Figure 3: Preparation of Radiopharmaceuticals.....	9
Figure 4: The Ideal Imaging Strategy.....	12
Figure 5: Live/dead Staining of Tumor Spheroids.....	20
Figure 6: <i>Ex vivo</i> tumor autoradiography.....	119
Figure 7: [ <sup>18</sup> F]FE@SUPPY uptake in mouse brain.....	120
Figure 8: <i>Ex vivo</i> metabolic stability.....	121
Figure 9: Solvent effects on the internalization rate of [ <sup>125</sup> I]-AB-MECA.....	122
Figure 10: FE@SUPPY competitively blocks [ <sup>125</sup> I]-AB-MECA internalization.....	122
Figure 11: [ <sup>125</sup> I]-AB-MECA binding to tumor cells.....	123
Figure 12: H&E Staining of tumor spheroids.....	123
Figure 13: A <sub>3</sub> AR expression in multicellular tumor spheroids.....	124
Figure 14: Chemical structures of 2-CI-IB-MECA and MRS3771.....	134